Commission on Controlled Source Seismology (CCSS)
Proceedings of the 1985 Workshop on
Interpretation of Seismic Wave Propagation
in Laterally Heterogeneous Terranes

Susono, Shizouka, Japan
August 15-18, 1985

Interpretations of the SJ-6 seismic reflection/refraction profile, south central California, USA

Editors

Allan W. Walter and Walter D. Mooney
U.S. Geological Survey
345 Middlefield Road
Menlo Park, CA 94025

U.S. Geological Survey
Open-file Report 87-73

Table of Contents

Preface

Critical to scientific progress is a continual assessment of the underlying assumptions and methodologies which are brought to bear on the problems we choose to examine. The Commission on Controlled Source Seismology (CCSS) has attempted over the past ten years to assess the state of controlled source seismology by holding intensive workshops where a common data set is analysed by many individuals or groups. This report summarizes the results of the most recent workshop which analysed coincident seismic reflection and refraction data from south central California, USA. The data set, seismic profile SJ-6, was provided by the U. S. Geological Survey.

The workshop was held from August 15-19, 1985 at FIT (Fuji Institute of Training), Susono, Shizuoka Prefecture, Japan with fourteen scientists from various parts of the world in attendance. This meeting was the fourth workshop to compare the individual analyses of data which had been distributed to the participants beforehand. The Susono meeting focused on the problems of interpreting seismic reflection/refraction data from laterally heterogeneous terranes, and like the previous workshops, discussions during the meeting enhanced the individual analyses. I hope the results summarized in this report are of value, not only to the Susono workshop participants, but also to those who were unable to attend.

Lastly, because the CCSS workshops have been so successful, I think continuing the comparative analyses of seismic data at our future meetings is important. I urge all members of CCSS to stimulate the activity within the CCSS by encouraging discussion amongst us of what should be the focus of our next workshop.

Hideki Shimamura

Hokkaido University
Geophysical Institute
Sapporo, Japan

Introduction

This report presents interpretations by a variety of authors of coincident seismic refraction and reflection data from central California, USA. The purpose of this report is to illustrate and document the various approaches to the analysis of coincident reflection/refraction data currently being employed by seismologists worldwide. The individual papers reproduced here are revised versions of the interpretations presented at the 1985 CCSS workshop in Japan. One of us (AW) has taken the liberty of editing the contributions and we hope that the author's meaning has not been altered by his doing so. It is hoped that this report will contribute to the sophistication with which such data are collected and interpreted, and encourage the collection of new coincident data sets.

The data analysed for this report were distributed in December 1984 to interested individuals who responded to a CCSS circular describing the plans for the August 1985 workshop. The seismic refraction data were collected by the U.S. Geological Survey (USGS) in 1982 as part of a larger investigation of the deep crustal structure of the California Coast Ranges and the adjacent Great Valley. The seismic reflection data (line SJ-6, for San Joaquin Valley line 6) were collected by Western Geophysical in 1981 and were purchased by the USGS in 1983 to complement the seismic refraction data.

For the purposes of the workshop, neither the seismic reflection nor refraction data were made available on magnetic tapes. The refraction data were made available to the investigators in the form of a USGS Open-File Report that included large plates of the record sections displayed in trace normalized and true-amplitude format (Murphy and Walter, 1984). The reflection data were made availble as paper copies of the 12-second record sections in migrated and unmigrated format. Addtional information distributed to participants included a location map and a biography of relevant geologic literature.

To avoid possible biasing of the interpretations, pre-prints or reprints of USGS interpretations of this data were not distributed to the participants. No suggestions were made regarding the method or scope of analysis to be applied to the data. Since the entire data set is rather large it was suggested that investigators should feel free to choose to limit their investigations to a portion of the data.

Acknowledgements

We thank Prof. Stephan Mueller and Jorge Ansorge (both of ETH, Zurich, Switzerland) for their early planning of this meeting and Prof. Hideki Shimamura for his hospitality during the meeting. Not all of the papers in this volume were presented at the meeting in Japan, and we thank those unable to attend for mailing us their contributions. Finally, we thank all of the participants for their enthusiasm and interest in this study.

The Editors

Interpretation of coincident seismic reflection and refraction data in laterally inhomogeneous structure: A discussion of the results

Walter D. Mooney and Allan W. Walter
U.S. Geological Survey
345 Middlefield Road, MS 977
Menlo Park, CA 94025

The papers in this volume present a variety of approaches to the analysis of coincident seismic reflection and refraction data. In this contribution we summarize the various methods of analysis applied to the seismic data and compare various authors' results.

Methods

Several of the papers approached the interpretation of the seismic refraction data separately from the consideration seismic reflection data. papers 2 through 5 (see Table of Contents) used some variation of the following analysis steps (see individual papers for details):

1. Correlation of the phases in the record sections.
2. Identification of these phases as refracted, reflected, or multiple arrivals on the basis of apparent velocity, curvature of the phase's traveltime, parallelism with an earlier traveltime branch, or a similar observation.
3. First-arrival analysis for dipping layers using slope-intercept methods.
4. Mapping of near-surface velocity variations between shotpoints using time-term, delay-time or similar methods.
5. One-dimensional (1-D) interpretation of first and secondary arrivals using Herglotz-Wiechert inversion or rapid iterative traveltime fitting.
6. Creation of a two-dimensional (2-D) model by joining adjacent 1-D models and information from steps 3 and 4. Adjustment of the model via 2-D raytracing.
7. Further refinement of the 2-D model based on the comparison of synthetic seismograms produced by this model with the observed refraction data.

Papers 6 through 9 follow the same basic approach, with the difference that the geometry of the seismic discontinuities in the starting 2-D model was also constrained by the seismic reflection section. The inclusion of information from seismic reflection sections can be regarded as step 6A:

6A. Adjustment of initial 2-D velocity model for consistency with seismic reflection section.

A further refinement of the 2-D model, which has not been presented in this volume but which has since been applied to this data, is the quantitative modeling of the seismic reflection section by calculation of the synthetic seismograms for near-vertical incidence. This is sometimes referred to as "AIMS modeling" in reference to the commonly utilized software package of GeoQuest International. Papers 8 and 9 approximated this comparison by plotting the reflection times on seismic refraction depth sections. We regard this procedure as the last modeling step:

8. Evaluation of seismic refraction 2-D velocity model by comparison of the vertical-incidence synthetic seismograms produced by this model with the observed reflection record section.

Papers 10 and 11 used linearized inversion methods to analyse the seismic refraction data. These methods have the advantage of all inverse methods in that they are less sensitive to the subjective biases of the data analyst. However, it is generally more difficult to include known geologic and geophysical constraints into the inverse modeling, whereas these can easily be included with iterative forward modeling.

Paper 12 applies image processing techniques to a sample of the seismic reflection data. The processing method described in the paper is accompanied by figures which show how various features of the reflection record section can be either highlighted or muted.

Comparison of the Velocity Models

It is not practical to attempt to compare and contrast all of the velocity models presented in this volume. Instead, we describe some of the common features of the models for which the authors have completed at least the first six of the analytic steps described above. In Tables 1 and 3 we list the approximate depths to selected velocity contours below each of the shotpoints and in Tables 2 and 4 we compare the principal structural features present or absent in the models. Tables 1 and 2 describe models east of the San Andreas fault (SP4-SP8) and Tables 3 and 4 describe models west of this fault (SP1-SP4).

Overall, the models east of the San Andreas fault are in closer agreement than those west of the fault. Below, we compare some of the structural features revealed by these models, but we urge the reader to make his or her own detailed comparisons by examining the model illustrations presented in each of the papers.

Models for the eastern section of the SJ-6 profile: SP4-SP7

Velocity models for the eastern SJ-6 profile (Morro Bay to Cholame Valley) are given in papers 3, 4, 6, 7, 9, 10, and 11. Examination of Tables 1 and 2 reveals that all of the models show: the sediments (1.9-5.0 km/s) thickening westward across the San Joaquin Valley, the higher velocity (4.0-5.0 km/s) sedimentary strata elevated between SP5 and SP4 by a eastward thinning wedge of intermediate velocity rocks (5.0-6.0 km/s), and a continuous basement whose average velocity increases rapidly with depth to over 6.5 km/s. In addition, the models of papers 6, 7, 9, and 10 include a low velocity zone (LVZ) within the strata above basement. Paper 10 models the LVZ between SP4 and SP8, whereas the other papers model the LVZ between SP8 and SP5.

The models mostly differ at the top of the basement. The velocity at the top of the basement (V_b) is laterally uniform in all of the models except that of paper 6 which shows V_b decreasing eastward from SP6. West of SP6, the models of papers 4, 9, and 10 show V_b increasing from 6 km/s to 6.5 km/s over a few kilometers of depth, whereas the models of papers 3, 6 and 7 show V_b increasing abruptly to 6.4 km/s or greater. All of the models lack velocity inversions within the basement and all have the higher velocity contours (6.5+ km/s) rising eastward. Paper 10 models the Moho at 27 km depth between SP5 and SP6, but we believe this depth is speculative. It is our assessment that the model which shows the best agreement with both the known geology and the seismic reflection data is that of paper 6.

Models for the western section of the SJ-6 profile: SP1-SP4

Seismic velocity models for the western end of the profile (Morro Bay to Cholame Valley) are given in papers 2, 4, 5, 8, 9, and 10. These models, with the exception of that of paper 2, all show abrupt changes in the shallow velocity structure at the Rinconada and San Andreas faults. Between the Rinconada and San Andreas faults the lower velocity sediments thicken eastward, and below these sediments, the velocities within the Salinian batholith are higher than those modeled at equivalent depths within the Franciscan terranes both west of the Rinconada Fault and east of the San Andreas Fault.

The models significantly differ in the structures proposed for the lower crust. Papers 2 and 10 model the crust below 13 km depth with velocities $\geq$6.5 km/s. However, papers 4, 5 and 8 interpret delayed high-amplitude secondary phases seen on the record sections of shotpoint 1 and 2 as evidence for low velocity zones within the lower crust. The model of paper 4 shows a velocity inversion plunging westward from 4 km depth at the San Andreas Fault to 27 km depth near SP2. In paper 5, the authors project a laterally uniform LVZ across the model between 12.2 km and 22 km depth. And in paper 8, the authors identify three separate LVZs within the lower crust: one plunges eastward from ~12.5 km depth beneath SP1 to 22 km depth just west of SP3, the second is defined at the base of the Salinian batholith (12-14 km depth), and the third is within the San Andreas fault zone. Both papers 5 and 8 model the base of the LVZs near 22 km depth; in paper 5, the base is the top of a 7.0-km/s layer and in paper 8, it is the Moho. Of the two models, we believe that of paper 8 best explains the seismic data in terms of what is presently known about the geologic and tectonic history of the region.

Conclusions

As evident from the discrepancies observed from model to model, there is not agreement everywhere along profile SJ-6. The discrepanices are in part due to the fact that not all of the analyses included all eight of the interpretational steps list above. For example, some authors adopted lower crustal velocities from the literature, some assumed laterally uniform velocities in the middle and lower crust, some did not calculate 2-D synthetics for their velocity models, and some gave no consideration to the constraints provided by the reflection data. It is likely that a more complete modeling by all of the authors would have resulted in closer agreement amongst the models.

Nevertheless, even if all of the interpretational steps are completed, the velocity resolution is still limited by the shortcomings of the data. The reflection data do resolve the geometry where the reflections are absent or ambiguous, and in modeling the refraction data, differences in depth can be traded off against lateral variations in velocity.

The uncertainties in the velocity structure along the SJ-6 profile could be reduced by minimizing the degrees of freedom in the 2-D model. This could most easily and cost effectively be accomplished by increasing the density of the refraction data rather than acquiring additional reflection data. The velocity resolution would improve immensely with:

1) Closer shotpoint spacings (10-15 km). Ideally, shotpoints should be located so that the structure between adjacent shotpoints is uniform (i.e. without any major changes in the dip or composition).

2) Smaller station intervals (<0.5 km). A finer sampling of the travel-time curves would make it easier to detect and correlate seismic phases.

3) An offset between the outermost reversing shotpoints large enough to record a reversed P_n phase. The lower crustal velocities are better constrained once the depth and geometry of the Moho is determined.

4) Additional seismic profiles recorded within and parallel to the structural strike of the terranes crossed by profile SJ-6. These supplementary profiles would intersect the SJ6 profile thereby tying the structures of the separate terranes to the modeled cross-section.

Table 1

Eastern SJ-6 profile
Approximate depth to velocity contours

Site	Velocity (km/s)	Paper Number in Table of Contents 3	4	6	7	9	10	10B*	11
SP4	4.0+	-1	-1	-1	-1	-1	1.1	-1	-1
	5.0+	3.6	6.5	3.5	3.2	2.5	2.0	6.1	-
	5.5+	13.5	12.5	17.0	3.2	14.0	2.5	10.0	-
	6.0+	13.5	16.0	17.0	16.0	14.0	10.0	12.8	-
	6.5+	13.5	21.0	17.0	16.0	17.5	11.0	15.7	-
	7.0+	-	25.0	-	21.0	-	20.0	21.2	-
SP8	4.0+	1.4	1.3	1.3	2.1	1.6	1.4	2.0	2.0
	5.0+	5.8	5.6	6.4	6.5	4.2	2.0	4.4	4.5
	5.5+	13.4	8.3	14.8	6.5	13.0	2.5	10.2	-
	6.0+	13.4	11.7	14.8	15.2	13.2	12.2	13.0	-
	6.5+	13.4	16.5	14.8	15.2	16.7	16.0	15.8	-
	7.0+	-	21.0	-	20.2	-	20.0	21.3	-
SP5	4.0+	4.9	4.8	4.6	4.4	4.8	3.2	3.6	4.0
	5.0+	7.9	9.0	7.7	8.8	6.8	6.8	5.7	7.0
	5.5+	9.4	9.0	8.7	8.8	9.9	8.8	8.0	9.2
	6.0+	9.4	9.0	8.7	8.8	9.9	9.2	9.5	11.6
	6.5+	9.4	12.1	8.7	8.8	13.0	11.0	11.5	12.7
	7.0+	-	19.1	20.0	14.0	19.9	19.2	18.9	14.2
SP6	4.0+	4.0	4.2	3.8	4.0	3.7	3.6	3.8	3.3
	5.0+	5.7	5.7	5.7	5.6	4.8	4.9	5.5	5.0
	5.5+	5.7	5.7	5.7	5.6	5.9	6.0	6.1	5.7
	6.0+	5.7	5.7	5.7	5.6	5.9	6.4	6.8	6.7
	6.5+	5.7	8.8	6.7	5.6	8.0	8.3	7.2	7.7
	7.0+	-	15.3	19.0	11.0	15.8	20.4	15.7	11.7
SP7	4.0+	-	1.6	1.1	-	1.5	1.0	1.5	-
	5.0+	-	1.6	1.1	-	2.0	1.3	1.9	-
	5.5+	-	1.6	1.1	-	2.2	1.4	2.2	-
	6.0+	-	1.6	2.7	-	2.3	1.6	2.5	-
	6.5+	-	4.6	6.0	-	3.2	3.5	3.0	-
	7.0+	-	11.7	16.0	-	-	21.0	11.2	-

Table symbol code:
decimal numbers indicate approximate depth in kilometers
-1 = less than 1.0 km depth
- = outside the boundaries of the velocity model

*Paper 10 has two models, 10B is the model of Baranova.

Table 2

Eastern SJ-6 profile
Elements of 2-D velocity models from SP4-SP7:

1. Westward thickening of higher velocity sedimentary units
2. Elevation of higher velocity sedimentary units west of SP5
3. LVZ within strata above basement
4. Wedge of 5.0 to 6.0-km/s rocks west of SP5
5. Continuous westward dipping basement surface
6. Velocity near top of crystalline basement <6.2 km/s at SP6
7. Laterally uniform velocity modeled along top of basement
8. LVZ within basement
9. Lower crust with velocities $\geq$ 6.9 km/s
10. 6.5-km/s velocity contours rise to depths < 5 km east of SP7
11. Moho modeled: depth (km)

		Paper Number in Table of Contents							
		3	4	6	7	9	10	10B*	11
Element	1.	Y	Y	Y	Y	Y	Y	Y	Y
	2.	Y	Y	Y	Y	Y	Y	Y	Y
	3.	N	N	Y	Y	Y	Y	N	N
	4.	Y	Y	Y	Y	Y	Y	Y	Y
	5.	Y	Y	Y	Y	Y	Y	Y	Y
	6.	N	Y	N	N	Y	Y	Y	Y
	7.	Y	Y	N	Y	Y	Y	Y	Y
	8.	N	N	N	N	N	N	N	N
	9.	-	Y	Y	Y	Y	Y	Y	Y
	10.	-	Y	N	Y	Y	Y	Y	-
	11.	-	>27	-	-	-	27	>30	-

Table symbol code:
Y = yes
N = no
- = outside the boundaries of the velocity model

*Paper 10 has two models, 10B is the model of Baranova.

Table 3

Western SJ-6 profile
Approximate depths to velocity contours

Site	Velocity (km/s)	Paper Number in Table of Contents 2	4	5	8	9	10	10B*
SP1	4.0+	-1	-1	-1	-1	-1	-1	-1
	5.0+	3.4	5.0	2.9	2.8	3.8	4.3	2.4
	5.5+	3.4	7.3	3.8	4.5	5.1	7.4	5.8
	6.0+	12.2	10.0	4.0	LVZ	6.2	8.6	9.2
	6.5+	12.2	13.0	LVZ	-	-	13.	11.4
	7.0+	24.7	27.0	22.0	-	-	-	16.0
SP2	4.0+	-1	-1	-1	-1	-1	1.0	-1
	5.0+	3.0	1.0	2.0	2.0	-1	1.4	-1
	5.5+	3.0	1.5	4.4	4.3	-1	5.0	3.2
	6.0+	12.2	2.0	5.8	10.0	1.1	6.1	8.0
	6.5+	12.2	9.1	LVZ	LVZ	-	10.8	11.4
	7.0+	24.7	27.0	22.0	22.0	-	-	16.0
SP3	4.0+	-1	2.0	1.7	1.5	1.4	2.0	1.7
	5.0+	1.9	2.0	1.8	2.5	2.6	2.4	2.6
	5.5+	1.9	2.0	2.0	3.3	2.6	3.1	3.0
	6.0+	12.2	2.4	8.0	5.1	2.6	3.9	4.6
	6.5+	12.2	9.8	LVZ	LVZ	-	8.0	8.2
	7.0+	-	LVZ	22.0	22.5	-	-	15.7
SP4	4.0+	-1	1.8	1.0	1.0	-	1.1	-1
	5.0+	2.7	4.0	3.3	3.1	-	2.0	6.1
	5.5+	2.7	4.0	3.9	5.8	-	7.1	9.8
	6.0+	12.2	4.0	4.9	-	-	10.0	12.8
	6.5+	12.2	LVZ	LVZ	-	-	11.0	15.7
	7.0+	-	-	22.0	-	-	-	21.2

Table symbol code:
decimal numbers indicate approximate depth in kilometers
LVZ = low velocity zone
-1 = less than 1.0 km depth
- = outside the boundaries of the velocity model

*Paper 10 has two models, 10B is the model of Baranova.

Table 4

Western SJ-6 profile
Elements of 2-D velocity models from SP1-SP4:

1. Lateral change in shallow structure across Rinconada Fault
2. Lateral change in deep structure across Rinconada Fault
3. Lateral change in shallow structure across San Andreas Fault
4. Lateral change in deep structure across San Andreas Fault
5. Depression of velocity contours (LVZ) at San Andreas Fault
6. Eastward thickening of sedimentary strata between SP2 and SP3
7. V_{ave} of Franciscan rocks (SP1) < V_{ave} of Salinian batholith (SP3)
8. LVZ in lower crust beneath SP 2: depth to top (km)
9. LVZ in lower crust beneath SP 3: depth to top (km)
10. Lower crustal layer with velocities $\geq$ 6.5 km/s west of SP2
11. Lower crustal layer with velocities $\geq$ 6.5 km/s east of SP2
12. Moho modeled: depth (km)

		Paper Number in Table of Contents						
		2	4	5	8	9	10	10B*
Element	1.	N	Y	N	Y	Y	Y	Y
	2.	N	N	N	N	N	N	N
	3.	N	Y	Y	Y	Y	Y	Y
	4.	N	Y	N	Y	-	Y	Y
	5.	N	Y	N	Y	N	N	N
	6.	Y	Y	Y	Y	Y	Y	Y
	7.	Y	Y	N	Y	Y	Y	Y
	8.	N	N	9.7	15	-	N	N
	9.	N	16.4	9.7	13.5	-	N	N
	10.	Y	Y	Y	N	-	Y	Y
	11.	Y	Y	Y	N	-	Y	Y
	12.	25	27	>30	22	-	-	>30

Table symbol code:
Y = yes
N = no
- = outside the boundaries of the velocity model

*Paper 10 has two models, 10B is the model of Baranova.

Upper-crustal velocity structure between Morro Bay and the San Joaquin Valley, California, USA, as determined from seismic-refraction data

Kiyoshi Ito
Regional Center for Earthquake Prediction,
Faculty of science, Kyoto University

The upper-crustal P-wave velocity structure between Morro Bay and the San Joaquin Valley was modeled from seismic-refraction data provided by the U.S.G.S. (Murphy and Walter, 1984). The analyzed profile extends northeasterly from Morro Bay to the Kettleman Hills through four shotpoints (SP1-SP4) and ~70 observation sites. The total profile length is ~100 km and the site spacing is 1-3 km. The first-arrival traveltimes from the four shotpoints were analyzed in two stages to derive a crustal velocity model.

For the first stage, the dipping-layer slope-intercept method was applied to the first arrivals of the three pairs of adjacent shots: SP1-SP2, SP2-SP3 and SP3-SP4. The apparent velocities of the first-arrivals suggests two sedimentary layers overlying a crystalline basement. Traveltime curves for these three refractors were selected to satisfy the reciprocity of traveltimes between reversing shotpoints. Moreover, the time-term method was applied to all refractions through the basement layer to determine a mean basement velocity. The average shot spacing, ~25 km, is too large to determine the velocity throughout the surface layer, so the surface layer velocity at each shotpoint was extrapolated to half the distance to the next shotpoint. The velocity structures calculated for the three pairs of adjacent shotpoints were combined into a composite 2-D structure by modifying the boundary depths so that the boundaries continue smoothly beneath SP2 and SP3.

For the second stage of analysis, the 2-D ray-tracing method (Červený and others, 1977) was applied to the composite model; the velocity structure was then iteratively modified to improve the agreement between the calculated and observed traveltimes. Observed secondary arrivals from the deep crust were fit by assuming a horizontally-layered uniform velocity structure similar to that reported by Walter and Mooney (1982).

The final 2-D velocity model is shown in Figure 1. The velocities within the sedimentary strata vary from 2.0 to 4.9 km/s, and the velocity at the top of the basement varies from 5.7 km/s in the southwest to 5.9 km/s in the northeast. The mean upper basement velocity determined by the time-term method is 5.9 km/s. Between Morro Bay (SP1) and the San Andreas Fault (SP4), the depth of the sediment-basement boundary ranges from 3.2 to 2 km with offsets at the Riconada Fault (SP2) and northeast of SP3. Northeast of SP4, the basement plunges to ~8 km depth beneath the Kettleman Hills; however, the depth here is not well-constrained because this section of the profile is unreversed. Additional horizontal velocity boundaries were inserted in the model at ~12 and ~25 km depth to define the top of the lower crust and the Moho; these boundaries were based on the velocity structures reported for similar geologic terranes (Walter and Mooney, 1982). The lower crust was assumed to have an average velocity of 6.5 km/s and the velocity below the Moho was assumed to be 7.9 km/s.

References

Červený, V., I.A. Moltikov, and I. Pšenčík, 1977, Ray method in seismology, Univ. Karlova, Prague, 214 p.

Murphy, J. M. and A. W. Walter, 1984, Data report for a seismic-refraction investigation: Morro Bay to the Sierra Nevada, California, U.S. Geol. Surv. Open-File Rep. 84-642.

Walter, A. W., and W. D. Mooney, 1982, Crustal Structure of the Diablo and Gabilan Ranges, Central California, Bull. Seism. Soc. Amer. 72, pp. 1567-1590.

Figure Caption

Fig. 1 Velocity cross-section between Morro Bay and the Kettleman Hills. Model was derived by 2-D ray-trace modeling of the refraction traveltimes recorded from shotpoints (SP) 1-4 of line SJ-6.

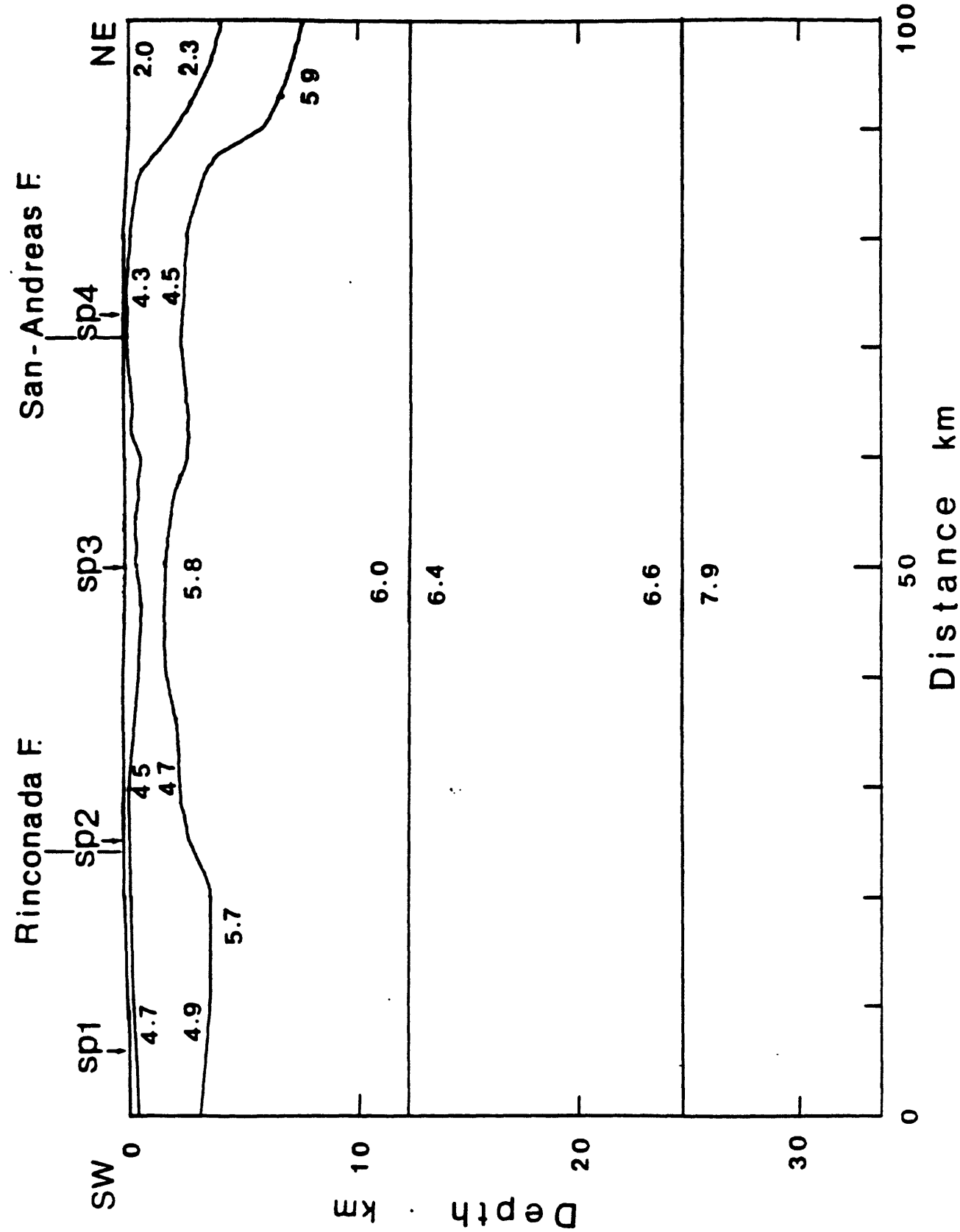
SW
NE
Rinconada F.
San-Andreas F.
sp1
sp2
sp3
sp4
4.7
4.9
4.5
4.7
5.7
5.8
4.3
4.5
2.0
2.3
5.9
6.0
6.4
6.6
7.9
0
10
20
30
Depth · km
0
50
100
Distance km

An interpretation of the seismic-refraction data recorded between Cholame Valley and the Sierra Nevada, California, USA

Kazuki Kohketsu and Shuzo Asano
Earthquake Research Institute
University of Tokyo, Tokyo, Japan

The crustal velocity structure along the section of line SJ-6 that lies between the San Andreas Fault and the Sierra Nevada foothills was imaged using the first-arrival traveltime data recorded from four shotpoints: SP4, SP8, SP5, and SP6 (Murphy and Walter, 1984). Data from the adjacent seismic-reflection survey were used to constrain the model geometry.

Interpretation

1. Western and eastern ends of the profile

The velocity structures at the western and the eastern ends of the profile, in the Diablo Range and the San Joaquin Valley, respectively, were obtained by classical dipping-layer analysis of the first-arrival traveltimes (Fig. 1). In the Diablo Range, the data of SP4 and SP8 reveal a 2.65-km/s surface layer overlying a 4.45-km/s layer. The 2.65-km/s traveltime branch has non-zero intercept time at SP8, so an additional thin layer of lower velocity sediments must exist there. In the San Joaquin Valley the data of SP5 and SP6 reveal three layers: 1.90, 3.47, and 6.58-km/s, and based on the results derived for the Diablo Range, we assumed a 4.5-km/s layer exists between the 3.47 and 6.58-km/s layers.

These initial velocity structures were refined by ray-tracing calculations which included the surface topography (SEIS83, Červený and Pšenčík, 1983). The structure was modeled using a linear vertical interpolation between isovelocity interfaces, that is, the model was specified by giving only the 2-D shape of the interfaces and velocities immediately above and below them. Ray-traced model diagrams and traveltime plots for the eastern and western ends of the profile are shown in Figure 2.

2. Whole model

We constructed a composite velocity cross-section for the entire profile (SP4-SP6) by integrating the velocity structures derived for the Diablo Range and San Joaquin Valley. This was accomplished using the 2-D ray-tracing method with the following constraints:

1) For the central section of the profile, SP8-SP5, the initial boundary shapes were adapted from the seismic-reflection section which shows a folded structure across South Dome of the Kettleman Hills.
2) Because the velocity of the surface layer differs at the respective ends of the profile (2.65 and 1.90 km/s), we divided the surface layer into two segments with different, but laterally uniform, velocities east and west of South Dome; the bottom of this layer was then determined by iterative ray tracings for the profiles SP8 East and SP5 West (Fig. 3a-b).
3) The 3.5-km/s layer observed in the San Joaquin Valley was assumed to vanish near SP8 because it is not observed in the Diablo Range to the west.
4) A 5.35-km/s layer was introduced into the western half of the model in order to model the apparent velocities of the first arrivals observed at ranges beyond 30 km west of SP5 (Fig. 3b) and at ranges 25-50 km east of SP4 (Fig. 4a).
5) The deepest layer in the composite model was assumed to have a velocity of ~6.5 km/s because this value was obtained for the fourth layer under

the San Joaquin Valley. The shape of the upper boundary of the deepest layer is constrained by the refraction data recorded at distant observation sites on the reversed profile between SP4 and SP6 (Fig. 4). The upper boundary of the deepest layer is almost flat from SP4 to 40 km east from which point it rises eastward under the San Joaquin Valley.

Discussion

Our final composite velocity model is shown in Figures 5 and 6. The following points remain for further refinement of the model:

1) The vertical boundary in the top layer could be moved horizontally up to 5 km. If it is relocated, the shape of the lower boundary requires modification to maintain the agreement between the calculated and observed traveltimes.

2) An unexplained traveltime advance of 0.2 s is observed ~35 km west of SP5 (Fig 3b); thus, further adjustments are needed for the upper boundary of the 5.35-km/s layer under the South Dome.

3) Under the Diablo Range the depth to the upper boundary of the deepest modeled layer was not well-constrained because the only data available for constraints are from SP6 West (Fig. 4b).

References

Červený, V. and I. Pšenčík, 1983, 2-D Seismic Ray Package, SEIS83, Prague.

Murphy, J.M. and A.W. Walter, 1984, Data Report for a Seismic-Refraction Investigation: Morro Bay to the Sierra Nevada, California, U.S. Geol. Surv. Open-File Rep. 84-642.

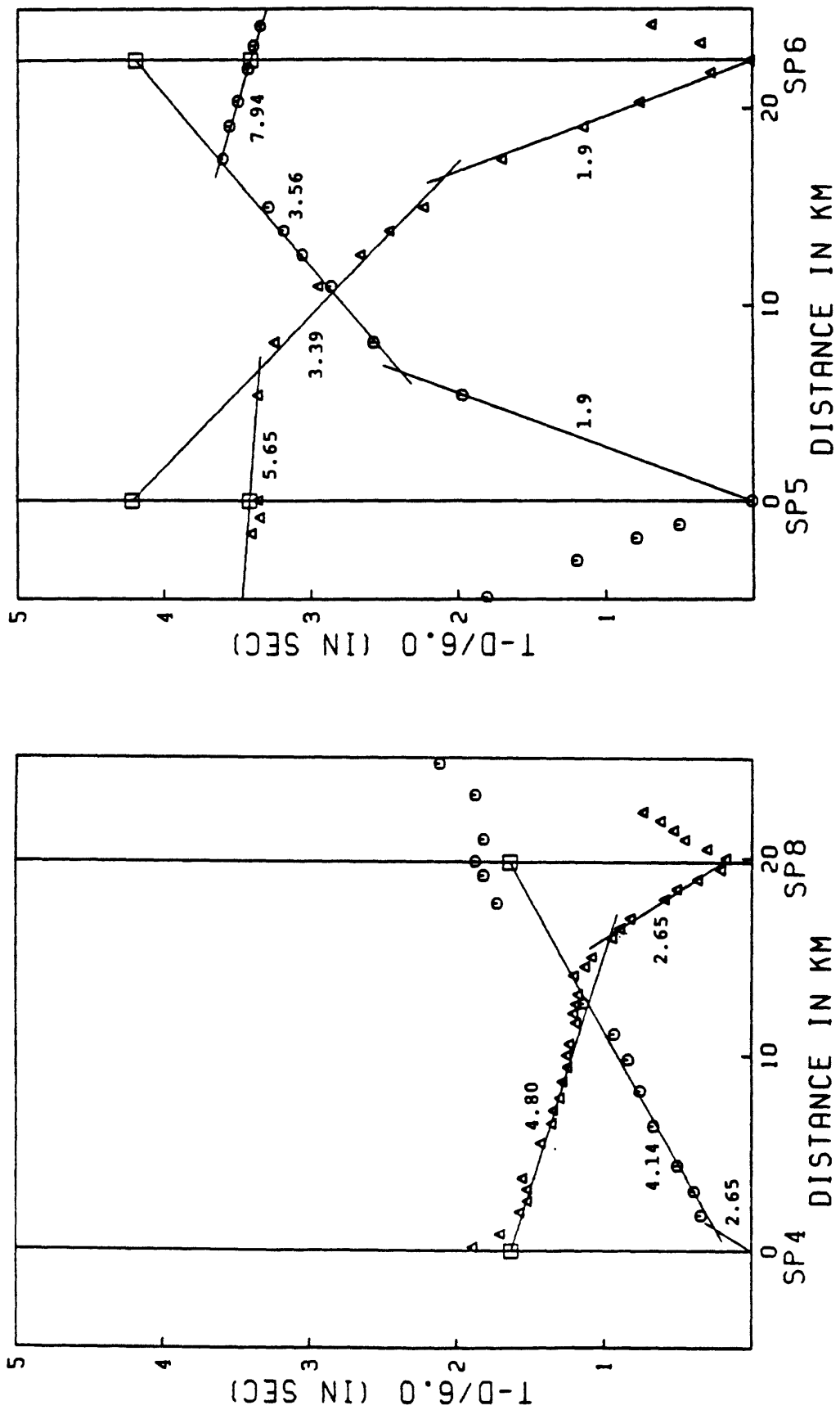

Fig.1. Reduced travel time plots of the reversed profiles (a) SP4-SP8 and (b) SP5-SP6. Numbers beside lines are P-wave velocities in km/sec. Squares indicate reciprocating travel times.

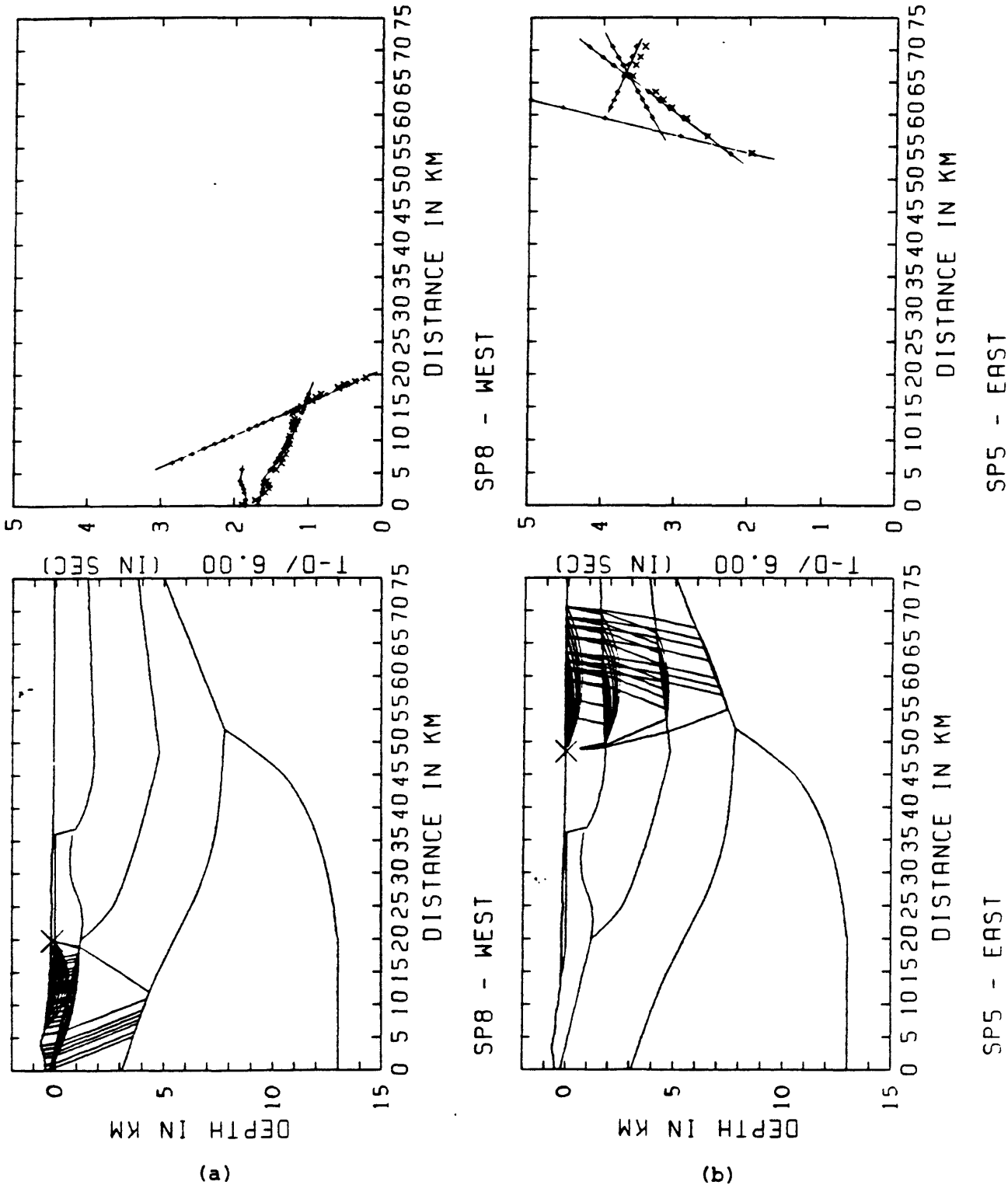

Fig.2. Ray and travel time diagrams for the (a) western and (b) eastern profiles. In travel time diagrams big crosses indicate observed arrivals, and small pluses combined by curves are calculated ones.

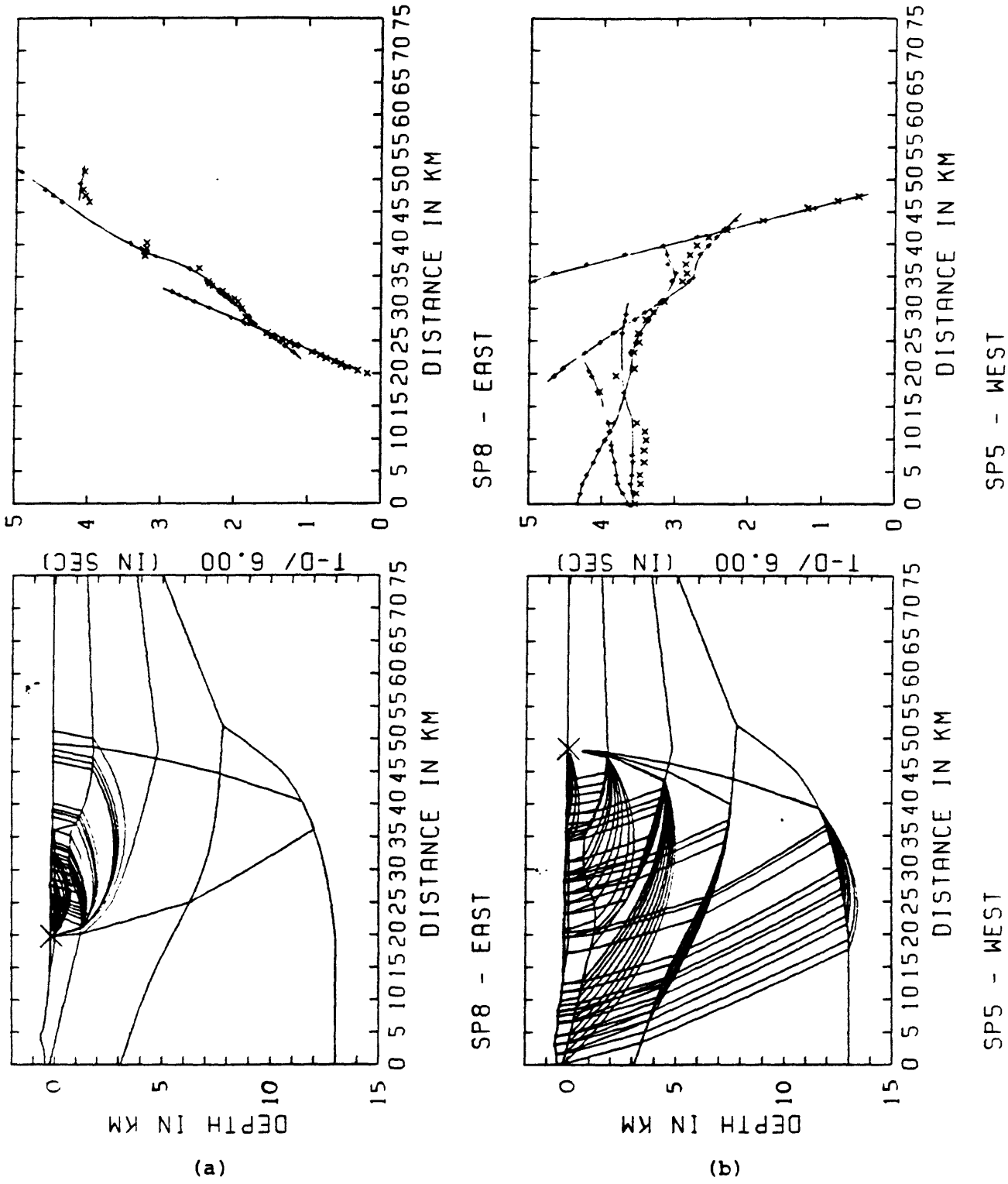

Fig.3. Ray and travel time diagrams for the profiles (a) SP8 East and (b) SP5 West. These profiles are situated near South Dome in the central part of the whole profile.

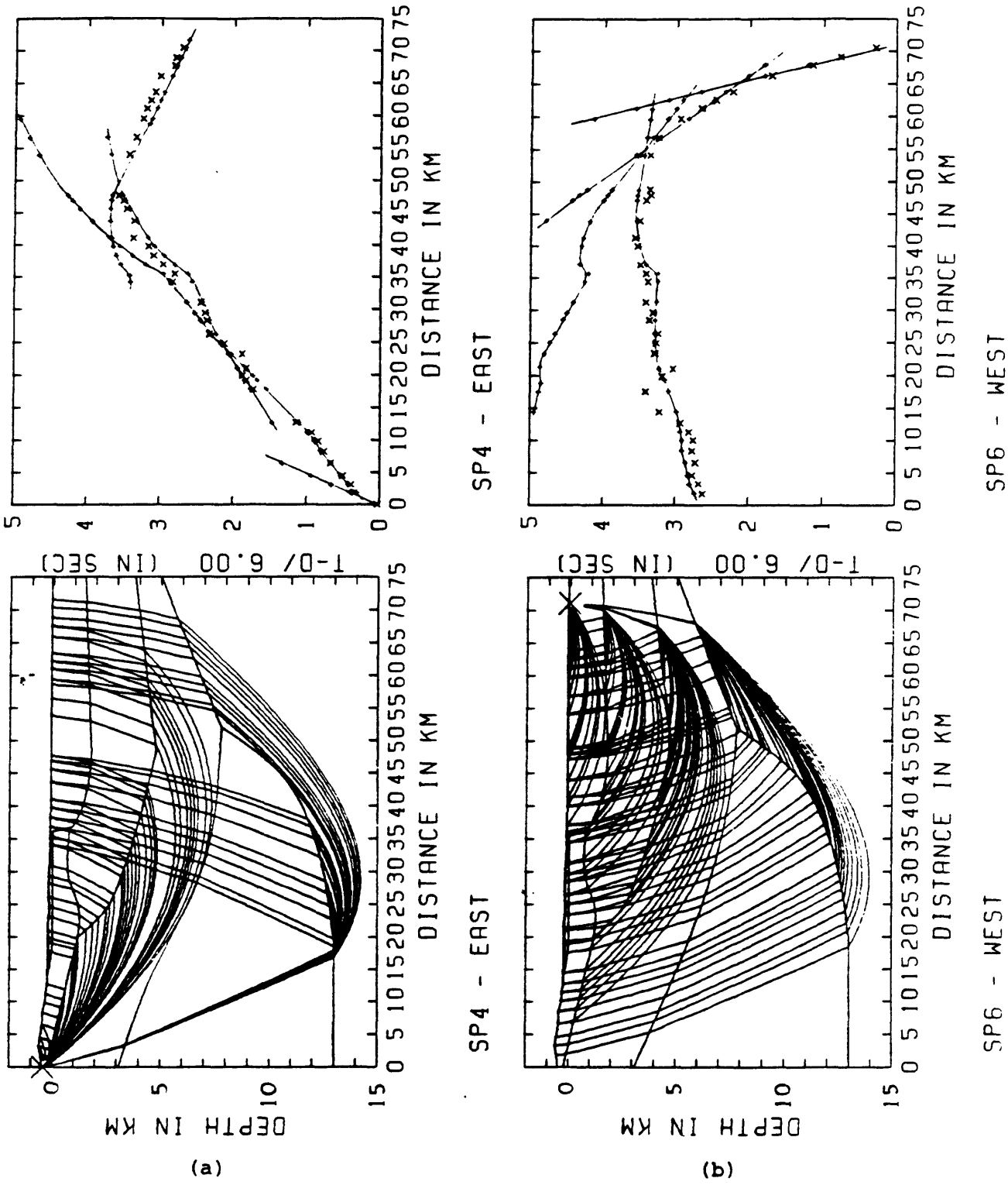

Fig.4. Ray and travel time diagrams for the long-ranges in the profiles (a) SP4 East and (b) SP6 West.

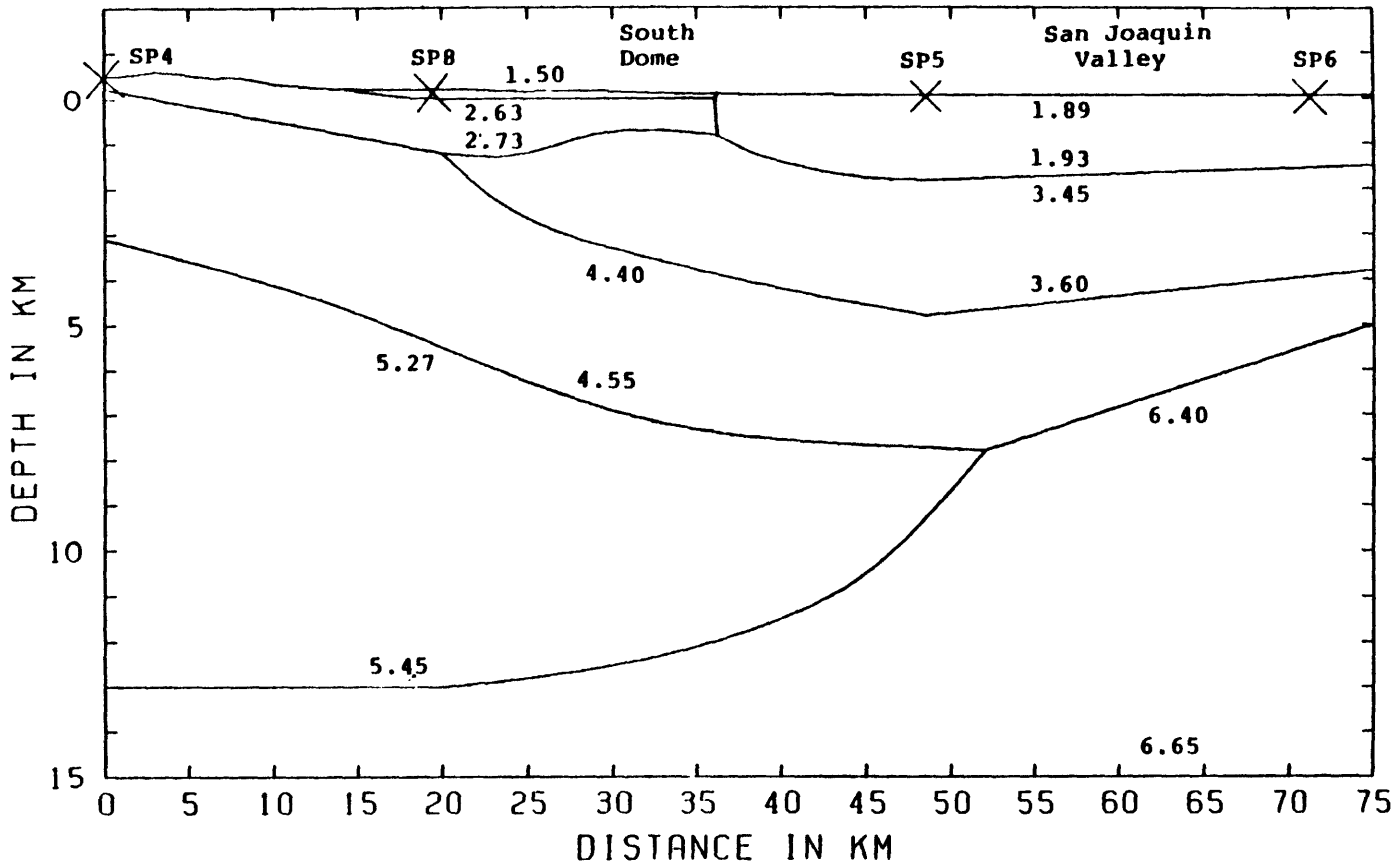

Fig.5. Final velocity model along the whole profile from Cholame Valley to Sierra Nevada. Numbers immediately above or below interfaces are P-wave velocities in km/sec. A velocity varies linearly with a depth in each layer.

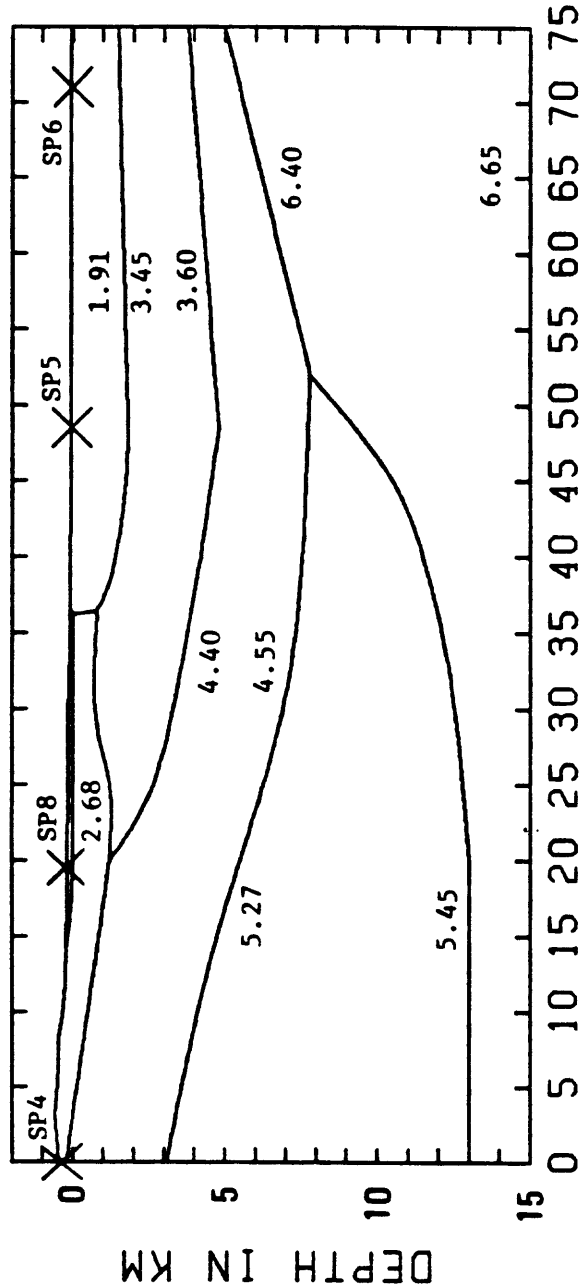

Fig.6. Final velocity model. Horizontal scale 1:500000.

An interpretation of the seismic-refraction data recorded along profile SJ-6: Morro Bay-Sierra Nevada, California, USA

R. F. Mereu
Dept. of Geophysics, University of Western Ontario
London, Ontario, Canada, N6A5B7

Modeling procedure

The seismic-refraction data were modeled using an iterative 2-D ray-tracing method. First, a simple starting velocity model was created from a delay-time analysis of the first arrivals. In order to handle both vertically and laterally varying structures, this model was divided up into a set of triangular blocks, each with its own linear velocity gradient. This form of the gradient ensured that the ray-paths traced within each block formed an arc of a circle, thus enabling the rays to be traced relatively quickly.

For a given modeling iteration, rays were traced from the source locations in the model and their calculated traveltimes were compared to the observed data. Small adjustments were then made to the gradients and boundary positions to improve the fit between the theoretical and all observed traveltimes. These adjustments were made by varying both the positions of the vertices as well as the seismic velocity at each vertex. The modeling iterations continued until a good fit was obtained between the theoretical and observed traveltimes. Further refinements to model were then made using a program which generates synthetic seismograms for laterally and vertically varying structures. Details of this program were given at the 1983 workshop held at Einsiedeln, Switzerland (Mereu, 1983).

Modeling results

The final block model for the profile, which required 184 triangles, is shown in Figure 1. The final velocity model with boundaries and smoothed velocity contour lines is shown in Figure 2a for the section west of the San Andreas Fault and in Figure 2b for the section east of the fault. Ray-traced model diagrams for seven of the eight shotpoints, SP1-SP6 and SP8, are shown in Figures 3a-g, and time-distance plots comparing the calculated traveltimes and observed traveltimes from these shotpoints are shown in Figures 4a-g. Synthetic record sections for SP4, SP5, and SP6 are shown in Figures 5a-c.

Conclusions

1) It is assumed that the 6-km/s contour line marks the boundary between the sedimentary rocks and the basement.
2) Near surface velocities vary laterally from a low value of ~1.9 km/s near SP5 to ~5 km/s in areas where the sediments are thin or absent such as near SP2 and SP4.
3) The shallow velocity structure differs east and west the Rinconada Fault. The basement is closer to the surface on the east side of the fault.
4) The sedimentary strata found west of the San Andreas Fault are relatively thin and broken compared to those found east of the fault.
5) West of the San Andreas Fault, a reflector, possibly the Moho, is modeled at a depth of 27 km to account for a set of secondary arrivals seen on the record section of SP1.
6) The San Andreas Fault effects the refraction observations in that the refractions do not directly cross it. A wedge of low-velocity material had to be inserted in the San Andreas frontal zone so that energy arriving

from the west would be deflected downwards and arrive at the surface at a delayed time. The manner in which this is done may be seen in Figures 3a-c. Interestingly, the fault trace is not imaged by the adjacent seismic-reflection survey along line SJ-6.

7) East of the San Andreas Fault and west of SP5 in the San Joaquin Valley, an 11-km thick section of sedimentary strata is deformed to such a degree that the seismic-reflection method poorly images the deep structure in this area (Fig. 2b). The seismic-refraction observations suggest a relatively horizontal basement beneath the folded sediments.
8) Across the San Joaquin Valley (SP5-SP7), the basement uniformly rises towards the surface with the overlying wedge of sediments being undisturbed.

Acknowledgements

I would like to thank the hosts Professor S. Asano and Professor H. Shimamura and their colleagues for the work they have done in selecting the site and making the workshop in Susono a great success. Special thanks also be extended to Dr. W. D. Mooney and his colleagues at the U. S. Geological Survey for kindly supplying us with a very interesting data set.

This research was supported by the Canadian Natural Sciences and Engineering Research Grant No. A1793.

References

Mereu, R.F., 1983, The generation of synthetic seismograms for 2-D laterally inhomogeneous media, in The International Association of Seismology and Physics of the Earth's Interior - Commission on Controlled Source Seismology Workshop Meeting on "The interpretation of seismic wave propagation in laterally heterogeneous structures", Einseideln, Switzerland.

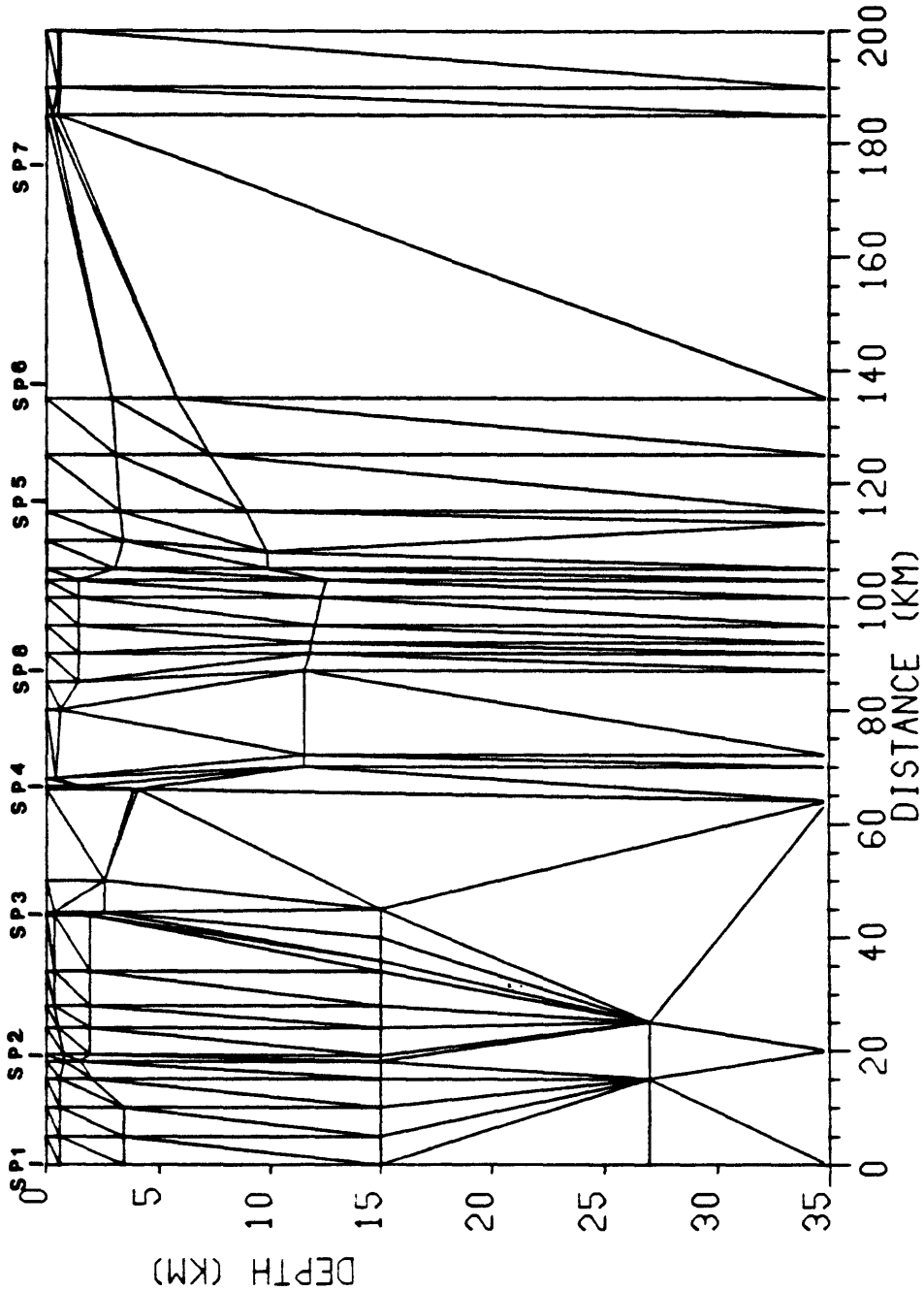

Figure 1. Triangular block model

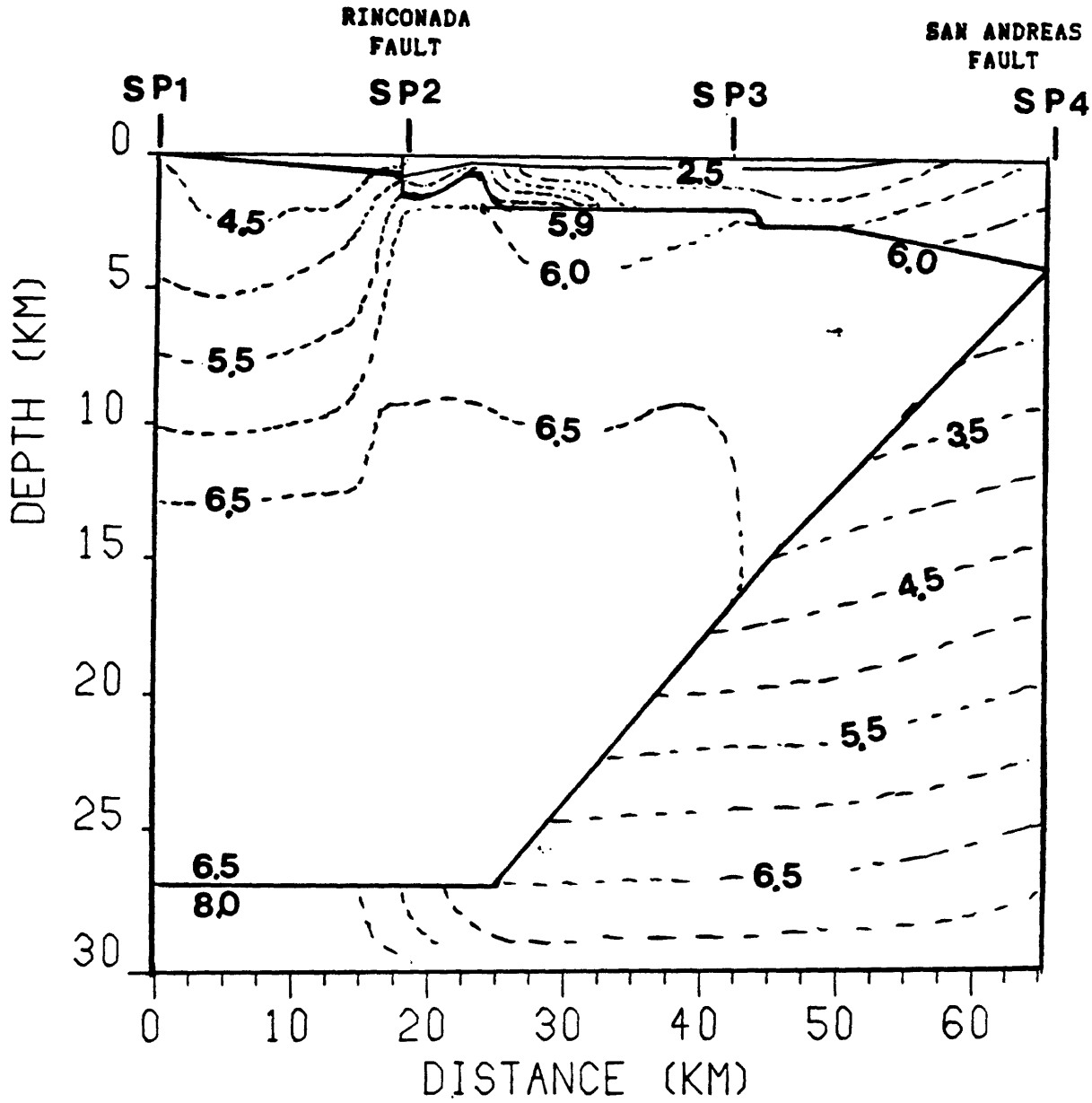

Figure 2a. Final model for area west of San Andreas fault. Dotted lines are velocity contour lines. Solid lines are discontinuities.

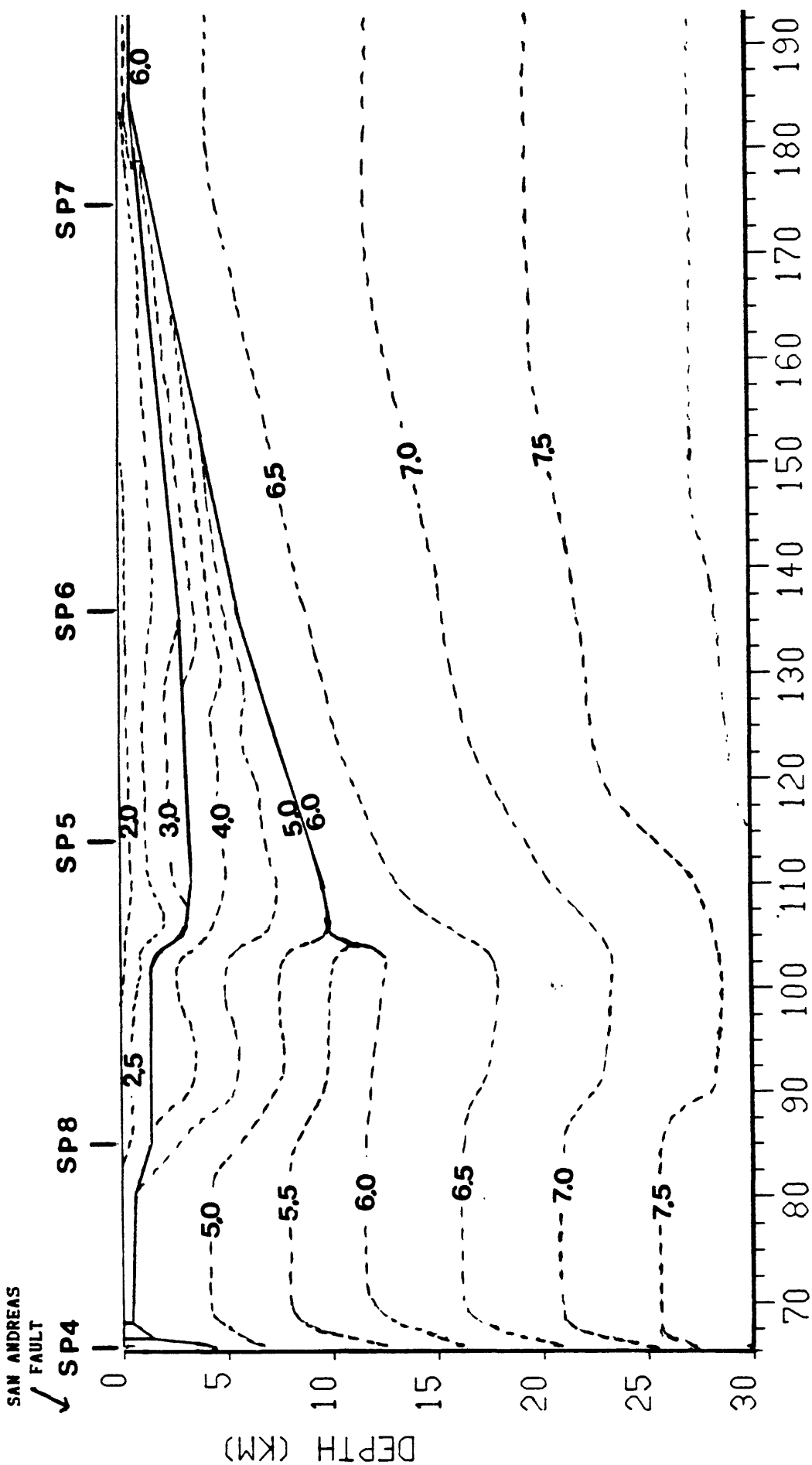

Figure 2b. Final model for area east of San Andreas fault.
Dotted lines are velocity contour lines.
Solid lines are discontinuities.

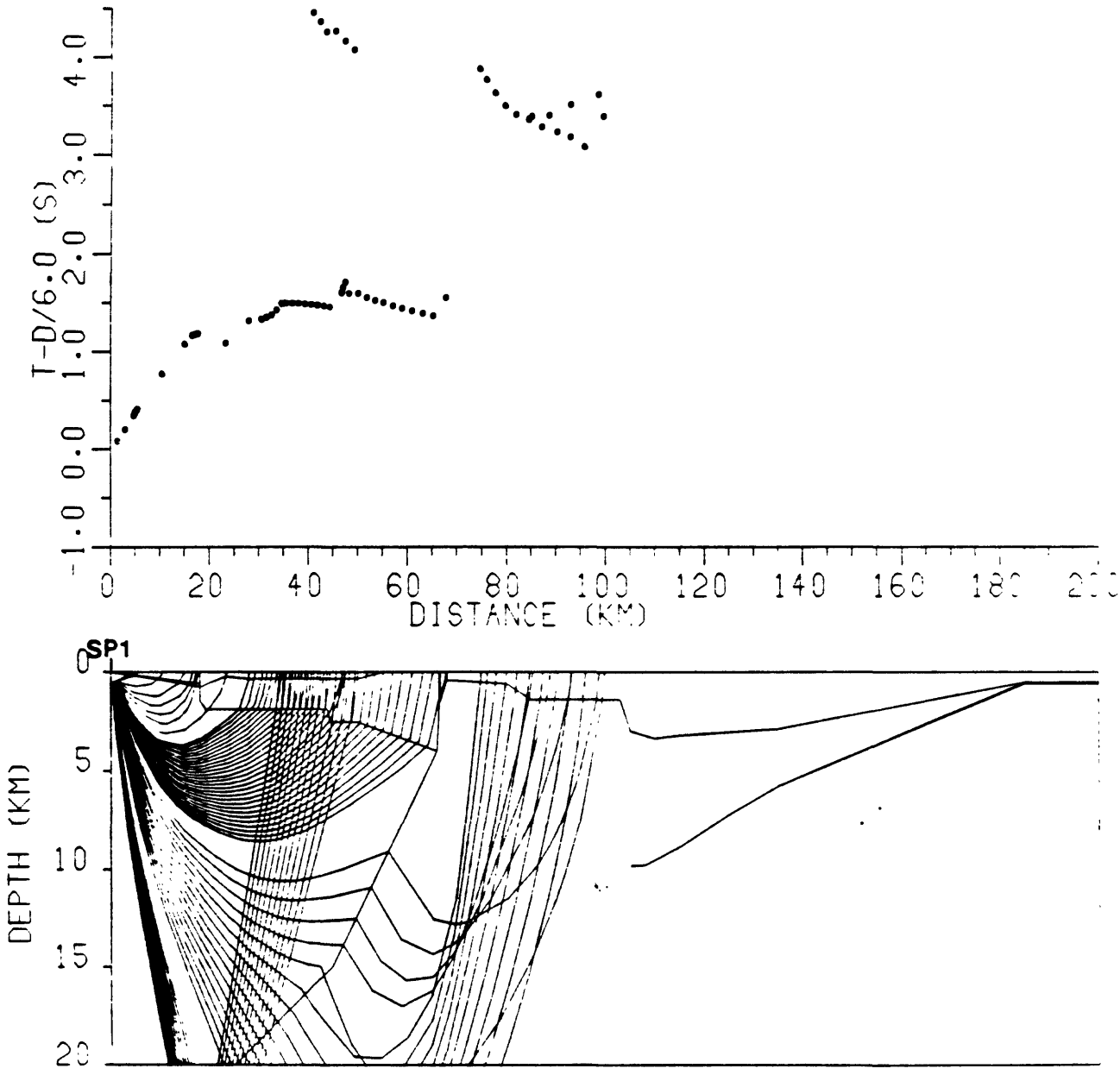

Figure 3a. Ray tracing diagram for Shot Point 1.

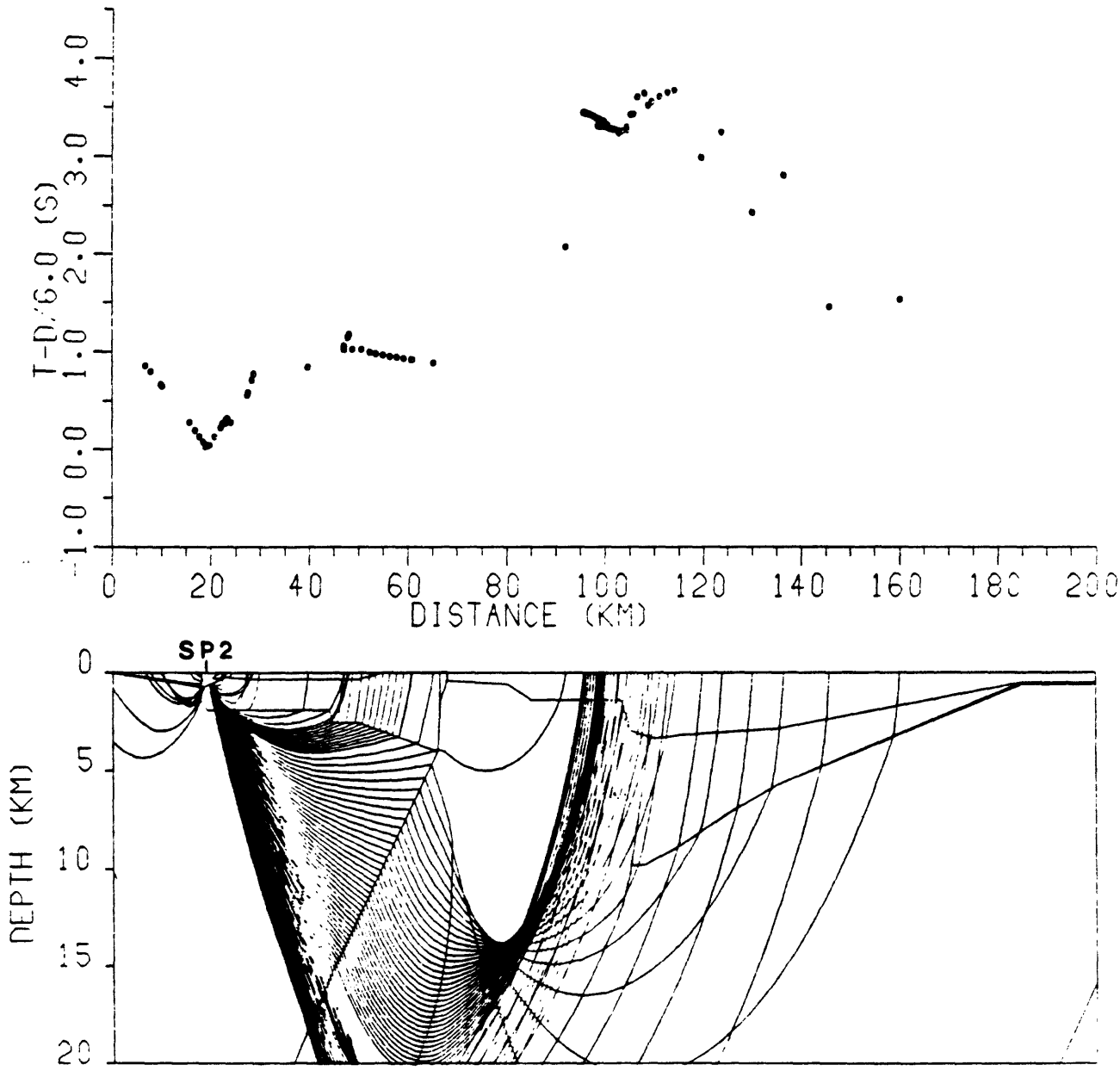

Figure 3b. Ray tracing diagram for Shot Point 2.

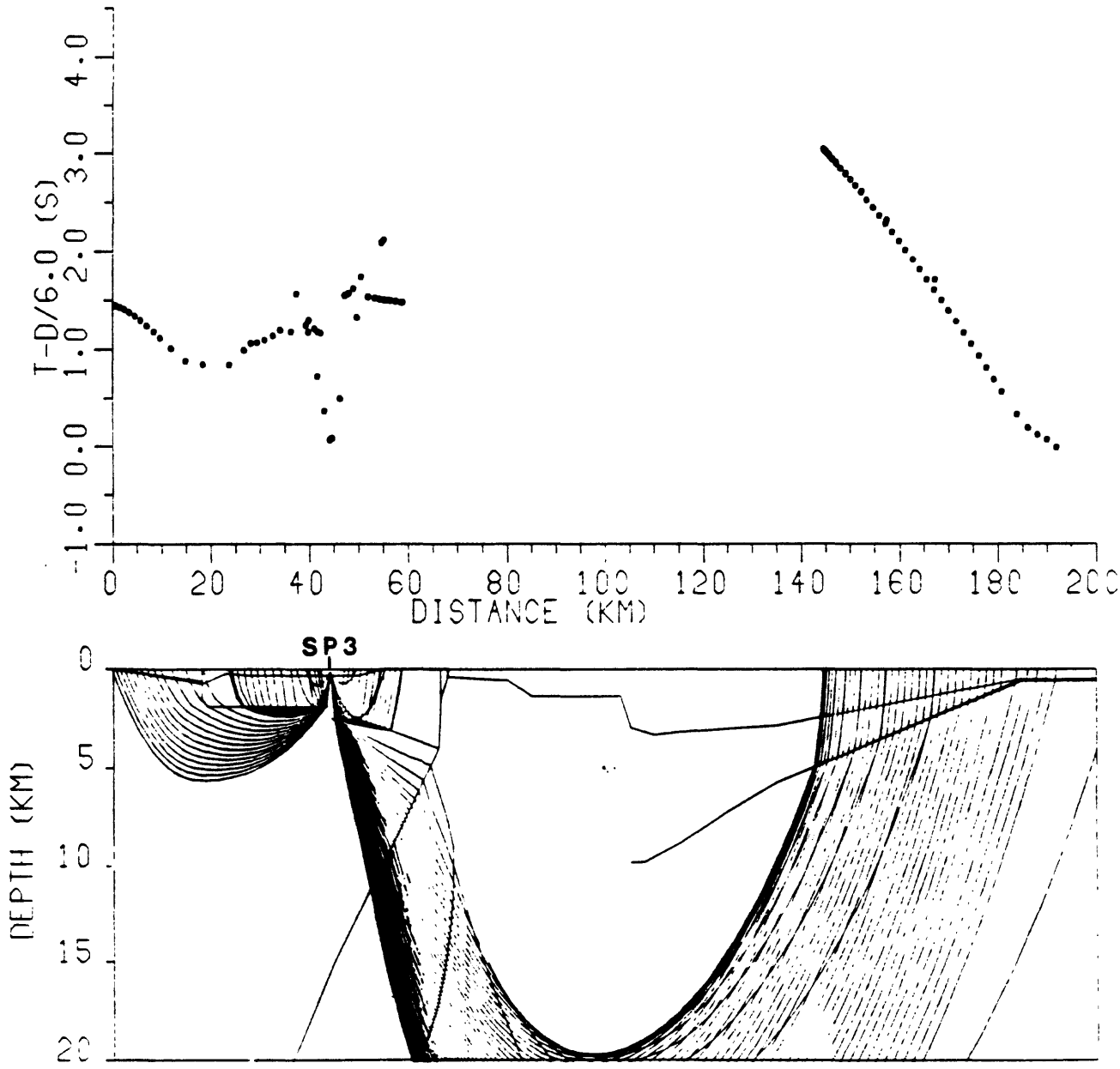

Figure 3c. Ray tracing diagram for Shot Point 3.

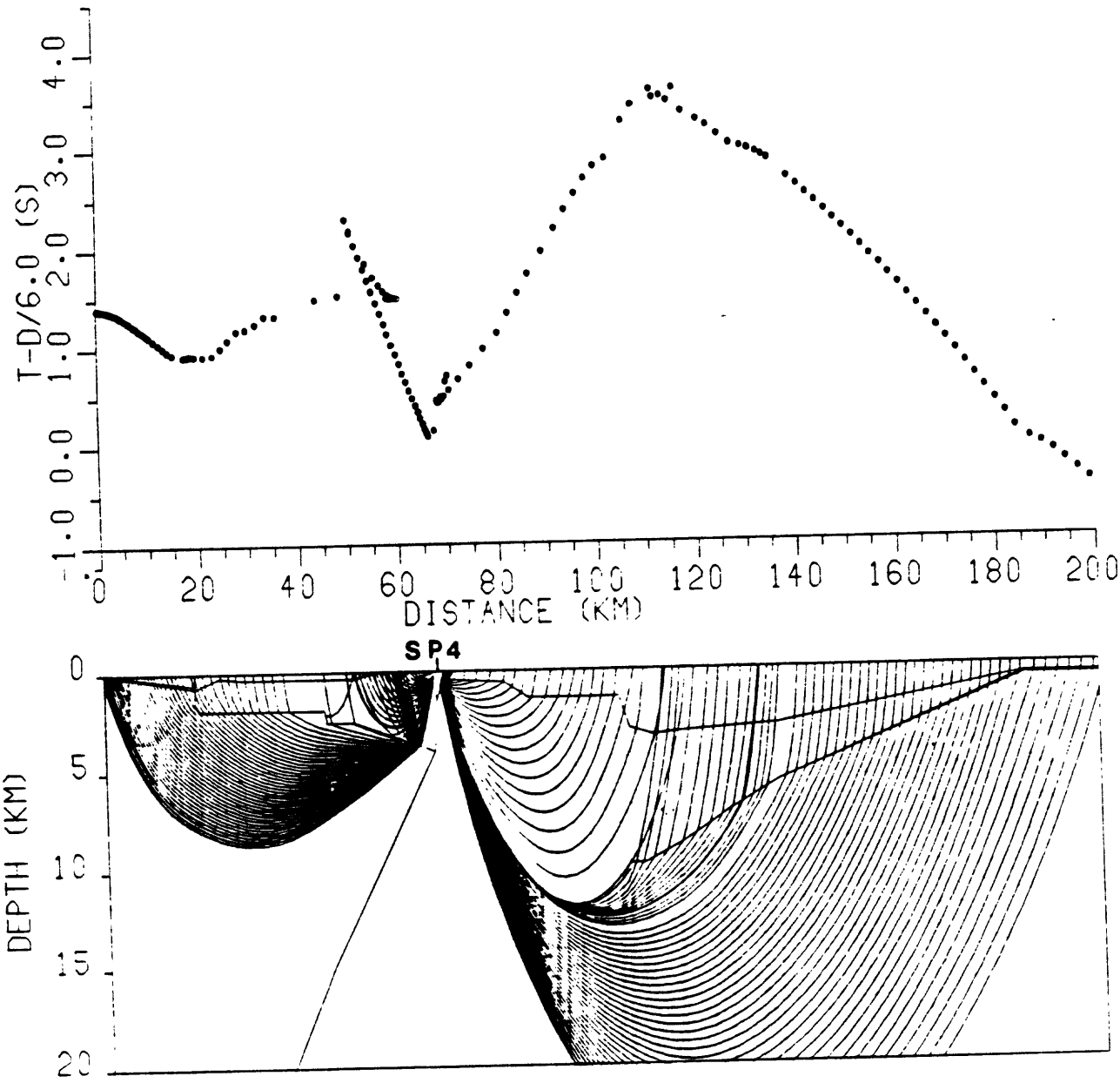

Figure 3d. Ray tracing diagram for Shot Point 4.

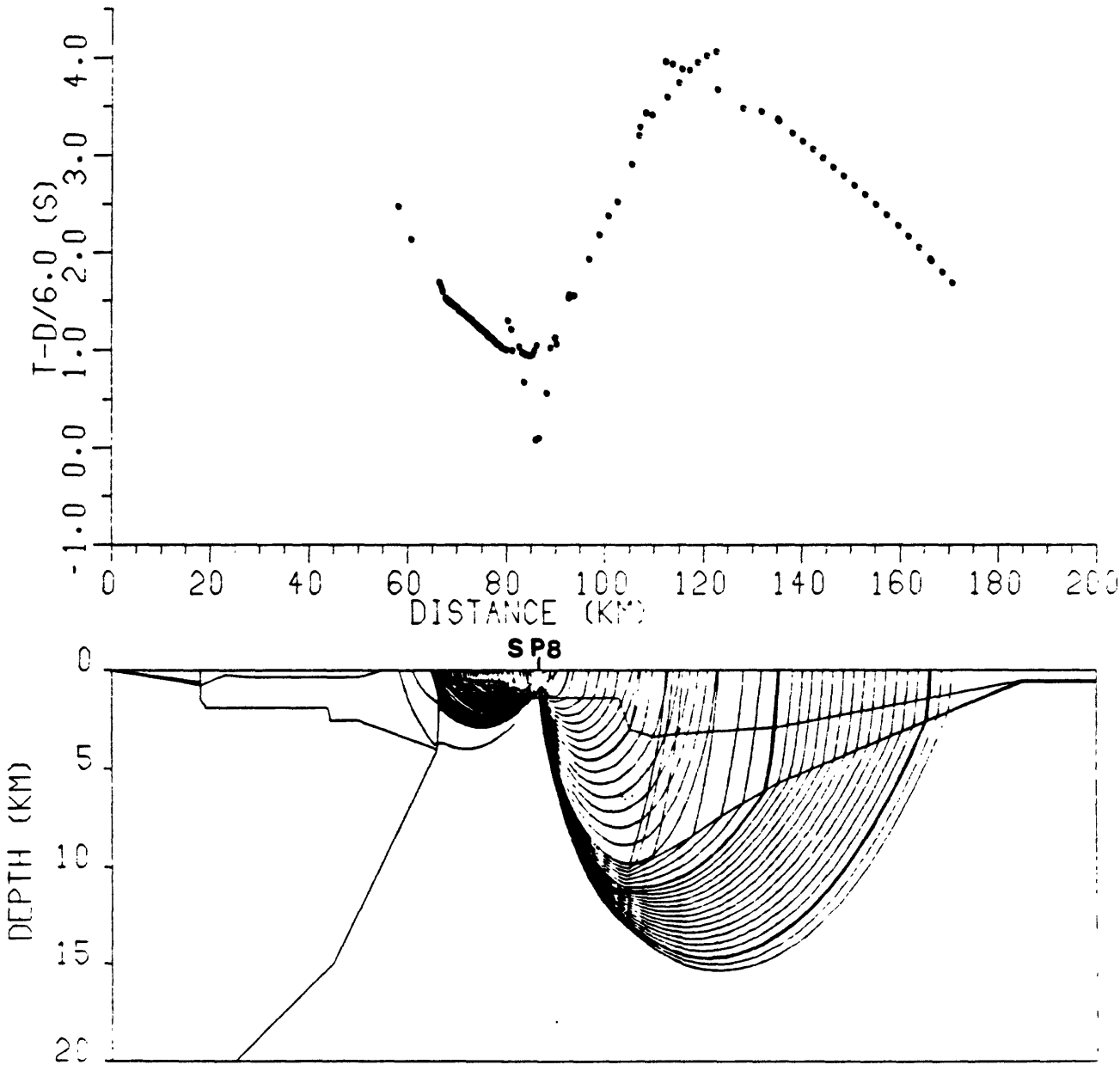

Figure 3e. Ray tracing diagram for Shot Point 8.

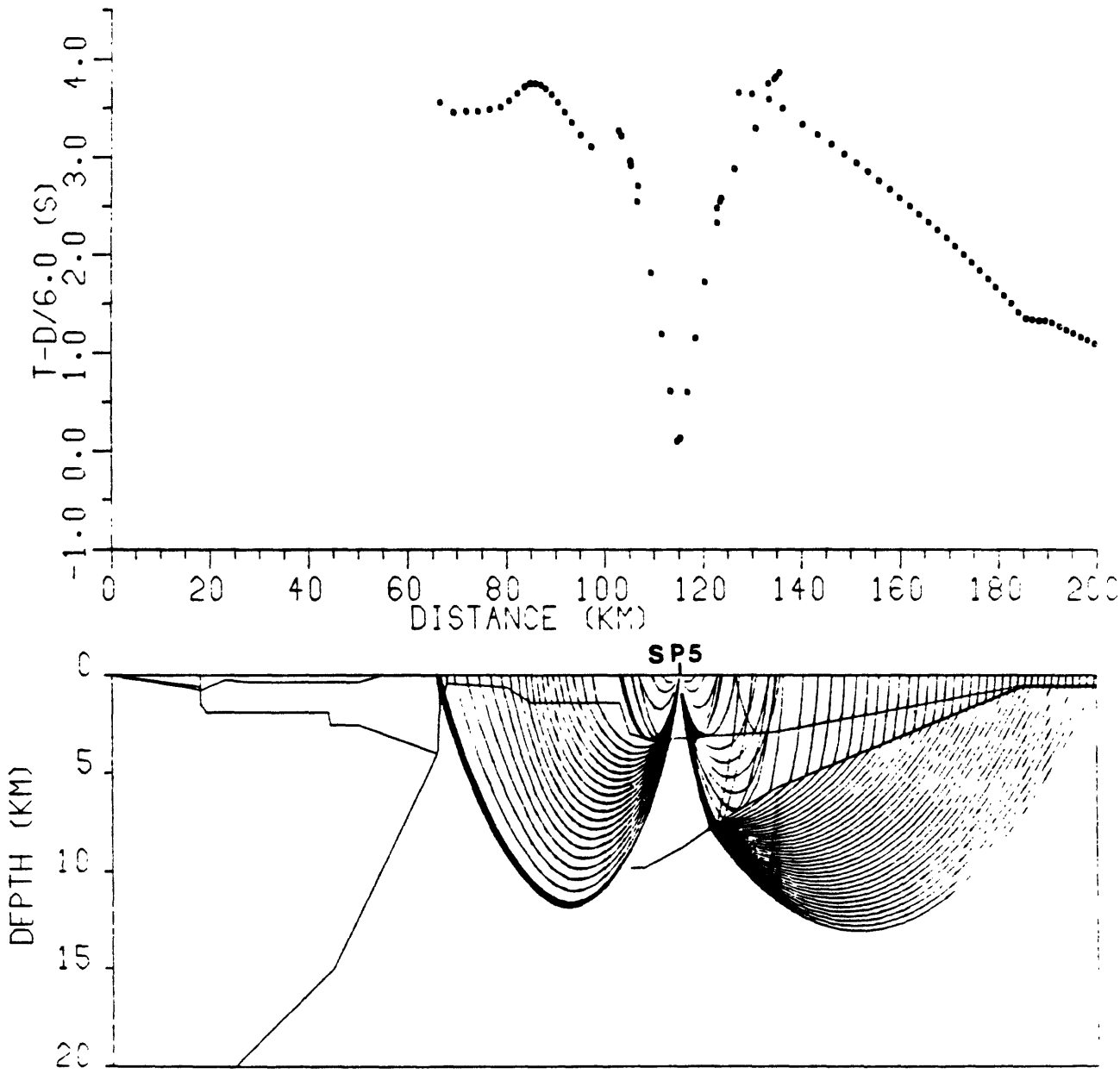

Figure 3f. Ray tracing diagram for Shot Point 5.

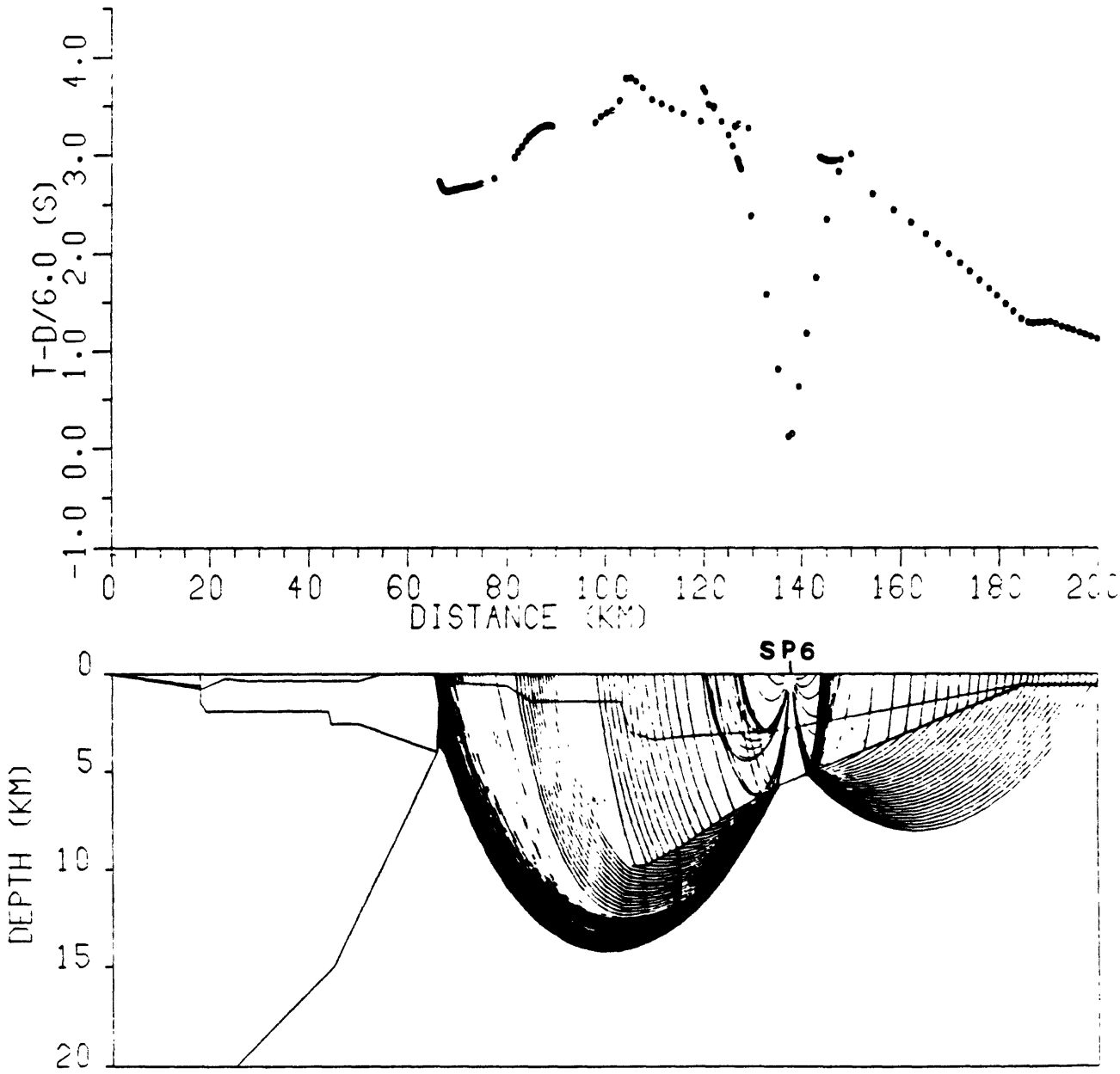

Figure 3g. Ray tracing diagram for Shot Point 6.

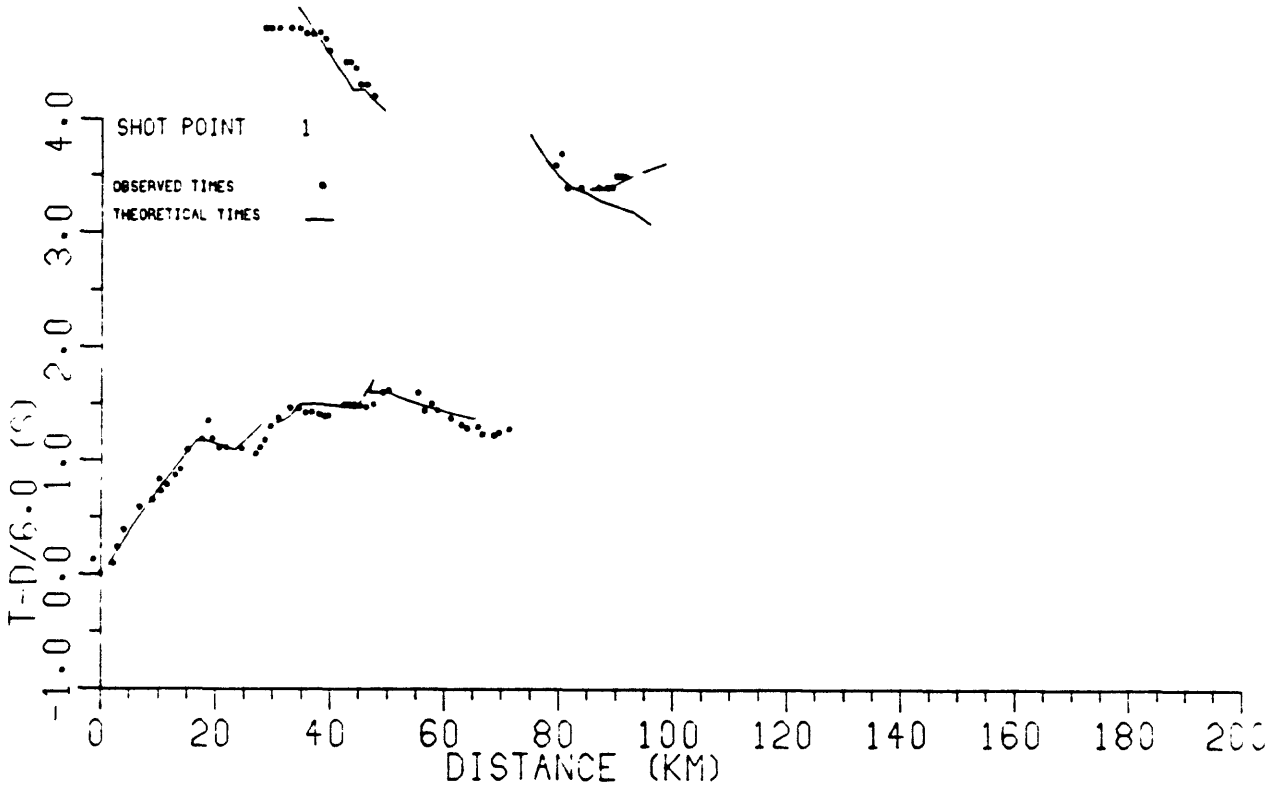

Figure 4a. Comparison of theoretical and observed times for Shot Point 1.

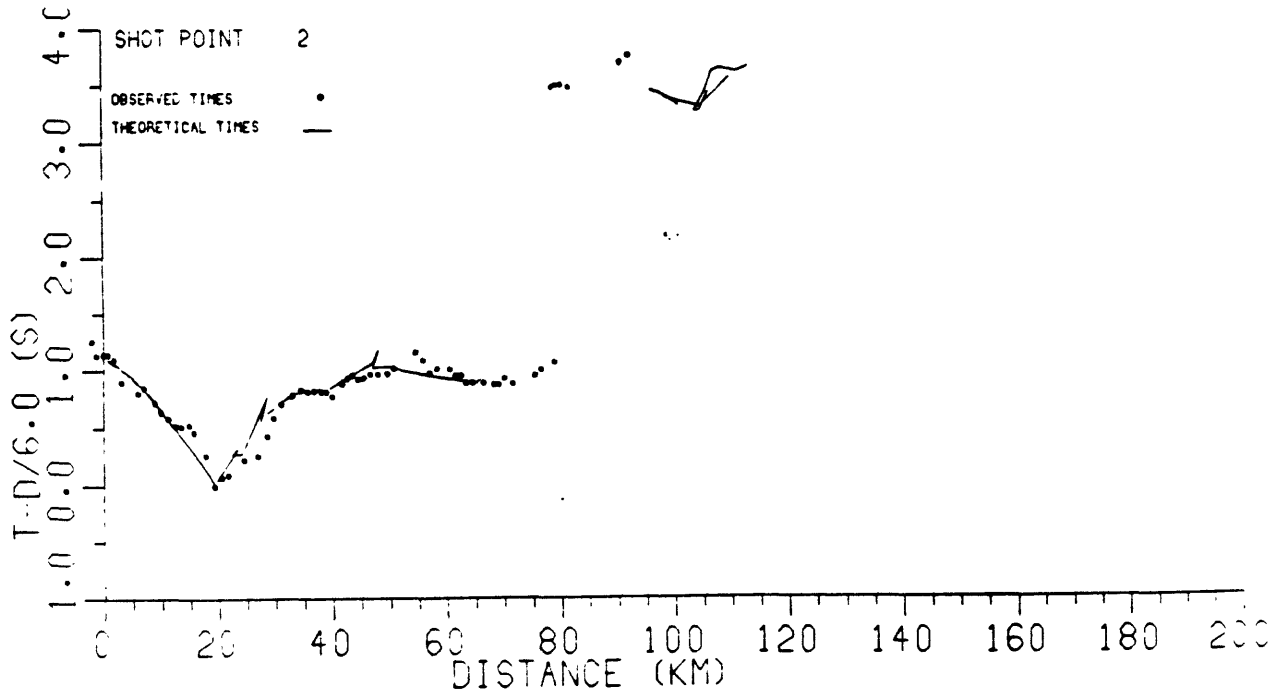

Figure 4b. Comparison of theoretical and observed times for Shot Point 2.

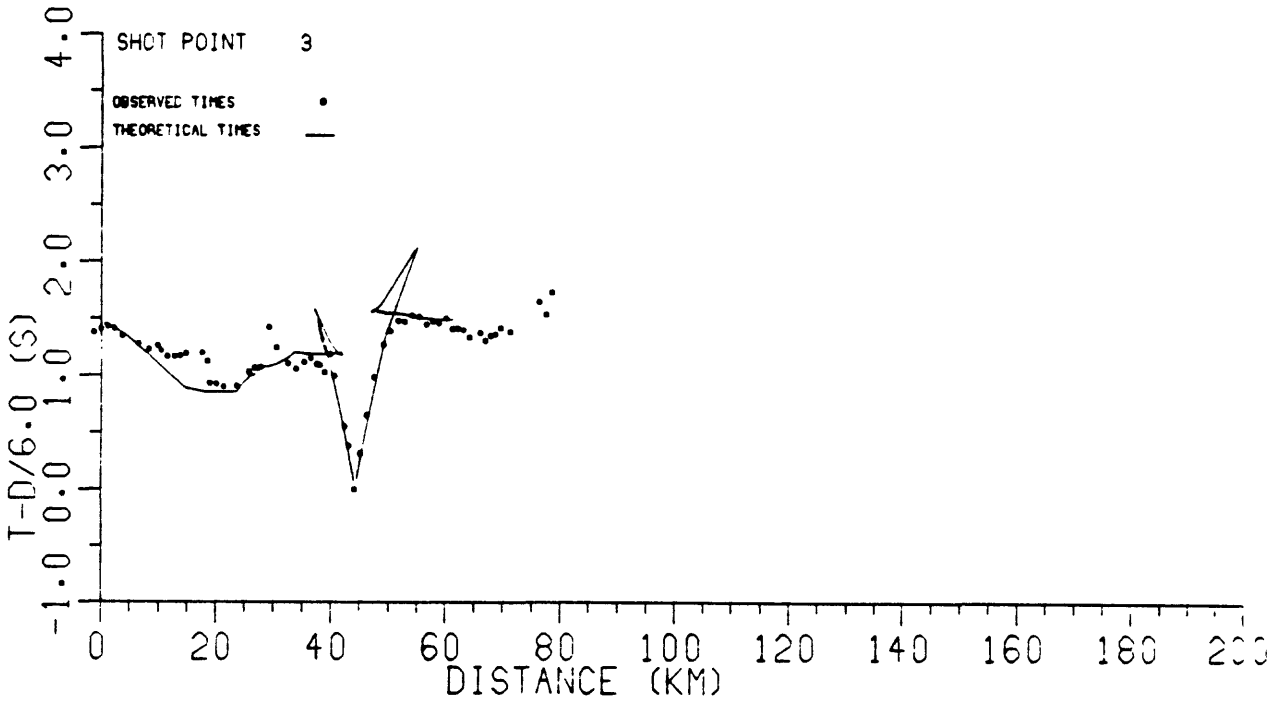

Figure 4c. Comparison of theoretical and observed times for Shot Point 3.

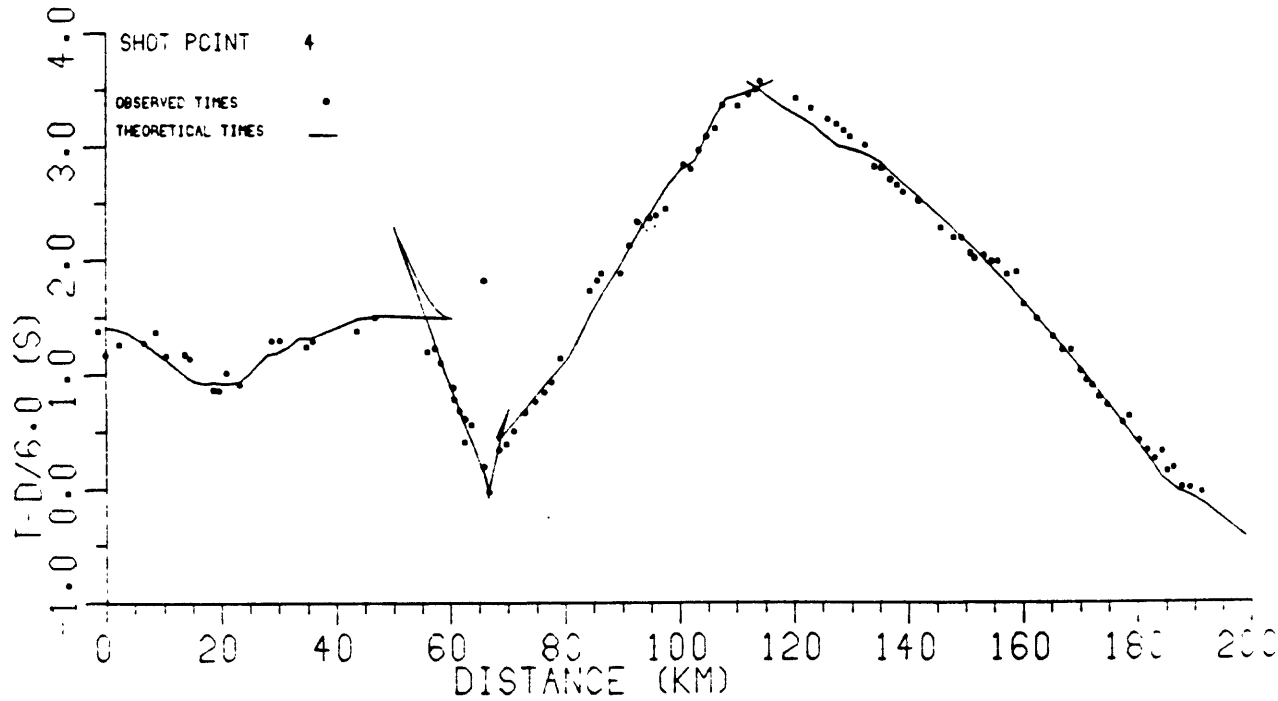

Figure 4d. Comparison of theoretical and observed times for Shot Point 4.

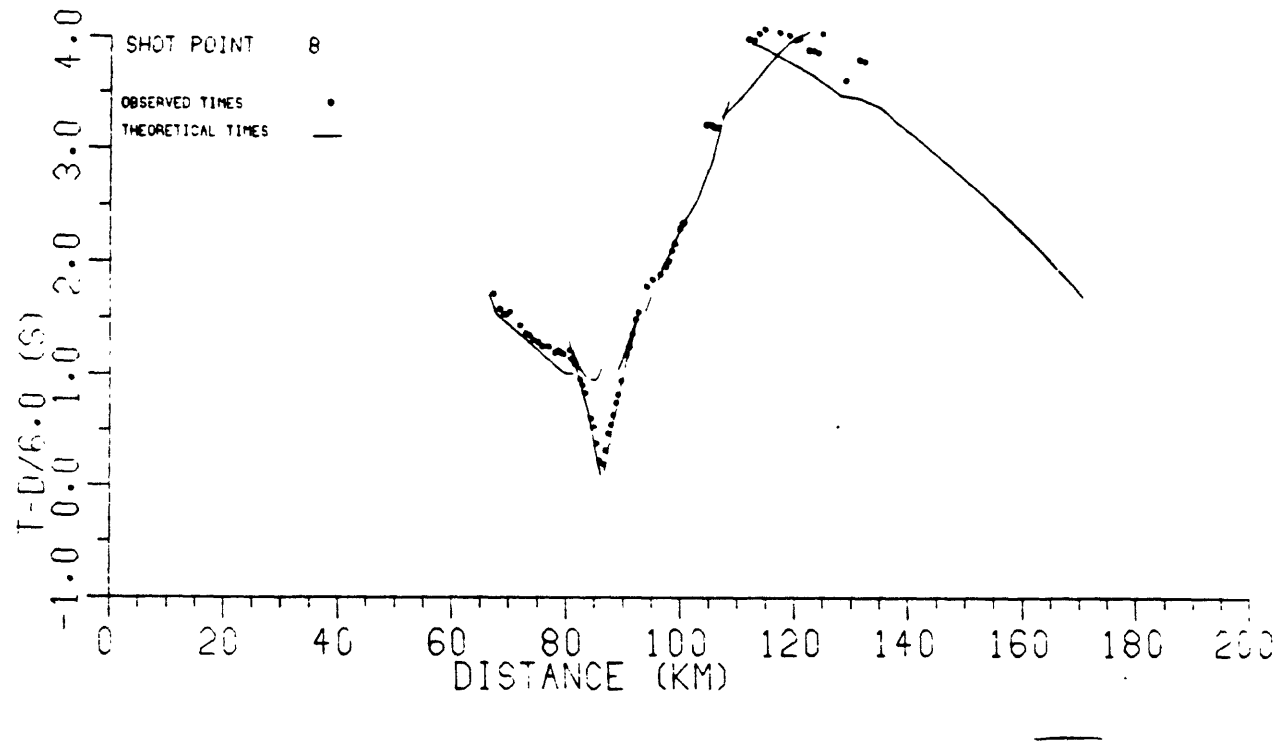

Figure 4e. Comparison of theoretical and observed times for Shot Point 8.

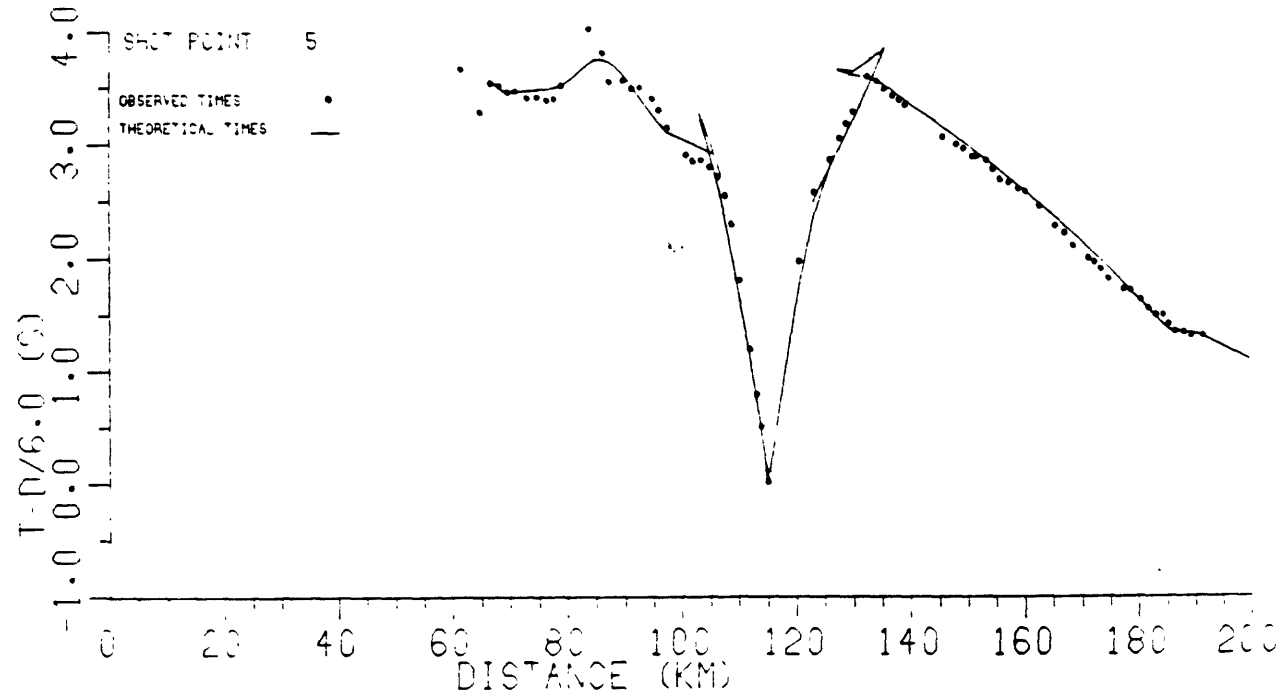

Figure 4f. Comparison of theoretical and observed times for Shot Point 5.

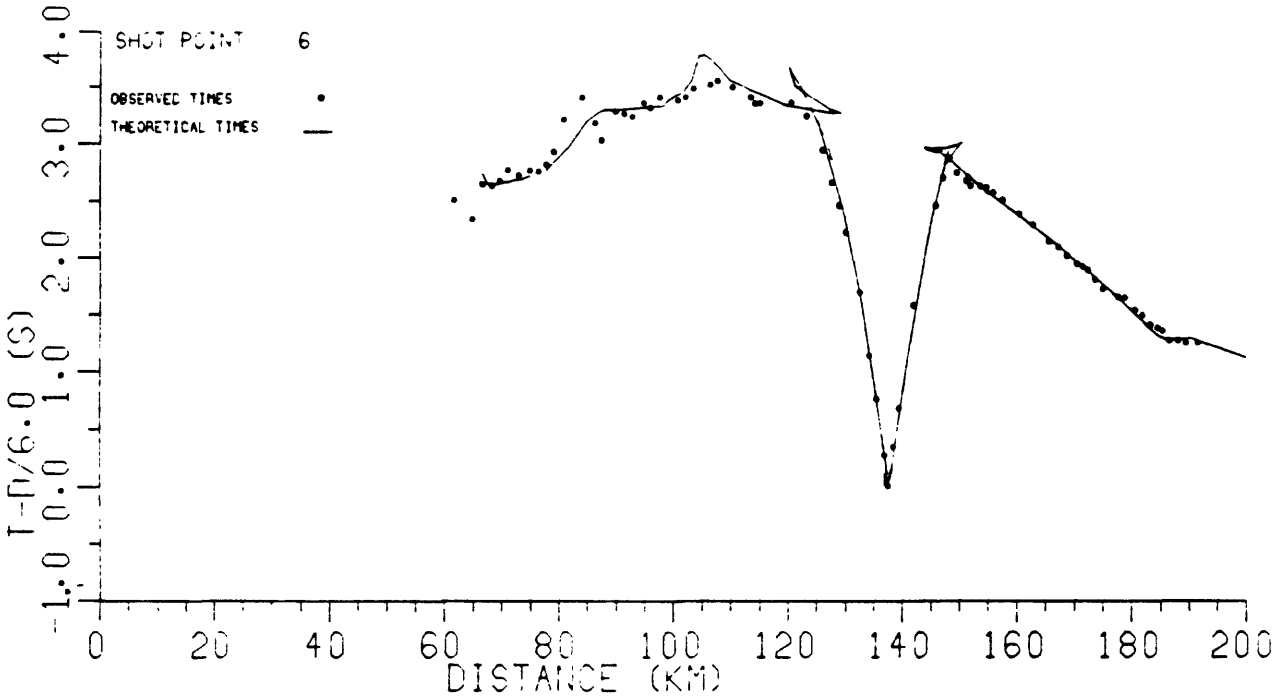

Figure 4g. Comparison of theoretical and observed times for Shot Point 6.

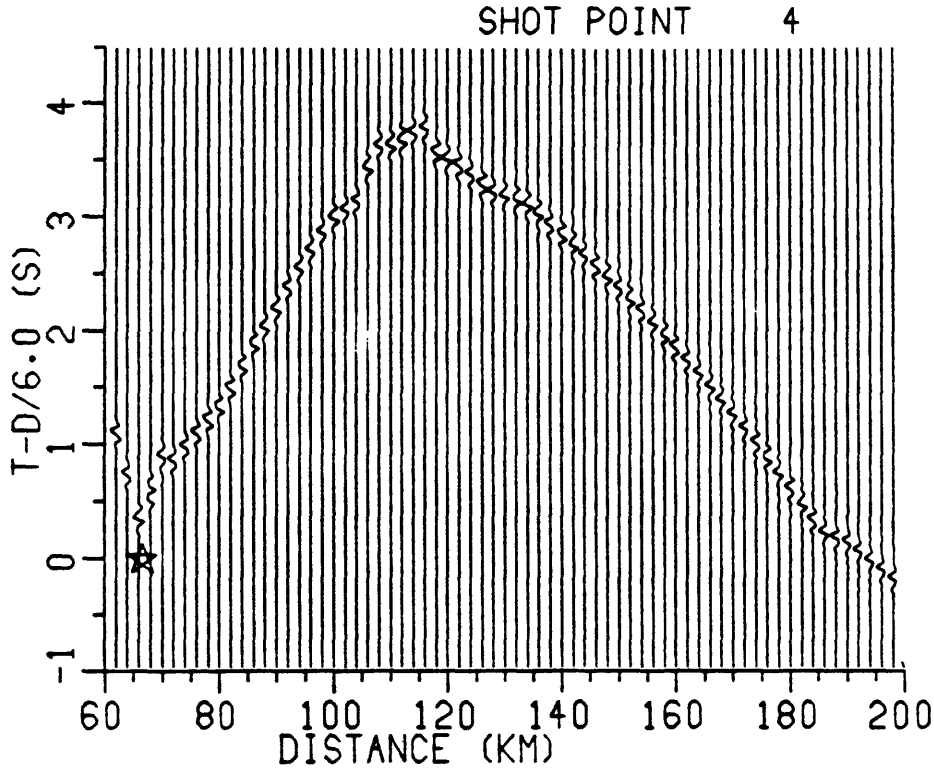

Figure 5a. Synthetic seismic section for Shot Point 4.

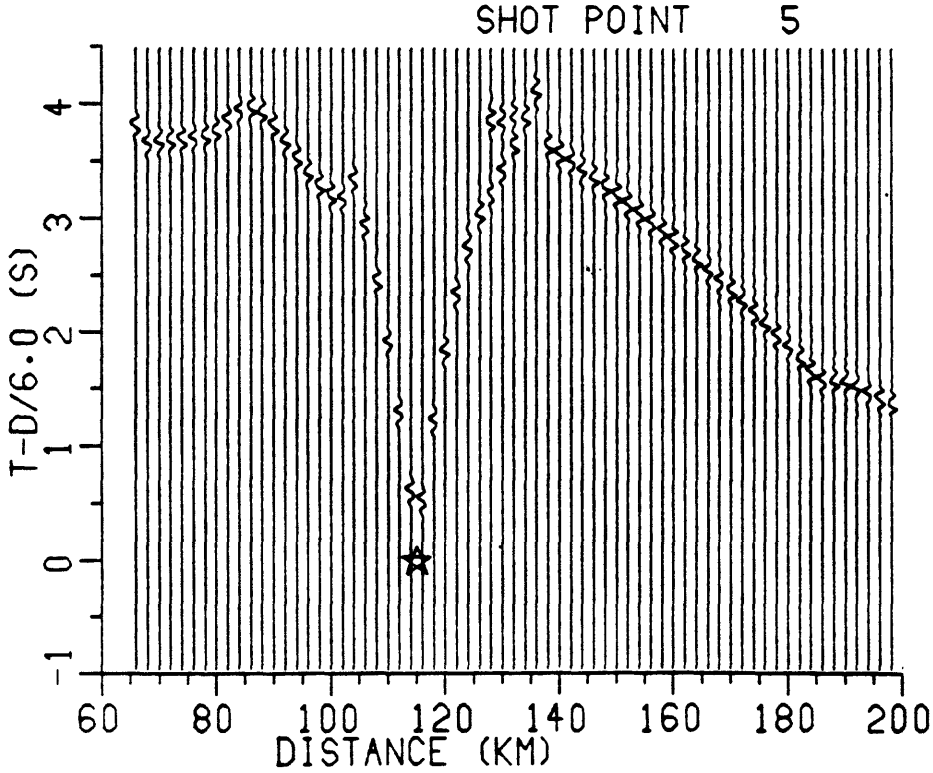

Figure 5b. Synthetic seismic section for Shot Point 5.

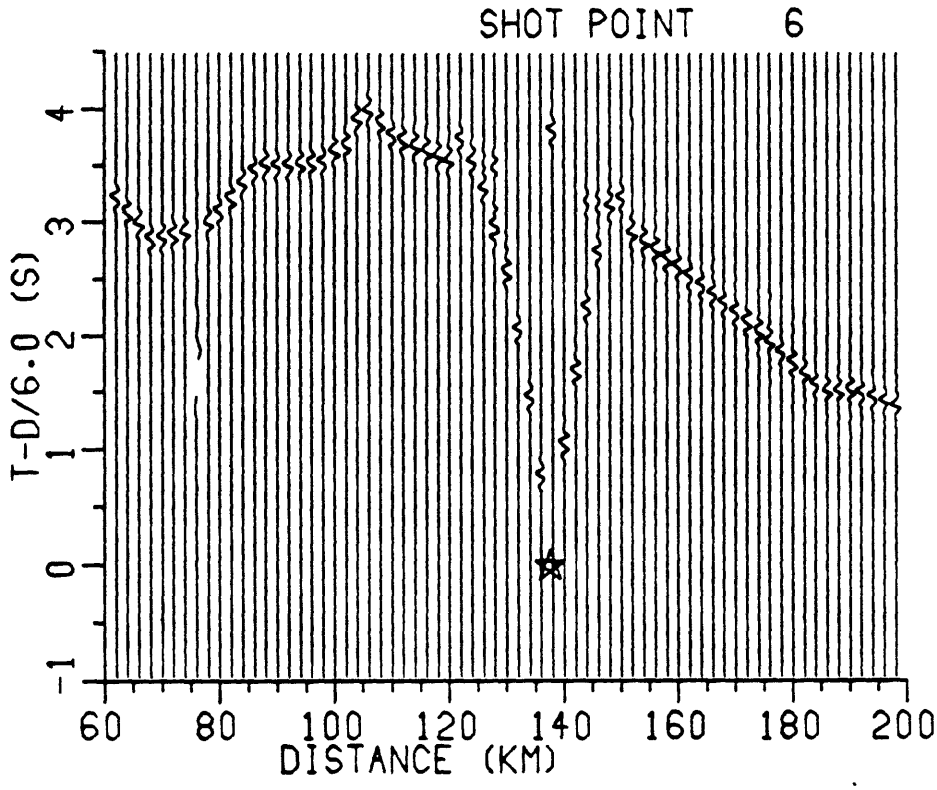

Figure 5c. Synthetic seismic section for Shot Point 6.

Upper-crustal velocity structure along seismic profile SJ-6: Morro Bay-Sierra Nevada, California, USA

V. G. Krishna and K. L. Kaila
National Geophysical Research Institute, Hyderabad 500 007, India

Abstract

The upper-crustal P-velocity structure along the line SJ-6 in south central California has been determined from the analysis of seismic-refraction data recorded along two overlapping sections of the line: Morro Bay-Kettleman Hills and Cholame Valley-Sierra Nevada.

Two-dimensional iterative ray-tracing and synthetic seismogram modeling of the seismic-refraction data recorded along the Morro Bay-Kettleman Hills section yielded a laterally heterogeneous upper crustal structure with detailed velocity information across the Rinconada and the San Andreas faults. Southwest of the Rinconada Fault, the basement is at 4-5 km depth; northeast of the fault, it is uplifted to ~2 km depth and dips gently toward the San Andreas Fault. Northeast of the San Andreas Fault, the basement plunges to ~10 km depth under the Kettleman Hills. The P-velocity of the crust increases with depth to 6.1 km/s at 9.6 km depth, below which, a prominent low velocity layer (LVL) of 5.2 km/s velocity is inferred to extend to a depth of ~22 km. The LVL coincides with the observed cutoff of the seismicity at ~10 km depth in central California.

Analysis of first-arrival traveltime data along the Cholame Valley-Sierra Nevada profile yielded a refraction depth section which reveals some of the important structural features in the Diablo Range, Kettleman Hills and the San Joaquin Valley. In the Diablo Range, ~5.9-km/s Franciscan assemblage rocks underlie a 5-6 km thick section of 4.4-4.6-km/s Great valley sequence. The underlying ~7.0-km/s basement has a continuous downdip from the eastern margin of the San Joaquin valley westward to the Diablo Range.

Introduction

A combined seismic refraction and reflection data set from west central California and its interpretation in terms of laterally heterogeneous crustal structure was discussed during the 1985 CCSS Workshop at Susono, Japan. The entire data set consists of three parts: 1) a ~130-km-long seismic-refraction profile extending eastward from Cholame valley to the Sierra Nevada; 2) a ~100-km long seismic-refraction profile extending northeastward from Morro Bay to the Kettleman Hills; and 3) a ~100-km VIBROSEIS reflection section of ~12 s two way time, extending from ~25 km west of the San Andreas Fault eastward through the Diablo Range to the San Joaquin Valley. In this paper we present a detailed analysis of the data set part 2 and a preliminary interpretation of the data set part 1. Figure 1 shows the location map for the SJ-6 seismic-reflection and seismic-refraction profiles.

Morro Bay-Kettleman Hills seismic-refraction profile

Data

This 100-km-long SW-NE profile crosses two major faults, the San Andreas and Rinconada Faults, which respectively define the northeast and southwest borders of the Salinian block (Murphy and Walter, 1984). About 70 observation stations, spaced 1-3 km apart, recorded four shots, SP1-SP4, spaced 20-25 km apart. True-amplitude and normalized record sections of the trace data, tables of the shotpoint and station locations, and tables of the first-arrival times were provided by the USGS. To model the velocity structure, we used the

first-arrival traveltimes as supplied, as well as the traveltimes of the prominent secondary arrivals that we picked from the supplied record sections (Figs. 2-5).

Modeling and interpretation

The following methods of modeling and interpretation were used to construct the 2-D upper-crustal velocity structure between Morro Bay and the Kettleman Hills.

1. Identification and correlation of refracted and reflected phases on the individual record sections as shown in Figures 2 to 5.

For example, on the record sections of SP1 and SP2 (Figs. 2-3), a prominent secondary phase at 4-5 s reduced time is more or less parallel to the first arrivals (P_g phase) which are attenuated beyond distance ranges of 70 km and 50 km, respectively. The occurrence of the attenuation together with the delayed secondary phase suggests a low velocity layer (LVL) within the lower crust. Therefore, we interpret the prominent secondary phase to be a wide-angle reflection from the base of the LVL.

2. Analysis of first-arrival traveltime data, using various shotpoint pairs, by applying the dipping-layer slope-intercept method and inferring the refracting boundaries.

Figure 6 shows the velocity-depth section derived from this simple method of analysis. In the cross-section, two sedimentary layers are discontinuously delineated with velocities between 2.3 and 5.0 km/s and the basement has a velocity of 5.7-5.8 km/s. The abrupt deepening of the basement southwest of SP2 results from an offset at the Rinconada Fault. Northeast of the San Andreas Fault (SP4), the basement plunges beneath the thick sedimentary cover of the Kettleman Hills.

3. Inversion of P_g traveltimes by the Herglotz-Wiechert method for various sections to determine the velocity gradient at shallow depths.

4. Deriving 1-D velocity models at the shotpoints by travel-time and amplitude modeling in reversing directions along profile.

An improved velocity model was derived using a 1-D ray-tracing computer algorithm (LAUFZEIT). The velocity-depth functions near each shotpoint were refined iteratively until a good fit was obtained between the computed and the observed traveltimes. These functions were then used to compute ray-synthetic seismograms (Červený and others, 1977), and where necessary, adjustments were made to the functions to improve the agreement between calculated and observed amplitudes.

A total of seven velocity-depth functions were derived between SP1 and SP4. The models for SP1NE and SP2NE reveal an LVL from ~9 to 22 km depth with a minimum velocity of 5.2 km/s, and the models for SP3SW and SP3NE show a slightly thicker LVL. Comparison of the final synthetic record sections (Fig. 8 to 11) with the observed record sections reveals that the synthetic wide-angle reflection from the bottom of the LVL (~22 km depth) reasonably matches the observed large-amplitude secondary arrivals.

5. Two-dimensional travel-time modeling by iterative ray-tracing.

In the 2-D modeling of traveltimes we considered only three phases: 1) waves refracted in the heterogeneous layers above the LVL ; 2) waves reflected from the top of the LVL; and 3) waves reflected from the bottom of the LVL.

The algorithm chosen for 2-D modeling is based on standard ray method in its zero-order approximation and is described in detail by Červeny and Pšenčík (1981). The 1-D velocity models described above were used to construct a starting model for iterative 2-D ray-tracing. The velocity model was then adjusted over several interations to improve the fit between the calculated and observed data. Figure 12 shows our final 2-D velocity model for the Morro Bay-Kettleman Hills profile plotted as isovelocity contours; in Figure 13 the same model is shown subdivided by symbol fields into selected velocity ranges. Velocity-depth functions at various distance ranges along the model are shown in Figure 14. The traveltime curves calculated using this model are plotted on the record sections in Figures 2 to 5; the associated ray-diagrams are shown in Figures 15 to 18.

The 2-D model has a laterally heterogeneous upper crust down to the LVL with changes in structure evident on opposing sides of the Rinconada and the San Andreas fault zones. In the lower crust the velocities are not well-constrained by the refraction data, so we assumed a horizontal LVL with a uniform velocity of 5.2 km/s between 9.6 and 22.0 km depth; below this LVL, we assumed a uniform velocity of 7.0 km/s to a depth of 30 km.

6. Synthetic seismograms for the two dimensional model computed using the software SEIS 81 (Červeny and Pšenčík, 1981).

Figures 19 to 22 show the normalized synthetic record sections for SP1-SP4. Comparing the data in Figures 2 to 5 with the synthetic record sections in Figures 19 to 22, we conclude that the main features observed in the data, including the wide-angle reflection from the bottom of the LVL, are adequately reproduced by the synthetics.

Discussion of the model

Comparing the simple model shown in Figure 6 with the further refined 2-D model shown in Figure 12, we conclude that the latter reveals more details of the velocity structure. However, if we assume the 5.6 km/s isovelocity line represents the basement P-velocity, the basement configuration in the two sections is similar. Overall the basement dips northeast and abrupt depth changes are evident near both the Rinconada and the San Andreas faults: southwest of the Riconada Fault the basement is at depth of 4-5 km, but between the Rinconada and San Andreas faults the basement is uplifted several kilometers (2-km depth at SP3), and northeast of the San Andreas Fault (SP4), the basement plunges to great depths.

It is interesting to compare the depths of the seismicity in west central California with the velocity depth-section derived in the present study. In the Coyote Lake area of the Calaveras Fault, a branch of the San Andreas Fault ~200 km north of the SJ-6 profile, the majority of the hypocentral locations are between 5 and 10 km depth (Reasenberg and Ellsworth, 1982). It is a interesting coincidence that most of the seismicity there occurs above the top of our modeled LVL. Possibly the presence of a LVL is responsible for the observed cutoff of seismicity. Nevertheless, with the growing interest in accurate hypocentral locations, detailed information on the 2-D crustal velocity structure in central California is vital, so we hope that the model derived in the present study, maybe with some refinement, will be useful in this direction.

Cholame Valley-Sierra Nevada profile

Data

This ~130-km-long profile extends eastward from the Cholame Valley across the Diablo Range, the Kettleman Hills and the San Joaquin Valley to the Sierra Nevada foothills. Seismograph stations spaced 0.5-3.0 km apart were used to record five shots spaced 20-30 km apart: SP4, SP8, SP5, SP6 and SP7 (Murphy and Walter, 1984). The explosive charge at the easternmost shotpoint, SP7, failed to detonate completely, so reversing traveltime data exists only between SP4 and SP6.

We confined our analysis to the first-arrival times and used the provided traveltime tables to construct traveltime curves. The time available to us for analysis was insufficient for the construction of an iterative ray-trace model, so we analysed the traveltime curves using the dipping layer slope-intercept method. The refraction velocity-depth section obtained using this simple method of analysis reveals interesting structural details which are presented below.

Analysis of the first-arrival traveltime data

Composite traveltime curves for the five shots are plotted on their respective record sections in Figures 23 to 27. We made use of all possible combinations of shotpoint pairs to analyze the reversed refraction data. For this purpose we adopted the single-ended refraction data analysis of Cunningham (1974) as well as the split-spread refraction data analysis of Johnson (1976). However, we slightly modified these two techniques in order to replace the planar dipping refractors by more realistic structures with possible undulations. In our analysis, we reduced the computation to a two-layer case by approximating the vertically inhomogeneous structure above the refractor by a single velocity, the average velocity of the entire overburden. Adequate care was taken to satisfy the required reciprocity of traveltimes for a particular refractor between a given pair of shotpoints. Figure 28 shows the velocity-depth section thus derived for the profile.

Discussion of the model

SP4 is situated in Tertiary sedimentary rocks of the Diablo Range which have a near surface velocity of ~3.05 km/s. Between SP4 and SP8, the refractor delineated by a velocity of 4.4 to 4.6 km/s at depths of 1.0 to 1.5 km is inferred to be a Cretaceous sedimentary unit of the Great Valley Sequence (GVS) because similar velocities were reported for the GVS elsewhere (Mooney and Walter, 1980). The thickness of the GVS in this region appears to be 5-6 km. Underlying the GVS is a refractor with a velocity of ~5.9 km/s, which is the velocity reported for the Franciscan assemblage in the central Diablo Range (Walter and Mooney, 1982). Thus, we conclude that the Franciscan assemblage also underlies the Great Valley Sequence here.

Farther eastward, between SP8 and SP5, the seismic-reflection time-section shows a very complicated folded and faulted structure near the Kettleman Hills. Although it is not possible to resolve all structural details using the first-arrival refraction data, the refraction data from SP5 and SP8 do support an upwarp of the 5.9-km/s refractor in this area.

Within the San Joaquin Valley the near surface sediments between SP5 and SP7 have velocities of 1.7-1.9 km/s and overlie Tertiary units with velocities of 2.8-3.3 km/s. The other refractors discussed above, the GVS and Franciscan assemblage, appear to pinch out eastward and are not evident east of SP6. The basement beneath this sedimentary cover rises continuously eastward as evident

from both the seismic-reflection data and the high apparent velocities (7.6-7.8 km/s) observed east of SP4, SP5 and SP6. According to our refraction calculations, the basement between SP4 and SP7 rises from ~10.5 km to ~3.0 km depth and has a true velocity of ~7.0 km/s. This velocity is typical of the mafic crystalline rocks found in oceanic terranes.

Comparison with the structural model derived from the seismic-reflection data

In Figure 29 we reproduce a regional geologic map of California which shows the locations of several E-W seismic-reflection profiles that cross the Great Valley between the Sierra Nevada and the Coast Ranges (Wentworth and Zoback, 1986). On the basis of these seismic-reflection lines and other geophysical and geologic evidence, Wentworth and others (1984) modeled the eastern margin of the Franciscan assemblage as a wedge thrust eastward between the Great Valley Sequence and underlying mafic basement. Their model shown in Figure 30 is similar our seismic-refraction model (Fig. 28); thus, even our simple refraction analysis without ray-tracing revealed the main structural elements lying between the San Joaquin Valley and Diablo Range.

Conclusions

Proper identification and correlation of observed phases in the record sections is the most important step in the interpretation of seismic-refraction profiles. Even one dimensional modeling, if carried out with extreme care, can lead to results which need only a few iterations of 2-D modeling to obtain a satisfactory reproduction of the observations. In regions of smooth structural variations, the two-way times computed to various horizons using the refraction velocity models match reasonably well with the events observed on the seismic-reflection time seismic sections. In regions where the structure is complicated the available refraction data are not sufficient to delineate the structure. Here both seismic refraction and reflection profiling are needed to resolve the structure with adequate velocity information.

In summary, for the Morro Bay-Kettleman Hills profile, 2-D iterative ray-tracing and synthetic seismogram modeling of the refraction data yielded:

1) A laterally heterogeneous upper crustal velocity structure which has major changes occurring across the Rinconada and the San Andreas faults.
2) A basement in which the velocity increases to 6.1 km/s at 9.6 km depth.
3) A low velocity layer with a velocity of 5.2 km/s between 9.6 and 22.0 km depth. The depth to the top of the LVL is approximately the cutoff depth for the seismicity observed in central California.

The dipping-layer analysis of first-arrival refraction data of the Cholame Valley-Sierra Nevada profile yielded:

1) in the Diablo Range, a 5-6-km thick section of Great Valley Sequence rocks (4.5 km/s) underlain by an eastward thinning wedge of Franciscan rocks (5.9 km/s).
2) in the San Joaquin Valley, a westward thickening section of sedimentary strata (1.9-3.3 km/s) underlain by a westward dipping mafic basement (7.0 km/s).

Acknowledgements

We are grateful to the Director, National Geophysical Research Institute, Hyderabad, for kind permission to publish this paper. Our thanks are also due to Prof. H. M. Iyer, U.S. Geological Survey (presently at NGRI) for helpful discussions and to Messers A.S.N. Murthy and A. R. Sridhar for their help in the compilation of the results.

References

Červený, V., and I. Pšenčík, 1981, SEIS 81 Computer Program, 2-D seismic ray package, Prague.

Červený, V., I.A. Moltikov, and I. Pšenčík, 1977, Ray method in seismology, Univ. Karlova, Prague, 214 p.

Cunningham, A.B., 1974, Refraction data from single-ended refraction profiles, Geophysics, 39, p. 292-301.

Johnson, S.H., 1976, Interpretation of split-spread refraction data in terms of plane dipping layers, Geophysics, 41, p. 418-424.

Mooney, W.D., and A.W. Walter, 1980, Seismic-refraction studies in the coast ranges, central California, (Abstract), EOS, 62, p. 328.

Murphy, J.M., and A.W. Walter, 1984, Data report for a seismic-refraction investigation: Morro Bay to the Sierra Nevada, California, U.S. Geol. Surv. Open-File Rep. 84-642.

Reasenberg, P., and W.L. Ellsworth, 1982, Aftershocks of the Coyote Lake, California earthquake of August 6, 1979: a detailed study, J. Geophys. Res., 87, pp. 10637-10655.

Walter, A.W., and W.D. Mooney, 1982, Crustal structure of the Diablo and Gabilan Ranges, central California: a reinterpretation of existing data, Bull. Seism. Soc. Am., 72, pp. 1567-1590.

Wentworth, C.M., M.C. Blake, Jr., D.C. Jones, A.W. Walter, and M.D. Zoback, 1984, Tectonic wedging associated with emplacement of the Franciscan assemblage, California coast Ranges, Soc. Econ. Paleon. and Mineral., Pacific Section, 43, p. 163-173.

Zoback, M.D., and C.M. Wentworth, 1986, Crustal studies in central California using an 800-channel seismic-reflection recording system, in M. Barazangi and L. Brown eds., Reflection Seismology: A Global Perspective, Geodynamics Series 13, p. 183-196.

Figure Captions

Fig. 1 — Map showing location of the two seismic-refraction profiles recorded along seismic-reflection line SJ-6 in south central California: Morro Bay-Kettleman Hills profile (shotpoints SP1-SP4) and Cholame Valley-Sierra Nevada profile (shotpoints SP4-SP8).

Figs. 2-5 — Morro Bay-Kettleman Hills profile: The normalized record sections of shotpoints SP1-SP4 superimposed with the traveltime curves calculated using the final 2-D velocity model (Fig. 12).

Fig. 6 — Morro Bay-Kettleman Hills profile: The upper-crustal velocity cross-section derived from the analysis of first-arrival traveltime data.

Fig. 7 — Morro Bay-Kettleman Hills profile: The velocity-depth functions derived to compute ray-synthetic record sections for SP1-SP4 (Figs. 8-11).

Figs. 8-11 — Morro Bay-Kettleman Hills profile: The normalized ray-synthetic record sections for SP1-SP4 computed using 1-D velocity models (Fig. 7).

Fig. 12 — Morro Bay-Kettleman Hills profile: The final 2-D upper-crustal velocity model derived by iterative ray-tracing.

Fig. 13 — Morro Bay-Kettleman Hills profile: The final velocity model (Fig. 12) presented in the format output by the SEIS 81 computer program (Červený and Pšenčík, 1981).

Fig. 14 Morro Bay-Kettleman Hills profile: The velocity-depth functions at selected points along the final velocity model (Fig. 12).

Figs. 15-18 Morro Bay-Kettleman Hills profile: The ray-diagrams for shotpoints 1-4 computed using the final velocity model (Fig. 12).

Figs. 19-22 Morro Bay-Kettleman Hills profile: The normalized ray-synthetic record sections for shotpoints 1-4 computed using the final velocity model (Fig. 12).

Figs. 23-27 Cholame Valley-Sierra Nevada profile: The normalized record sections of shotpoints 4-8. The apparent velocities of the first arrivals are labeled in km/s.

Fig. 28 Cholame Valley-Sierra Nevada profile: The upper-crustal velocity cross-section derived from the analysis of first-arrival traveltime data.

Fig. 29 Regional geologic map of California showing the E-W seismic-reflection profiles located between the Great Valley and Coast Ranges that were analysed by the U.S.G.S. (reproduced from Zoback and Wentworth, 1986).

Fig. 30 Geologic interpretation of the west half of reflection line CC-1 (Fig. 29) showing an inferred wedge of Franciscan assemblage rocks thrust between the Great Valley basement and the overlying Great Valley sedimentary rocks (reproduced from Zoback and Wentworth, 1986).

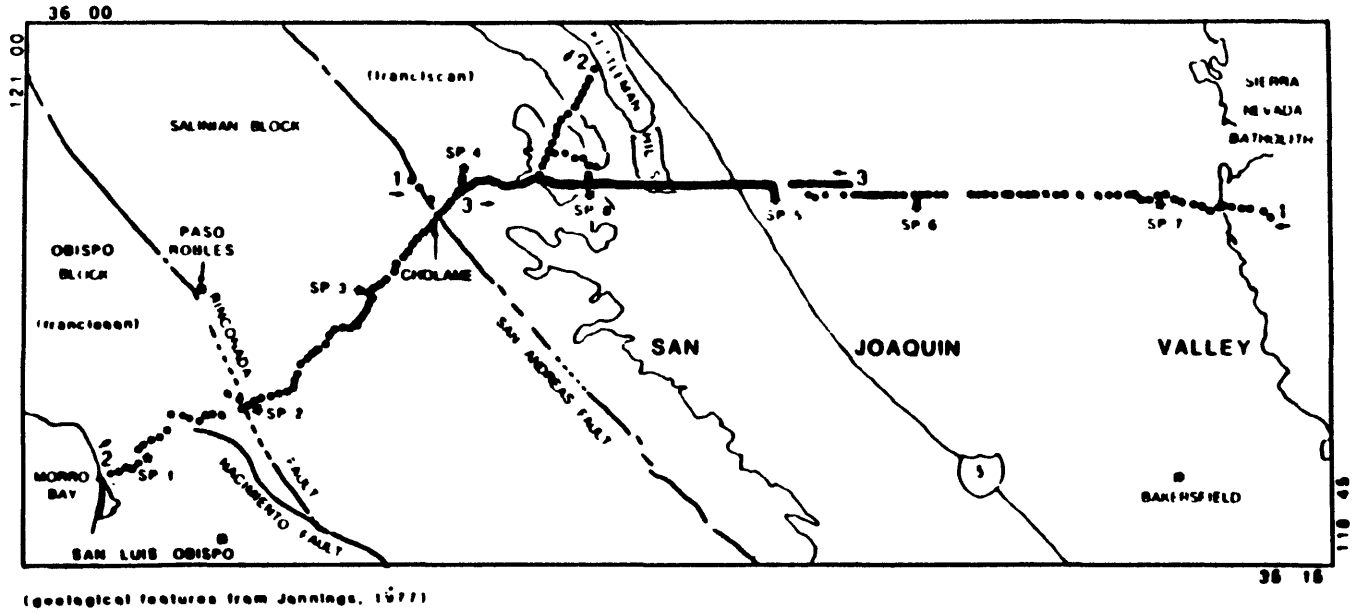

(geological features from Jennings, 1977)

Figure 1. 1982 and 1983 profiles. Dots indicate seismic recorder locations. Each deployment lies between two numbers marking the profile:

1 Cholame Valley to Sierra Nevada (1982)
2 Morro Bay to Kettleman Hills (1982)
3 Cholame Valley to San Joaquin Valley (1983)

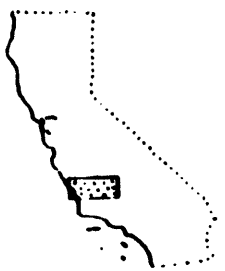

Figure 1

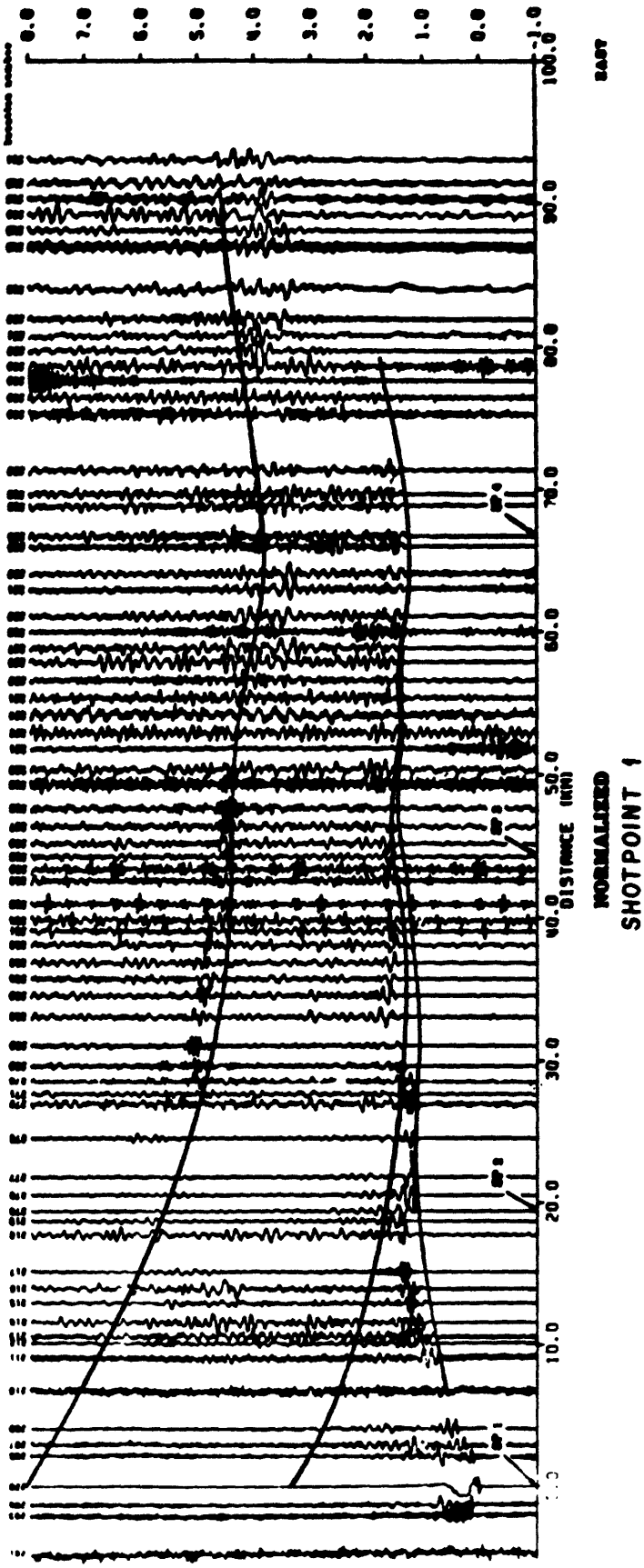
8.0
7.0
6.0
5.0
4.0
3.0
2.0
1.0
0.0
-1.0
100.0
EAST
90.0
80.0
70.0
60.0
50.0
40.0
30.0
20.0
10.0
DISTANCE (KM)
NORMALISED
SHOTPOINT 1

Figure 2

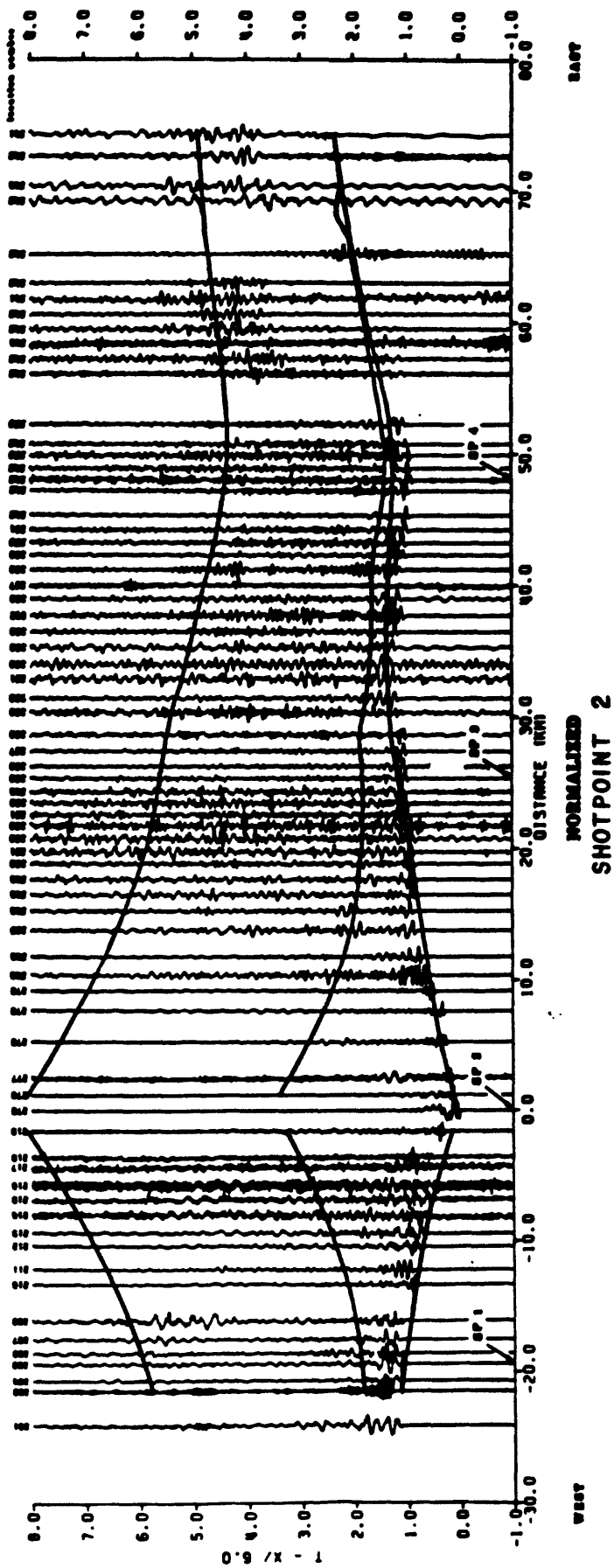

Figure 3

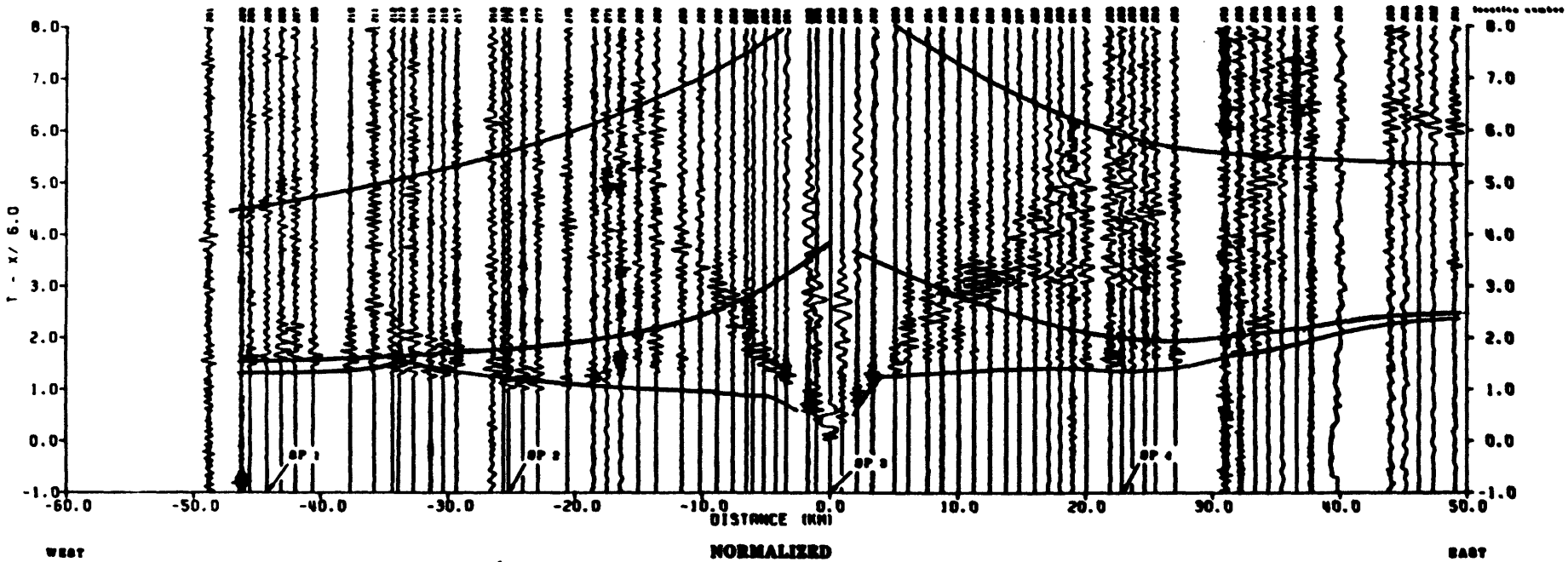

RECORD SECTIONS
MORRO BAY TO KETTLEMAN HILLS
SHOT 8, SHOTPOINT 3

by

J. M. Murphy and A. W. Walter

1984

Figure 4

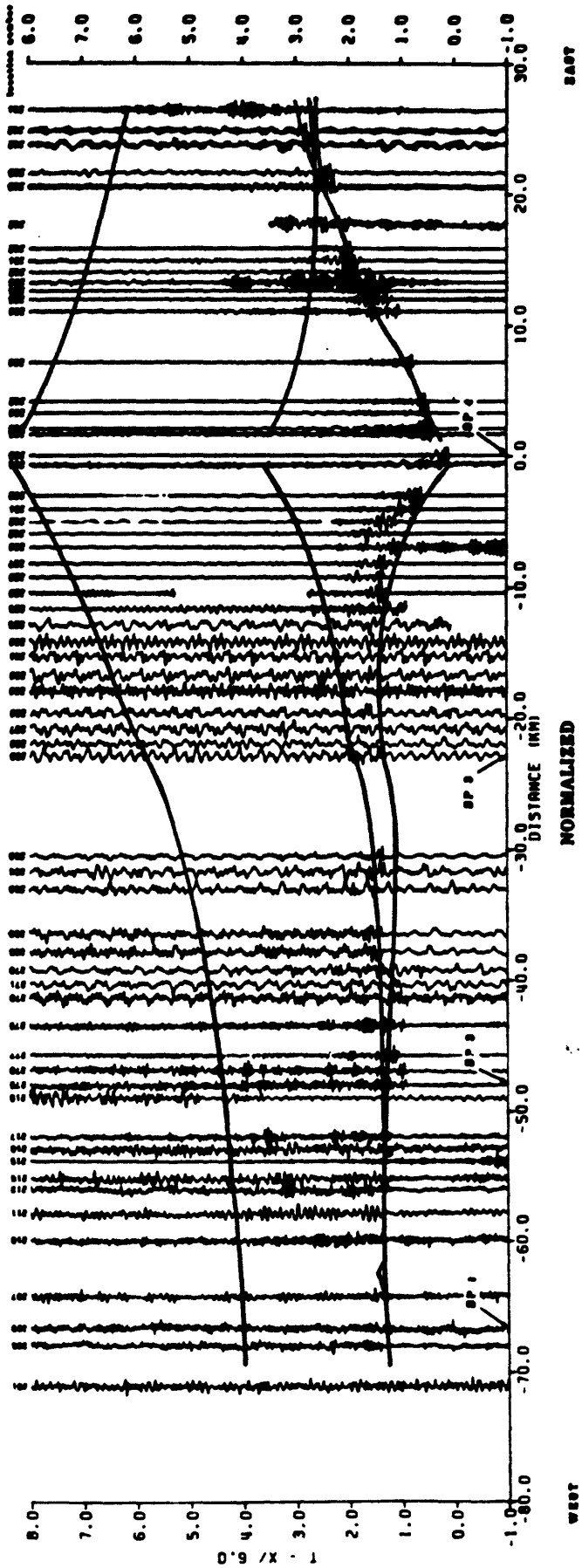
RECORD SECTIONS
MORRO BAY TO KETTLEMAN HILLS
SHOT 5, SHOTPOINT 4
by
J. M. Murphy and A. W. Walter
1964
NORMALIZED
DISTANCE (KM)
WEST
EAST
T - X/ 6.0

Figure 5

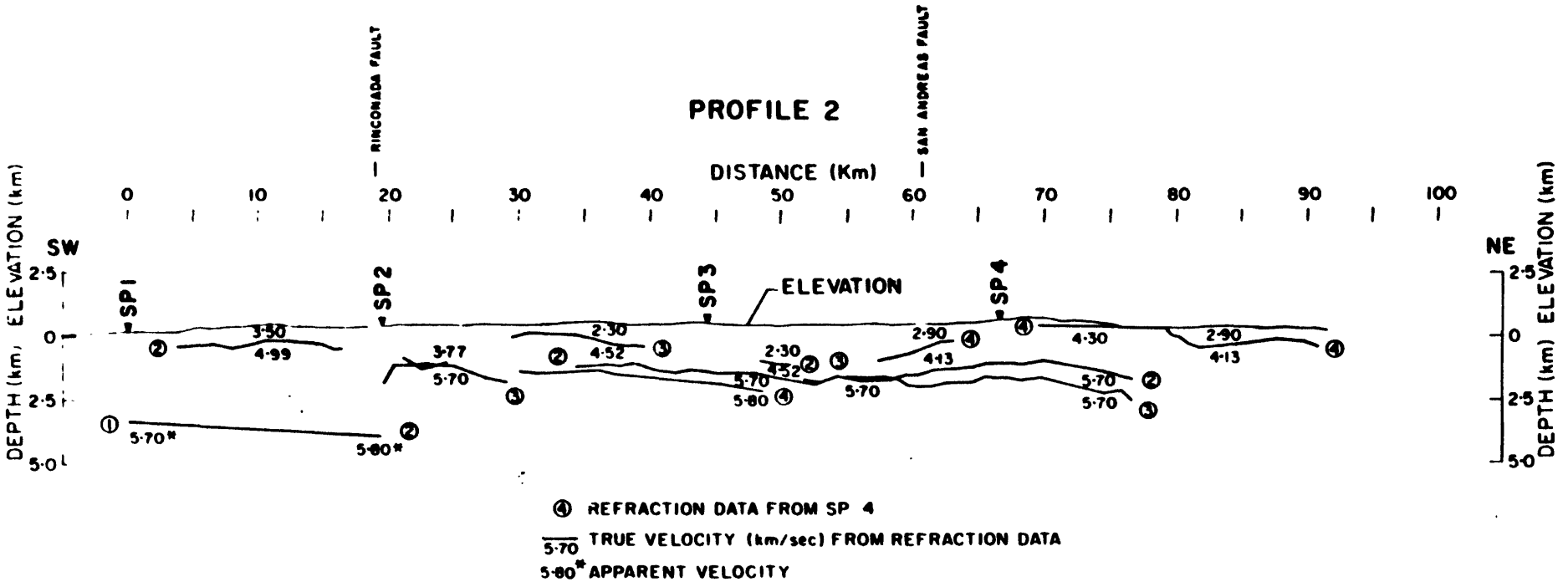
PROFILE 2
RINCONADA FAULT
SAN ANDREAS FAULT
DISTANCE (Km)
0
10
20
30
40
50
60
70
80
90
100
SW
NE
DEPTH (km), ELEVATION (km)
DEPTH (km) ELEVATION (km)
2·5
0
2·5
5·0
SP1
SP2
SP3
SP4
ELEVATION
3·50
4·99
3·77
5·70
2·30
4·52
2·30
4·52
5·70
5·80
2·90
4·13
4·30
2·90
4·13
5·70
5·70
5·70*
5·80*
④ REFRACTION DATA FROM SP 4
5·70 TRUE VELOCITY (km/sec) FROM REFRACTION DATA
5·80* APPARENT VELOCITY

Figure 6

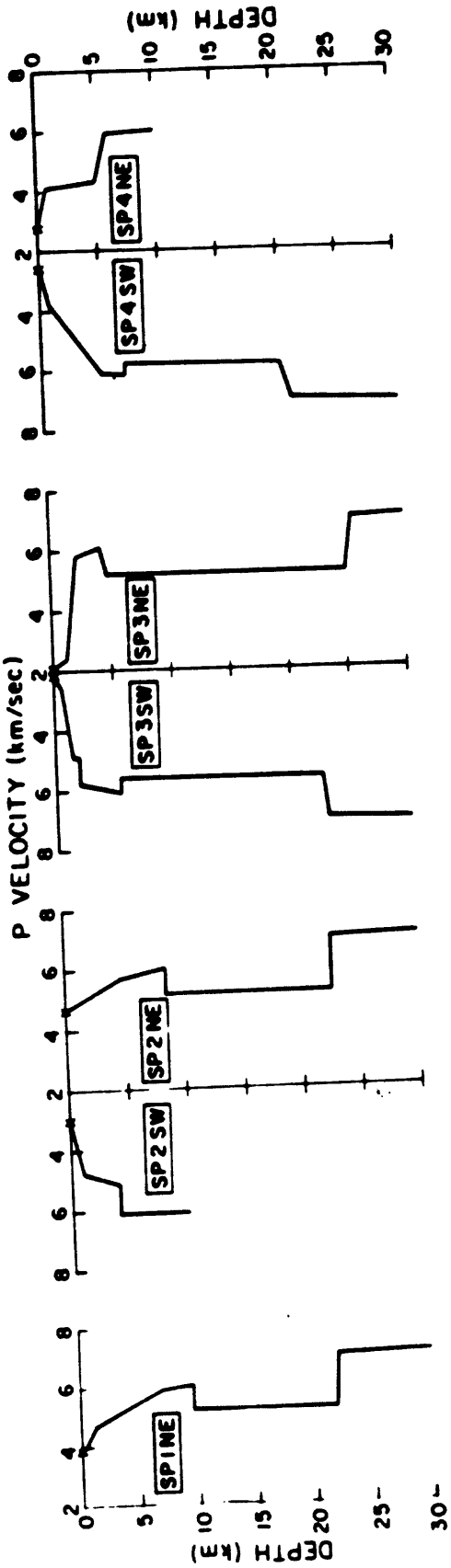
P VELOCITY (km/sec)
DEPTH (km)
SP1NE
SP2SW
SP2NE
SP3SW
SP3NE
SP4SW
SP4NE

Figure 7

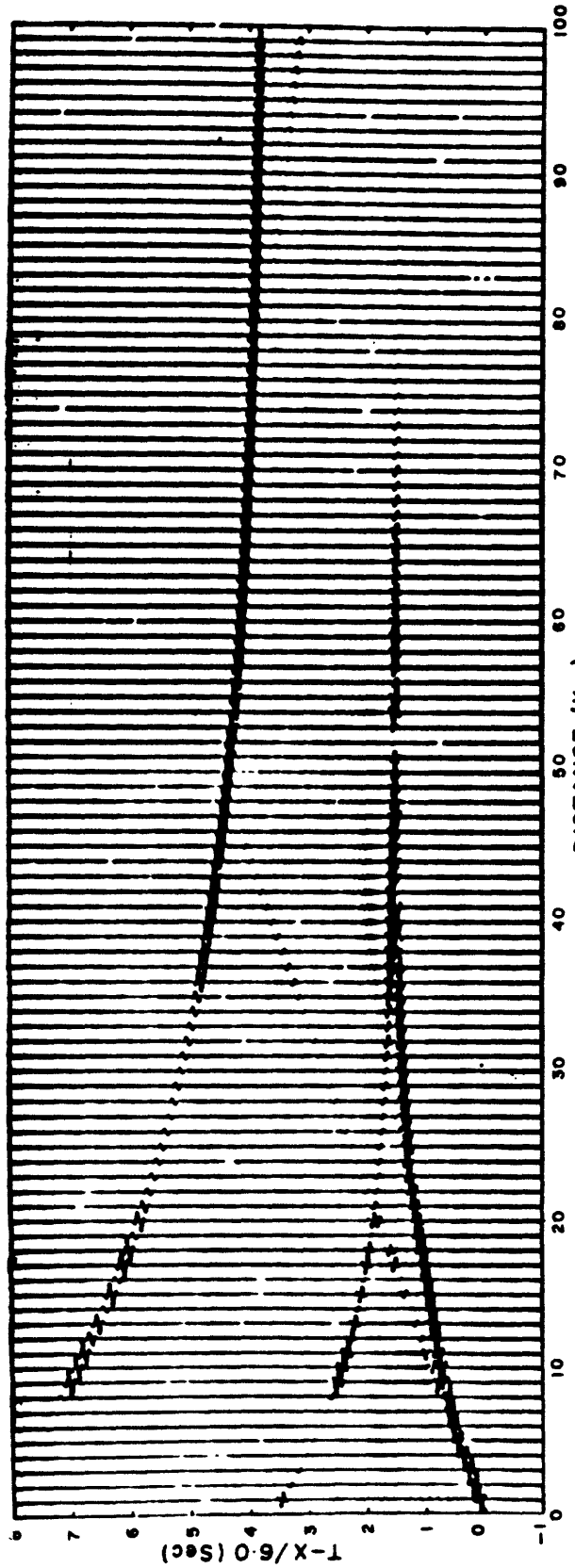

Figure 8

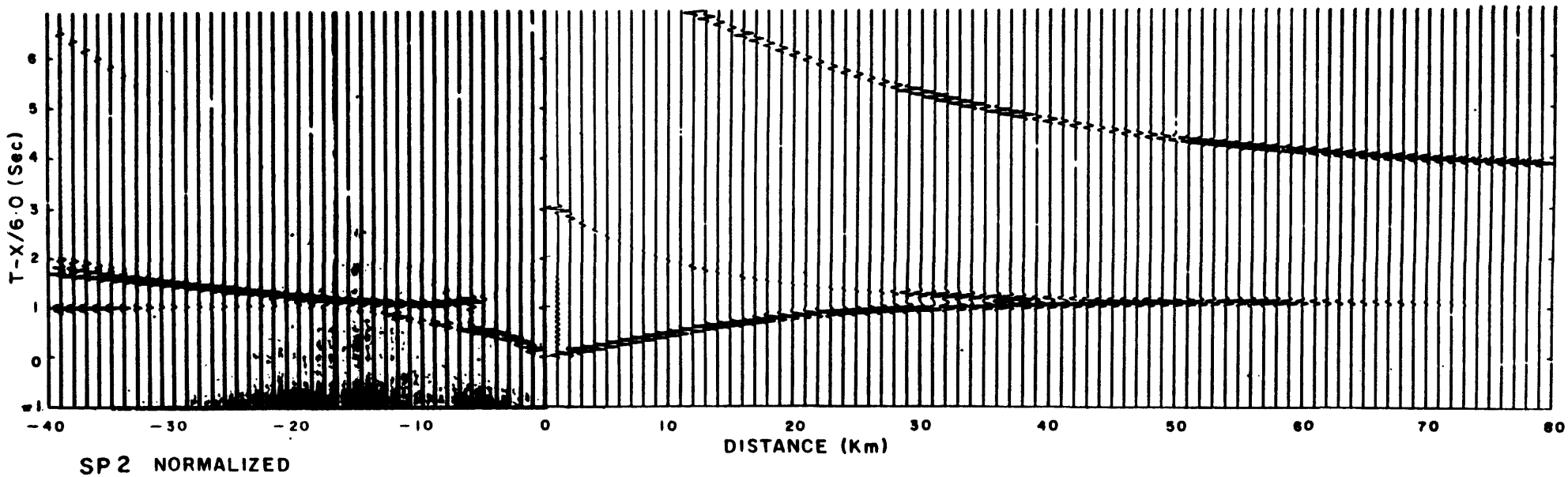
T-X/6·0 (Sec)
6
5
4
3
2
1
0
-1
-40
-30
-20
-10
0
10
20
30
40
50
60
70
80
DISTANCE (Km)
SP 2 NORMALIZED

Figure 9

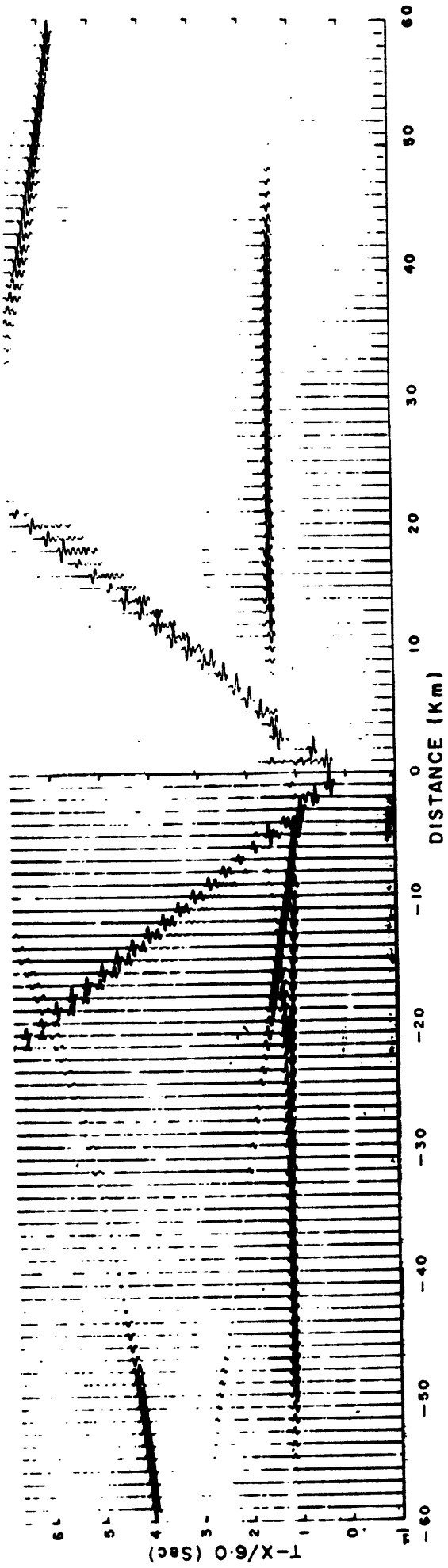
SP 3 NORMALIZED
T-X/6.0 (Sec)
DISTANCE (Km)
60
50
40
30
20
10
0
-10
-20
-30
-40
-50
-60
6
5
4
3
2
1
0

Figure 10

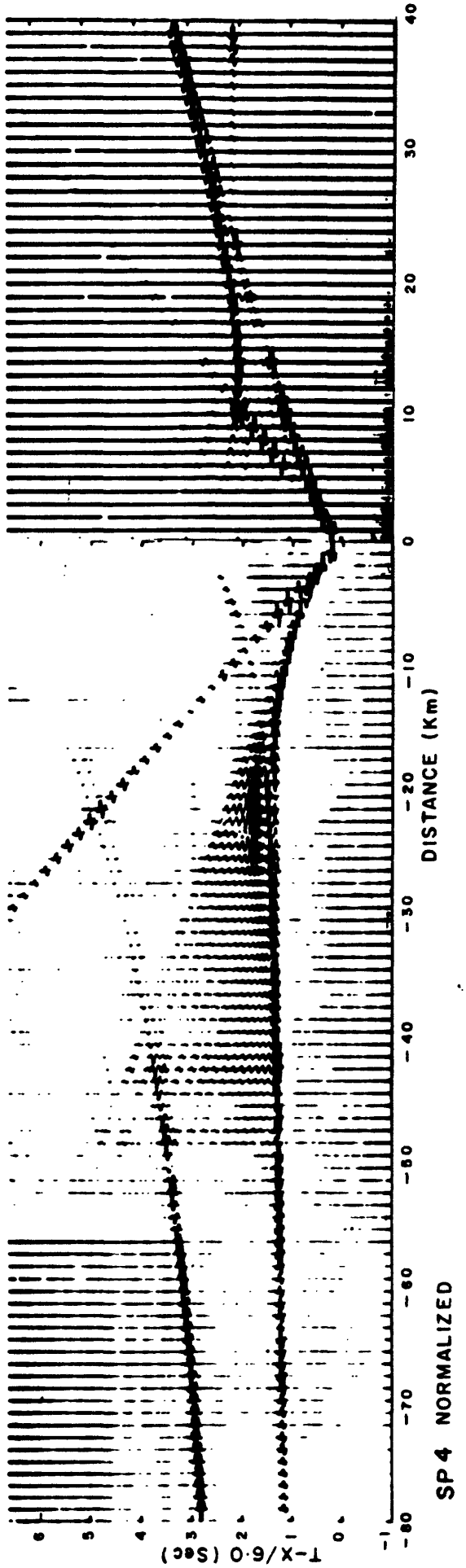

Figure 11

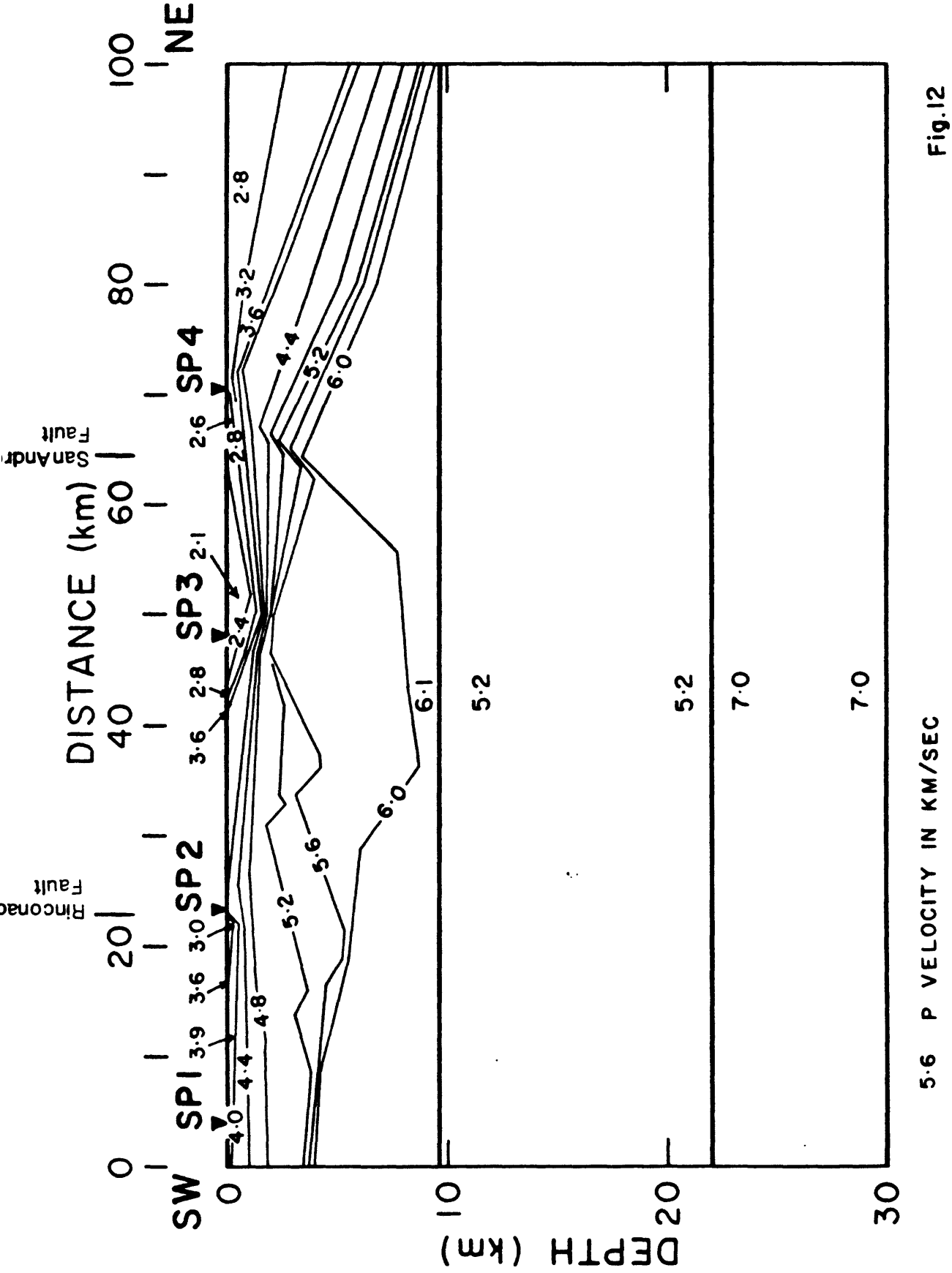

Fig.12

Figure 12

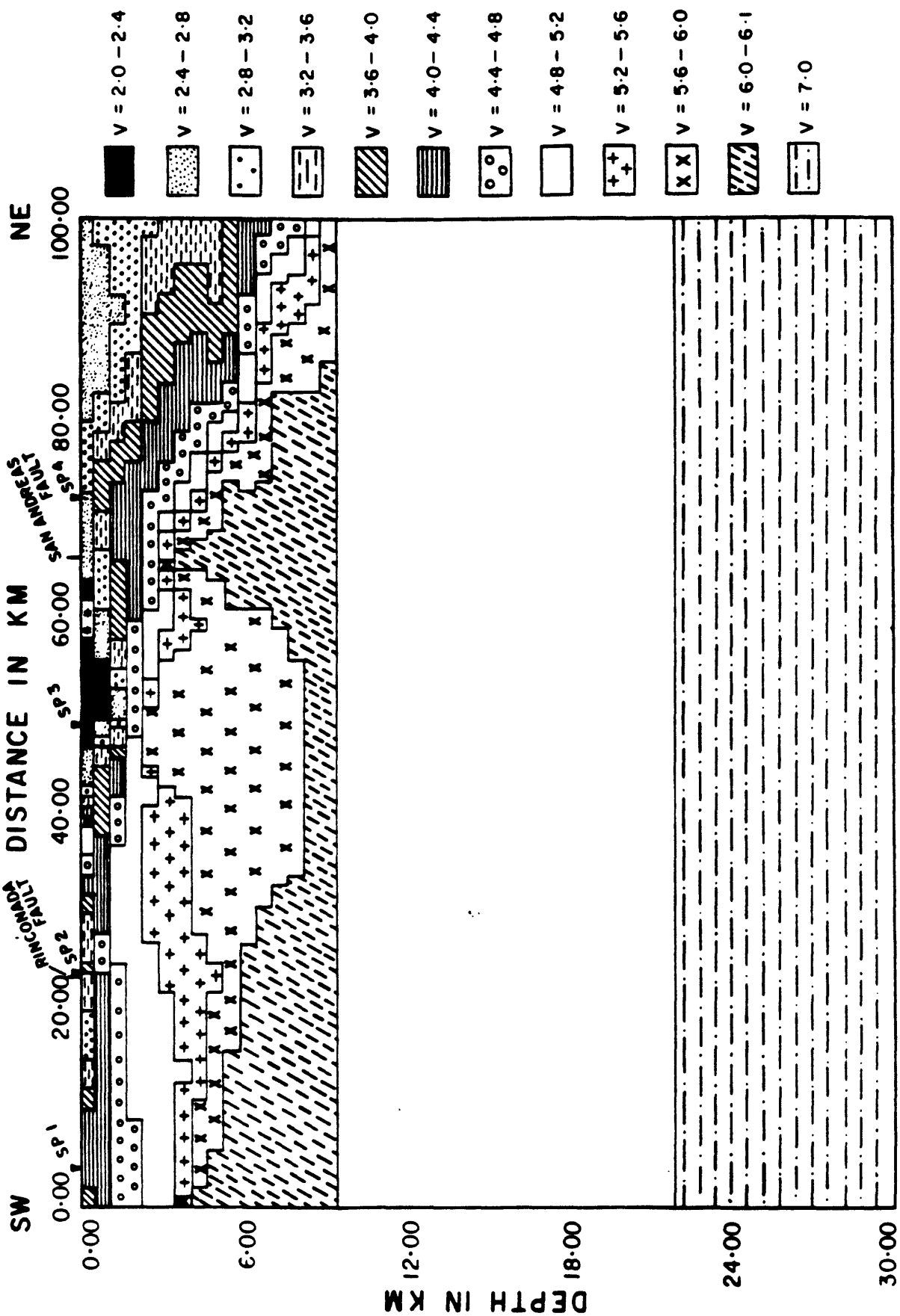
SW
NE
DISTANCE IN KM
0·00
20·00
40·00
60·00
80·00
100·00
SP1
SP2
SP3
SP4
RINCONADA FAULT
SAN ANDREAS FAULT
DEPTH IN KM
0·00
6·00
12·00
18·00
24·00
30·00
V = 2·0 – 2·4
V = 2·4 – 2·8
V = 2·8 – 3·2
V = 3·2 – 3·6
V = 3·6 – 4·0
V = 4·0 – 4·4
V = 4·4 – 4·8
V = 4·8 – 5·2
V = 5·2 – 5·6
V = 5·6 – 6·0
V = 6·0 – 6·1
V = 7·0

Figure 13

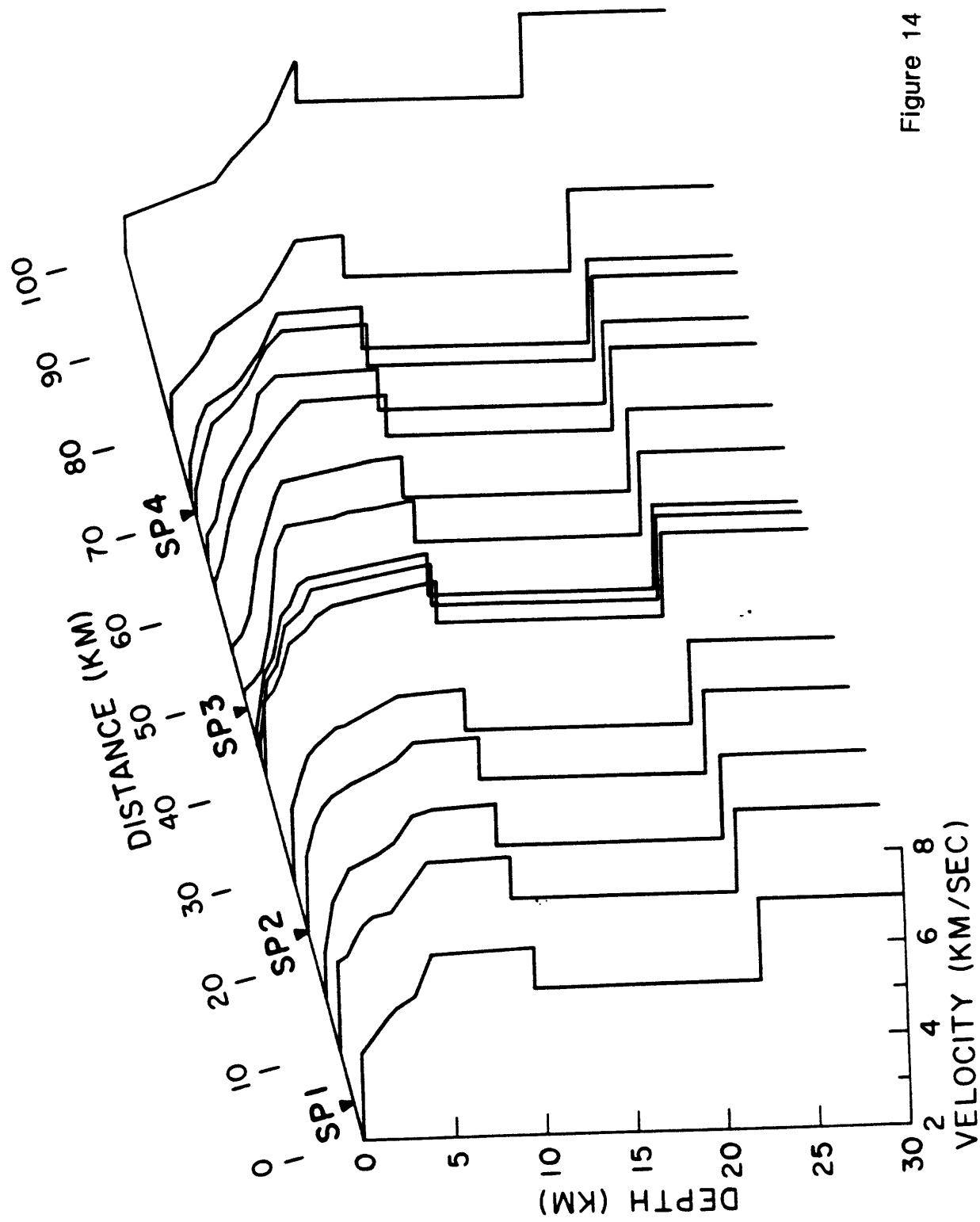
DISTANCE (KM)
0
10
20
30
40
50
60
70
80
90
100
SP1
SP2
SP3
SP4
DEPTH (KM)
0
5
10
15
20
25
VELOCITY (KM/SEC)
2
4
6
8
30

Figure 14

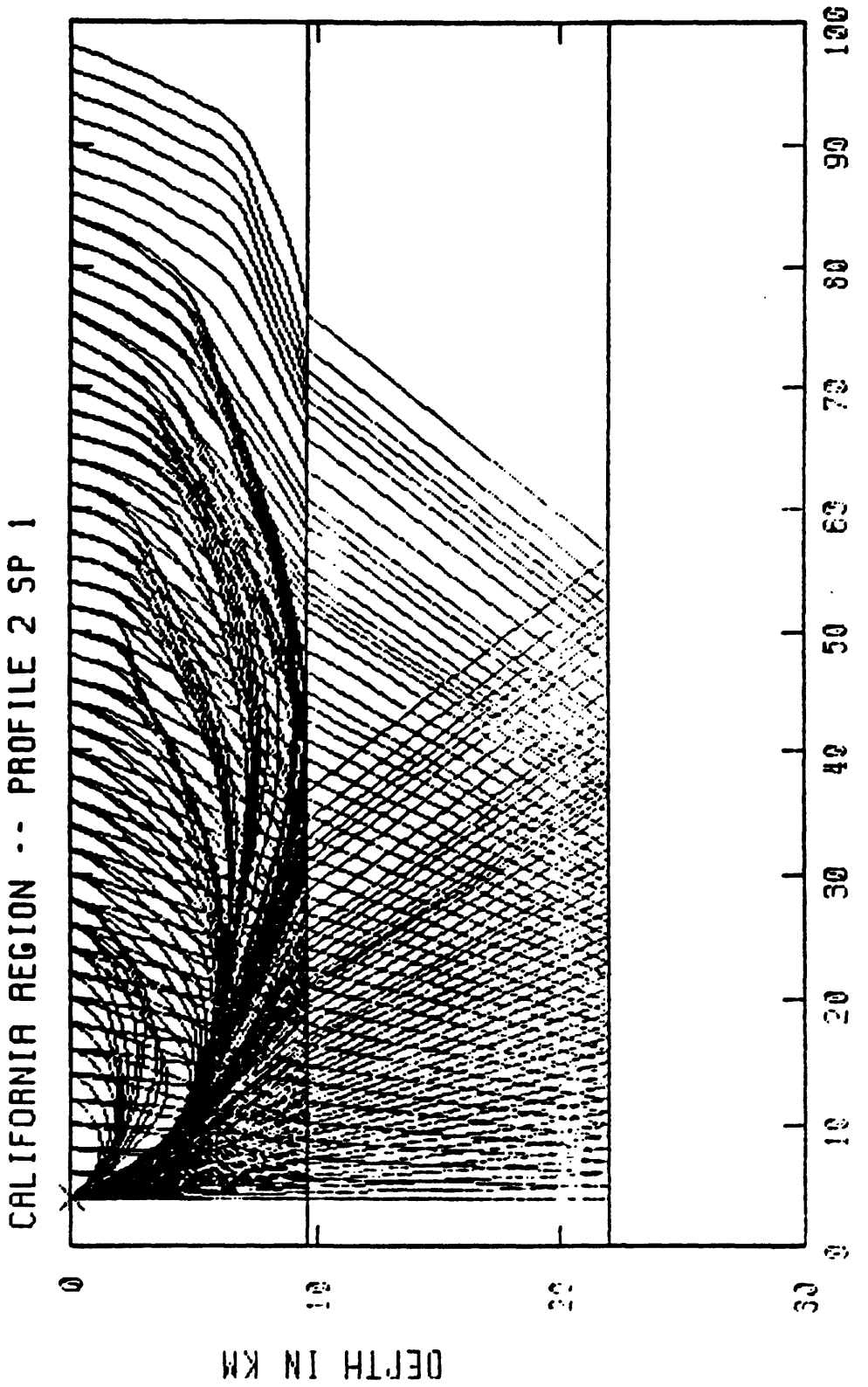
CALIFORNIA REGION -- PROFILE 2 SP 1
DEPTH IN KM
0
10
20
30
0
10
20
30
40
50
60
70
80
90
100
DISTANCE IN KM

Figure 15

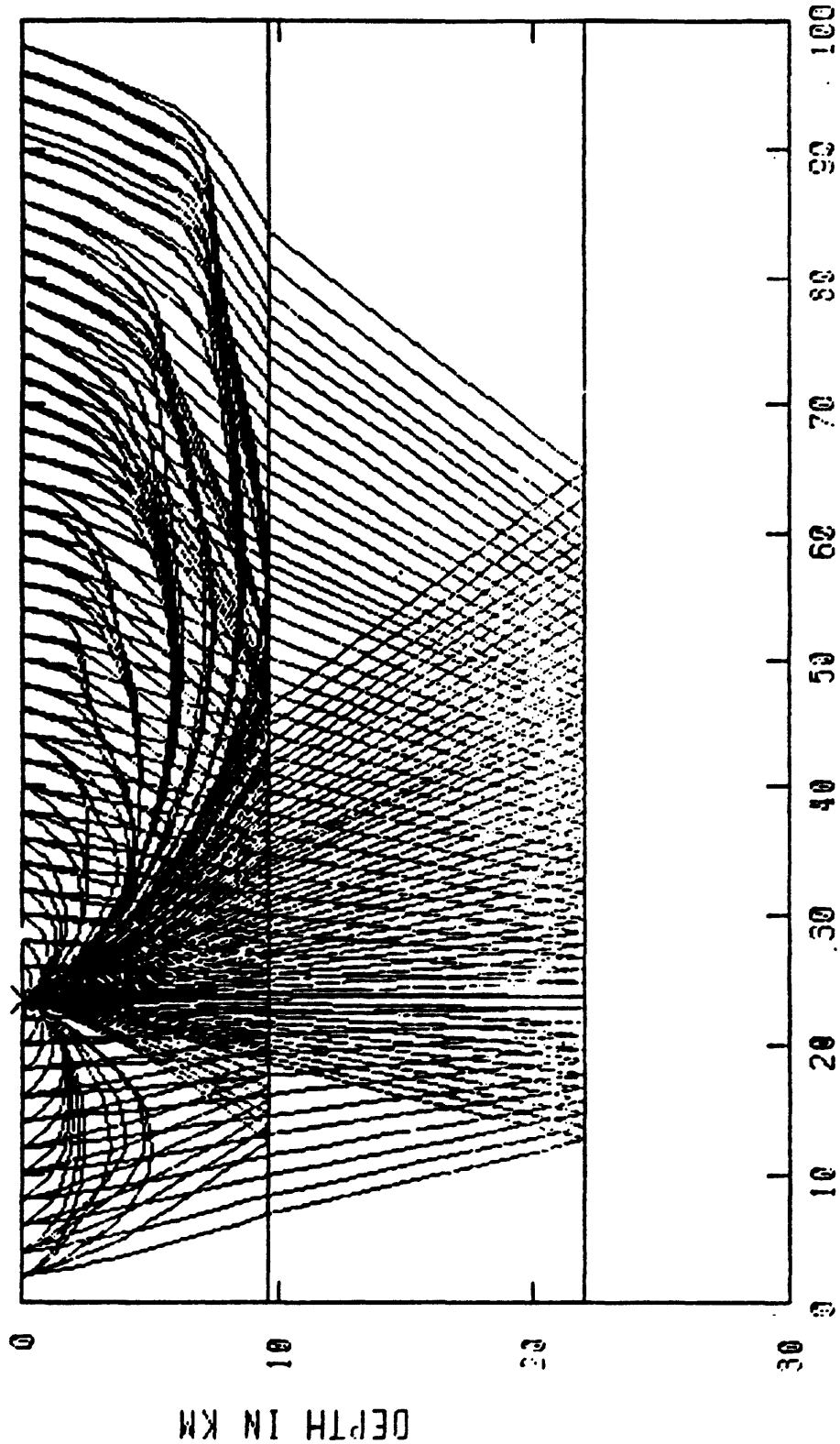
CALIFORNIA REGION -- PROFILE 2 SP 2
DEPTH IN KM
0
10
20
30
0
10
20
30
40
50
60
70
80
90
100
DISTANCE IN KM

Figure 16

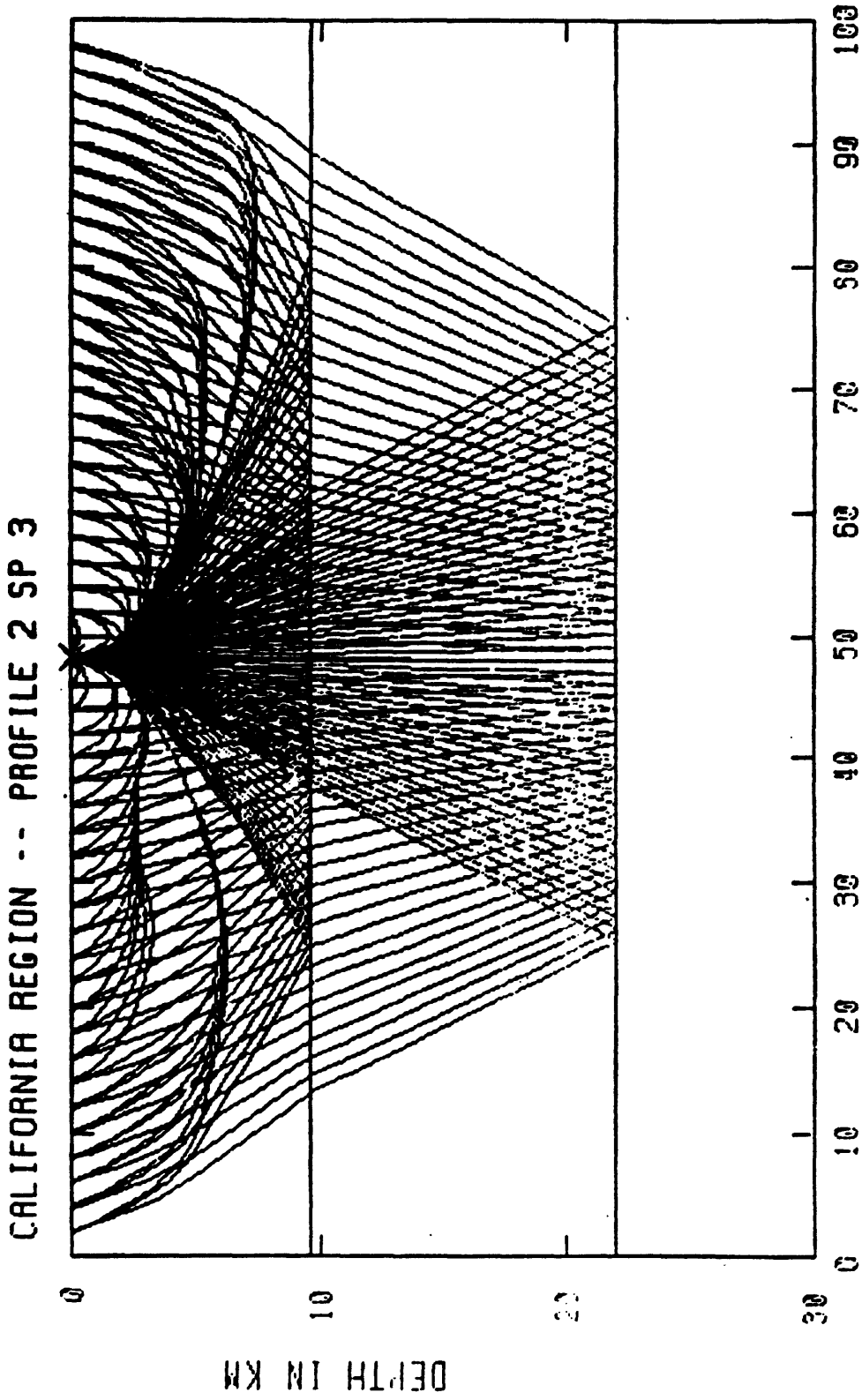
CALIFORNIA REGION -- PROFILE 2 SP 3
DEPTH IN KM
0
10
20
30
0
10
20
30
40
50
60
70
80
90
100
DISTANCE IN KM

Figure 17

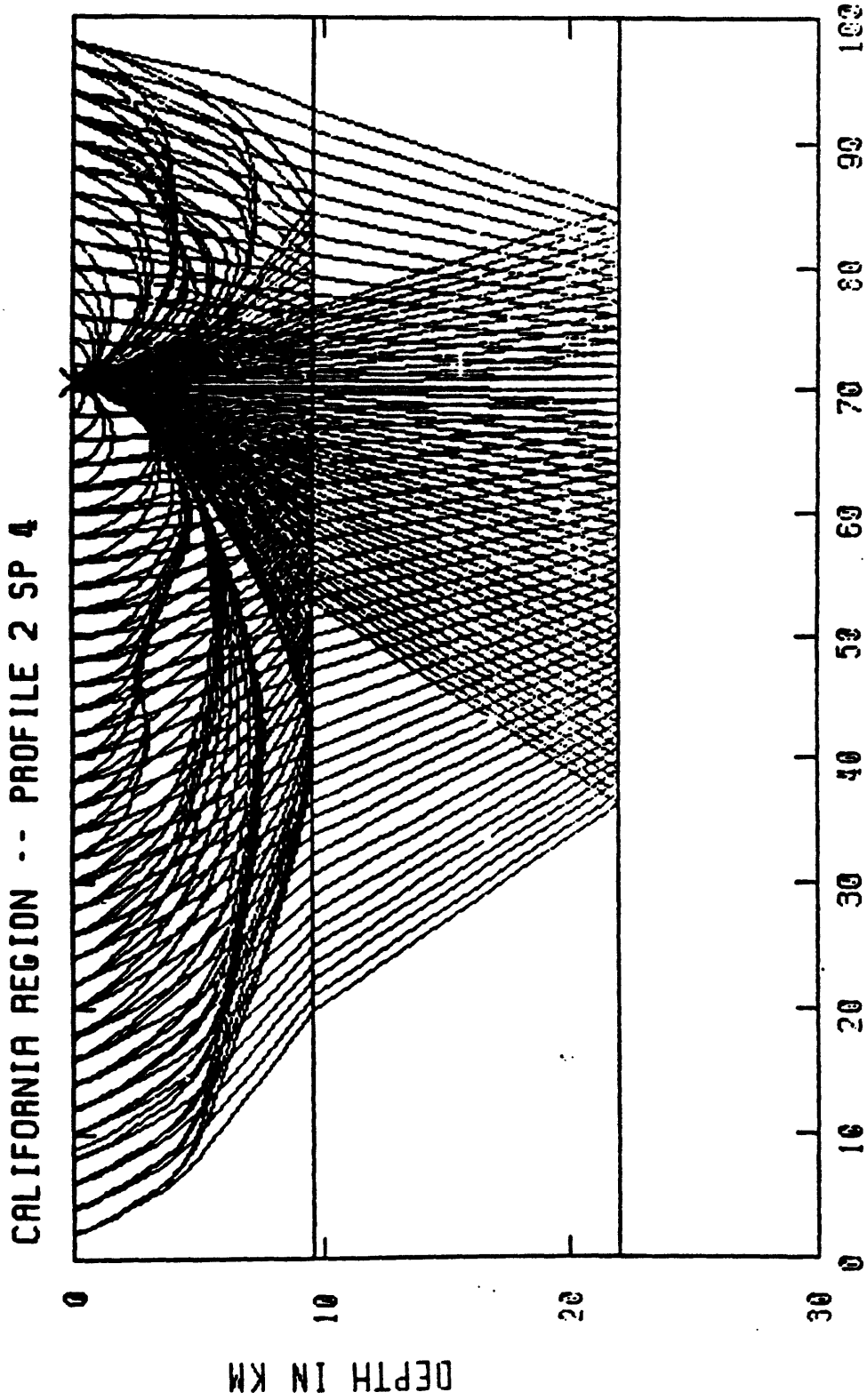
CALIFORNIA REGION -- PROFILE 2 SP 4
DEPTH IN KM
0
10
20
30
0
10
20
30
40
50
60
70
80
90
DISTANCE IN KM

Figure 18

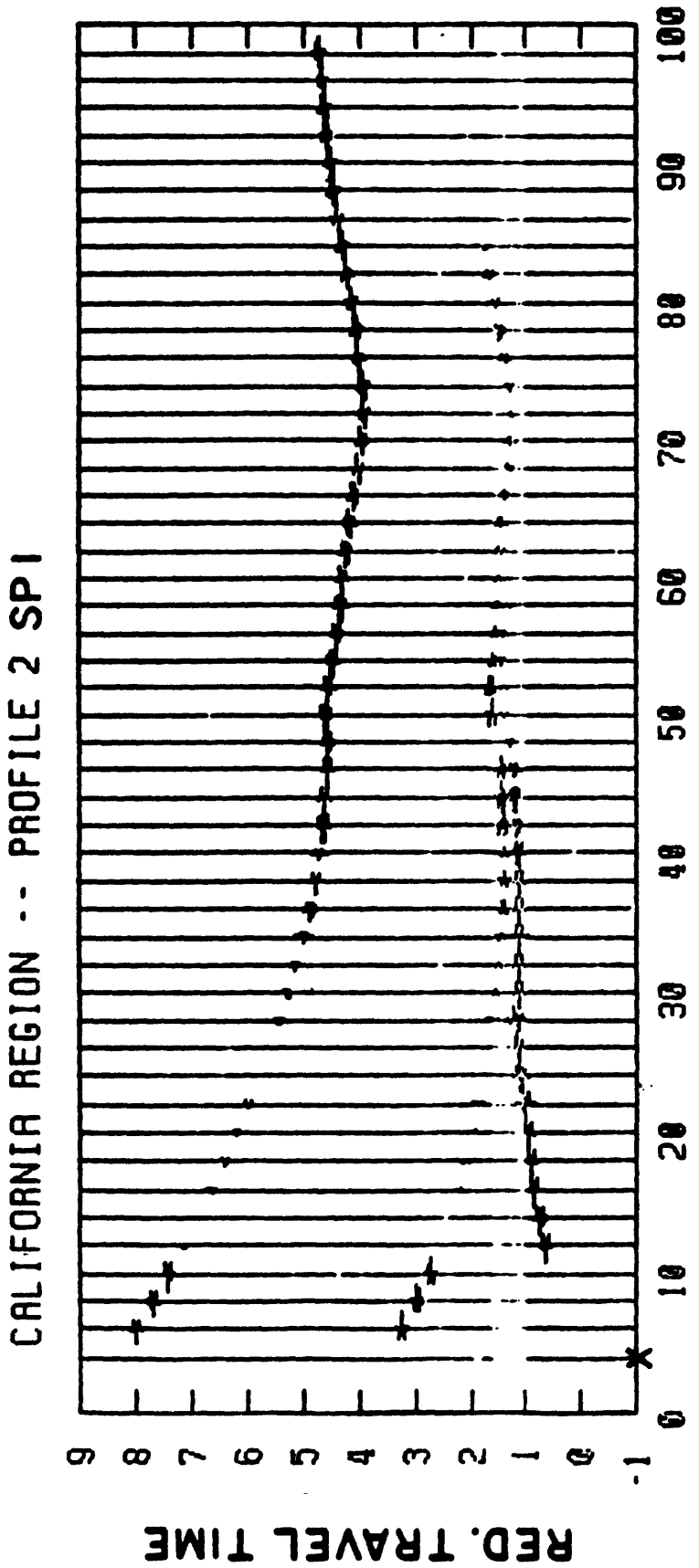
CALIFORNIA REGION -- PROFILE 2 SP1
RED. TRAVEL TIME
9
8
7
6
5
4
3
2
1
0
-1
0
10
20
30
40
50
60
70
80
90
100
DISTANCE IN KM
VRED= 6.00KM/SEC
VERTICAL

Figure 19

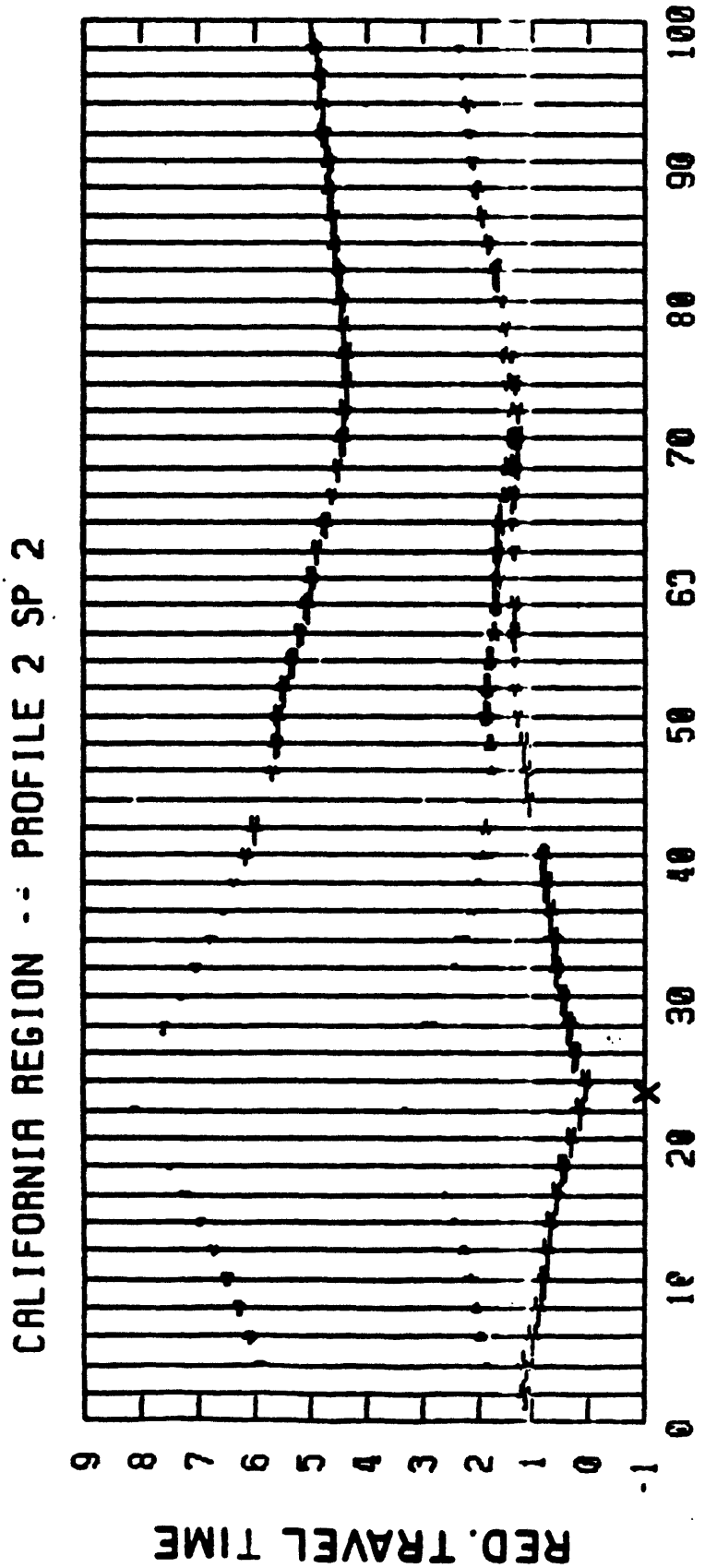
CALIFORNIA REGION -: PROFILE 2 SP 2
RED. TRAVEL TIME
9
8
7
6
5
4
3
2
1
0
-1
0
10
20
30
40
50
60
70
80
90
100
DISTANCE IN KM
VRED= 6.00KM/SEC
VERTICAL

Figure 20

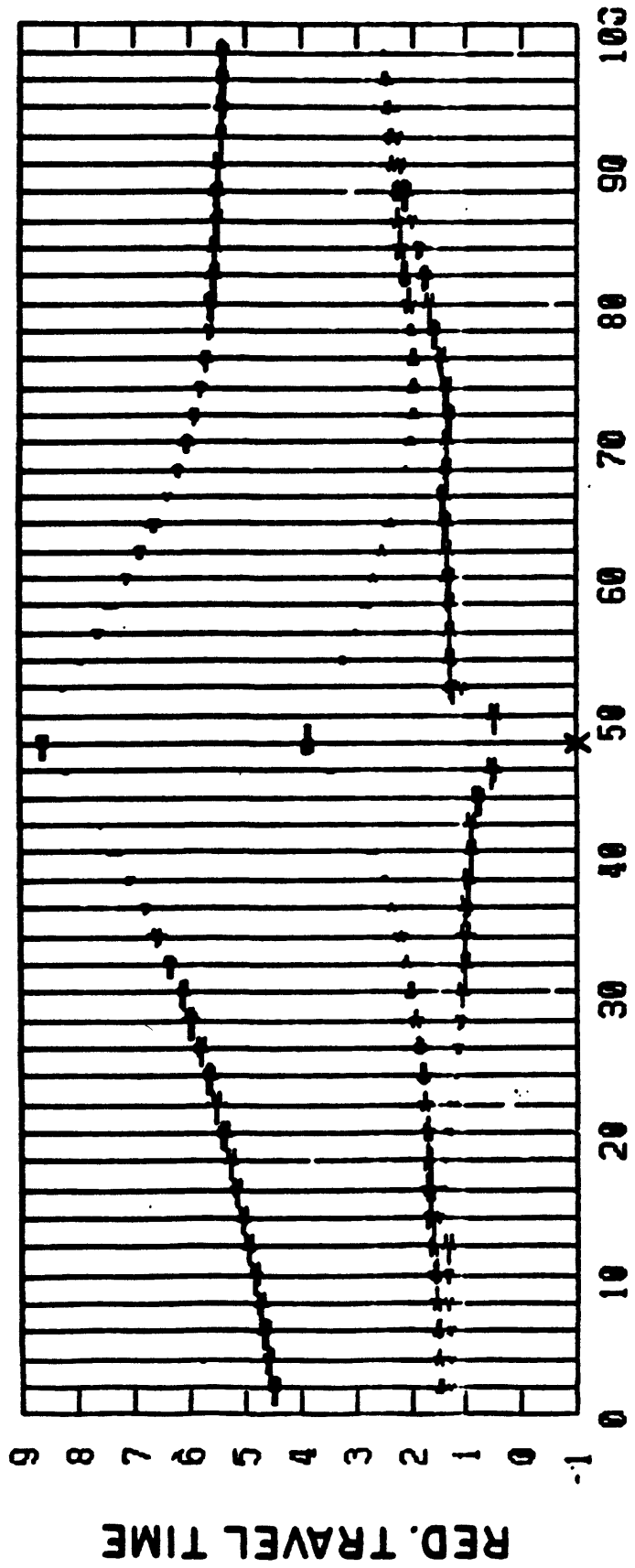
CALIFORNIA REGION -- PROFILE 2. SP 3
RED. TRAVEL TIME
9
8
7
6
5
4
3
2
1
0
-1
0
10
20
30
40
50
60
70
80
90
100
DISTANCE IN KM
VRED= 6.00KM/SEC
VERTICAL

Figure 21

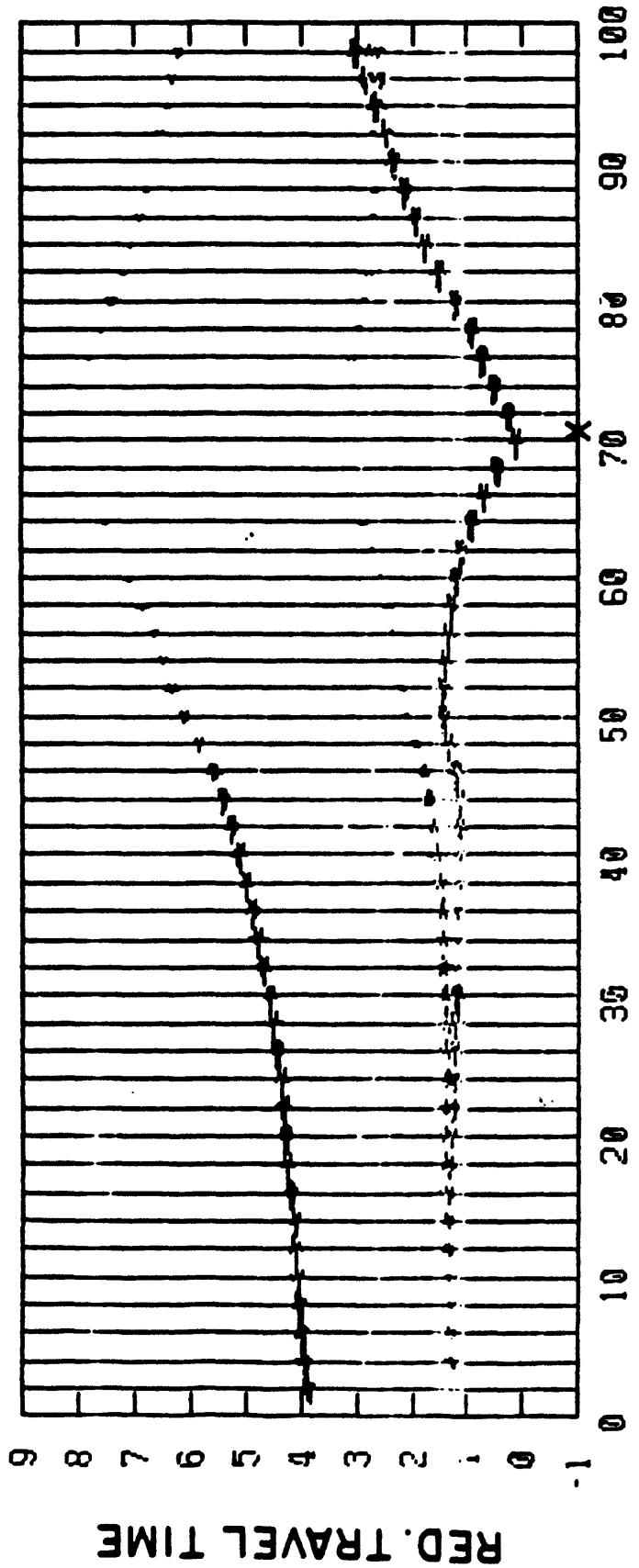
CALIFORNIA REGION -- PROFILE 2 SP 4
RED. TRAVEL TIME
9
8
7
6
5
4
3
2
1
0
-1
0
10
20
30
40
50
60
70
80
90
100
DISTANCE IN KM
VRED= 6.00KM/SEC
VERTICAL

Figure 22

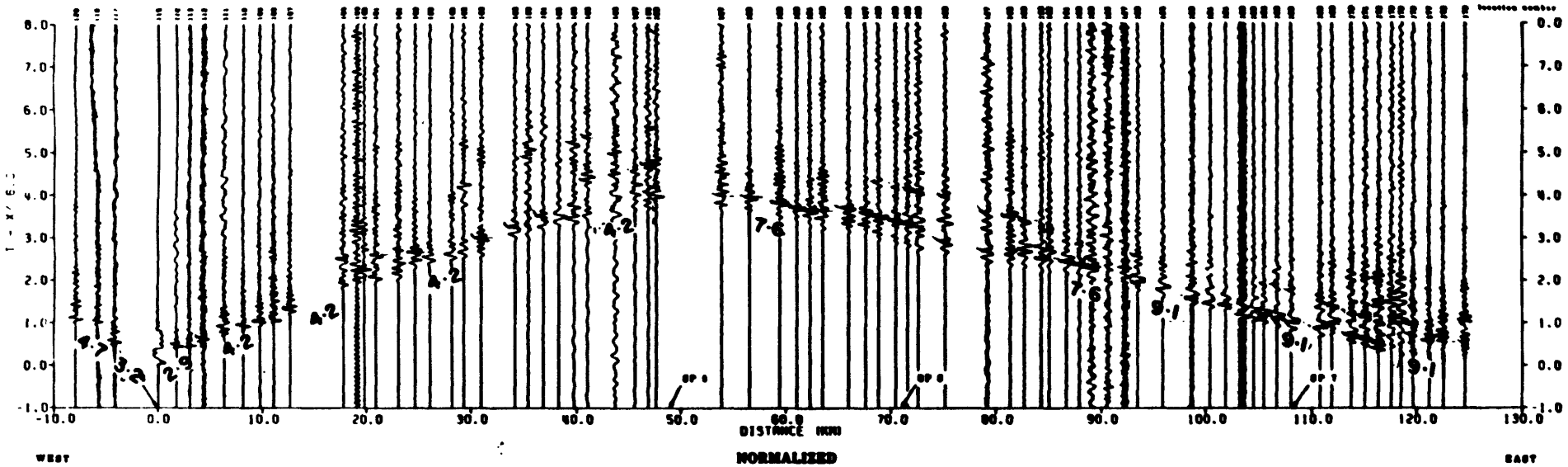

RECORD SECTIONS
CHOLAME VALLEY TO SIERRA NEVADA
SHOT 3, SHOTPOINT 4

by

J. M. Murphy and A. W. Walter

1984

Figure 23

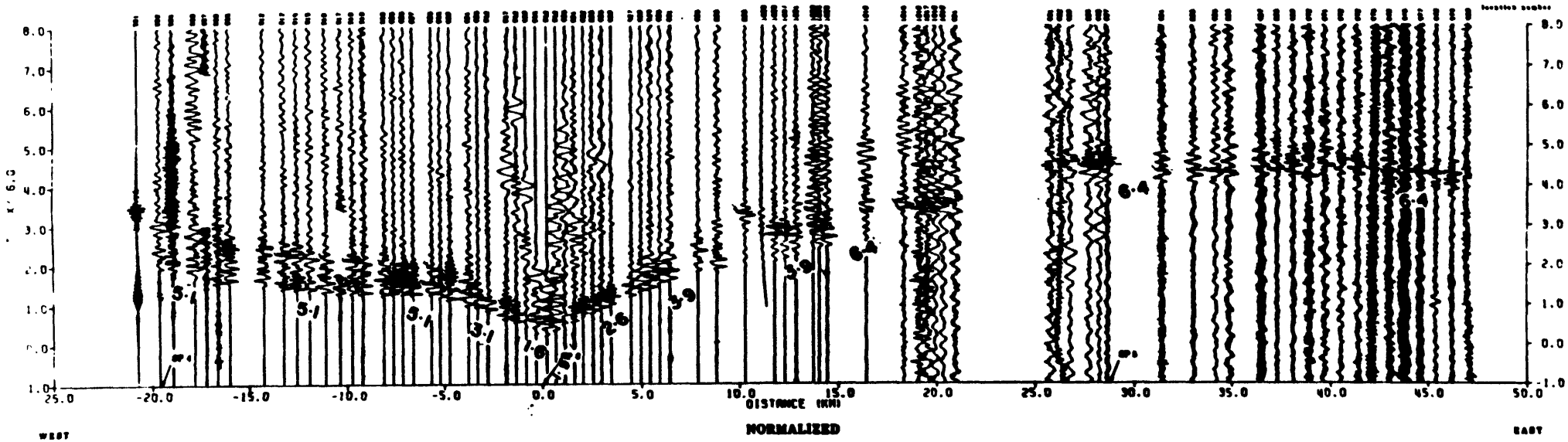

RECORD SECTIONS
SHOT 9, SHOTPOINT 8
CHOLAME VALLEY TO SAN JOAQUIN VALLEY

by

J. M. Murphy and A. W. Walter

1984

Figure 24

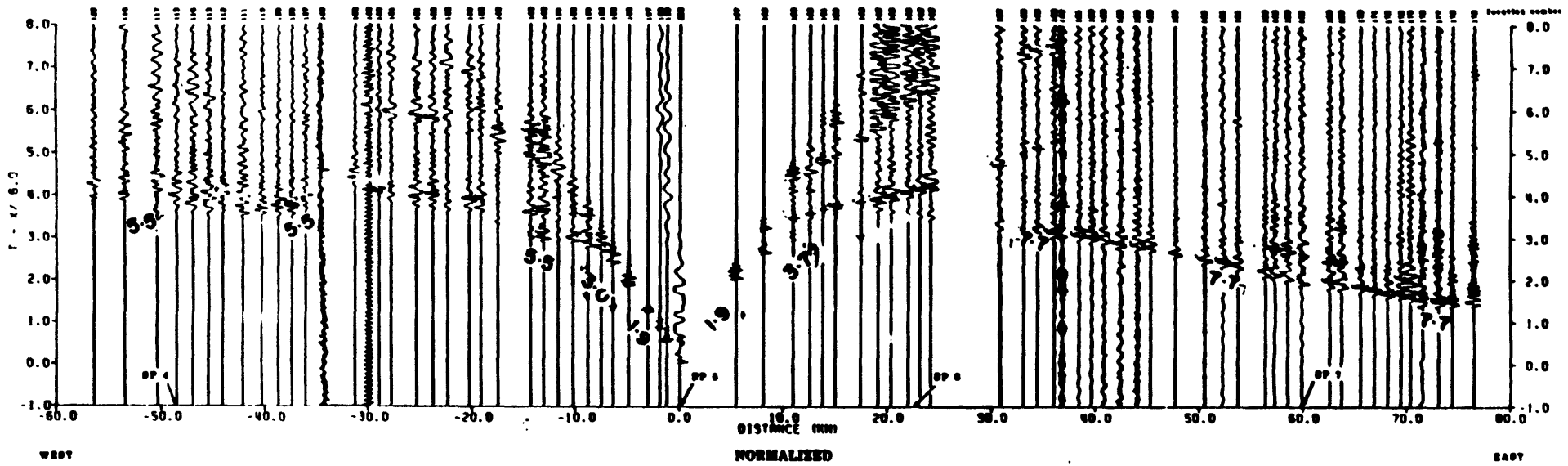

RECORD SECTIONS
CHOLAME VALLEY TO SIERRA NEVADA
SHOT 2, SHOTPOINT 5

by

J. M. Murphy and A. W. Walter

1984

Figure 25

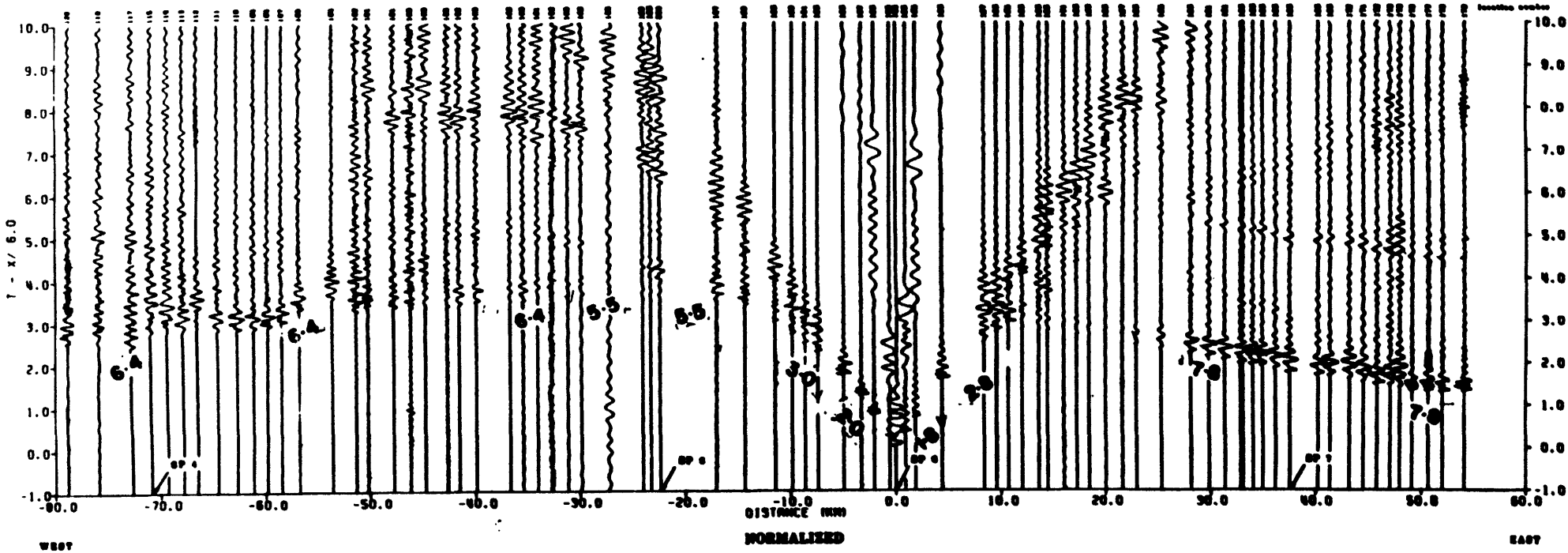

RECORD SECTIONS
CHOLAME VALLEY TO SIERRA NEVADA
SHOT 4, SHOTPOINT 6

by

J. M. Murphy and A.W. Walter

1984

Figure 26

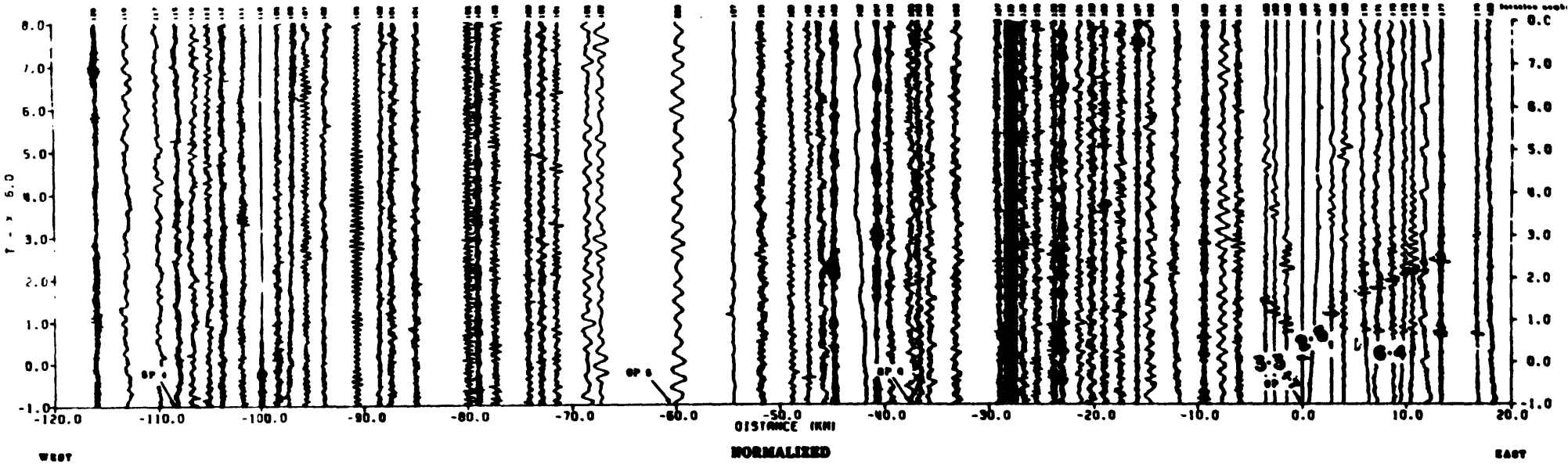

RECORD SECTIONS
CHOLAME VALLEY TO SIERRA NEVADA
SHOT 1, SHOTPOINT 7

by

J. H. Murphy and A. W. Walter

1984

Figure 27

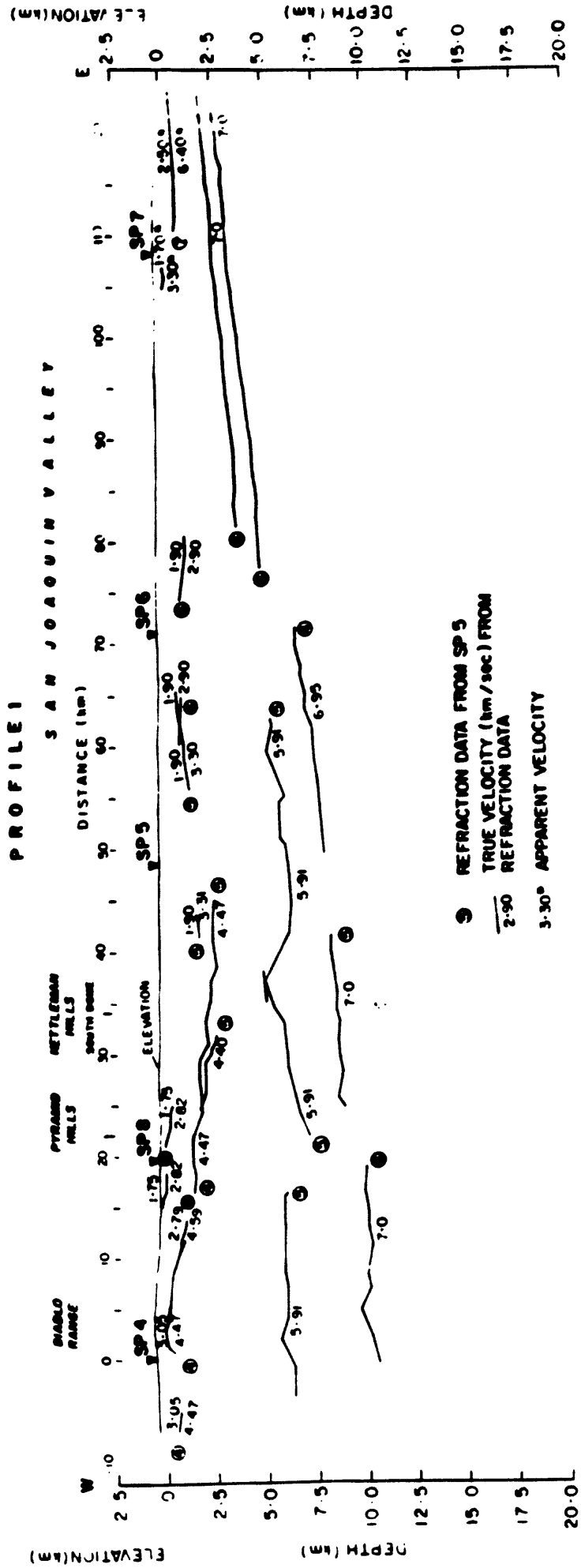
PROFILE I
SAN JOAQUIN VALLEY
DISTANCE (km)
ELEVATION
DEPTH (km)
W
E
SP4
SP5
SP6
SP7
SP8
DIABLO RANGE
PYRAMID HILLS
KETTLEMAN HILLS
SOUTH DOME
REFRACTION DATA FROM SP 5
TRUE VELOCITY (km/sec) FROM REFRACTION DATA
APPARENT VELOCITY

Figure 28

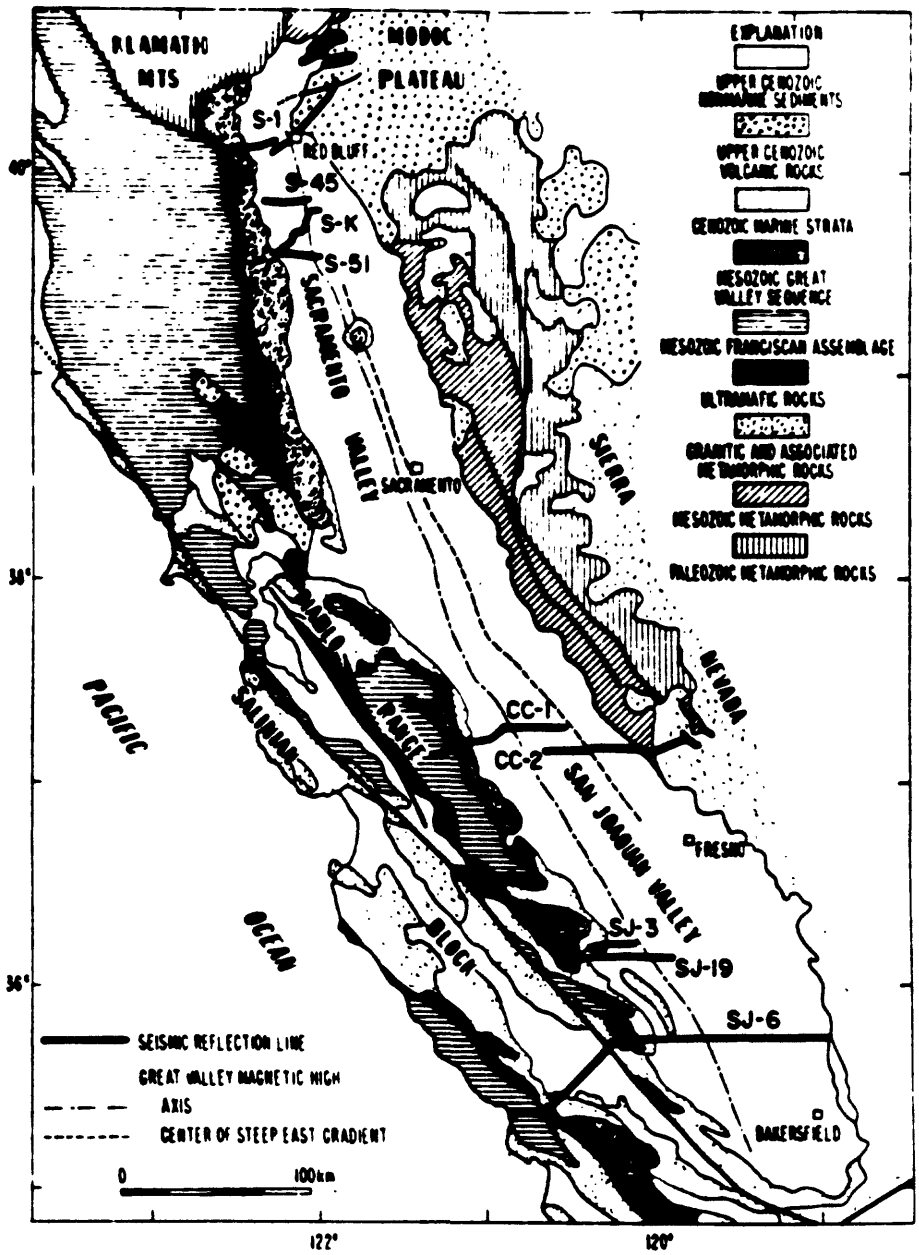
KLAMATH MTS
MODOC PLATEAU
S-1
RED BLUFF
S-45
S-K
S-51
SACRAMENTO VALLEY
SACRAMENTO
SIERRA NEVADA
SALINIAN BLOCK
CC-1
CC-2
SAN JOAQUIN VALLEY
FRESNO
SJ-3
SJ-19
SJ-6
BAKERSFIELD
PACIFIC OCEAN
40°
38°
36°
122°
120°
EXPLANATION
UPPER CENOZOIC MARINE SEDIMENTS
UPPER CENOZOIC VOLCANIC ROCKS
CENOZOIC MARINE STRATA
MESOZOIC GREAT VALLEY SEQUENCE
MESOZOIC FRANCISCAN ASSEMBLAGE
ULTRAMAFIC ROCKS
GRANITIC AND ASSOCIATED METAMORPHIC ROCKS
MESOZOIC METAMORPHIC ROCKS
PALEOZOIC METAMORPHIC ROCKS
SEISMIC REFLECTION LINE
GREAT VALLEY MAGNETIC HIGH
AXIS
CENTER OF STEEP EAST GRADIENT
0
100km

Figure 29

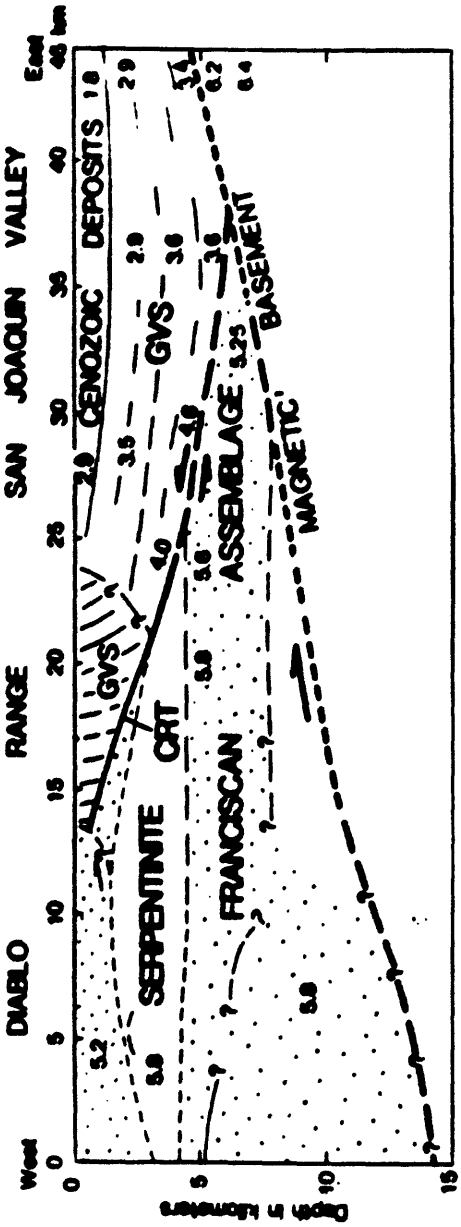
West
DIABLO
RANGE
SAN JOAQUIN VALLEY
East
40 km
0
5
10
15
20
25
30
35
40
CENOZOIC DEPOSITS
GVS
GVS
SERPENTINITE
ORT
FRANCISCAN
ASSEMBLAGE
BASEMENT
MAGNETIC
Depth in kilometers
0
5
10
15

Figure 30

Combined interpretation of seismic-refraction and reflection data along the Cholame Valley-Sierra Nevada segment of the SJ-6 profile, California, USA

A. Egger and J. Ansorge
Institute of Geophysics, ETH Hoenggerberg, CH-8093 Zurich, Switzerland

The following comments summarize a partial interpretation of the seismic-refraction and reflection data recorded along line SJ-6 in south central California. These data were provided by the U.S. Geological Survey (Murphy and Walter, 1984) for the 6th workshop of the IASPEI Commission on Controlled Source Seismology (CCSS) on the "Interpretation of Seismic Wave Propagation in Laterally Heterogeneous Structures". Our work focused of the determination of the upper-crustal structure along the section of the SJ-6 line extending from the San Andreas Fault across the Diablo Range, the Kettleman Hills and San Joaquin Valley to the Sierra Nevada batholith. This section passes through the five shotpoints labelled from west to east SP4, SP8, SP5, SP6 and SP7.

Method of analysis

The seismic-refraction data were modeled using a 2-D ray-tracing program which was originally developed by Gebrande (1976) and later modified. In this program, the layers of the model are defined by velocity isolines which are continuous across the model; the velocities are then interactively adjusted to improve the agreement between the calculated and observed traveltimes. Layers can have negligible thickness.

We started modeling the refraction traveltime data where the reflection time-section shows the least complicated sedimentary structure, between SP5 and SP6 (Figs. 1 and 2). The short-range refraction data did allow resolution of individual sedimentary layers, so the major structural interfaces were taken from the reflection data. Velocities assigned to the layers in the starting model were chosen from the observed apparent velocities of the first arrivals. Outpinching layers were modeled in accordance with the geological map of California, especially across the folds visible on the reflection time-section between the San Joaquin Valley and the Diablo Range. Additional constraints were taken from Wentworth and others (1983) who have interpreted the same data. By working our way westward towards SP8 and SP4 (Figs. 3 and 4) and eastward to SP7 (Fig. 5) we were able to construct an upper-crustal velocity model (Fig. 6) which satifies most of the refraction data reasonably well.

Upper crustal velocity model

The overall model (Fig. 6) is characterized by a smoothly westward dipping interface between the sedimentary layers and the crystalline basement. The velocity at the top of the basement increases continuously westward from 5.5 km/s near the surface contact with the Sierra Nevada batholith to 6.6 km/s at a depth of ~15 km close to the San Andreas Fault (Fig. 6). The buried contact between the supposedly mafic basement on the west and the Sierra Nevada batholith on the east could not be located using the available seismic data. The velocity gradient in the basement had to be reduced eastward to satisfy the apparent velocities observed in the eastern part of the San Joaquin Valley, particularly those observed from SP7.

The sedimentary structure located between SP5 and SP8, the Kettleman Hills and Pyramid Hills, is probably oversimplified. In our model the well-defined deeper sedimentary layers of the San Joaquin Valley extend continuously with

increasing thickness all the way to SP4 where they outcrop at the surface. Here, their thickness amounts to ~4 km, whereas the greatest depth of these units, ~8 km, is reached under the Kettleman Hills anticline. The remaining wedge of material found below the sedimentary strata west of the Kettleman Hills has velocities between 5.2 km/s and 5.55 km/s and could belong to the Franciscan assemblage.

Some doubts remain about the smooth continuation of the upper crustal structure, especially between SP4 and SP5. Travel-times computed from SP4 and SP8 eastward to respective distance ranges of 50-70 km and 40-60 km are early compared to the observed times (Fig. 3 and 4); in contrast, those computed from SP5 westward to ranges of 20-40 km are late (Fig. 1). Although we could not resolve this discrepancy, the detailed transition from the San Joaquin Valley to the Franciscan units of the Diablo Range could possibly be resolved by interpreting the reflection data more carefully.

Acknowledgements

We would like to thank W. D. Mooney and the U.S. Geological Survey for providing this excellent set of data.

References

Gebrande, H., 1976, A seismic ray-tracing method for 2-D inhomogeneous media, in P. Giese, C. Prodehl, and A. Stein eds., Explosion Seismology in Central Europe, Springer Verlag, p. 162-167.

Murphy, J.M., and A.W. Walter, 1984, Data Report for a seismic refraction investigation: Morro Bay to the Sierra Nevada, California, U.S. Geol. Surv., Open File Rep. 84-642.

Wentworth, C.M., A.W. Walter, J.A. Bartow, and M.D. Zoback, 1983, Evidence on the tectonic setting of the 1983 Coalinga earthquakes from deep reflection and refraction profiles across the southeastern end of the Kettleman Hills, in H.J. Bennett and R.W. Sherburne eds., The 1983 Coalinga, California earthquakes, Calif. Div. of Mines and Geol., Special Publ. 66, p. 113-126.

Figure Captions

Fig. 1 Observed (X) and calculated (+) traveltime-distance plots and the ray-traced model diagram for shotpoint SP5. Distances are measured from SP4.

Fig. 2 Same as Fig. 1 for SP6.

Fig. 3 Same as Fig. 1 for SP8.

Fig. 4 Same as Fig. 1 for SP4.

Fig. 5 Same as Fig. 1 for SP7.

Fig. 6 Velocity-depth section derived between the San Andreas Fault (SP4) and the Sierra Nevada batholith east of SP7.

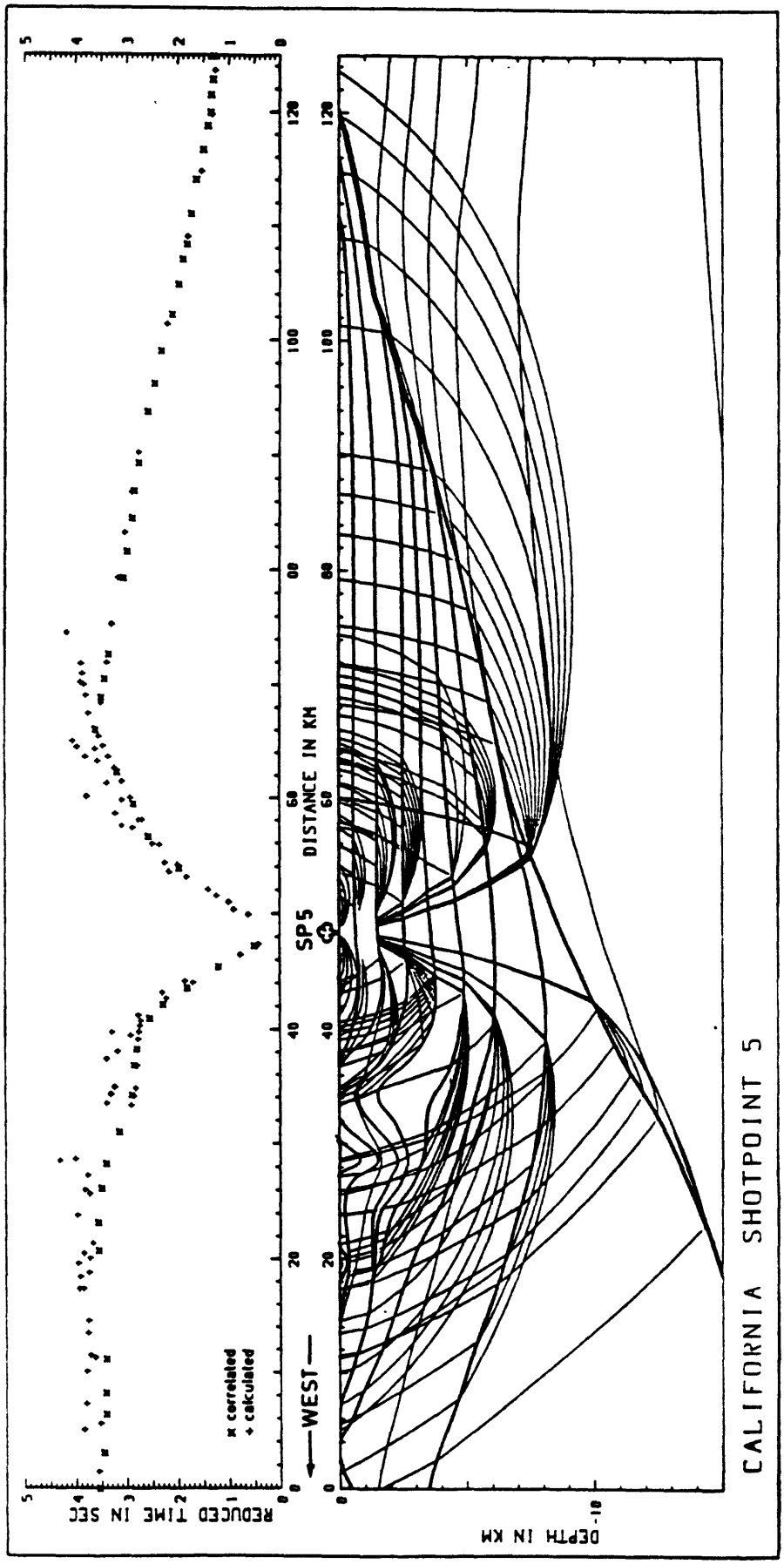
CALIFORNIA SHOTPOINT 5
DEPTH IN KM
REDUCED TIME IN SEC
DISTANCE IN KM
SP5
WEST
x correlated
+ calculated

Figure 1

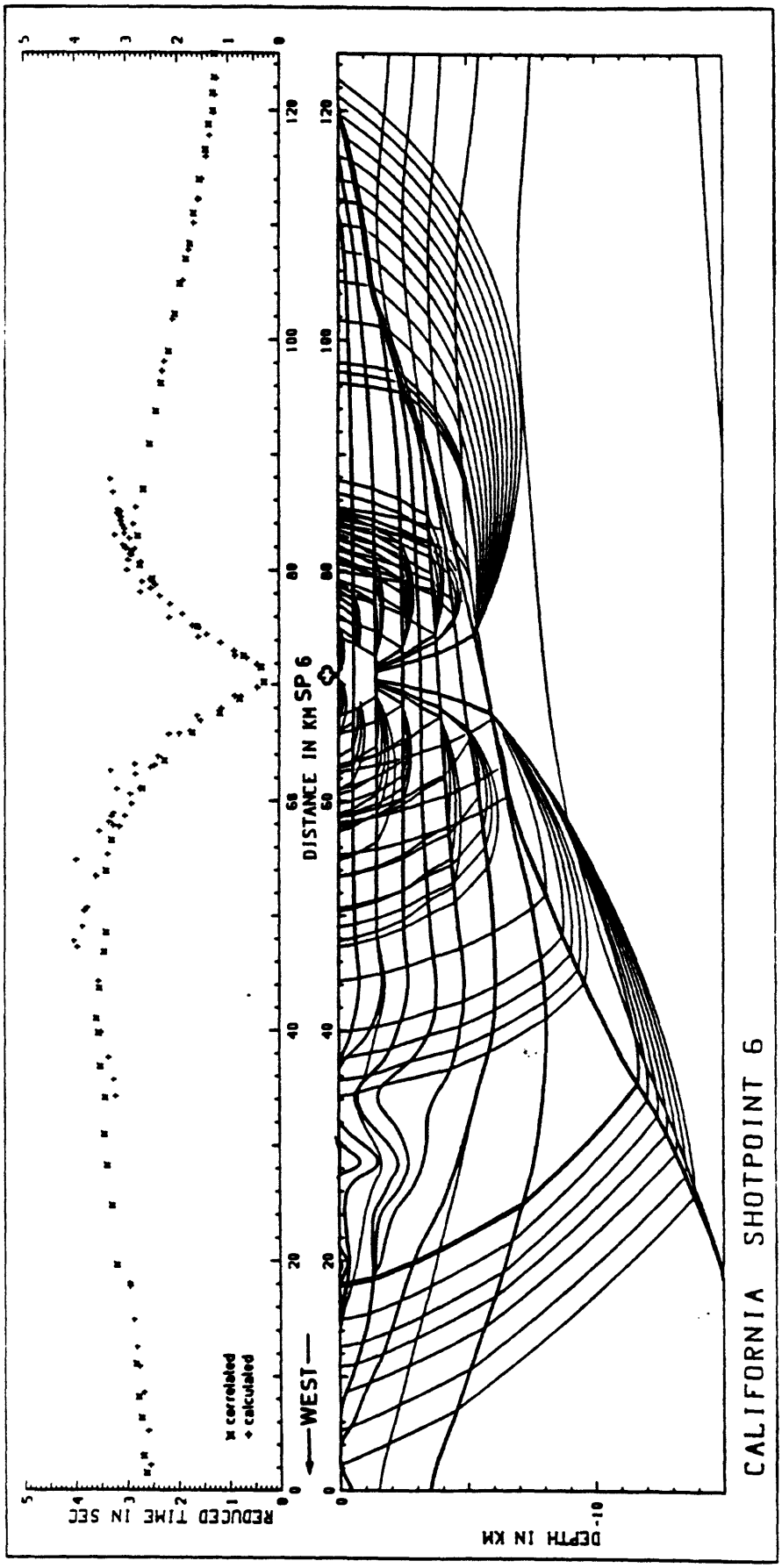
CALIFORNIA SHOTPOINT 6
DEPTH IN KM
DISTANCE IN KM
SP 6
WEST
REDUCED TIME IN SEC
x correlated
+ calculated

Figure 2

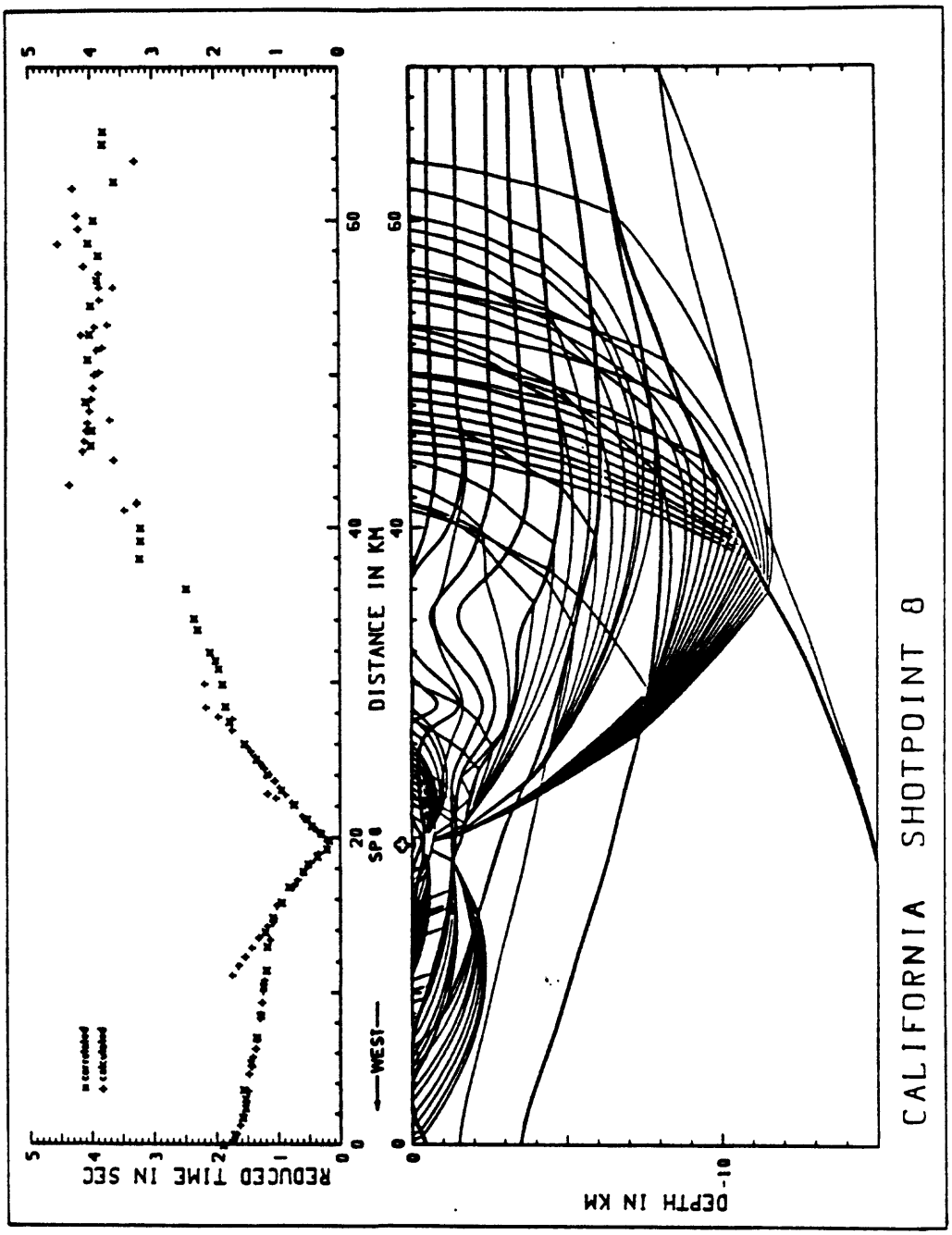
CALIFORNIA SHOTPOINT 8
DEPTH IN KM
DISTANCE IN KM
WEST
SP 8
REDUCED TIME IN SEC
observed
calculated

Figure 3

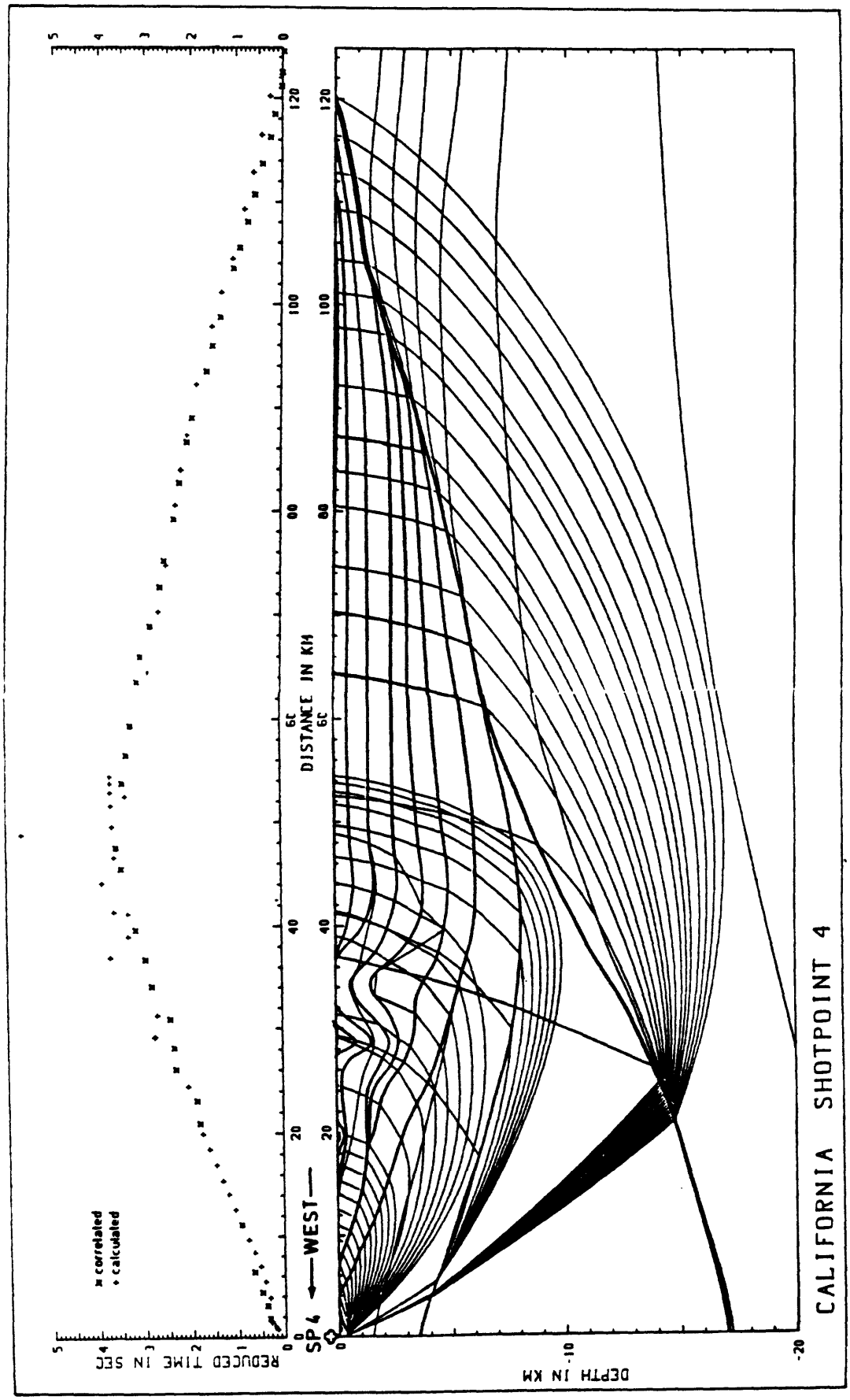
CALIFORNIA SHOTPOINT 4
DEPTH IN KM
DISTANCE IN KM
SP4 ←WEST—
REDUCED TIME IN SEC
x correlated
• calculated

Figure 4

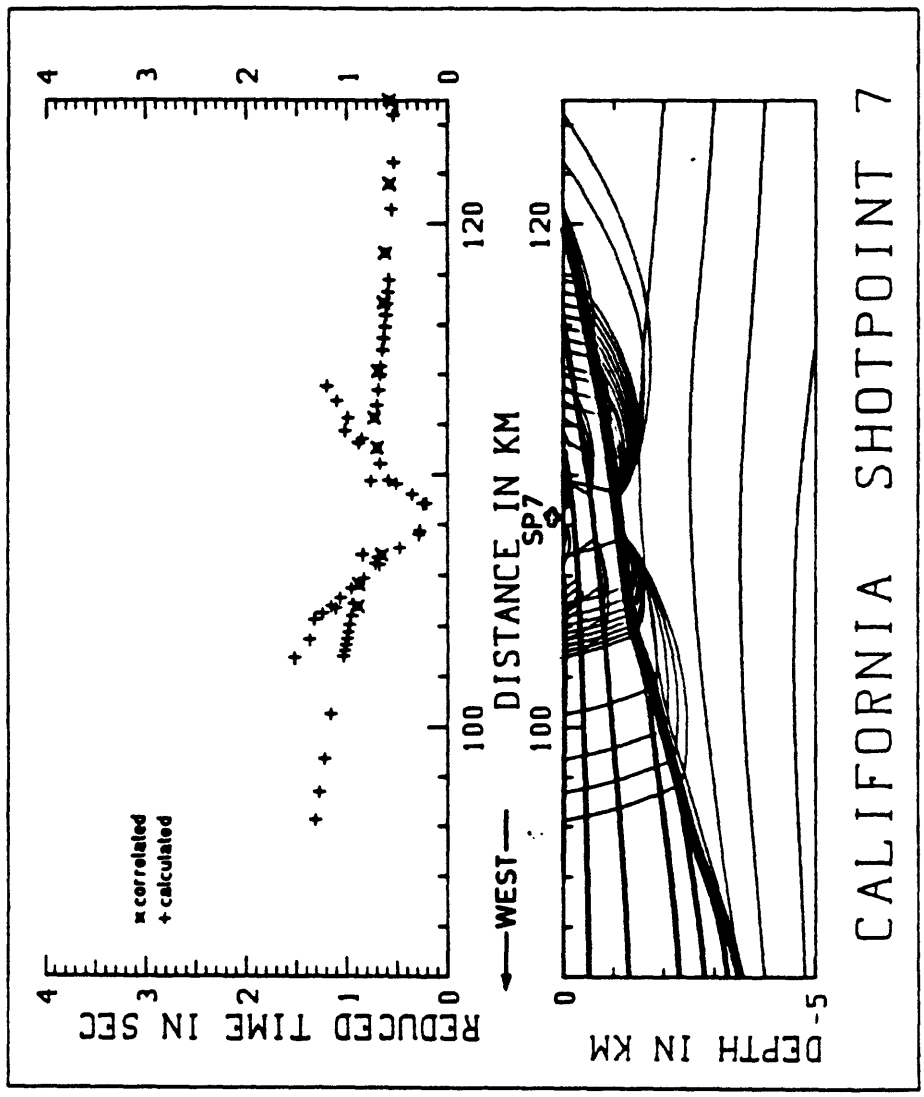
CALIFORNIA SHOTPOINT 7
DEPTH IN KM
0
-5
100
120
DISTANCE IN KM
SP7
WEST
REDUCED TIME IN SEC
0
1
2
3
4
x correlated
+ calculated

Figure 5

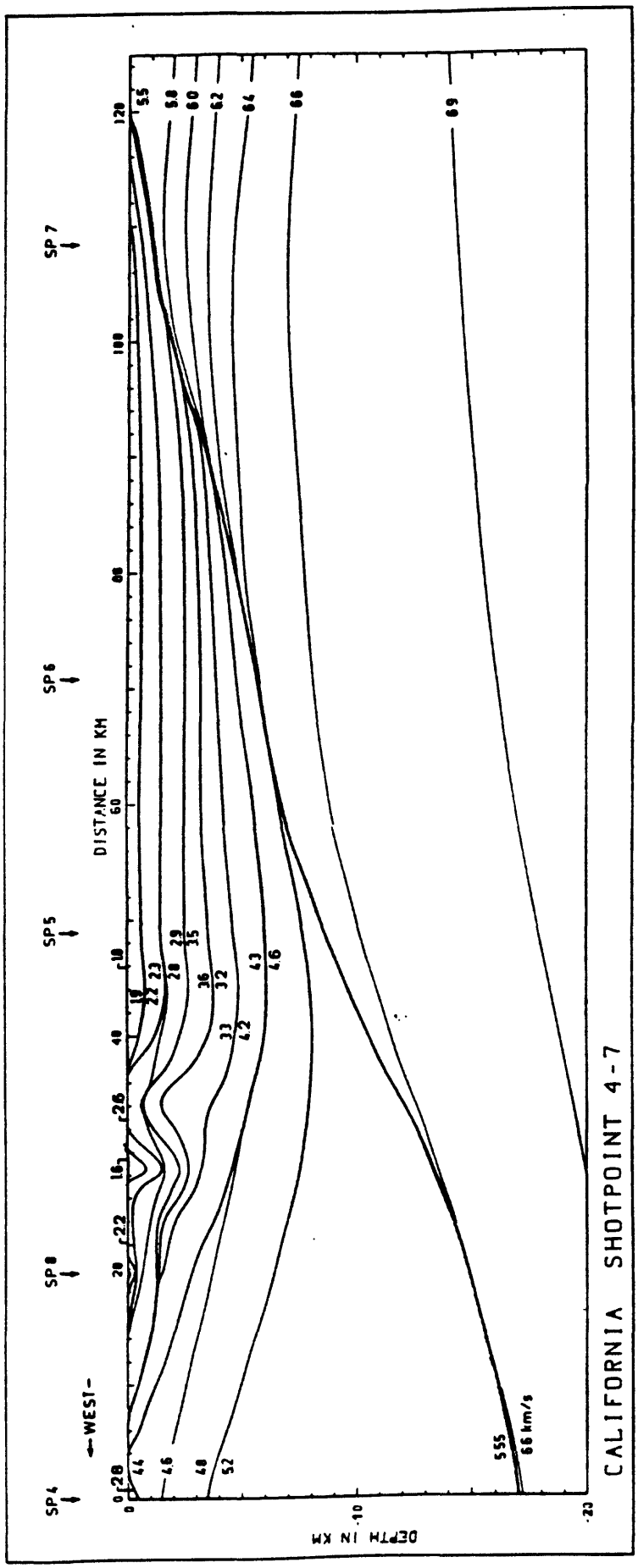
CALIFORNIA SHOTPOINT 4-7
DISTANCE IN KM
DEPTH IN KM
←WEST-
SP4
SP8
SP5
SP6
SP7
55
5.8
6.0
6.2
6.4
6.6
6.9
5.55
6.6 km/s

Figure 6

An interpretation of seismic reflection and refraction data recorded between Cholame Valley and the Sierra Nevada, California, USA

Allan W. Walter, Walter D. Mooney, and Carl M. Wentworth
U.S. Geological Survey
345 Middlefield Road, MS-977
Menlo Park, California, USA 94025

Introduction

The seismic reflection/refraction data set recorded along profile SJ-6 consists of two sections. One section extends northeastward from the coast at Morro Bay to the San Andreas Fault (refraction shotpoints 1-4), and the other extends from the San Andreas Fault to the Sierra Nevada (refraction shotpoints 4-7). This report summarizes our interpretation of eastern portion of the combined data set and is based on Wentworth and others (1983).

Seismic refraction data

Geographically, the data between the shotpoints (SP) 4, 8, 5, 6, and 7 encompass the Diablo Range (part of the Coast Ranges of California), the Kettleman Hills and the San Joaquin Valley (figures 1 and 2; Murphy and Walter, 1984). Two examples of refraction data with the calculated traveltime curves superimposed are shown in figure 3. The data of SP4 are characterized by apparent velocities less than 6.0 km/s to a range of 50 km, and by apparent velocities well in excess of 6.0 km/s beyond 50 km (figure 2a). The unusual arched shape of this traveltime curve is indicative of strong lateral velocity variations. We do not have a complete reversal of the profile since SP7 was an unsuccessful shot. However, the data from SP6 are very clear and show Pg apparent velocities somewhat greater than 6.0 km/s to the west of the shot point, and apparent velocities much greater than 6.0 km/s to the east (figure 2b).

Iterative 2-D raytracing was used to model the observed traveltimes for SP4, SP8, SP5, and SP6. The resultant 2-D velocity model (figure 4, Wentworth and others, 1983) shows some important features:

1) West of the Kettleman Hills, velocities greater than 6.4 km/s are found at depths greater than 15 km.
2) East of the Kettleman Hills, velocities greater than 6.4 km/s are found as shallow as 6 km. However, it is difficult with the present refraction data to determine the manner in which the 6.5 km/s layer deepens to the west.
3) Beneath and to the west of the Kettleman Hills the velocities above the 6.5 km/s layer range from 1.8 to 5.9 km/s, and no LVZ is interpreted within the crust.
4) East of the Kettleman Hills, velocities above the 6.5 km/s layer range from 1.8 to 4.8 km/s and a LVZ is interpreted at a depth of 4-6 km.
5) Beneath the Kettleman Hills is an area of complex variations in velocity structure. The present refraction data are insufficient to model this structure in detail.
6) West of the Kettleman Hills beneath SP8 Franciscan assemblage rocks (velocity of 5.7 km/s) underlie rocks of the Great Valley sequence. This conclusion is contrary to previous geologic models of the structure in this region.

Seismic reflection data

The seismic reflection profile which complements the refraction data is a 6-second VIBROSEIS profile collected in 1981 by Western Geophysical Company.

A portion of the profile was reprocessed to recover an additional 6 seconds of records. An interpretation of the seismic reflection data profile between the refraction shotpoints SP4 and SP6 is reproduced from Wentworth and others (1983) in figure 5, and an example of the data is shown in figure 6. Figure 5 is at the same scale as figure 4 to facilitate comparison.

Some key structural features of this reflection interpretation are:

1) The western San Joaquin Valley is underlain by gently westward-dipping horizons.
2) West of the valley, an anticline is evident at the Kettleman Hills, and a syncline is located immediately to the west (at 30 km on the distance scale of figure 5).
3) The deeper structure of the fold is interpreted with both northeast-dipping reverse faults and a southwest-dipping thrust fault beneath the anticline.
4) Under the Kettleman Hills the mafic basement underlying the valley steepens its dip reaching a depth of 15 km or greater beneath the easternmost Diablo Range (between SP4 and SP8).

Summary

The interpretation of this combined data set illustrates the advantages of utilizing seismic refraction data for velocity control and seismic reflection data for structural control. The two data sets are highly complimentary, and can be jointly interpreted.

Based on the experience gained from the present data we have identified some improvements which could be made in future reflection/refraction investigations. The first is to use smaller shotpoint and recorder intervals along the refraction profiles. The shotpoint spacing of ~25 km and recorder spacing of ~1 km along the SJ-6 profile is too large to adequately resolve the velocity structure in areas of strong lateral velocity inhomogeneities (e.g. the Kettleman Hills). Ten kilometer shotpoint spacing and 250 meter recorder spacing would provide much better velocity control and would greatly improve the ability to correlate the refraction velocity structure with the observed reflection structure. An additional need is for cross lines parallel to the geologic strike to better constrain the velocity structure along the SJ-6 profile. Cross lines in the Diablo Range, Kettleman Hills, and San Joaquin Valley are needed to constrain the lateral changes in the velocity structure.

References

Wentworth, C.M., A.W. Walter, J.A. Bartow, and M.D. Zoback, 1983, Evidence on the tectonic setting of the 1983 Coalinga Earthquakes from deep reflection and refraction profiles across the southeastern end of the Kettleman Hills, California Division of Mines and Geology Special Publication 66, p. 113-126.

Murphy, J. M. and A.W. Walter, 1984, Data report for a seismic refraction investigation: Morro Bay to the Sierra Nevada, California, U.S. Geological Survey Open-File Report 84-642, 37 p., 12 plates.

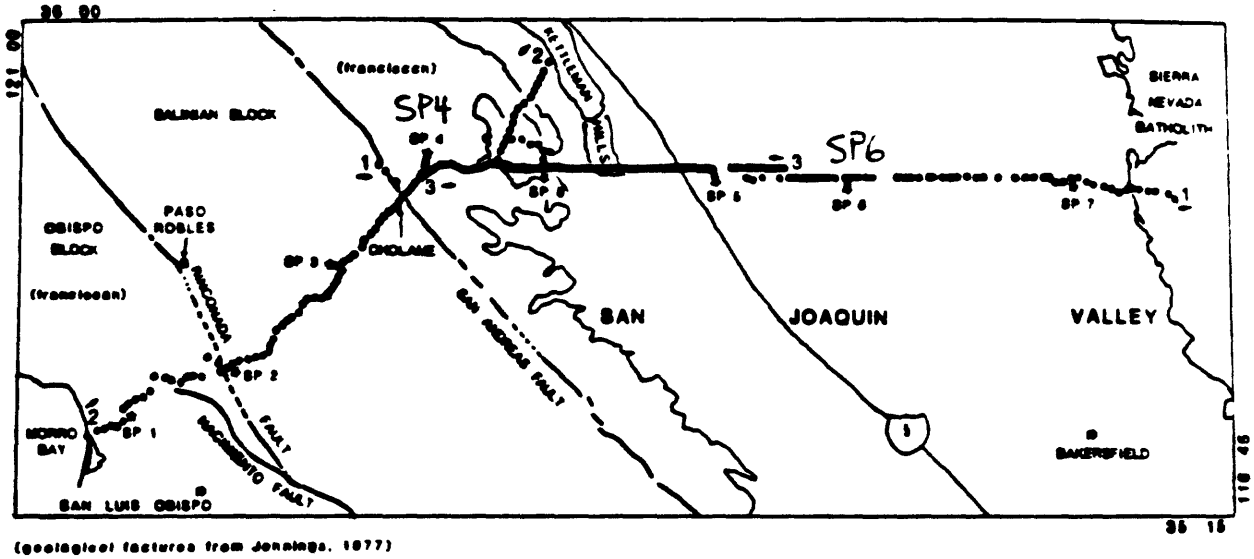

(geological features from Jennings, 1977)

FIGURE 1. Location map of seismic refraction profile. Only the interpretation of the portion of the profile between shot points (SP) 4 and 6 is discussed here.

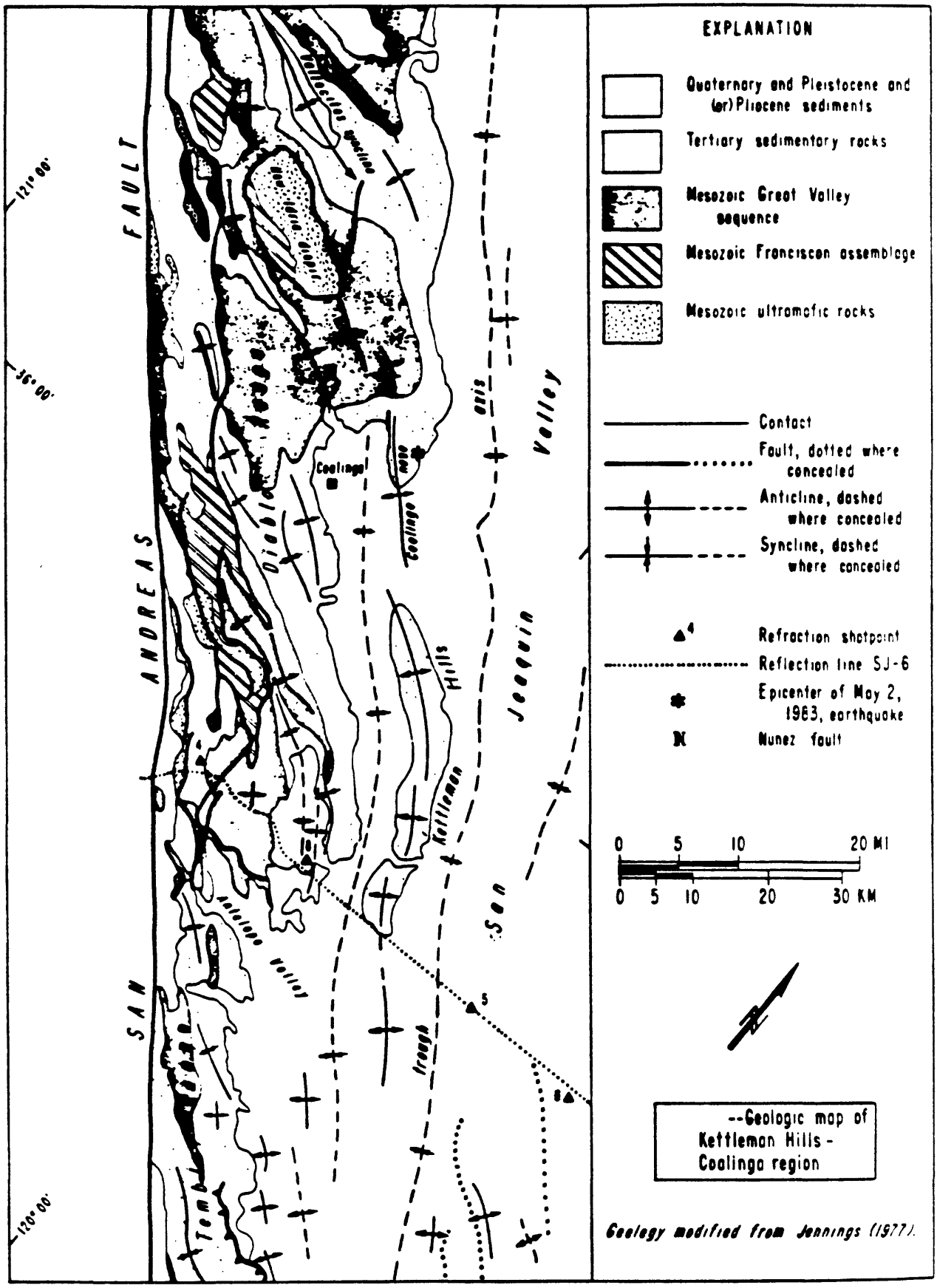

FIGURE 2. Geologic map of study area (from Wentworth and others, 1983).

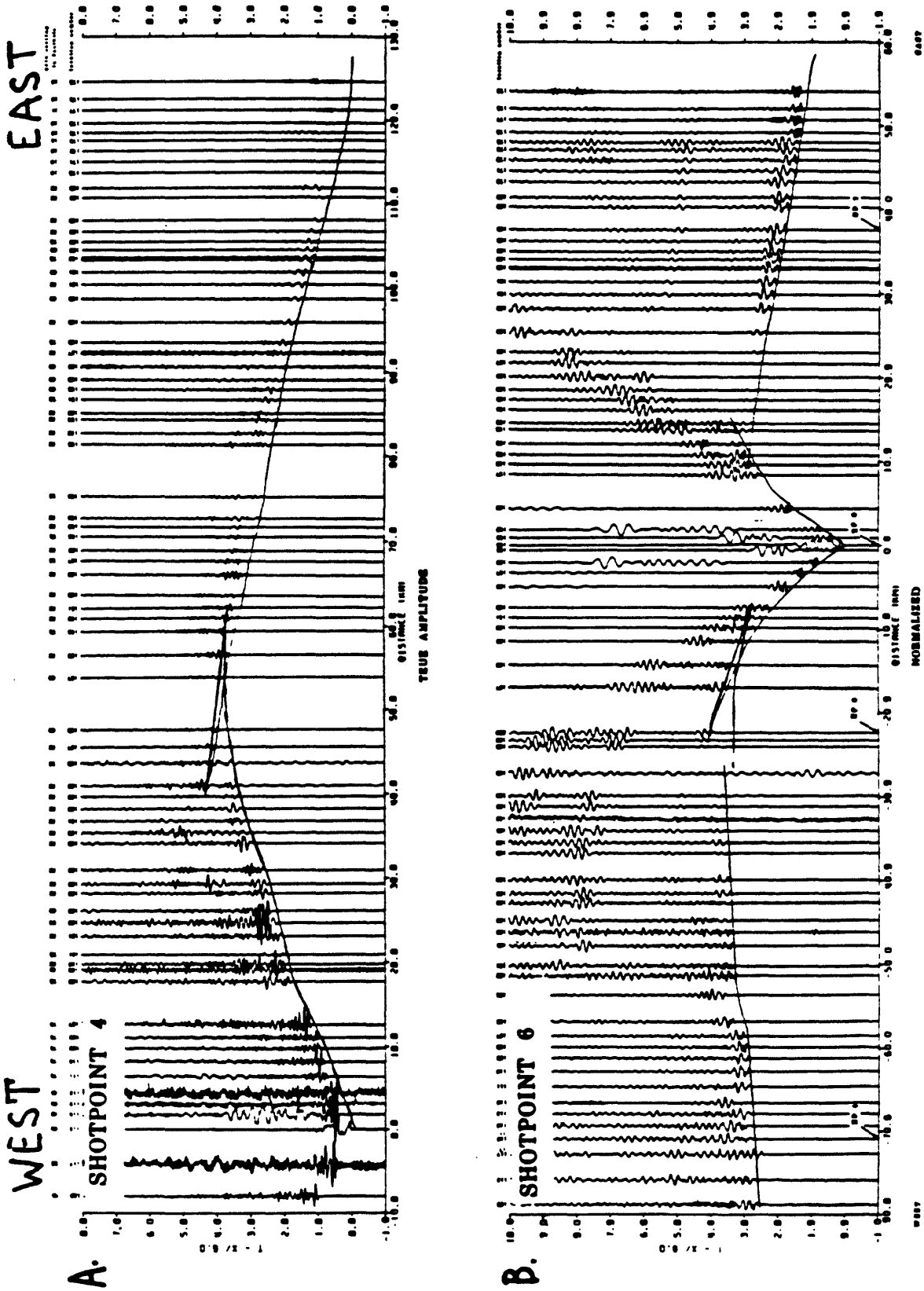

FIGURE 3. Record sections reduced by 6 km/s for SP 4 and SP 6.

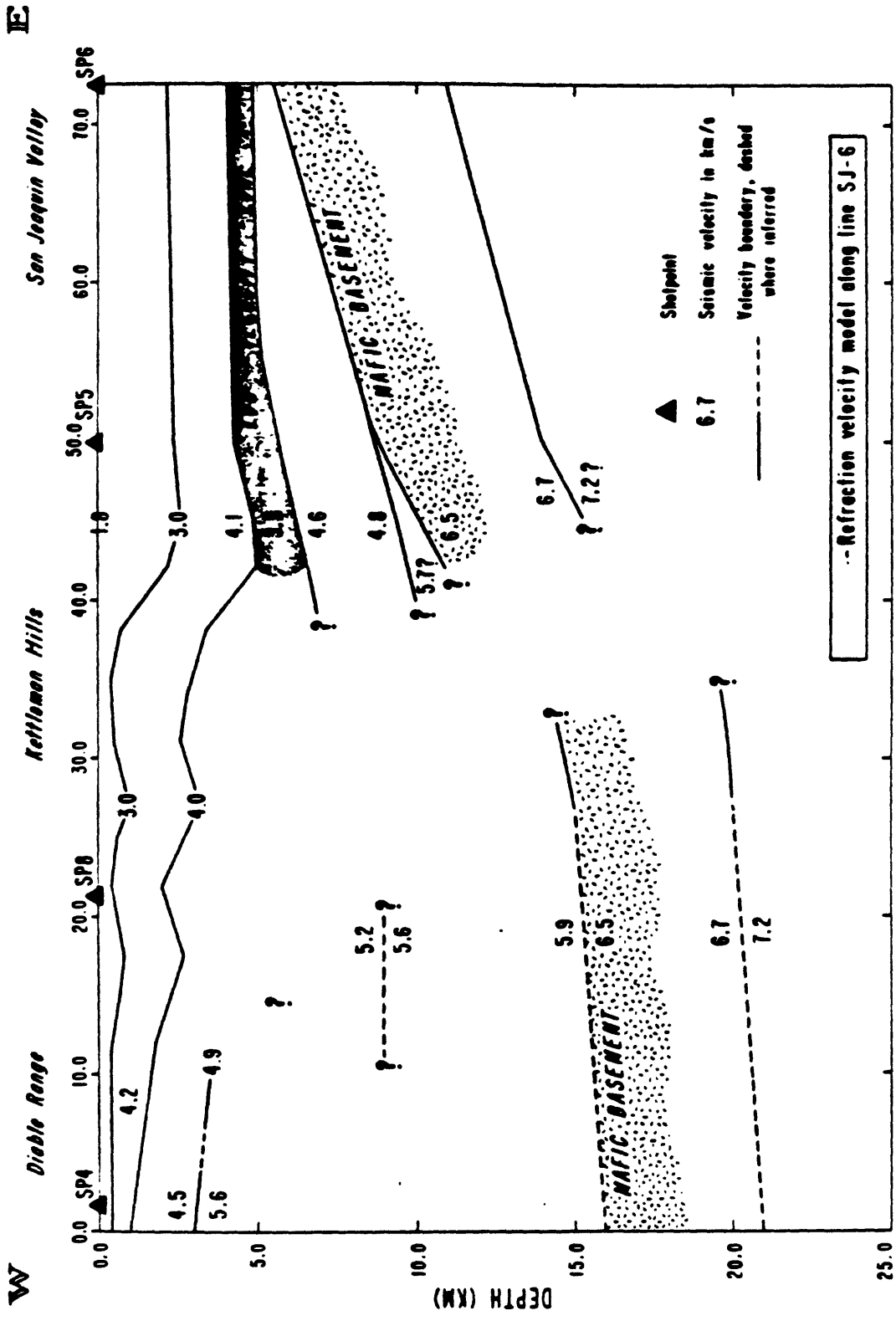

FIGURE 4. Interpretation of seismic refraction data between SP 4 and SP6. Velocities in km/s. From Wentworth and others, 1983.

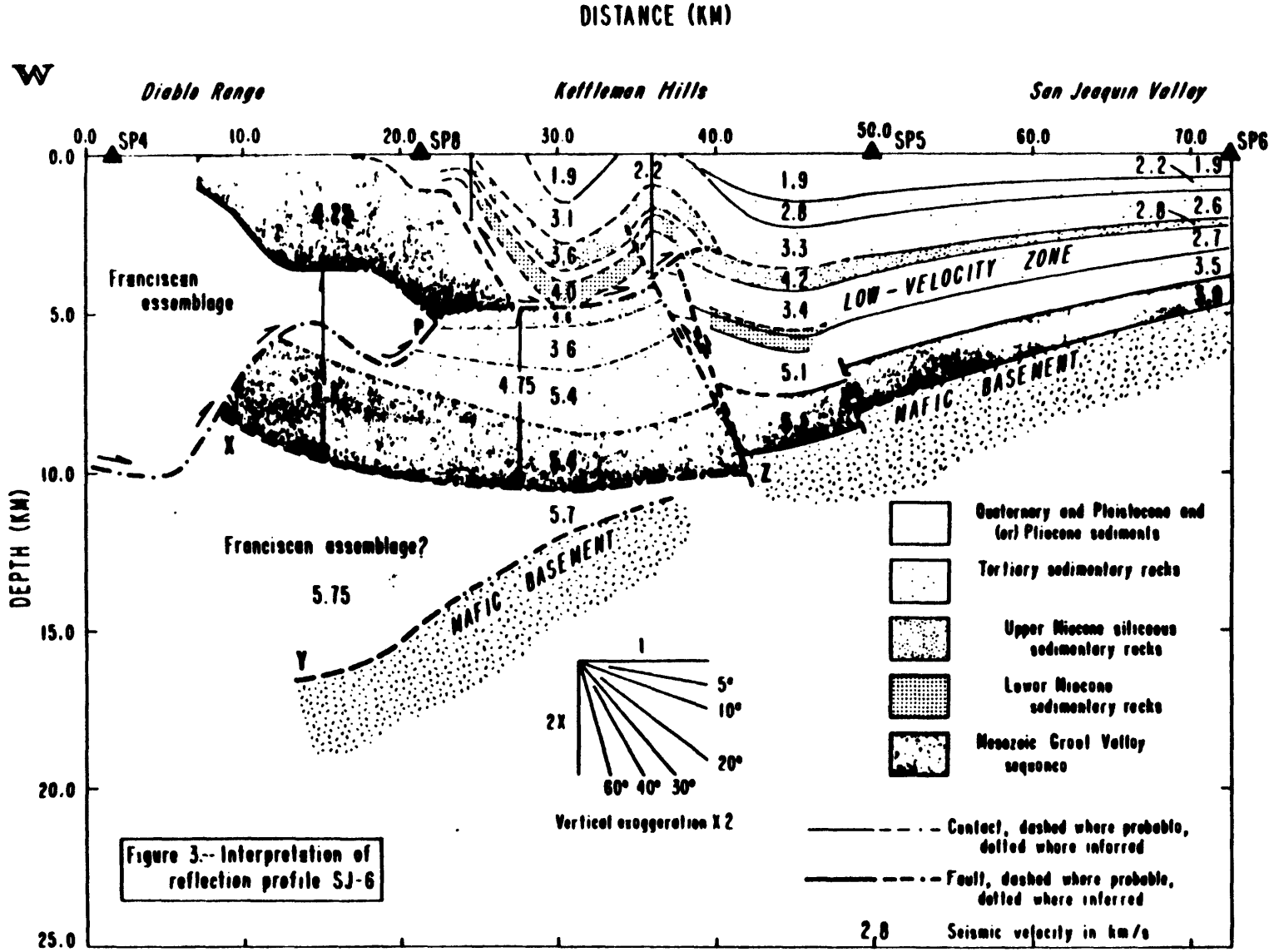

Figure 3.-- Interpretation of reflection profile SJ-6

FIGURE 5. Combined reflection/refraction interpretation. See text for description. From Wentworth and others, 1983.

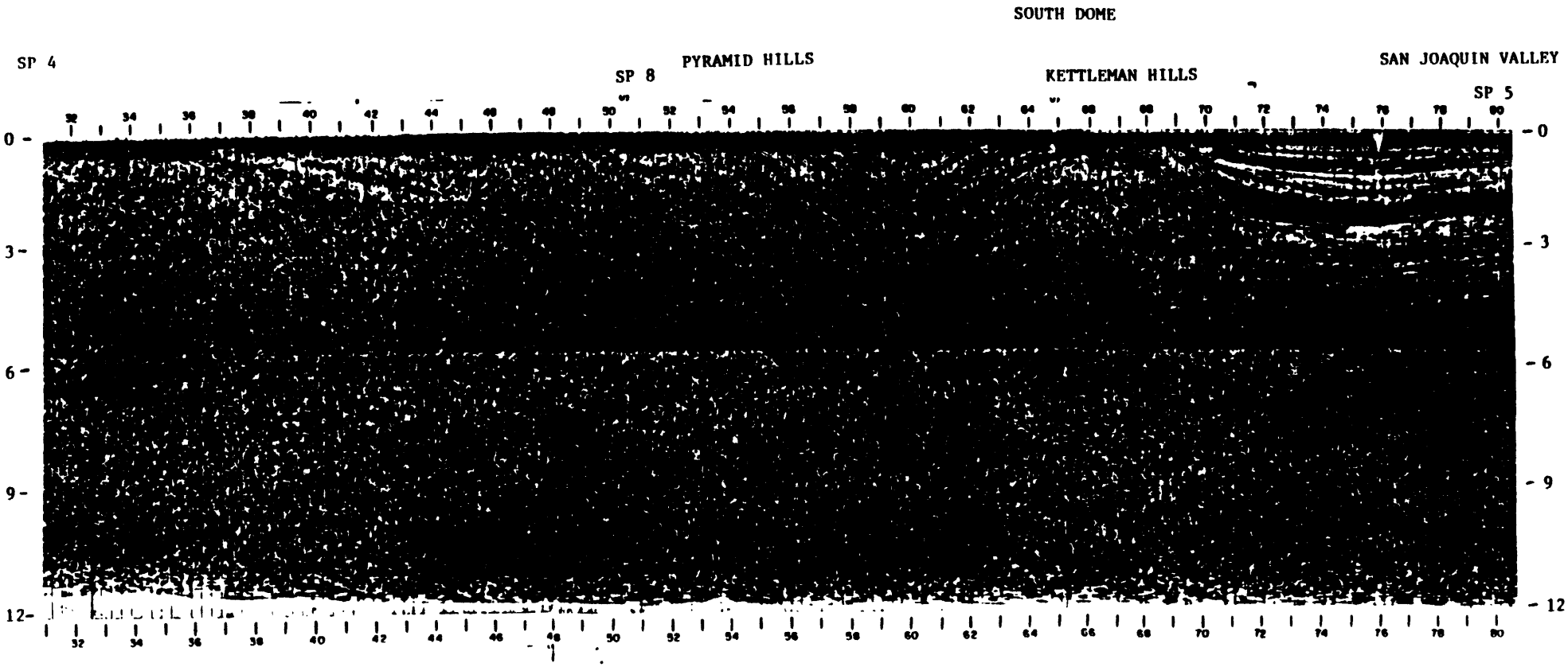

FIGURE 6. Portion of seismic reflection profile between SP 4 and SP 5. See figure 5 for interpretational section.

Possible evidence in the seismic data of profile SJ-6 for subducted sediments beneath the Coast Ranges of California, USA

Anne M. Trehu and Walter H. Wheeler*, IV
U.S. Geological Survey, Woods Hole, MA 02543
*Department of Geology, Duke University, Durham, NC 27708

Introduction

The studied section of the SJ-6 seismic refraction/reflection profile extends from the Pacific Coast near Morro Bay northeastward across the Coast Ranges to the San Andreas Fault near Cholame (Line 1, Fig. 1a). The primary objective of this study was to reprocess the VIBROSEIS data, which was originally processed as a 6-second record section, to yield a 14-second record section, and then, use this expanded reflection section to constrain the crustal structure for our 2-D ray-trace modeling of the seismic-refraction traveltime data (Fig. 1b).

Geologic Setting

A comprehensive review of the geology of this region has been presented by Page (1981) and is summarized in Figure 1. The western portion of the line SJ-6 crosses the Santa Lucia Range which is comprised of Mesozoic Franciscan assemblage locally overlain by pockets of Jurassic ophiolite and Great Valley-type sediments. We will refer to these rocks collectively as the San Simeon/Stanley Mountain (SS/SM) terrane (Champion and others, 1984). Eastward along profile, the Nacimiento and Rinconada Fault zones separate the SS/SM terrane from the Salinian Block, a terrane of granitic plutons similar in age and composition to the Sierra Nevada batholith which are locally overlain by a sequence of Miocene and younger sediments. The San Andreas Fault bounds the Salinian block on the east separating it from the Diablo Range which is comprised of Franciscan assemblage overlain by Great Valley Sequence and younger sediments. The Franciscan and Great Valley rocks show characteristics suggesting formation in an accretionary wedge-forearc basin environment. Most of the fore-arc basin analogue is missing in the terranes exposed west of the San Andreas Fault.

Reflection Data

The reflection data were acquired and originally processed by Western Geophysical Co. in 1981. A 48-channel, split-spread geometry was used with a station spacing of 67 m and an initial source-receiver offset of 268 m. This yielded nominal 24-fold coverage with a maximum offset of 1811 km, but some of the line was recorded along winding roads, so the actual fold coverage is quite variable. Twenty-six seconds of data were recorded from a 20-second VIBROSEIS upsweep containing frequencies ranging from 10-52 Hz, yielding a 6-second two-way time record.

These parameters are not ideal for deep crustal studies, for which one would prefer a longer record to image the lower crust and upper mantle and a larger maximum offset to better resolve velocities in the middle and lower crust. However, because the data were collected with a upsweep, we were able to append 8 seconds of zeros to the end of the field data and recorrelate this augmented data set with the source sweep to obtain a 14-second record (e.g. Okaya, 1985). Using this method, the high frequencies of the source are progressively lost in the correlated records as time increases beyond 6 s. Nevertheless, for the 20-second sweep used in this experiment, a signal frequency band of 10-40 Hz remained at a time of 14 s. We considered this

bandwidth adequate for studying the lower crust because the lower crustal reflections observed in the VIBROSEIS data contain primarily 10 to 20-Hz energy.

After recorrelation, the data were sorted and static corrections were applied using the velocities derived from the refraction results. The datum is 300 m, the average elevation of the line. Normal moveout (NMO) corrections for events in the upper 3-4 s of the data were determined from visual comparison of the NMO obtained from a series of velocity functions. For the deeper structure, and in places where no clear shallow reflectors could be observed, the velocities suggested by the refraction data were used instead. With the maximum offset being 1.8 km, the NMO of any lower crustal reflection is insensitive to the velocity assigned to the lower crust.

Figure 2 shows a line drawing of our reprocessed seismic reflection section. On the west side of the section (km 0 to km 25), no continuous reflectors are observed beneath the San Simeon terrane, but a band of sub-horizontal, discontinuous reflectors is seen between 1 and 2 s. The significance of these reflectors, is not understood at present. Farther east, between the Rinconada and San Andreas faults, the sedimentary section overlying the Salinian Block has well-defined reflectors. This section thickens eastward to ~2 s two-way time and shows both faulting (km 41) and infilling (km 52) above an irregular basement surface. Within this basement a band of westward-dipping reflections is observed at ~4-6 s (km 48 to km 61). These are similar to reflections observed in several other reflection profiles across granitic batholiths and are interpreted to represent the base of the Salinian batholith (Lynn and others, 1981).

Below the proposed base of the batholith is a band of eastward-dipping reflections observed from ~5-6 s at km 33 to ~9-10 s at km 56. An example from this band of reflections can be seen Figure 3. Note the wedge-shaped structure at about ~8 s beneath km 45-50. The interpretation of these reflections will be discussed jointly with the interpretation of the refraction data. The band of reflections terminates abruptly both on the western and eastern flanks on the Salinian block, approaching the Riconada and San Andreas Fault zones, respectively. We suspect that this indicates a difference in the propagation characteristics of the shallow crust between the Franciscan and Salinian terranes rather than the absence of deep reflectors. Because the termination of the deep reflections corresponds to a sharp increase in the frequency of the background noise level, a change in the recording environment probably also contributes to the poor signal/noise. This interpretation is supported both by the absence of a hyperbola of diffracted energy which would be expected if a distinct reflector ended abruptly and by the refraction data discussed below.

Refraction Data

A total of 93 vertical-component seismographs, spaced ~1.2 km apart, were used to record four shots along this section of profile SJ-6 (Fig. 1b). The experimental parameters and data are presented in Walter and Murphy (1984). We modeled the traveltimes observed from the four shotpoints using a 2-D ray-tracing computer algorithm (Červený and others, 1977). For a given modeling iteration, rays were traced from the sources through a laterally varying velocity structure, their calculated traveltimes were compared to the observed travetimes, and then, the velocity structure was modified so as to improve the agreement. The record sections for all four shots, together with the traveltimes calculated using our final velocity model, are shown in Figure 4a. Our final velocity model is presented as isovelocity contours in Figure

4b. Ray-paths from shotpoint (SP)1 and the approximate positions of the major reflections observed in the VIBROSEIS data are also superimposed on the model shown in Figure 4b.

Velocity model

On the west side of the model, the velocity in the upper 5 km of the San Simeon/Stanley Mountain terranes is well-constrained by the reversing traveltime curves of SP1 and SP2. The data indicate a strong velocity gradient of about 0.25 s^{-1} with a near-surface velocity of 4.3 km/s. In the central part of the model, the velocities (2.8-5.0 km/s) in the sedimentary section overlying the Salinian basement were determined from the reflection data. The refraction data of SP2 and SP3 indicate that the velocity of the Salinian basement increases rapidly to about 6.0 km/sec at ~4.5 km depth.

Deeper in the crust, the prominent low velocity zone (LVZ) extending beneath both the San Simeon/Stanley Mountain and Salinian terranes is based primarily on large-amplitude late arrivals from SP1 which we interpreted to be wide-angle reflections from the base of a LVZ (phase A in Figure 4a). The eastward-thinning of this LVZ is inferred from the eastward-dipping band of reflections observed in the re-processed reflection records. Using velocities obtained from both data sets to convert the reflection time section into a depth section, we find that the calculated depth to the top of the band of reflections is consistent with the depth at which the velocity decreases from 5.5 km/s to less than 5.0 km/s in the refraction model (Fig. 4b). The eastward thinning of this LVZ does not significantly alter the calculated range at which the reflection phase A is observed from SP1, but helps explain why this phase is not observed from SP2, SP3, and SP4. Also, the fact that phase A was not observed in the data of a previous refraction survey recorded along the axis of the Salinian block (line 4 in Figure 1a, Stewart, 1968; Walter and Mooney, 1982) suggests that this LVZ pinches out to the east.

Even so, arrivals similar to those of phase A are observed in the data of several refraction profiles recorded parallel to the axis of the Diablo Range east of the San Andreas Fault (lines 2 and 3 Fig. 1a; Blümling and Prodehl, 1983; Blümling and others, 1985). These arrivals are observed at greater ranges than those of phase A and their amplitudes are smaller (Figure 5a). The velocity-depth function (Figure 5b) derived by interpreting these arrivals as wide-angle reflections from the base of a LVZ under the Diablo Range (Blümling and Prodehl, 1983) has an LVZ that is both deeper and higher in average velocity than that modeled from phase A.

The velocity modeled within our eastward tapering LVZ, 4.5-5.0 km/s, is typical of unmetamorphosed sedimentary rocks, especially if the pore pressure is high. Since an inactive trench is located ~150 km off the western end of the reflection profile (Page and others, 1979), we propose that the LVZ is a wedge of sediments that was subducted landward from this trench. That the subduction of sediments is to be expected under certain conditions of pore pressure has been suggested on the basis of theoretical models of subduction zone mechanics (Davis and others, 1983; Wang and Shi, 1985). Although the maximum thickness of our proposed subducted wedge, 7 km (3 s), is thicker than the layers of subducting sediment observed in active subduction zones, we assume these sediments were imbricated after subduction, thickening the wedge in the manner described by Silver and others (1985). Subduction of sediments may also explain the LVZ reported beneath the Diablo Range (Blümling and Prodehl, 1983), although there, the relationship to subduction is further obscured by the strike-slip displacement along the San Andreas Fault.

East of the proposed wedge of subducted sediments, two other LVZs were introduced into the velocity model to explain the large-amplitude late arrivals from SP1 and SP2 observed at stations recording immediately east of the San Andreas Fault (phase B Figure 4a). In order to focus and delay the seismic energy arriving at these stations, the model requires both a depression of the velocity contours beneath the San Andreas and a velocity decrease from 6.4 to 6.1 km/s below the westward dipping reflections (4-6 s) in the Salinian block. The most probable explanation for the lowering of the velocities across the San Andreas Zone is the presence of fault gouge (e.g. Wang and others, 1978; Mooney and Ginzburg, 1986), but the cause of the the velocity inversion modeled in the Salinian block is less certain. One possibility, suggested by Stewart (1968) and Page (1981) is that the Salinian batholith is thrusted over the lower-velocity Franciscan Assemblage. More modeling, including modeling of the seismic amplitudes is needed to establish both the vertical and horizontal extent of the LVZs and their relationship to the tectonic history of the region.

Discussion

It must be noted that the proposed subduction model is almost certainly a gross oversimplification. A troubling aspect of the velocity model (Fig. 4b) is that it is necessary to impose a velocity of 8.0 km/sec immediately below the east-dipping LVZ in order to match the range and arrival time of phase A. Rather than implying that the oceanic crust has somehow been removed, this more probably reflects an error in the model. Although we were unable to find a model that had a velocity characteristic of oceanic crust (6.8-7.2 km/s) beneath the wedge, it was not possible to test all possible models and there may still be a reasonable combination of wedge geometry and velocity that will match the data and permit oceanic crust to underlie the low-velocity wedge.

Nevertheless, our interpretation of the prominent eastward-thinning LVZ as a subducted sedimentary wedge is supported by the interpretations of several seismic reflection profiles recorded across active trenches. For example, off the coast of Alaska and Barbados, 1-s thick layer of sediments appears to be subducted beneath a decollment zone (Westbrook and others, 1982; McCarthy and Scholl, 1985; von Huene, personal communication), and under Vancouver Island, ~200 km landward of an active trench, a 2-s thick underplated zone is inferred to overlie the downgoing crustal plate (Yorath and others, 1985). Other evidence for underplating is provided by seismic refraction data recorded across the Chugach and Peninsular/ Wrangellia terranes of Alaska 150-300 km landward of the active trench. These data indicate a series of high and low velocity zones interpreted to represent stacked slices of subducted oceanic crust and upper mantle (Page and others, 1986).

At the latitude of the SJ-6 profile, the tectonic regime of central California changed from the subduction to strike-slip about 20 my ago (Atwater, 1970; Page and Engebretson, 1984). Assuming that subduction ceased 20 my ago and that the subduction rate was 5 cm/yr, the toe of the wedge would have an age of at least ~ 23 my. Yet, observed recent faulting and seismicity on the Santa Lucia Bank (Fig. 1a), located landward of the filled trench, suggest that some subduction may even be occurring at present (McCulloch, 1980). If true, this would permit a slightly younger age for the sediments.

Given the uncertainties in the age (~23 m.y.) of our inferred sedimentary wedge and the uncertainties about the thermal and mechanical environment in a subduction zone, we cannot evaluate what degree of metamorphism to expect. Thermal models of subduction zones suggest that sediments may be dragged to great depth without undergoing significant metamorphism, depending on both the

position in the wedge and subduction rate (Cloos, 1982; Wang and Shi, 1984). Although the velocities of 4.5-5.0 km/s modeled in the wedge at depths of burial of 14-21 km seem low, seismic data from the heavily sedimented Atlantic continental margin (e.g. Sheridan and others, 1979) indicate velocities of about 5-5.5 km/s at a depth of about 10 km for clastic sediments that are presumed to be of middle Jurassic age (150-170 m.y.).

Another aspect of California geology to consider in evaluating the subduction model is the possibility of large strike-slip offsets along faults west of the San Andreas Fault. In fact, although the recent offset along onshore strike slip faults west of the San Andreas Fault appears minor (Page, 1981), strong evidence exists for 80-120 km of displacement during the Pliocene along the offshore Hosgri Fault (Hall, 1975; Graham and Dickinson, 1978). The effect of this offset on the model proposed here is uncertain. Although it might invalidate the projection of the wedge across the Hosgri Fault to the seafloor, it is also possible that the subduction zone was continuous and approximately parallel to the Hosgri Fault, then the strike-slip offset would not noticeably affect the observed depth to the subduction decollement plane. An additional possibility is that surficial strike-slip motion was decoupled from the deeper structure below the decollement.

Our modeling also did not adequately resolve the nature of the fault boundary between the San Simeon and Salinian terranes. Although the abrupt termination the reflections east of the surface trace of the Riconada Fault might be interpreted to indicate a vertical boundary, we argued above that we believe this to be an artifact of decreased signal/noise. The presence of the westward-dipping reflectors at ~ 4-6 s in the Salinian block together with the underlying LVZ modeled from the refraction data suggest sub-horizontal thrusting has occurred at depth.

Conclusion

The seismic data recorded between Morro Bay and the San Andreas Fault suggest the possibility of subducted sediments beneath Coast Ranges of California. A more definitive answer must await new reflection and refraction data, especially from the offshore region.

Acknowledgements

Many thanks to Carl Wentworth for having made available the reflection data tapes and to Janice Murphy, Allan Walter, and Walter Mooney for having collected and released the refraction data. Thanks to John Miller and David Okaya for helping us with the reflection data processing. Kim DeMello and Peggy Mons-Wengler typed the manuscript, Patty Forrestel and Jeff Zwinakis drafted the figures. Reviews of this paper by Debbie Hutchinson, Elizabeth Winget, John Schlee, John Nablek, and Walter Mooney are greatly appreciated.

References

Atwater, T., 1970, Implications of plate tectonics for the Cenozoic tectonic evolution of North America, Geol. Soc. Am. Bull., 81, p. 3513-3536.

Blümling, P., and C. Prodehl, 1983, Crustal structure beneath the eastern part of the Coast Ranges of central California from explosion-seismic and near-earthquake data, Phys. Earth Planet. Inter., 31, p. 313-326.

Blümling, P., W.D. Mooney, and W.H.K. Lee, 1985, Crustal structure of southern Calaveras Fault Zone, central California, from seismic refraction investigations, Bull. Seism. Soc. Am., 75, p. 193-209.

Červený, V., I.A. Moltikov, and I. Pšenčík, 1977, Ray method in seismology, Univ. Karlova, Prague, 214 p.

Champion, D.E., D.G. Howell, and C.S. Gromme, 1984, Paleomagnetic and geologic data indicating 2500 km of northward displacement for the Salinian and related terranes, California, J. Geophys. Res., 89, p. 7736-7752.

Cloos, M., 1982, Flow melanges: Numerical modeling and geologic constraints on their origin in the Franciscan subduction complex, California, Geol. Soc. Am. Bull., 93, p. 330-345.

Davis, D., J. Suppe, and F.A. Dahlen, 1983, Mechanics of fold-and-thrust belts and accretionary wedges, J. Geophys. Res., 88, p. 1153-1172.

Graham, S.A., and W.R. Dickinson, 1978, Evidence for 115 kilometers of right slip on the San Gregorio-Hosgri fault trend, Science, 199, p. 179-181.

Hall, C.A., Jr., 1975, Simeon-Hosgri fault system, coastal California: economic and environmental implications, Science, 190, p. 1291-1294.

Lynn, H.B., L.D. Hale, and G.A. Thompson, 1981, Seismic reflections from the basal contacts of batholiths, J. Geophys. Res., 86, p. 10633-10638.

McCarthy, J., and D.W. Scholl, 1985, Mechanisms of subduction accretion along the central Aleutian Trench, Geol. Soc. Am. Bull., 96, p. 691-701.

McCulloch, D.S., 1980, A summary of the geology and geologic hazard in proposed lease sale 53, central California outer continental shelf, U.S. Geol. Survey Open-File Rept. 80-1095.

Mooney, W.D., and A. Ginzburg, 1986, Seismic measurements of the internal properties of fault gouge, Pageoph., in press.

Murphy, J.M., and A.W. Walter, 1984, Data report for a seismic refraction investigation: Morro Bay to the Sierra Nevada, California, U.S. Geol. Surv. Open-File Rept. 84-642, 37 p., 12 plates.

Okaya, D., 1986, Seismic profiling of the lower crust: Dixie Valley, Nevada, in M. Barazangi and L. Brown eds., Reflection Seismology: The Continental Crust, Geodynamics Series vol. 14,, Am. Geophys. Un., p. 269-280.

Page, B.M., H.C. Wagner, D.S. McCulloch, E.A. Silver, and J.H. Spotts, 1979, Geologic cross section of the continental margin off San Luis Obispo, the southern Coast Ranges, and the San Joaquin Valley, California, Geol. Soc. Am. Map and Chart Series MC-286.

Page, B.M., 1981, The southern Coast Ranges, in W. G. Ernst ed., The Geotectonic Development of California, Prentice-Hall, Englewood Cliffs, N.J., p. 329-417.

Page, B.M. and D.C. Engebretson, 1984, Correlation between the geologic record and computed plate motions for central California, Tectonics, 3, p. 133-155.

Page, R.A., G. Plafker, G.S. Fuis, W.J. Nokelberg, E.L. Ambos, W.D. Mooney, and D.L. Campbell, 1986, Accretion and subduction tectonics in the Chugach Mountains and Copper River Basin, Alaska: Initial results of the Trans-Alaska Crustal Transect, Geology, 14, p. 501-505.

Silver, E.A., M.J. Ellis, N.A. Breen, and T.H. Shipley, 1985, Comments on the growth of accretionary wedges, Geology, 13, p. 6-9.

Stewart, S.W., 1968, Preliminary comparison of seismic traveltime and inferred crustal structure adjacent to the San Andreas Fault in the Diablo and Gabilan Ranges of central California, in W. R. Dickinson and A. Grantz eds., Geologic Problems of San Andreas Fault System Conference Proceedings, Stanford Univ. Publ. Geol. Sci., 11, p. 218-230.

Walter, A.W., and W.D. Mooney, 1982, Crustal structure of the Diablo and Gabilan Ranges, central California: a reinterpretation of existing data, Bull. Seis. Soc. Am., 72, p. 1567-1590.

Wang, C.Y., W.N. Lin, and F.T. Wu, 1978, Constitution of the San Andreas fault zone at depth, J. Geophys. Res. Let., 5, p. 741-744.

Wang, C.Y., and Y. Shi, 1984, On the thermal structure of subduction complexes: a preliminary study, J. Geophys. Res., 89, p. 7709-7718.
Wang, C.Y., and Y. Shi, 1985, High pore pressure generation in sediments in front of the Barbados Ridge Complex, Geophys. Res. Let., 12, p. 773-776.
Westbrook, G.K., M.J. Smith, J.H. Peacock, and M.J. Poulter, 1982, Extensive underthrusting of undeformed sediment beneath the accretionary complex of the Lesser Antilles subduction zone, Nature, 300, p. 625-628.
Yorath, C.J., A.G. Green, R.M. Clowes, A. Sutherland Brown, M.T. Brandon, E.R. Kanasewich, R.D. Hyndman, C. Spenser, 1985, Lithoprobe, southern Vancouver Island: Seismic reflection sees through Wrangellia to the Juan de Fuca plate, Geology, 13, p. 759-762.

Figure Captions

Fig. 1a Map of central California showing the locations of the geologic features and the seismic profiles referred to in the text (geology adapted from Page, 1981). Symbol key: SN, Sierra Nevada; GV, Great Valley; DR, Diablo Range; SB, Salinian Block; SS, San Simeon terrane; SAF, San Andreas Fault; S-NF, Sur-Nacimiento Fault; HF, Hosgri Fault; SLB, Santa Lucia Bank; FT, filled trench,; TR, Transverse Range. Line 1 is the section of the seismic profile SJ-6 modeled in this study; lines 2-4 are other seismic refraction profiles refered to this paper. The box outlines the study area shown in more detail in Figure 1b.

Fig. 1b Expanded map of the study area outlined in Figure 1a. Map shows the geologic features west of the San Andreas Fault and the locations of the SJ-6 seismic reflection profile (bold line), the refraction shotpoints (stars) and the shot recording sites (dots).

Fig. 2 Line drawing of the unmigrated SJ-6 seismic reflection record section between Morro Bay and the San Andreas Fault.

Fig. 3 Sub-section of the unmigrated seismic reflection data which shows the wedge-shaped structure discussed in the text.

Fig. 4a True relative amplitude record sections of the refraction shots. The ray traveltimes calculated using the velocity model shown in Figure 4b are shown as superimposed dots. The phases labeled A and B are discussed in the text.

Fig. 4b Velocity model derived by 2-D ray-tracing is shown with the ray diagram of shotpoint (SP)1 superimposed. The velocity contour interval is 0.5 km/s and the ray take-off angle interval is 0.5 degrees. Selected reflections observed on the reflection record section are shown as dotted lines; their depths were calculated assuming a constant velocity of 3.5 km/s in the sedimentary section and a velocity of 6.0 km/s in the basement.

Fig. 5a Comparison of the record section of shot 1 with example record sections from each of the two refraction profiles recorded east of the San Andreas Fault (Blümling et al., 1985). Phase A is modeled as a reflection from the base of a low velocity zone.

Fig. 5b Corresponding velocity-depth functions used to model phase A. The velocity-depth function shown for this study is taken from our velocity model (Fig. 4b) at a distance of 12 km east.

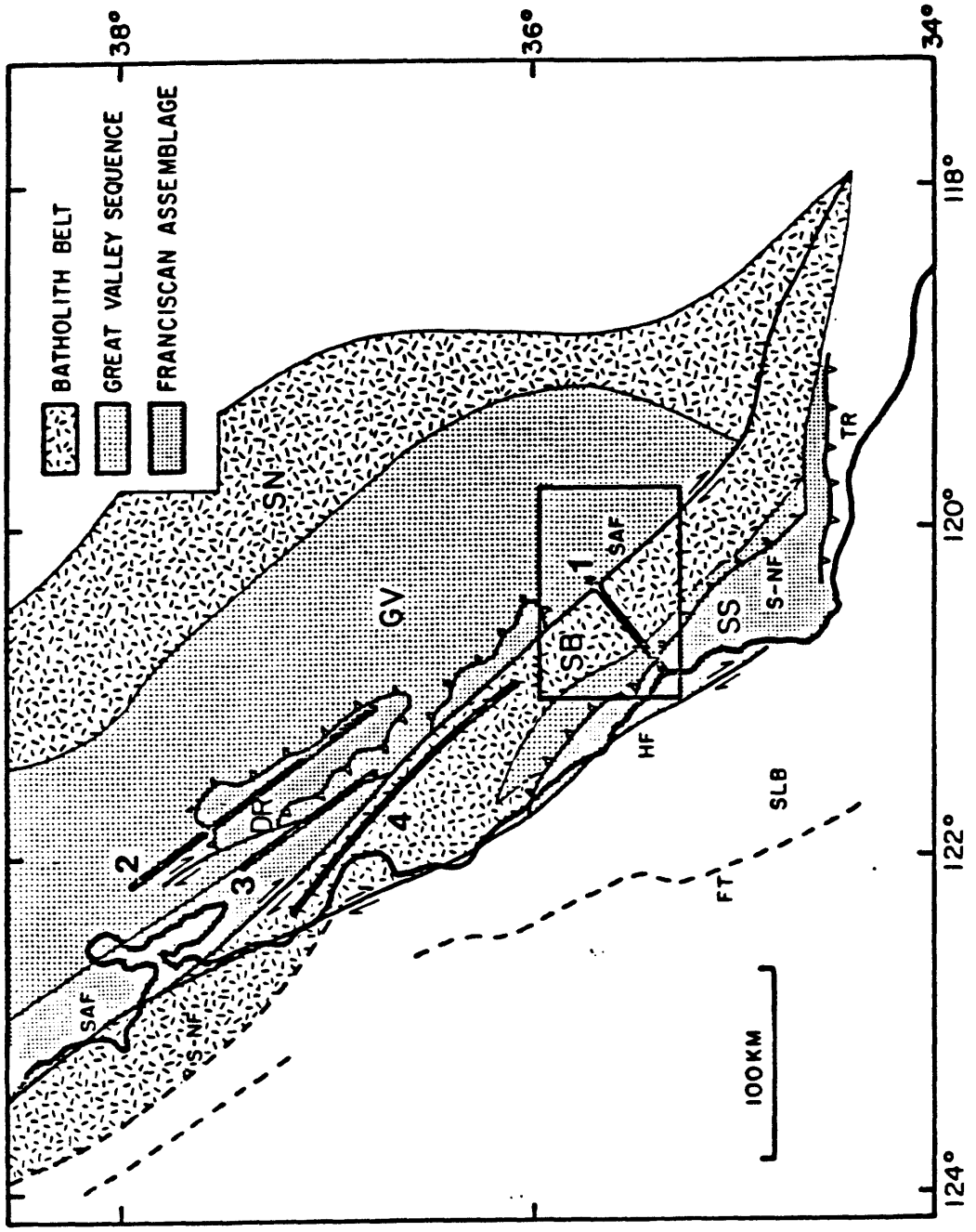
BATHOLITH BELT
GREAT VALLEY SEQUENCE
FRANCISCAN ASSEMBLAGE
38°
36°
34°
124°
122°
120°
118°
SN
GV
SB
1
SAF
SS
S-NF
TR
HF
SLB
FT
2
3
4
DR
SAF
S-NF
100 KM

Figure 1a

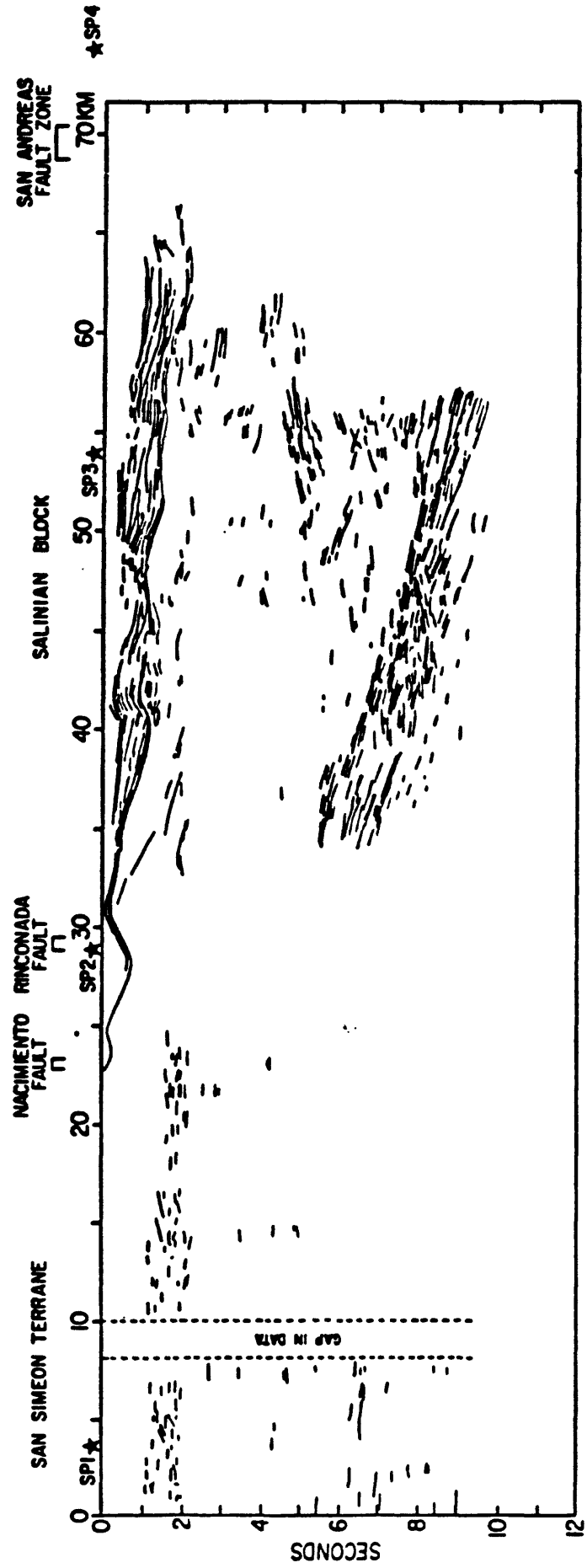
SAN SIMEON TERRANE
NACIMIENTO FAULT
RINCONADA FAULT
SALINIAN BLOCK
SAN ANDREAS FAULT ZONE
70KM
SP1
SP2
SP3
SP4
GAP IN DATA
SECONDS
0
2
4
6
8
10
12
10
20
30
40
50
60

Figure 2

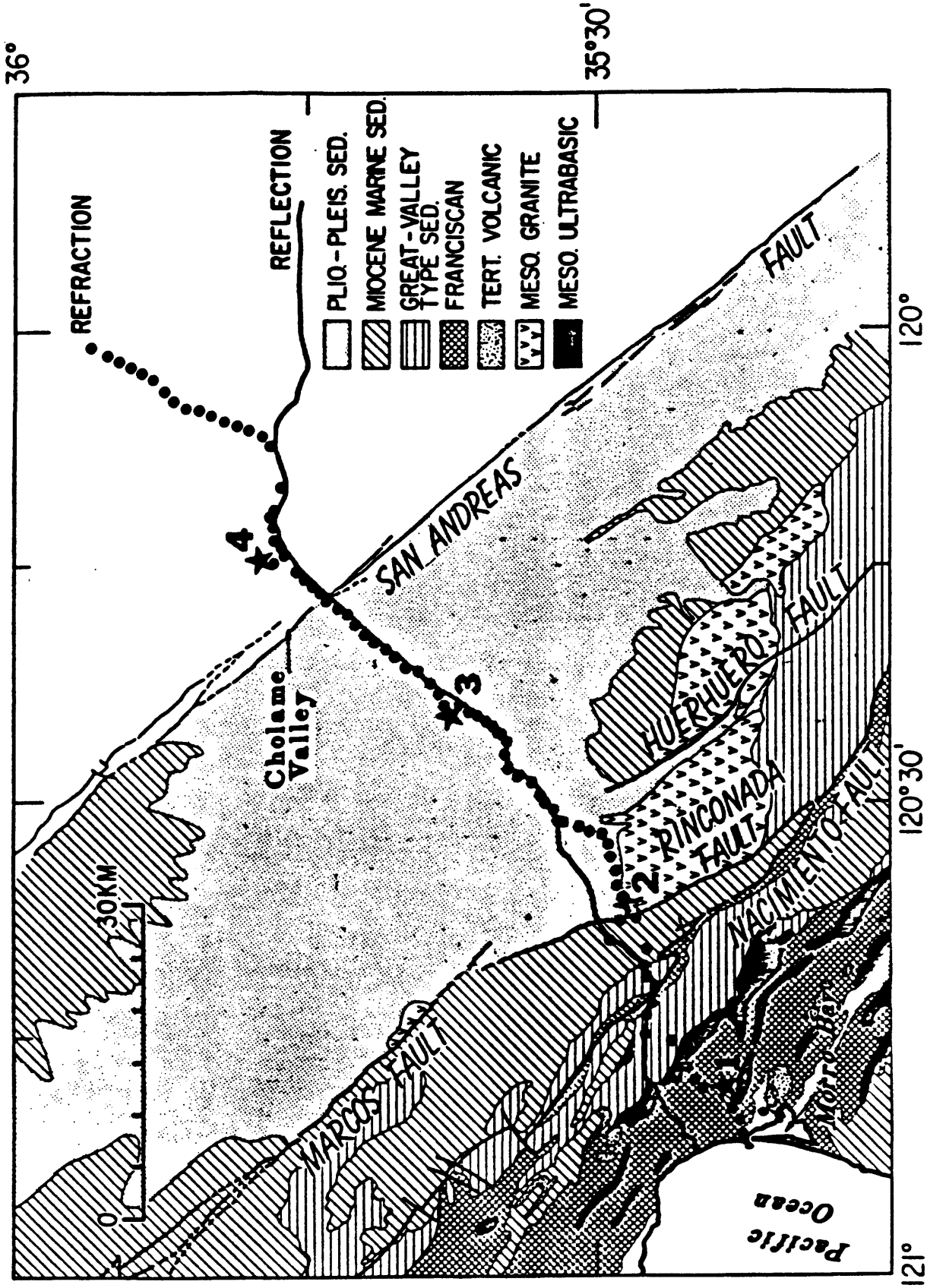
36°
35°30'
120°
120°30'
121°
REFRACTION
REFLECTION
PLIO-PLEIS. SED.
MIOCENE MARINE SED.
GREAT-VALLEY TYPE SED.
FRANCISCAN
TERT. VOLCANIC
MESO. GRANITE
MESO. ULTRABASIC
SAN ANDREAS FAULT
Cholame Valley
30KM
0
HUERHUERO FAULT
RINCONADA FAULT
NACIMIENTO FAULT
MARCOS FAULT
Pacific Ocean
1
2
3
4

Figure 1b

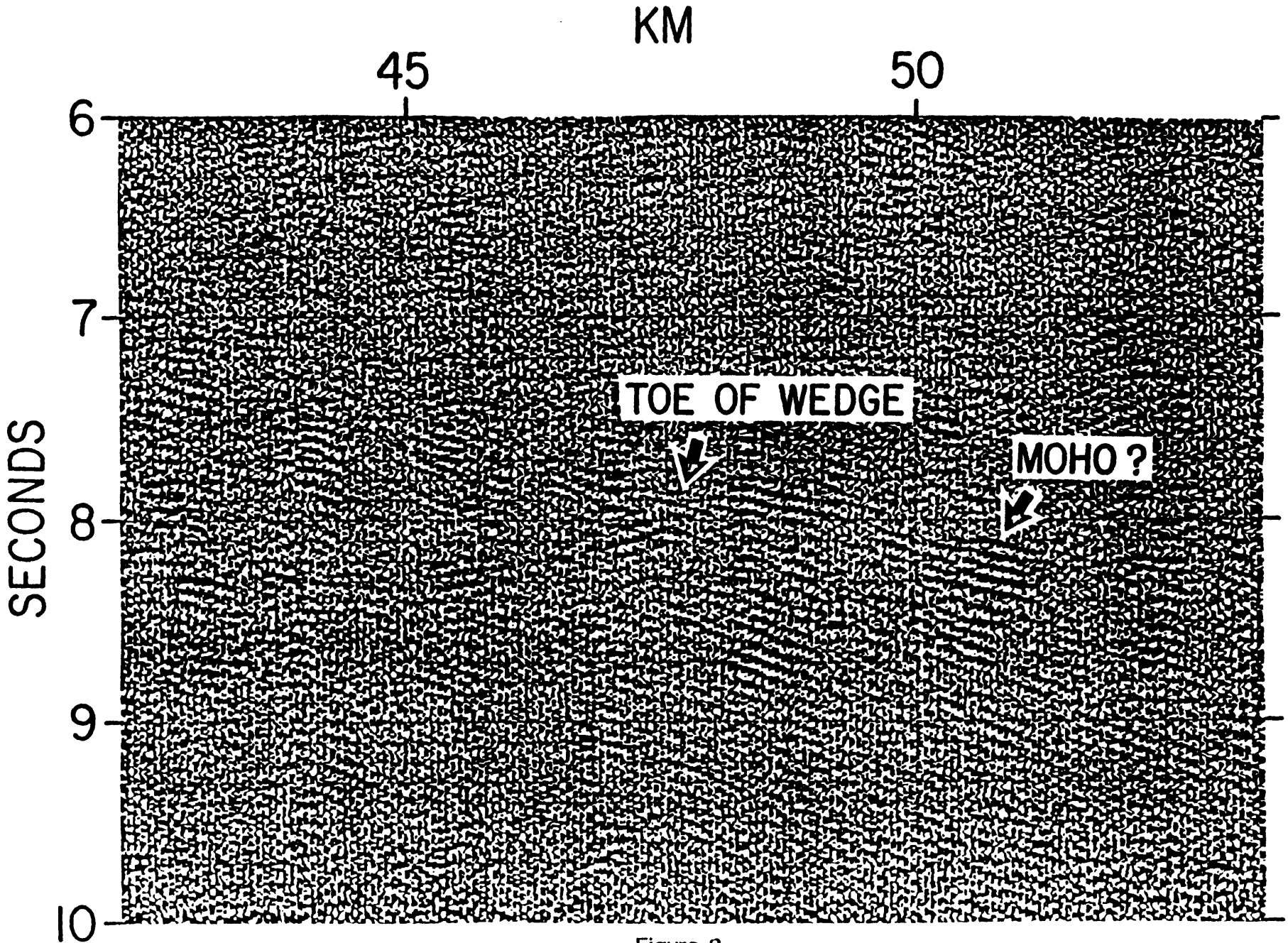

Figure 3

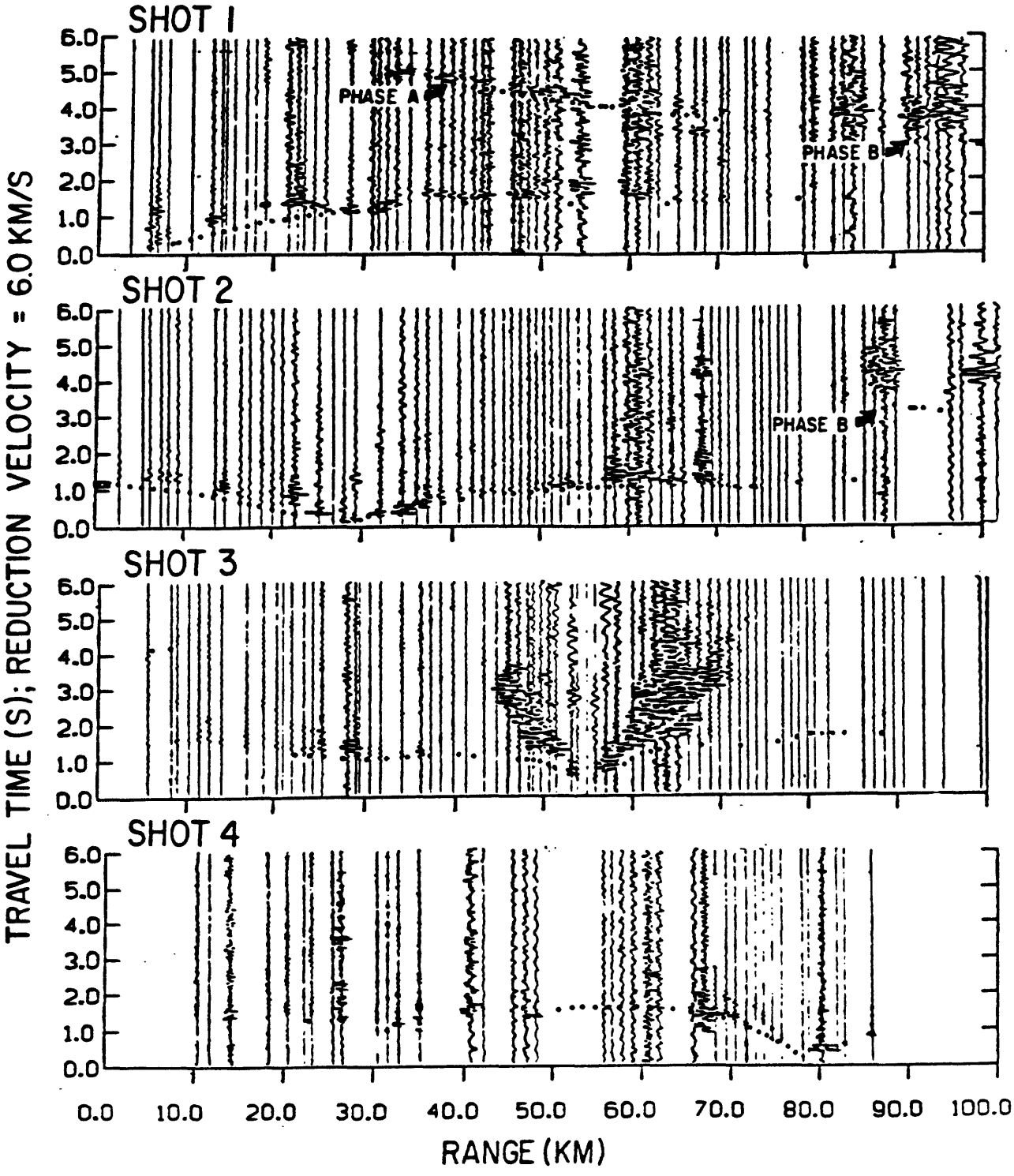
SHOT 1
PHASE A
PHASE B
SHOT 2
PHASE B
SHOT 3
SHOT 4
6.0
5.0
4.0
3.0
2.0
1.0
0.0
TRAVEL TIME (S); REDUCTION VELOCITY = 6.0 KM/S
0.0
10.0
20.0
30.0
40.0
50.0
60.0
70.0
80.0
90.0
100.0
RANGE (KM)

Figure 4a

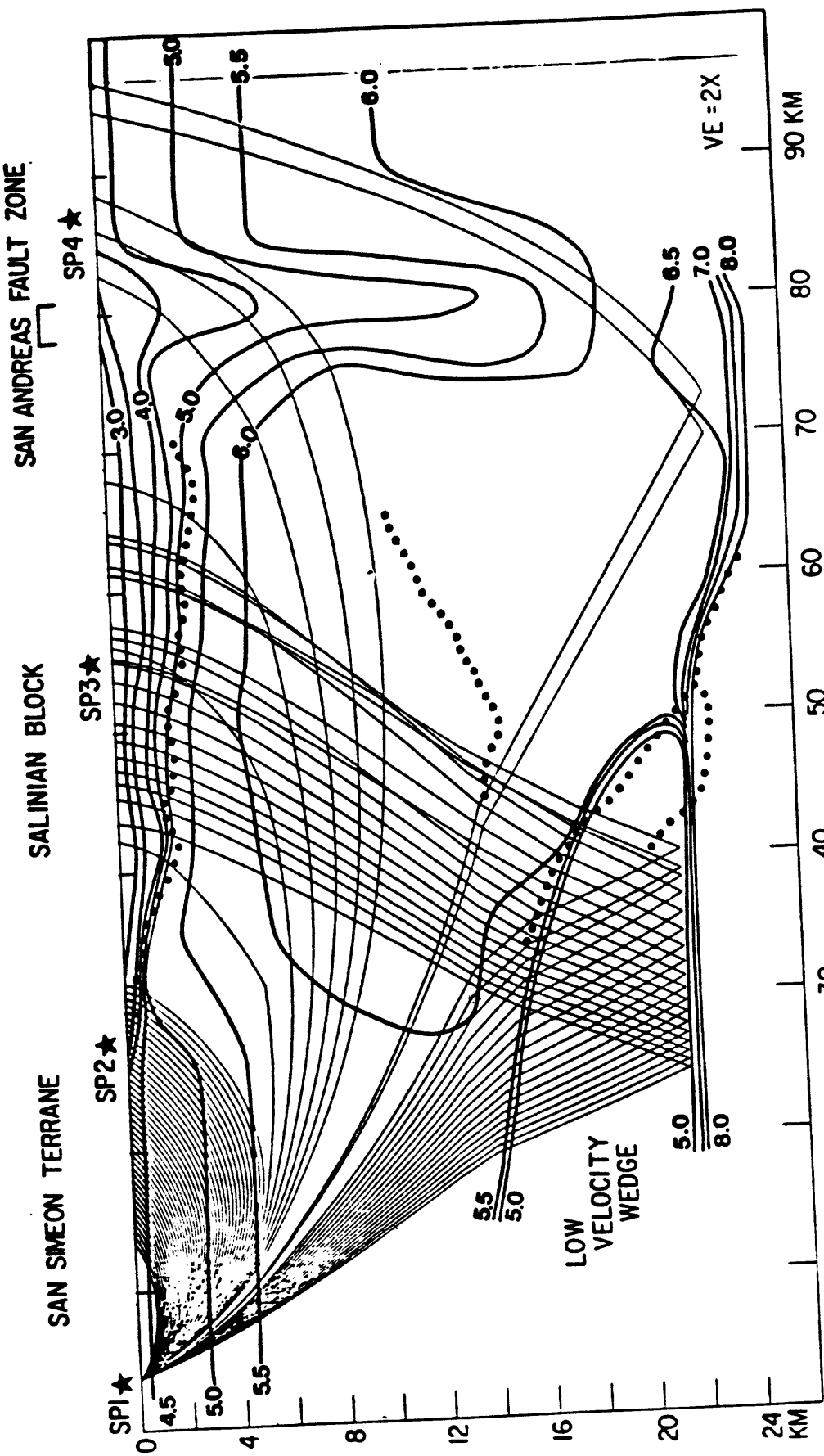
SAN SIMEON TERRANE
SALINIAN BLOCK
SAN ANDREAS FAULT ZONE
SP1
SP2
SP3
SP4
LOW VELOCITY WEDGE
VE = 2X
0
4
8
12
16
20
24 KM
10
20
30
40
50
60
70
80
90 KM
4.5
5.0
5.5
6.0
6.5
7.0
8.0

Figure 4b

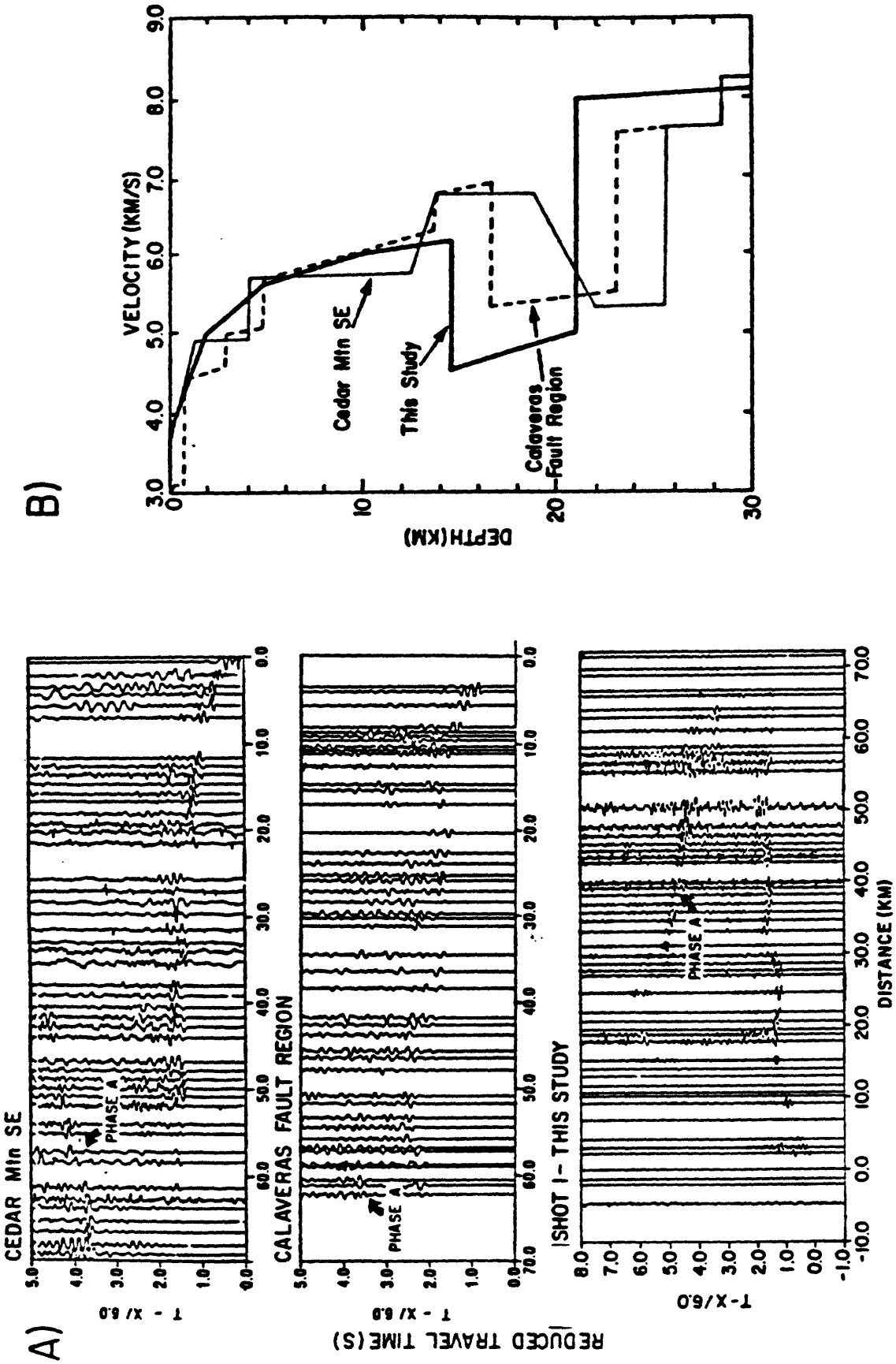
B)
VELOCITY (KM/S)
DEPTH (KM)
Cedar Mtn SE
This Study
Calaveras Fault Region
A)
CEDAR Mtn SE
CALAVERAS FAULT REGION
SHOT 1 - THIS STUDY
PHASE A
REDUCED TRAVEL TIME (S)
DISTANCE (KM)

Figure 5

Wave analysis and interpretation of the seismic-refraction data recorded along the SJ-6 profile, California, USA

N. I. Pavlenkova
Institute of the Physics of the Earth, Moscow

Line SJ-6 strikes northeastward from Morro Bay to the San Andreas Fault, from there, it strikes eastward across the Diablo Range and San Joaquin Valley to the Sierra Nevada. Both seismic-refraction and seismic-reflection (VIBROSEIS) data sets are available along line SJ-6. In this paper, the seismic-refraction data are first analysed independently of the seismic-reflection data in order to appraise the contribution of each of these data sets to the derivation of the velocity structure.

Seismic-refraction data

The seismic-refraction wave field changes significantly along the profile as manifested by the differences between the reversing traveltime curves of the eight shotpoints (SP1-SP8). The degree of non-parallelism of the overlapping sections of the traveltime curves, the sudden changes in the apparent velocity (v_a) of first arrivals along the profile, and the different patterns of latter arrivals indicate a complicated crustal structure.

The profile intervals from SP1 to SP4 and from SP4 to SP7 were recorded separately, so they were analysed separately as profile I and profile II. The analysis included the following steps: the correlation of the seismic phases, the determination of their wave-type, the calculation of individual parameters of a velocity model, the construction of a 2-D velocity model, and the improvement of this model by iterative adjustments.

Correlation of seismic phases for profile I

The profile extends ~90 km northeastward from SP1, and the northeastern-most reversing shotpoint, SP4, is at a range of ~67 km. First arrivals are easily distinquishable on the record sections to distance ranges of ~70 km, but at greater ranges they are attenuated (Fig. 1). Travel-time curves for the four shotpoints are shown in Figure 2.

The first arrivals were divided into two principal phases. The first is observed at ranges of 5-15 km from the shotpoints and has apparent velocities of 2.5 to 5.0 km/s. These velocities are characteristic of sedimentary rocks, so this phase is denoted P_{sed}. The second phase is observed at ranges from 5-15 km to 60-70 km and has an average velocity of ~6 km/s. This velocity is typical of basement rocks, so this phase is denoted P_{bas}. The crossovers from P_{sed} to P_{bas} are marked by arrows in Figure 2.

Differences between the traveltime curves of the four shotpoints are evident in the apparent velocity of P_{sed} and in the crossover distance (d_b) of P_{bas}. The minimum velocity of P_{sed} (~2.5 km/s) and the minimum d_b (~5 km) are observed from SP3. As observed from SP1, SP2, and SP4, the maximum velocity of P_{sed} is high (~5 km/s), so it is more difficult to determine d_b. Comparison of the reversing traveltime curves (Fig. 2) reveals intervals where a change in the apparent velocity is associated with a horizontal change in structure. For instance, the traveltimes are shifted by local changes in the basement depth or changes in the velocities of the sediments. The reversing traveltime curves for this profile do not show a lateral change in the velocity of P_{bas}.

The secondary arrivals show greater differences between shotpoints. From SP1, a large-amplitude phase with v_a = 6.5-7.0 km/s arrives 2-3 s behind the first arrivals. From the other shotpoints similar large-amplitude arrivals were observed, but their correlation over many traces is often impossible. If the traveltime curves of these larger-amplitude arrivals are grouped, a definite regularity becomes evident, that is, the apparent velocity increases as the offset from the shotpoint decreases.

Determination of wave-type

The shape of the reversed and overlapping traveltime curves can be used to establish whether the first arrivals are head waves propagating along a velocity boundary or refracted waves propagating in a high-velocity gradient medium and whether the secondary arrivals are simple or mutiple reflections or converted phases.

The most convenient means of the identifying the wave-type of the first arrivals is measurement of non-parallelism of their overlapping traveltime curves (Gamburzev and others, 1958). Near the shotpoints, the P_{sed} traveltime curves are not parallel, so they are best modeled as refracted or diving waves. P_{bas} traveltimes are practically parallel over the whole registration interval, therefore, they can be modeled as head waves.

Identification of the wave-type of secondary arrivals is hindered by the absence of reversed overlapping branches for them, but they are probably reflections because the apparent velocities of these waves are higher than those of the first arrivals, which is not the case for multiple reflections or converted waves. The difference in the apparent velocities observed in opposing directions from the shotpoints could result from the dip of a reflecting boundary.

The resolution of the present data is not sufficient to determine what causes the observed attenuation of the first arrivals at distance ranges greater than 70 km. One plausible explanation is that a downward dislocation of the basement surface causes not only a sudden delay of the arrivals ~80 km northeast of SP4, but also the observed wave attenuation. It should be noted, however, that the attenuation from SP1 is observed somewhat closer than from the other shotpoints, so another possibility is a low-velocity layer deep in the crust; its existence could be established if a much longer traveltime curve were recorded westward from SP4.

Parameters of the velocity model for profile I

Because P_{bas} is a head wave, the sediment-basement boundary was constructed using the method of t_i and t_Δ curves (Gurvich, 1975):

$$t_\Delta = t_1 + (T - t_2) = t_1 - t_2 + T$$

$$t_i = t_i + (T - t_2) = t_1 + t_2 - T$$

where t_1 and t_2 are the direct and reverse traveltimes of the wave P_{bas} from SP1 and SP4 and T is the reciprocal time (Fig. 2). The dip of the line t_Δ is numerically equal to twice the velocity along the refracting boundary, v_b = 6 km/s. The line t_i characterizes the boundary topography and can be used to calculate the refracting boundary depth H:

$H = t_i v_m/(2\cos(i))$ and $\sin(i) = v_m/v_b$, where v_m is the mean velocity to the refracting boundary.

The depths of the basement reflectors were determined from traveltimes of the secondary arrivals using the approximation: $H = 1/2((tv_m)^2 - d^2)^{1/2}$, where $v_m = (V_a d/t)^{1/2}$, which was equal to 6.5 km/s on the average (Fig. 6)

The resulting velocity model constructed along the profile has the following major elements: 1) a sedimentary layer in which the velocity varies from 2.5 km/s to 5 km/s; 2) a 6-km/s sediment-basement boundary which has depressions at distance ranges of 30-60 km east and beyond 80 km east; 3) a low velocity gradient within the basement; and 4) an eastward dipping reflecting boundary deep within the basement.

Seismic phases of profile II

As with profile I, the first arrivals were divided into two phases: one, associated with the sediments ,P_{sed}, the other, with the seismic basement, P_{bas}. P_{sed} is observed up to 20 km from the shotpoints and its traveltime curve shows a curvature indicative of a high velocity gradient. The apparent velocity of P_{sed} increases from 2.2 to 4.6 km/s at SP5 and SP6 and from 4.0 to 5.0 km/s at SP4 and SP8. True velocities can be estimated by solving the 1-D inverse problem (V. Yu. Burmin, 1980).

The apparent velocity of P_{bas} also varies along profile. For eastward propagation, the apparent velocity gradually increases from ~6 km/s at the basement crossover to ~6.5 km/s at a range of ~70 km. At still greater ranges, v_a increases up to ~9 km/s. For westward propagation, no velocity data is available from SP7, but the reversing traveltime curves recorded from SP5 and SP6 require the velocity just below the sediment-basement boundary to be less than 6.5 km/s. In addition, a vertical velocity gradient must exist within the basement because these traveltime curves are not parallel. Consequently, on the western side of the profile, P_{bas} is a refracted wave rather than a head wave.

The complicated character of the reversed and overlapping traveltime curves (Fig. 3) made it necessary to apply the method of reduced traveltime curves (Pavlenkova, 1979) to permit the separation of the effects of the horizontal and vertical inhomogeneities. Fig. 4 shows the reduced traveltimes of profile II plotted at half their distance from the source (d/2) The figure also shows both the envelopes of the traveltime curves and the lines of the time field (N.N. Puzyrev). The former are the lines joining the intercept times $t_i(x, v_r)$ for a given v_r and are used to determine the depth to v_r; the latter are the lines joining traveltimes at the same source distance, t(x, d=const) and qualitatively reflect the variability of the velocity section along the profile at depths above that of V_r.

The lines plotted in Figure 4 show that the velocities in the upper part of the crust diminish from SP4 to SP5 and increase from SP6 to SP7. A westward dip of the basement is supported by the shape of the envelope $t_i(x,V_r = 6.5)$ at the eastern end of the profile and by the fact that the traveltimes for a given d=constant are smaller at SP4 than at SP5 and SP8.

Low-velocity zone

A local low-velocity zone within the sedimentary section is suggested by the records of SP8 and SP5 (Fig. 3). On the record section of SP8, first arrivals observed at ranges 15-20 km east are attenuated and followed by secondary arrivals delayed by ~1 s. Similarly, on the reversing record section of SP5, the first arrivals observed over approximately the same section of the profile are delayed. These delays are not likely the result of a lateral change in the velocity structure because the reversing shotpoints would show opposite time offsets. The delays are best attributed to a low-velocity layer located between SP8 and SP5. Although the first arrivals from the other shotpoints do not show large delays over the postulated range of the low-velocity zone, a multiple-refraction recorded westward from SP6

does have a 0.5 s offset in its traveltime curve. The ratio of the reduced first-arrival times after the offset (the shadow zone) and the intercept time envelopes suggests the velocity inversion lies above the basement (the 6.0 and 6.5-km/s velocity contours).

On the record section of SP4, a delay of the first-arrival traveltimes and an accompanying reduction in the wave amplitude is observed at 13-18 km distance. However, the reversing first arrivals from SP5 and SP6 advance across the same region, so a lateral change in the local velocity structure rather than a low-velocity zone is the most probable cause.

Secondary arrivals and multiples

The major peculiarity of the secondary arrivals is the practical absence of phases with apparent velocities larger than the velocities of first arrivals. This implies an absence of deep reflectors. The shape of the traveltime curves of the secondary phases permits their definition as multiple refracted and reflected head waves. Close to the shotpoints, the multiples are curved and correspond to waves propagating in the high vertical-velocity-gradient medium (multiple refractions). At farther offsets, the multiples are parallel to the basement first arrivals and correspond to waves propagating along the basement surface after reflection between the basement and ground surface (reflected head waves).

For the n^{th} multiple refraction, the traveltime at a distance d is n times the first-arrival time at the distance of d/n. The apparent velocities of these waves are always less than those of the first arrivals and they gradually depart from them with the distance. For the reflected head waves, t_i is twice as large as for the initial head waves. The critical point of the reflected head wave and the traveltimes of the multiple refractions provide additional constraints on the depth and velocity of the basement boundary across the model.

Parameters of the model for profile II

Figure 5 presents the 1-D velocity-depth solutions derived from the analysis of the traveltime curves. Examination of Figure 5 shows the following structural elements:

1) The velocity in the sedimentary section increases rapidly with depth from 2.0 to over 5.0 km/s, and it is laterally heterogeneous, increasing from east to west along the profile.
2) A low-velocity zone exists in the sedimentary strata between SP5 and SP8.
3) Between SP5 and 7 the velocity contrast at the sediment-basement boundary is large and the boundary rises to the east.
4) The velocity in the basement increases rapidly with depth from 6.0 to 6.5 km/s and then gradually increases with depth to not more than 7.0 km/s.

Construction of the 2-D models for Profiles I and II

After careful analysis of the wave fields, the 1-D solutions were used to construct 2-D models for both profiles. These initial models were then improved by iterative ray-tracing for two iterations. At the end of the second iteration, all of the calculated traveltimes were within 0.18 s of the observed traveltimes.

It is interesting to compare the final 2-D velocity models (Fig. 6 and 7) with the one dimensional solutions (Fig. 5). If the ray penetration depth is still on the order of length of the traveltime curve, such as for the upper part of the model, the 1-D solutions give a fair representation of the velocity change with depth. But if the length of the traveltime curve is ten

times the depth of the ray penetration, the horizontal inhomogeneity strongly distorts the 1-D solutions (Fig. 5); for example, the high-velocity boundaries (V ~8 km/s) found at depths of 5 and 7 km in 1-D solutions of SP5 and SP6 are meaningless.

Discussion of results

The accuracy and resolution of the velocity models presented here can be appraised by comparison with the seismic-reflection data (common depth point technique) as well as with velocity models derived by other authors using the same refraction data.

Comparison with the seismic-reflection survey along line SJ-6

In Figures 6 and 7, some of the boundaries revealed in seismic-reflection data are superimposed on the refraction models of profile I and II; this was accomplished by converting the two-way reflection times to depths using the velocity structure of the appropiate refraction model. Note that the overall shapes of the reflection boundaries correlate with the shapes of refraction boundaries (velocity isolines). For example, at the western end of profile I, a steeply east-dipping event on the reflection section correlates with the reflecting boundary constructed at a depth of ~30 km in the refraction model (Fig. 6). This boundary may be the Moho, but it is not proved, because the maximum range of the recorded refraction data is less than that predicted for P_n first-arrivals. Along profile II (Fig. 7), the boundaries in the refraction model are more gently dipping than those observed in the the reflection cross-section. The discrepancy is most obvious in the region of the steep folds where the velocity isolines show only slight deflections.

The above the comparison demonstrates that refraction and reflection studies supplement one another. The seismic-reflection (CDP) sections show structure at shallow depths in great detail, particularly folds and faults, and the refraction records reveal the 2-D velocity distributions for these structures. More importantly, the refraction method yields important structural data deep in the crust where the seismic-reflection data is inherently less clear. For example, the refraction data on line SJ-6 reveal an essential difference in the composition or the degree of metamorphism in the basement on profiles I and II that cannot be discerned from the reflection data.

Comparison with other author's velocity models

A comparison of the velocity models presented in Figures 5 and 7 with those constructed by Kostyukevich and others (this volume) and by Mishenkina (this volume) shows that they differ principally in the presence or absence of low-velocity layers in the sedimentary section on the west end of profile II. Although it is difficult to interpret the wave pattern from SP8 without a low-velocity zone between SP8 and SP5, in Mishenkina's model the low velocity zone is absent and in Kostyukevich's model, a low-velocity zone is instead shifted westward between SP4 and SP8. The westward shift is based on a delay of the first arrivals east of SP4, but this delay, as discussed above, is better explained by a lateral change in the near-surface structure west of SP8. Another problem with Kostyukevich's model is the high velocity gradient between the 6.5 and 8.0-km/s velocity contours because the observed curvature of the overlapping traveltime curves supports a lower velocity gradient in the crust below the 6.5-km/s boundary.

Conclusions

The iterative interpretation of the data using the available computer algorithms produces a great number of details (sharp bends of velocity isolines, local inversion zones) in the velocity model thereby making it difficult to distinguish the uniform structural elements. Consequently, the most important stage in the interpretation of refraction data is the correct qualitative correlation of the phases from common structural elements, and not the quantitative determination of the absolute parameters. For both the qualitative and quantitative stages of the modeling, the wave-type and the amplitude characteristics of the waves need to be taken into account.

References

Burmin, V.Yu, 1981. Numerical solution of one-dimensional inverse seismic kinematic problem from traveltimes of refracted waves. Physics of the Earth, Moscow, N 12, p. 28-35.

Gamburzev, G.A., Yu.V. Riznichenko, I.S. Berson, A.M. Epinatieva, Ye.V. Karus, and I.P. Kosminskaya, 1952. Correlation method of the refracted waves. AN SSSR, Moscow.

Gurvich I.I., 1970. Seismic exploration, Moscow, Nedra, 552 p.

Pavlenkova N.I., 1982. The intercept-time method- possibilities and limitations, J. Geophys., 51, p. 85-95.

Figure Captions

Fig. 1 Record sections for shotpoints SP1 and SP2 of profile I.

Fig. 2 Travel-time curves for shotpoints SP1-SP4 of profile I. a) t(d), absolute traveltimes as function of distance; b) t_{red}, traveltimes reduced using V_{red}=6.0 km/s. The line t_i shows the intercept times, the line Δt characterizes the boundary velocity (6.0 km/s)

Fig. 3 Record sections for shotpoints SP5, SP6 and SP8 of profile II. The possible "shadow zones" resulting from a velocity inversion are marked.

Fig. 4 Travel-time curves for shotpoints SP4-SP8 of profile II. a) t(d), absolute traveltimes; b) $t_{red}(d/2, V_{red}=6.5$ km/s), traveltimes reduced using V_{red} = 6.5 km/s are plotted at half the distance range.

Fig. 5 1-D velocity solutions derived for shotpoints SP4, SP5, and SP6 compared to the 2-D velocity solution (Fig. 7).

Fig. 6 Velocity cross-section derived for profile I (thick lines are seismic boundaries.

Fig. 7 Velocity cross-section derived for profile II (dotted lines are seismic boundaries observed in the seismic-reflection time-section)

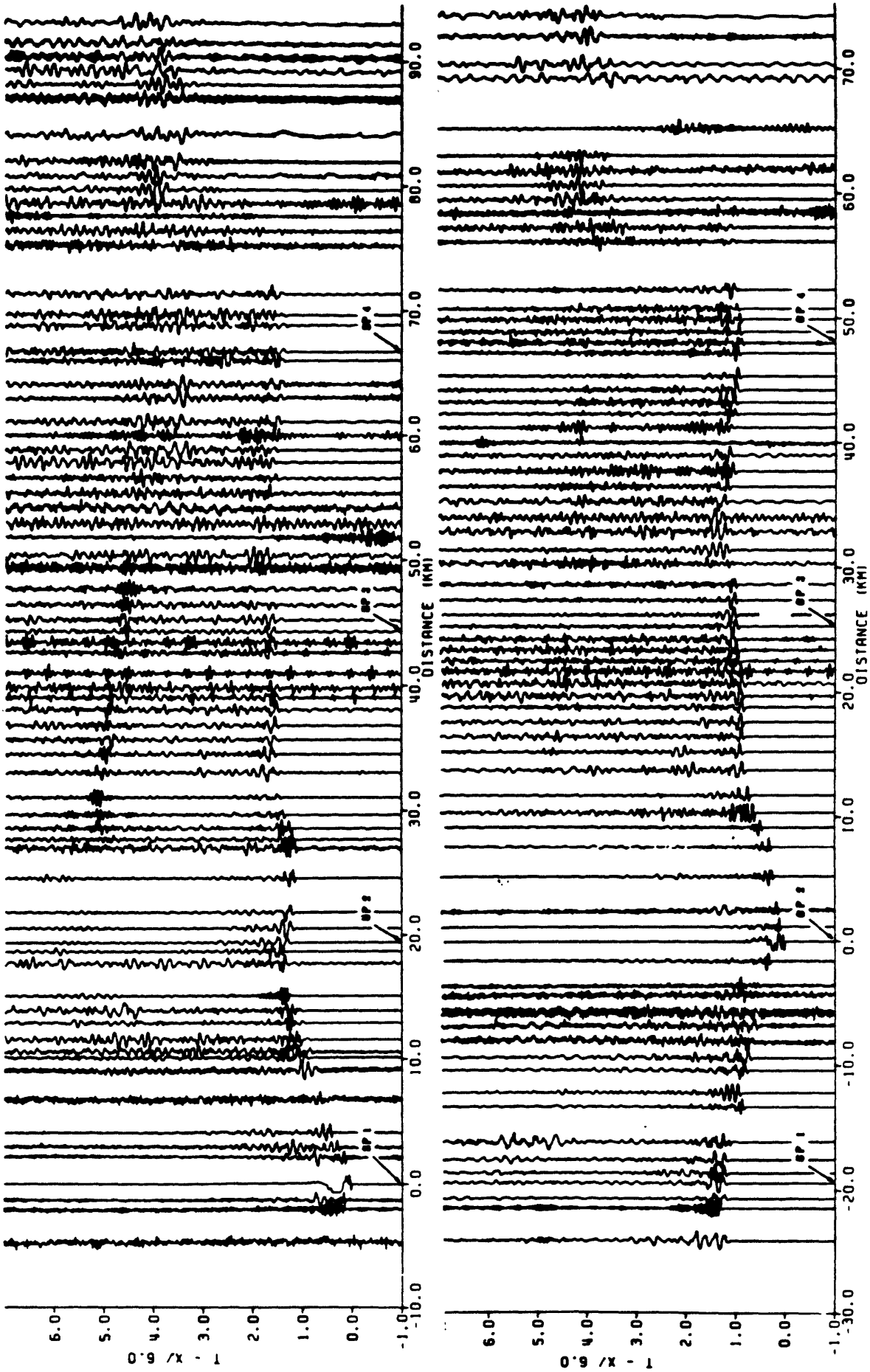

Figure 1

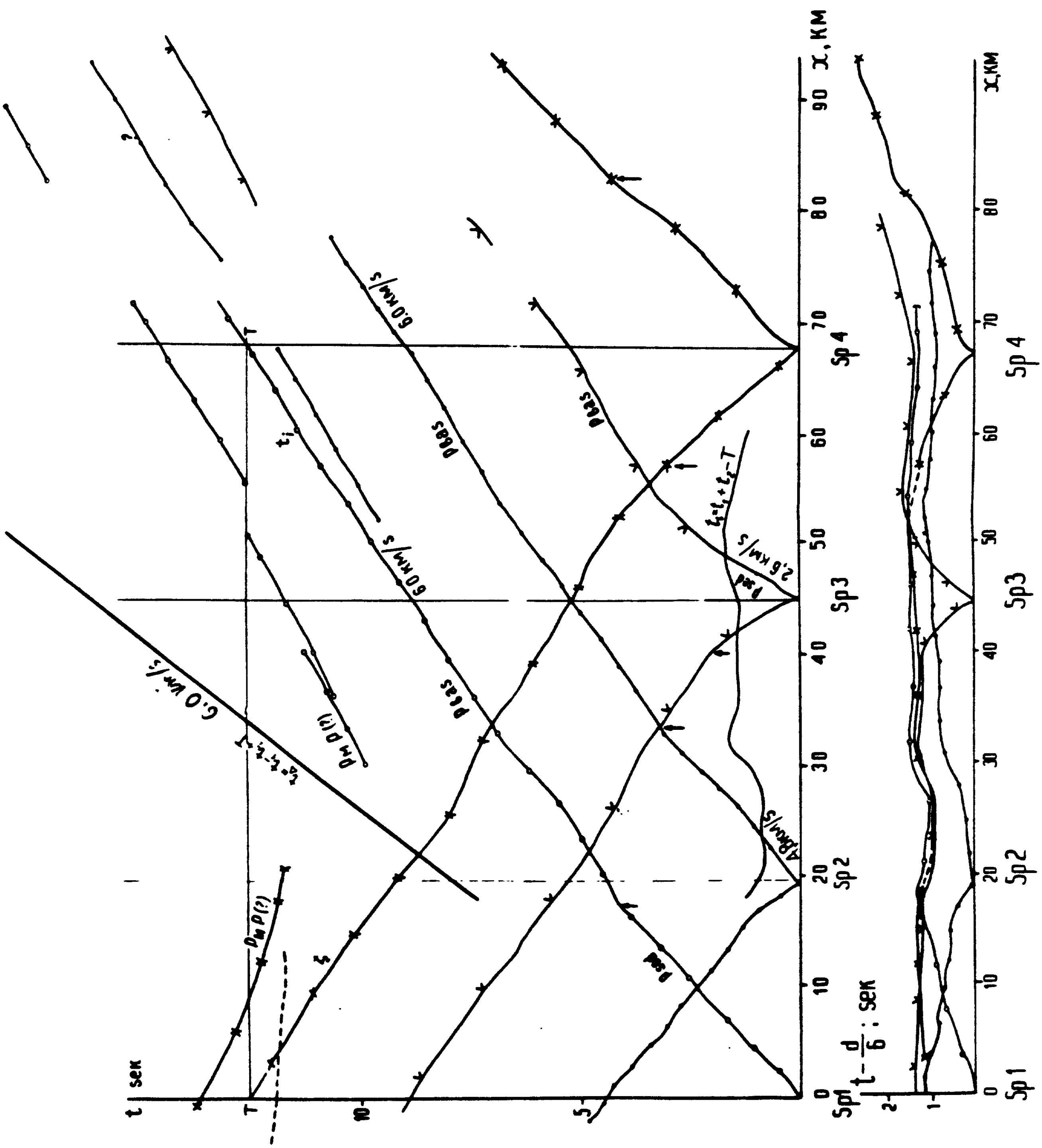

Figure 2

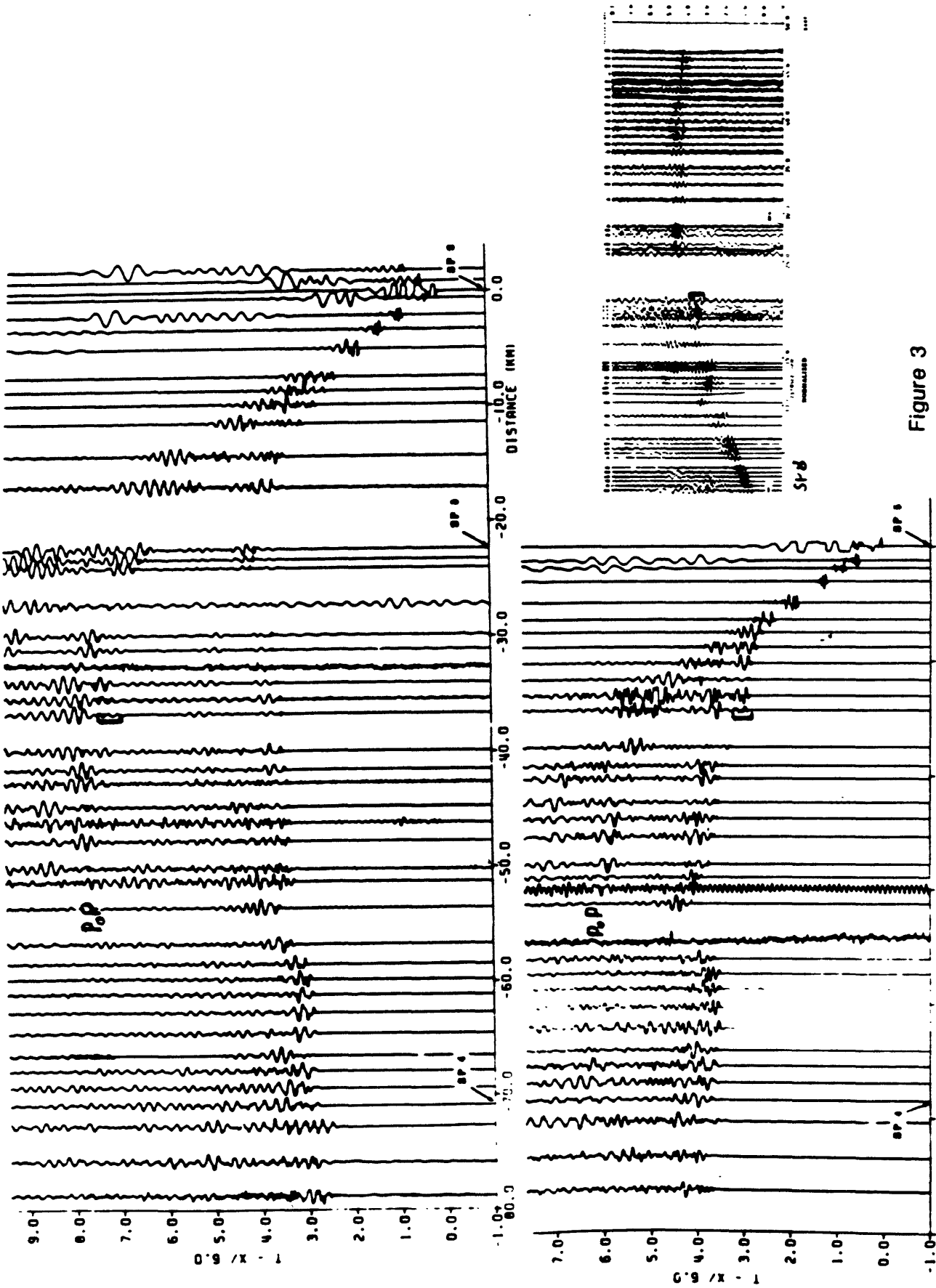
DISTANCE (KM)
0.0
-10.0
-20.0
-30.0
-40.0
-50.0
-60.0
-70.0
-80.0
SP 8
SP 4
P0P
PgP
T - X/ 6.0
9.0
8.0
7.0
6.0
5.0
4.0
3.0
2.0
1.0
0.0
-1.0

Figure 3

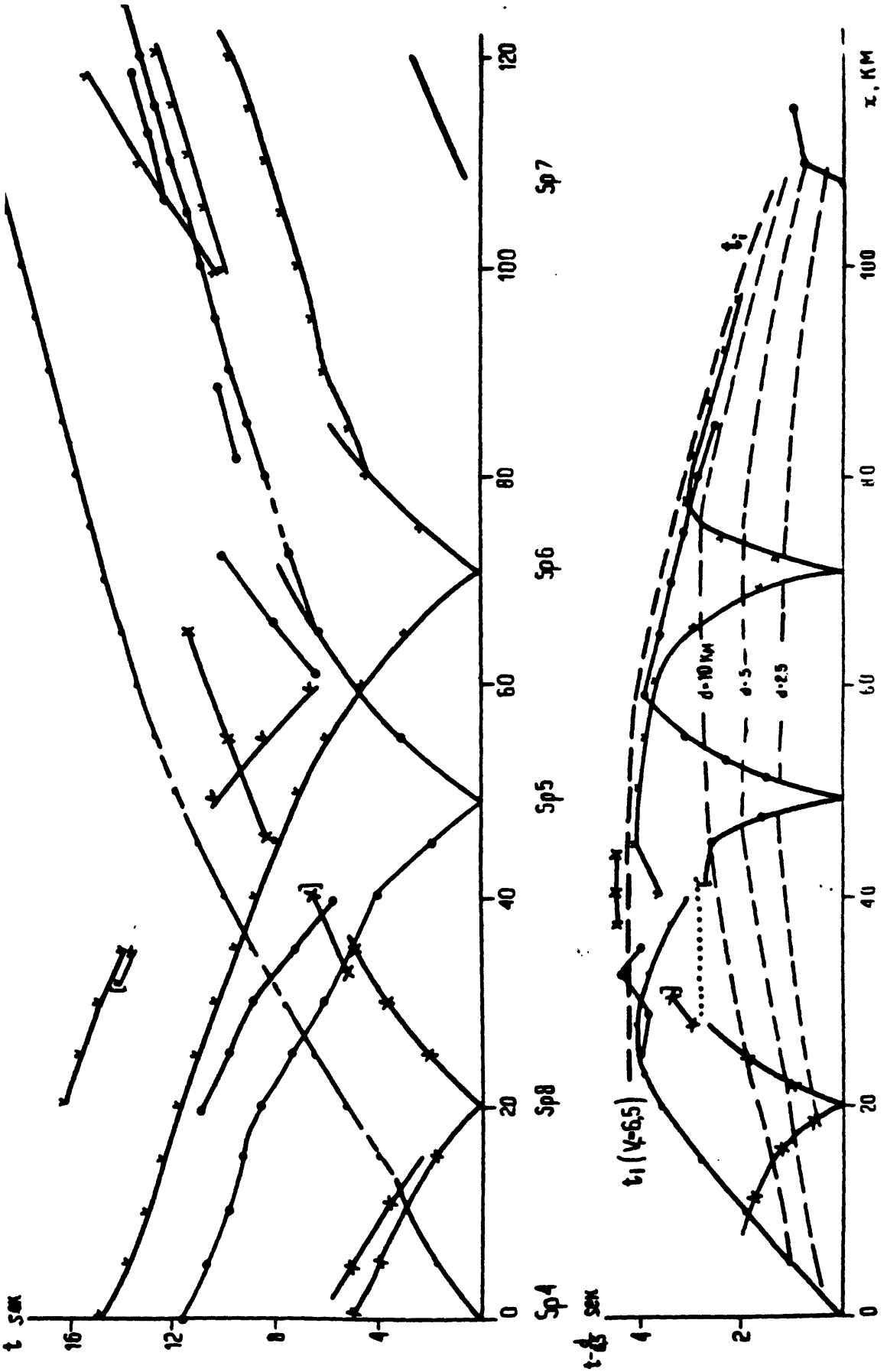
t sek
16
12
8
4
0
Sp4
Sp8
Sp5
Sp6
Sp7
20
40
60
80
100
120
t-t1 sek
4
2
0
t1 (V=6,5)
t1
d=10 km
d=5
d=2,5
x, KM
20
40
60
80
100

Figure 4

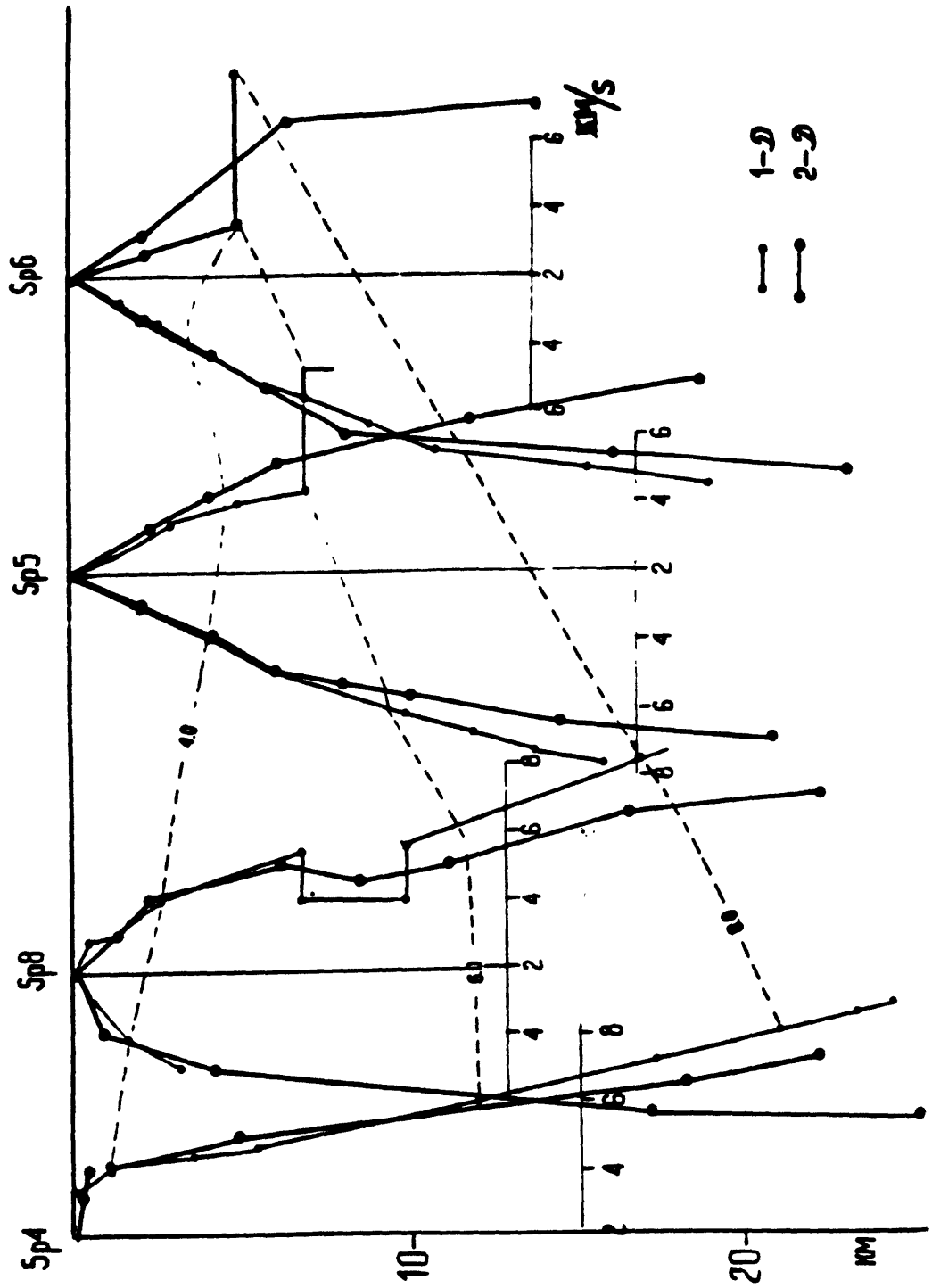

Figure 5

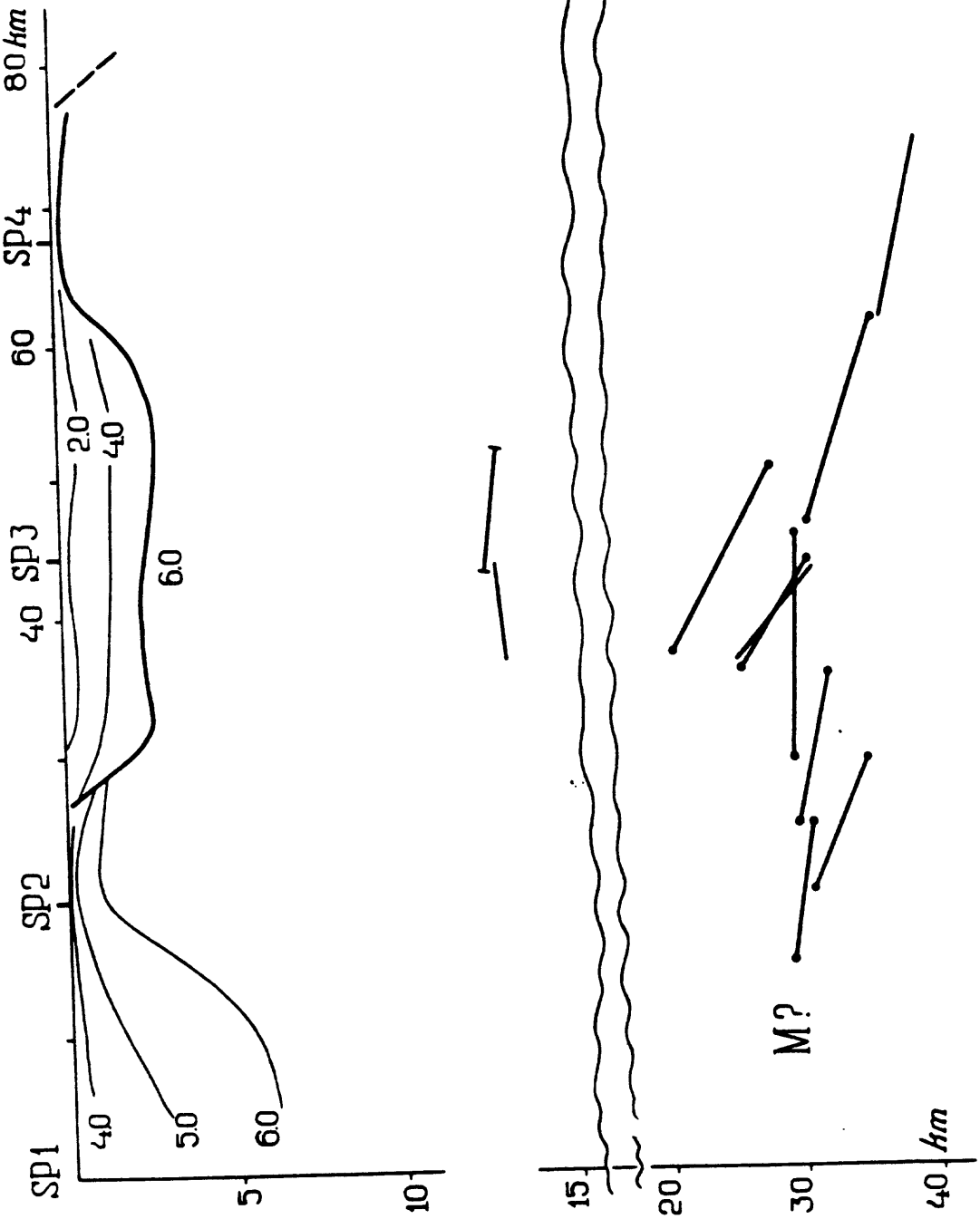

Figure 6

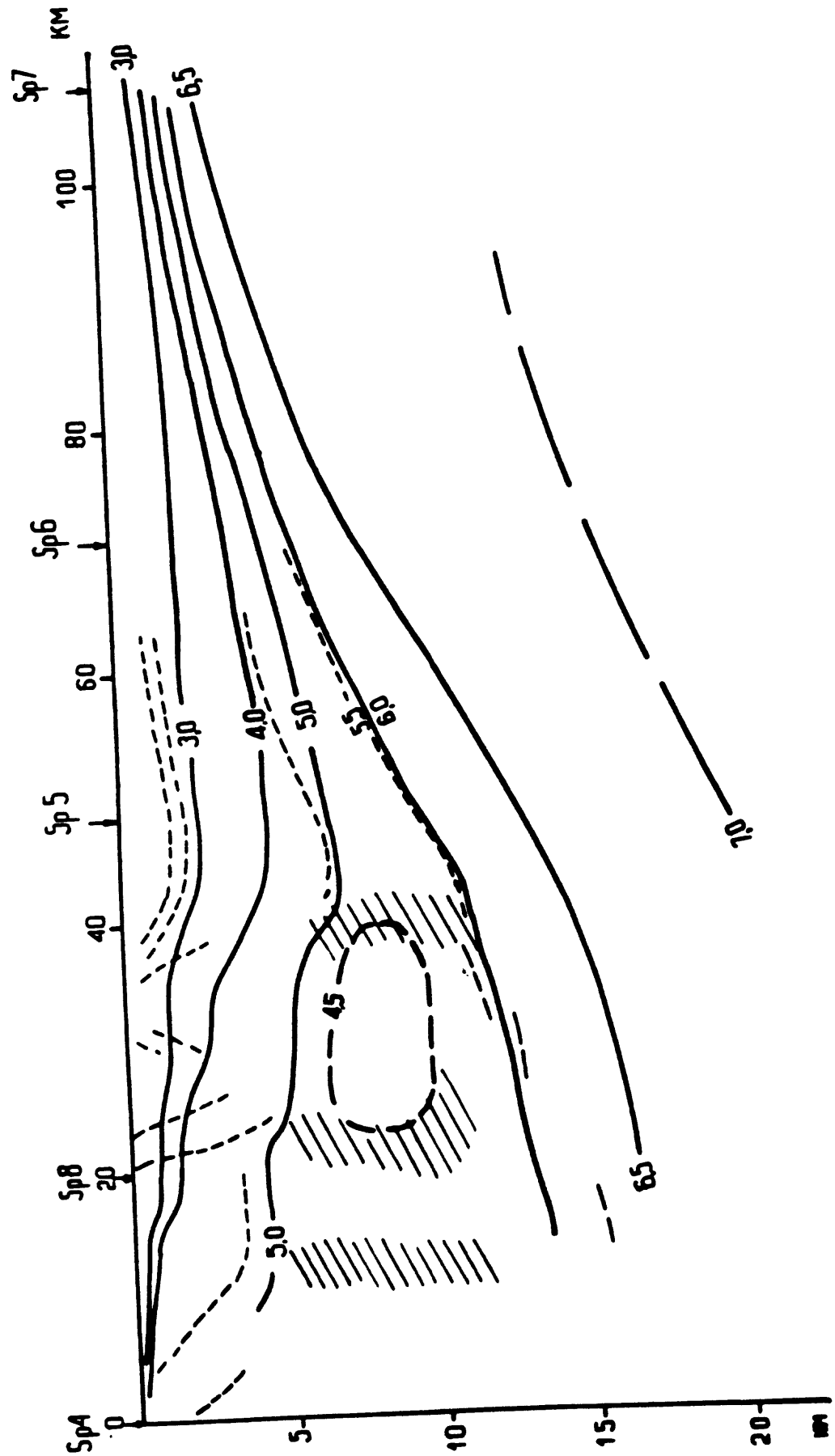
Sp7
KM
100
80
Sp6
60
Sp5
40
Sp8
20
Sp4
0
5
10
15
20
3.0
4.0
5.0
6.0
6.5
4.5
1.0
6.5

Figure 7

Crustal velocity structure along the SJ-6 seismic profile, California, USA

A. S. Kostyukevich, E. P. Baranova, and V. G. Kozlenko
S. I. Subbotin Institute for Geophysics, Academy of Sciences,
Ukr. SSR, Kiev, USSR

Two end-to-end seismic-refraction profiles comprise line SJ-6 (Fig. 1): one profile (CAL-1) extends eastward from the Cholame Valley to the Sierra Nevada through five shotpoints: SP4, SP8, SP5, SP6, SP7; the other (CAL-2), extends northeastward from Morro Bay to Cholame Valley through four shotpoints: SP1, SP2, SP3, and SP4).

Method of analysis

Crustal velocity models for the two seismic-refraction profiles were constructed using the traveltime curves of the first arrivals and the LINKMOD computer algorithm (Baranova and others, 1984). The algorithm, which is based on the concept of seismic tomography, iteratively solves the inverse linearized 2-D kinematic problem of seismics. For a given velocity model, V^i, where i is the step index, a system of rays, R_i, is calculated from each source of excitation over the entire range of observation (a direct 2-D kinematic problem). From these calculations a set of equations are then derived for the velocity anomalies in the discrete volumes of the cross-section under study (A^i_j, j being the volume index). Linearization results from the assumption that the geometry of the ray system, R^i, is independent of A^i_j. The simultaneous use of the whole ray system R^i, and correspondingly, of all first-arrival times, imposes a limitation on the values A^i_j in various portions of the cross-section. The resulting matrix of anomalous velocities (A^i) is employed by the interpreter to compile the next approximation of the velocity cross-section: $V^i+A^i \rightarrow V^{i+1}$. Modeling iterations continue provided that the process keeps converging, that is, the anomalous velocity values in A_i decrease as i increases.

Results of analysis

Authors Kostyukevich and Baranova independently modeled the first-arrival traveltime data selected from the shot records by author Kozlenko. All modeling was stopped at the end of the sixth iteration, and the resulting 2-D velocity models for the two profiles were tied together at SP4 to obtain alternative composite models for line SJ-6. Figures 2 and 3 present the velocity model derived by Kostyukevich (M6K) and Figure 4 that of Baranova (M6B). Within the accuracy of the velocity contours, the structural features of model M6K (Fig. 3) are similar those of model M6B (Fig. 4) with two exceptions: a velocity inversion present between SP4 and SP8 in model M6K is not implicit in model M6B, and the 7.0-km/s velocity contour subhorizontal at ~20 km depth in M6K parallels the eastward rise of the basement surface in model M6B. The first-arrival traveltimes calculated using model M6K (Fig. 3) have a standard deviation of 0.12 s and a maximum deviation of 0.18 s from the observations. Those calculated using model M6B (Fig. 4) have a standard deviation of 0.09 s and a maximum deviation of 0.22 s.

References

Baranova E.P., V.G. Kozlenko, and A.S. Kostyukevich, 1984, Interpretation of data set I by ray approximation.- Report 258 Bureau MRGG, Camberra, p. 90-95.

Figure Captions

Fig. 1 Composite velocity model derived for the line-sections CAL-1 and CAL-2 after the first step of solving the inverse kinematic problem. Number key: 1, initial model contours $v_0(z)$ in km/s; 2, contour lines and boundaries in the model of the next approximation, $v_1(z)$.

Fig. 2 Kostyukevich's composite velocity model for line SJ-6 at end of the sixth iteration (model M6K). Number key: 1, velocity boundaries; 2, contour lines; 3, abrupt offsets of the contour and boundary positions.

Fig. 3 Figure 2 model with velocity contours. Numbers are velocity values in km/s.

Fig. 4 Baranova's model (model M6B) with velocity contours.

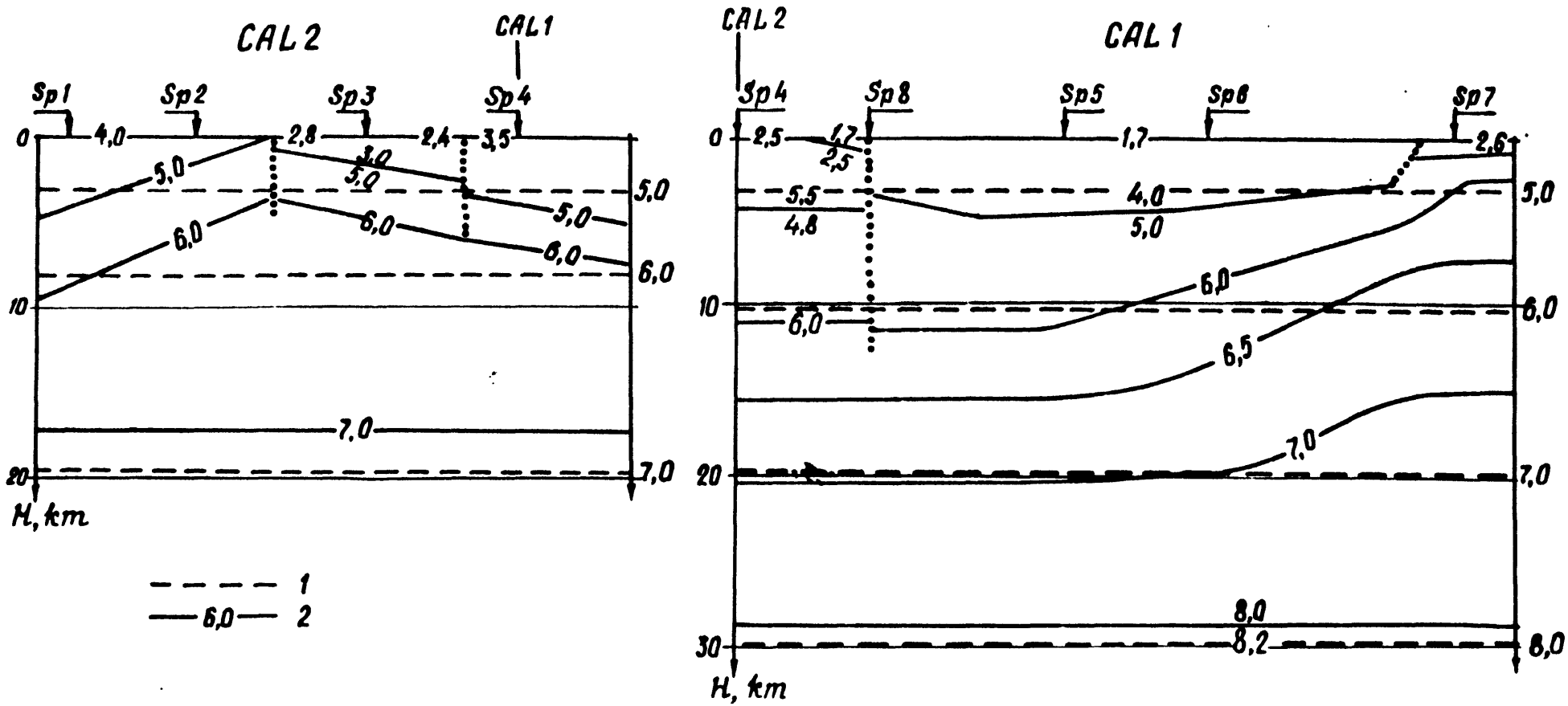
CAL 2
CAL 1
Sp 1
Sp 2
Sp 3
Sp 4
Sp 8
Sp 5
Sp 6
Sp 7
0
10
20
30
4,0
2,8
2,4
3,5
2,5
1,7
2,6
5,0
6,0
7,0
8,0
8,2
5,5
4,8
6,5
H, km
1
2

Figure 1

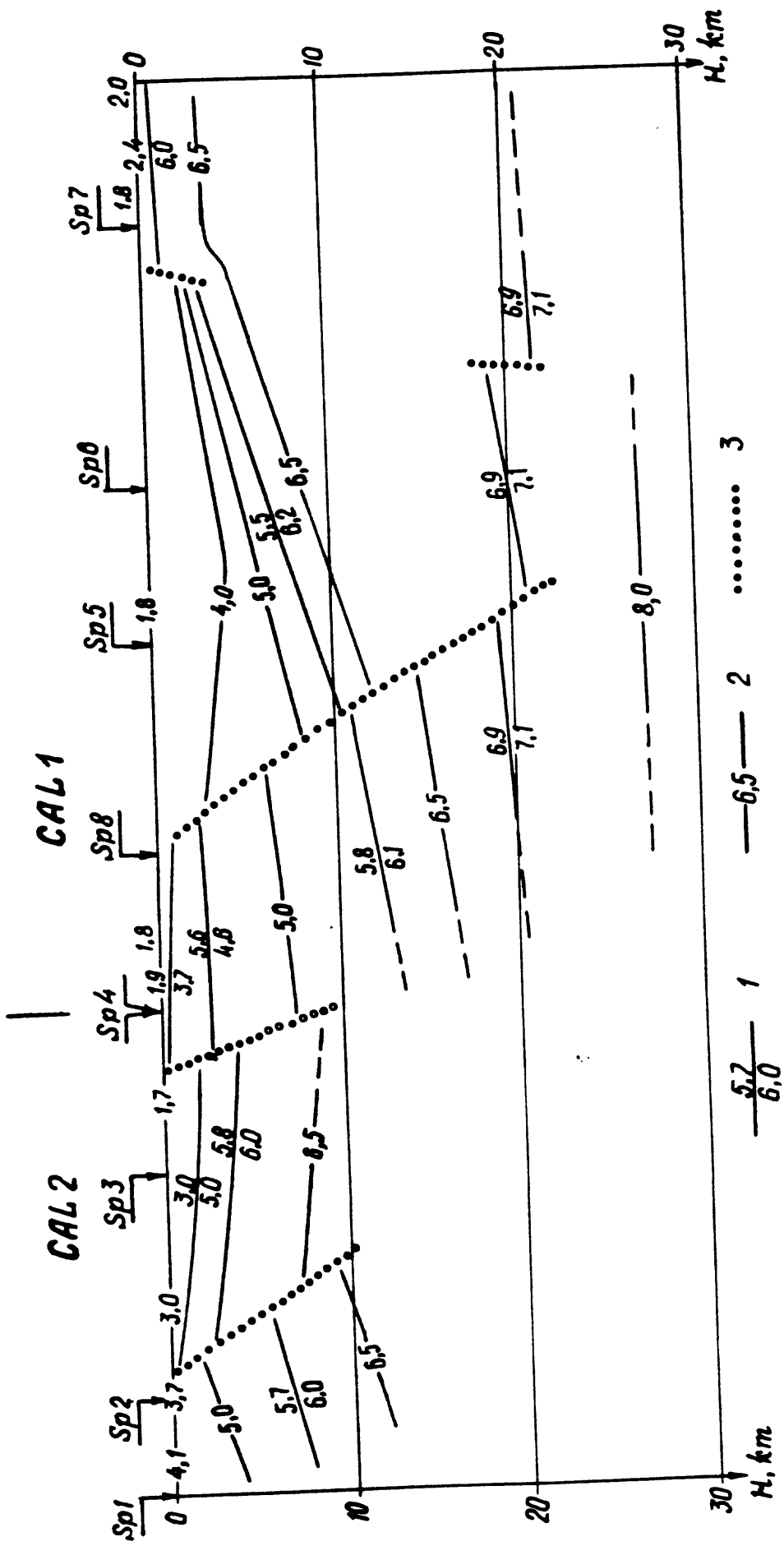

Figure 2

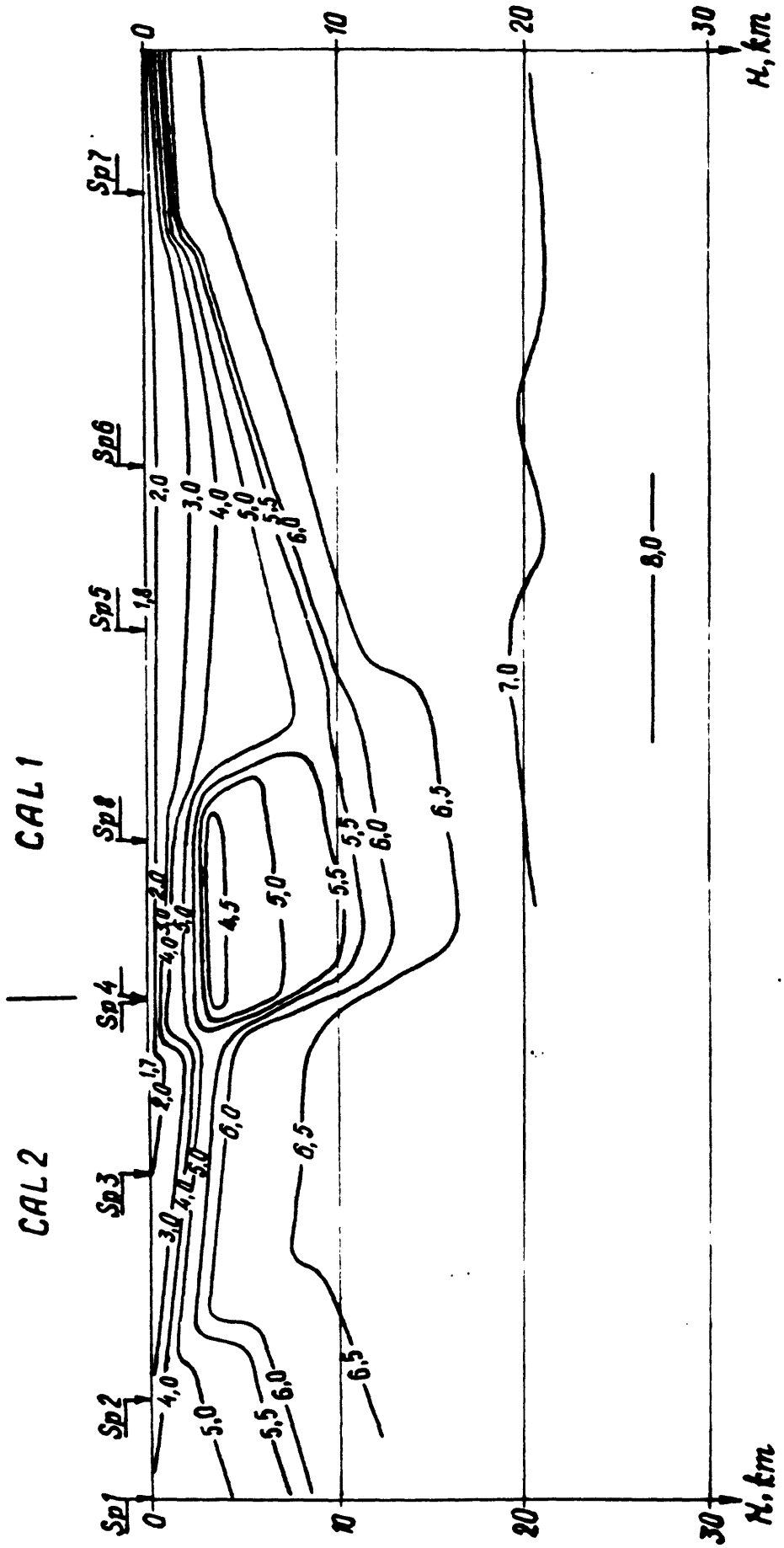
CAL 1
CAL 2
Sp1
Sp2
Sp3
Sp4
Sp5
Sp6
Sp7
0
10
20
30
H, km
2,0
3,0
4,0
5,0
5,5
6,0
6,5
7,0
8,0
4,5

Figure 3

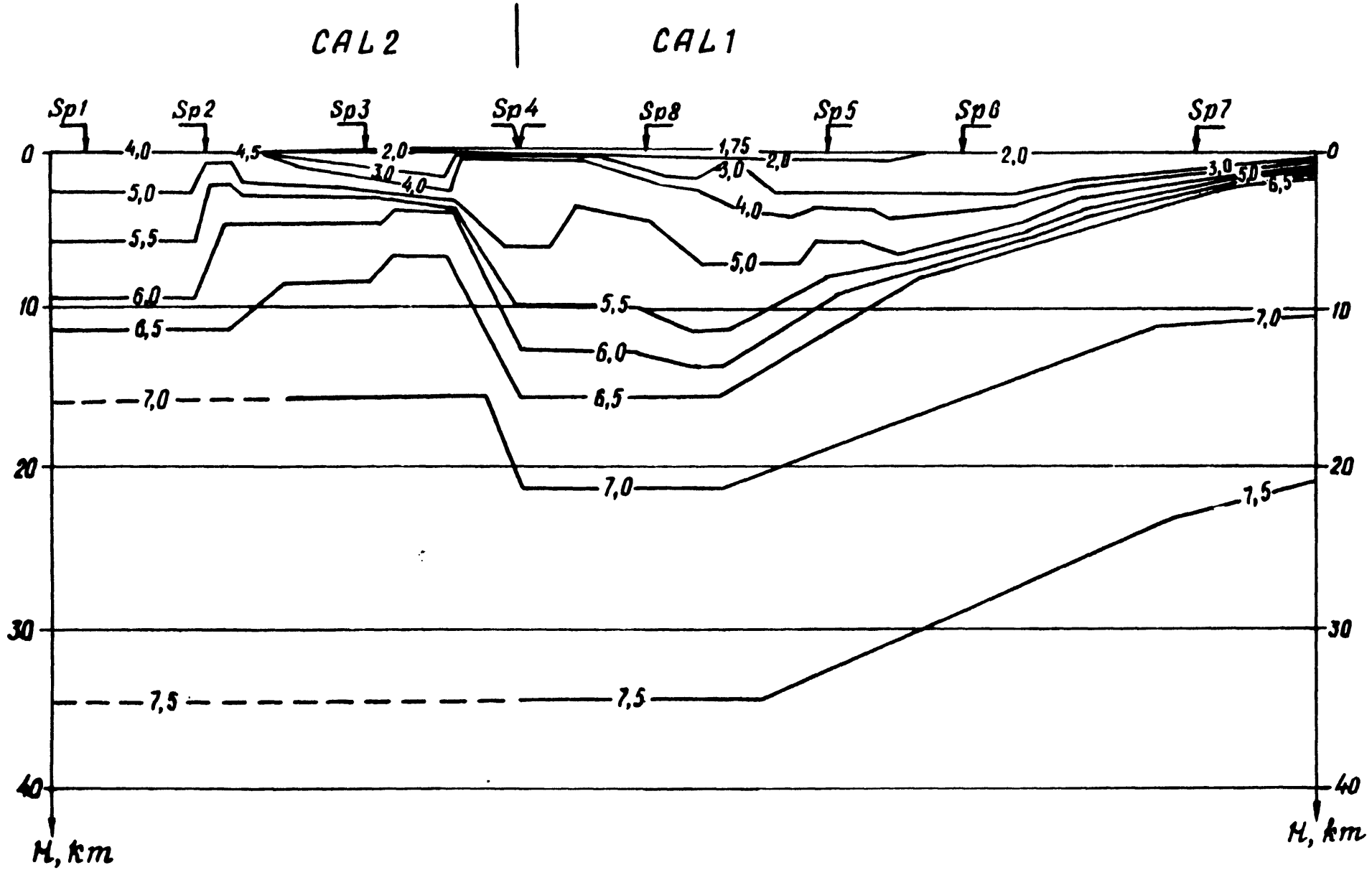
CAL2
CAL1
Sp1
Sp2
Sp3
Sp4
Sp8
Sp5
Sp6
Sp7
0
10
20
30
40
4,0
4,5
2,0
3,0
4,0
1,75
2,0
2,0
3,0
5,0
6,5
5,0
5,5
6,0
6,5
7,0
5,5
6,0
6,5
7,0
7,0
7,5
7,5
H, km
H, km

Figure 4

An interpretation of the velocity structure between Cholame Valley and the Sierra Nevada, California, USA

Z. R. Mishenkina
Institute of Geology and Geophysics, Novosibirsk, USSR

An upper-crustal velocity model for the ~105-km section of line SJ-6 located between Cholame Valley and the Sierra Nevada was constructed using the first-arrival traveltime curves of five shotpoints: SP4-SP8 (Fig. 1a). The longest of the traveltime curves extends ~120 km eastward from SP4, but the easternmost reversing shotpoint, SP7, had a very weak signal, so the longest reversing curve extends ~70 km westward from SP6.

Seven apparent velocity branches (v*) were distinguished in the first-arrival data (Fig. 1a), but the intervals over which the velocities are observed are relatively short, 3-15 km. The set of observations is incomplete and it does not permit clear detection and correlation of every velocity branch along the profile, thus making it difficult to determine correct layer velocities and interface depths.

Although accurate determination of the layer velocities and thicknesses is impossible, the available data were used to determine a schematic velocity cross-section (Fig. 1b). The depths of six velocity interfaces were computed under the assumption that the model can be approximated by a series of homogeneous layers bounded by horizontal interfaces. The velocities in the upper 3 layers were equated to the average values of the observed apparent velocities and the velocities in the lower four layers were determined by the formula $1/v = 1/2(1/{>_V} + 1/{<_V})$

In the schematic model shown in Figure 1b, the sedimentary section is represented by a series of five layers with velocities of 2.0, 2.5, 2.9, 3.6, and 4.5 km/s, respectively. The three uppermost layers thin westward of SP5 with the 3.6 and 4.5-km/s layers approaching the surface near SP4. The 4.5-km/s layer thins rapidly east of SP8. The basement is comprised of two layers: a 6.4-km/s layer above a 6.9 km/s-layer. These layers rise eastward toward SP7.

An alternative velocity cross-section for the profile interval x = 10-90 km (where x = 0 is SP4) was constructed in terms of isovelocity lines by modeling the traveltime curves as continuous refractions rather than as seven separate head waves. The modeling was accomplished using the computer program INVERS (Mishenkina and Krylov, 1983; Mishenkin and others, 1983). This program is based on a linearization method developed for converting the refraction time field t(x,l) into a velocity cross-section v(x,z), where x is distance along line of observation, l is the distance between shotpoint and station, and z is the depth. The time field (Fig. 2) was built from the first-arrival traveltimes using discretization intervals of x=10 km and l=5 km. In this time field, the lines t(x,l=const) qualitatively characterize the velocity isoline form, that is, the distances between the lines determine the layer velocity. It is to be pointed out that because the average interval between the shotpoints is ~27 km, the traveltime data do not have the the resolution of the chosen discretization of the time field. Thus, the cross-section shown in Figure 3 gives only an approximate presentation of the gross features of the 2-D velocity distribution.

References

Mishenkina, Z.R. and S.V. Krylov, 1983, Utilization of the linearized formulation of the inverse kinematic problem for two-dimensional time fields t(x,1) of refracted waves, in Numerical methods in seismic research, Nauka, Novosibirsk

Mishenkin, B.P., Z.R. Mishenkina, and I.F. Sheludko, 1983, Detailed study of the earth's crust in the Baikal rift zone using refracted wave data, Soviet Geology and Geophysics, v. 24, no. 12, p. 73-80.

Figure Captions

Fig. 1a First-arrival traveltime curves from the five shotpoints (SP4-SP8) located on the Cholame Valley-Sierra Nevada section of line SJ-6. Number Key: 1-8, separate head waves; 9, reversed intervals; 10, observation intervals of the same phases; 11, value of apparent velocities, km/s.

Fig. 1b Schematic seismic-velocity cross-section between SP4 and SP7 assumes 7 homogeneous layers. Number key: 12, layer interfaces; 13, layer velocities in km/s.

Fig. 2 First-arrival time field t(x,1). Figure shows the lines 1= constant, the traveltime curves t(1), and the inverse of the time field gradient labeled in km/s (the layer velocity).

Fig. 3 Velocity cross-section v(x,z) between SP4 and SP7 constructed from the time field t(x,1) shown in Figure 3. Velocity isolines are labeled in km/s.

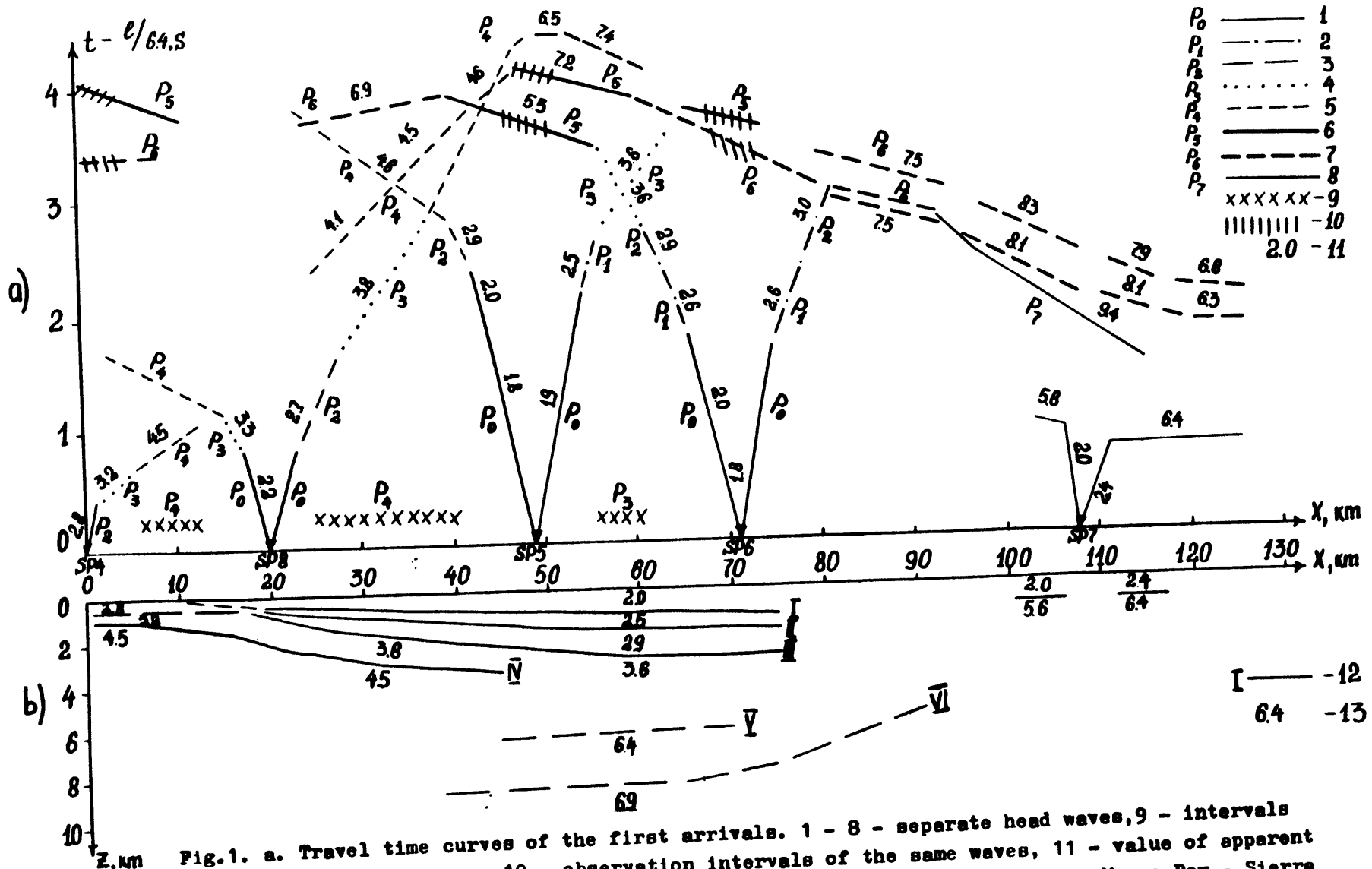

Fig.1. a. Travel time curves of the first arrivals. 1 - 8 - separate head waves, 9 - intervals of reversed curves, 10 - observation intervals of the same waves, 11 - value of apparent velocities, km/s. b. Schematic seismic cross-section along the profile Morro Bay - Sierra Nevada (interval SP4 - SP7), 12 - sharp interfaces, 13 - value of boundary velocities, km/s

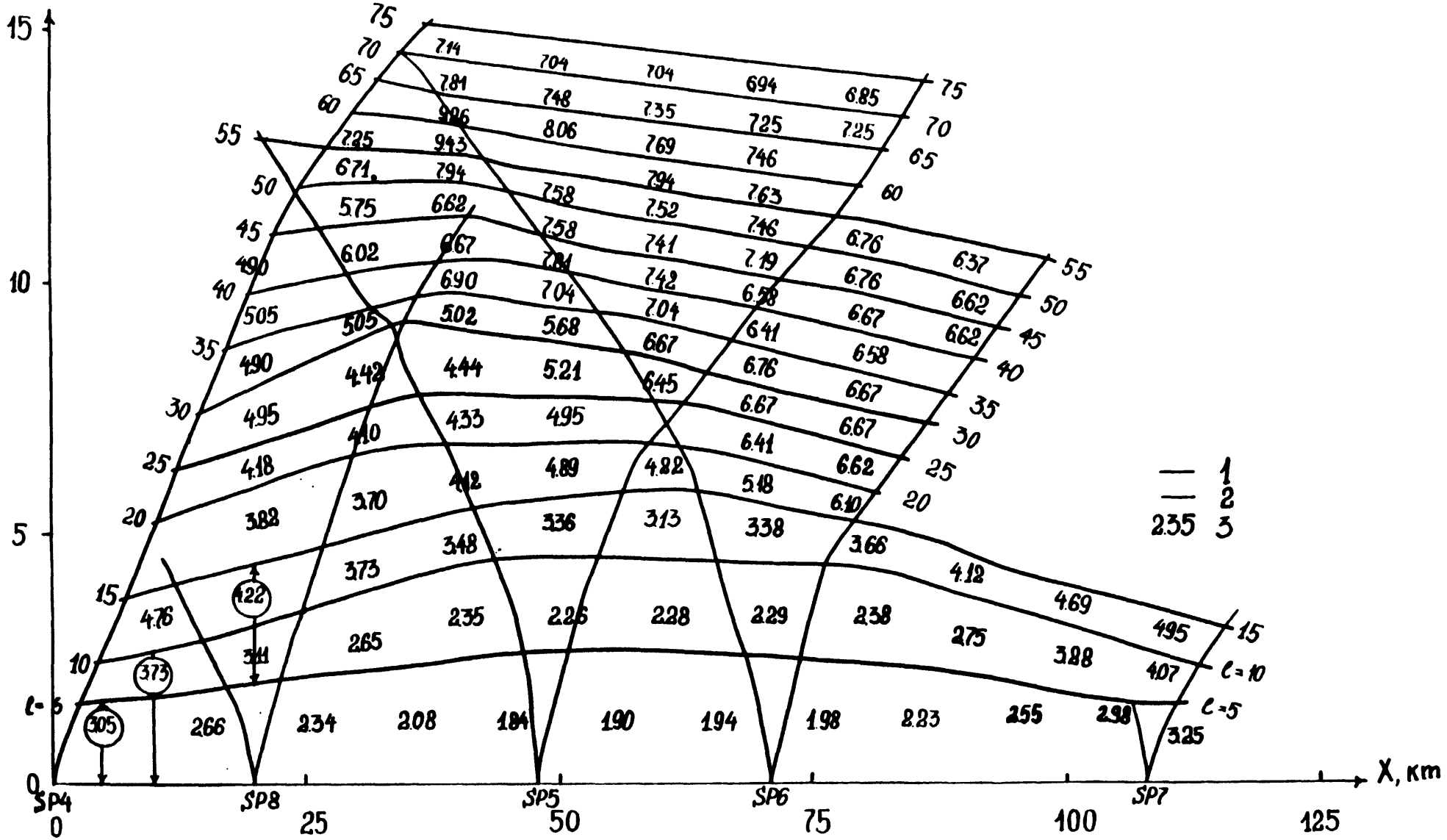

Fig.2 Time field t(x,z·) of the first arrivals. 1 - line l=const, 2 -travel time curves t(l), inversed time field gradient (layer velocity),km/s.

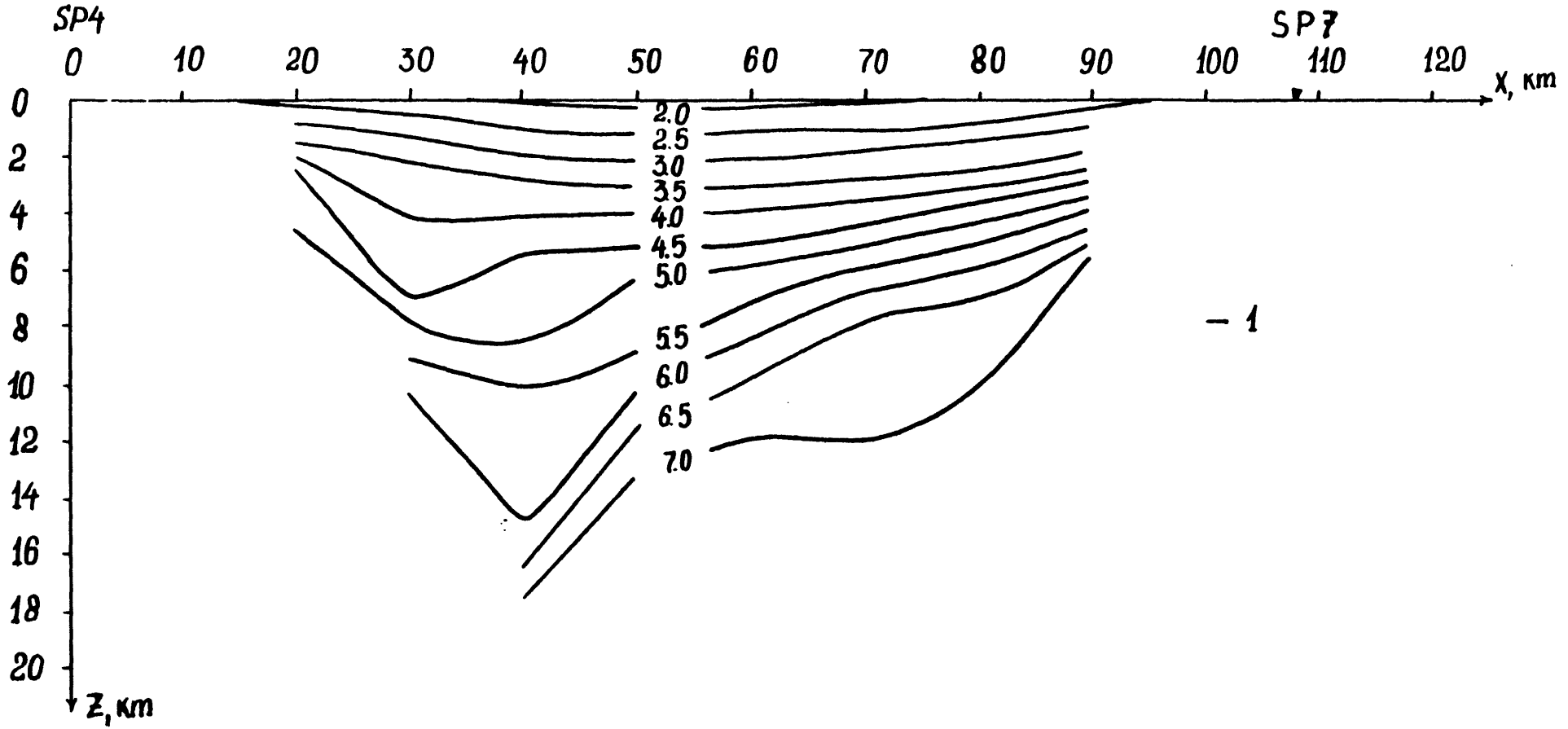

Fig.3 Cross-section v(x,z) along the profile Morro Bay - Sierra Nevada (interval SP4 - SP7)
1 - isoline v=const,km/s.

Image processing of seismic-reflection data from line SJ-6, California, USA

Akira Ikami
School of Science, Nagoya University, Nagoya 464, Japan

This paper reports on an image analysis of a sample of seismic-reflection data from line SJ-6. The data was available only in paper record-section format, so the reflection image was digitized with an optical scanner. At a given sample point, the output of the scanner was reduced to two levels (0 and 1); one binary word of computer memory contained information on 16 image points.

The algorithm adopted for processing the image is simple: first, the data points are stored in a matrix A(i,j), where i is taken from top to bottom and j, from left to right. The matrix elements have values of 0 or 1 to respectively indicate a low inter-signal level or a high intra-signal level. The algorithm then uses a second matrix, B(i,j), to store the transformation of the image as follows: (1) where three continuous points in the j-direction have high levels, the high level is expanded to include five points to emphasize the horizontal continuation of the reflected signals, that is, if A(i,j-1)*A(i,j)*A(i,j+1) =1, then A(i,j-2) to A(i,j+2) are set to high level; (2) where one of three continuous points in the i-direction has a low level, all three points are set to low level. This second step is carried out from top to bottom, overwriting 0 or 1 on the matrix B(i,j), with the result that the upper side of the high-level positions remain as they were, but the high-level image becomes thinner because information is faded away from the lower side of the reflection.

Figure 1 shows the successive transformations of the digital image: Figure 1(a) is the original data; Figure 1(b) the result after emphasizing horizontal continuity (step 1); and Figure 1(c) to 1(f) the transformed digital images processed by fading away the non-reflected waves (step 2) one, two, three and four iterations, respectively.

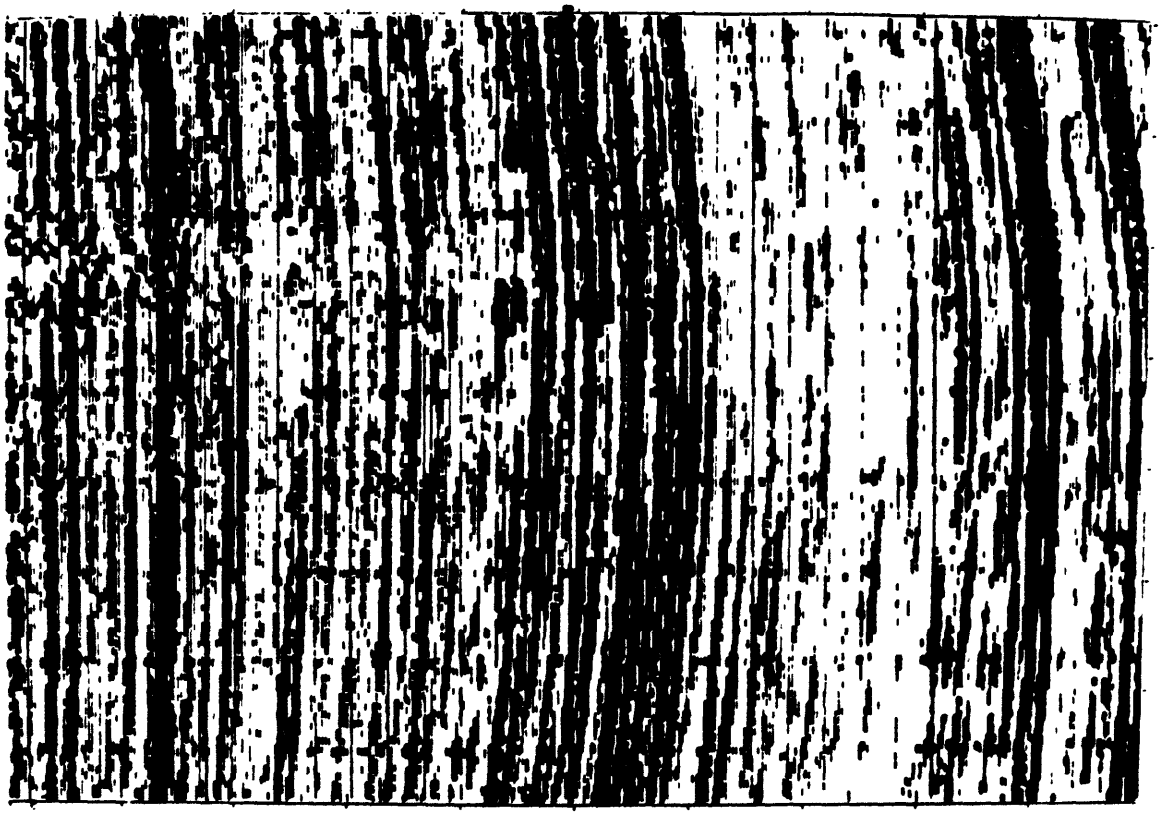

Figure 1(b)

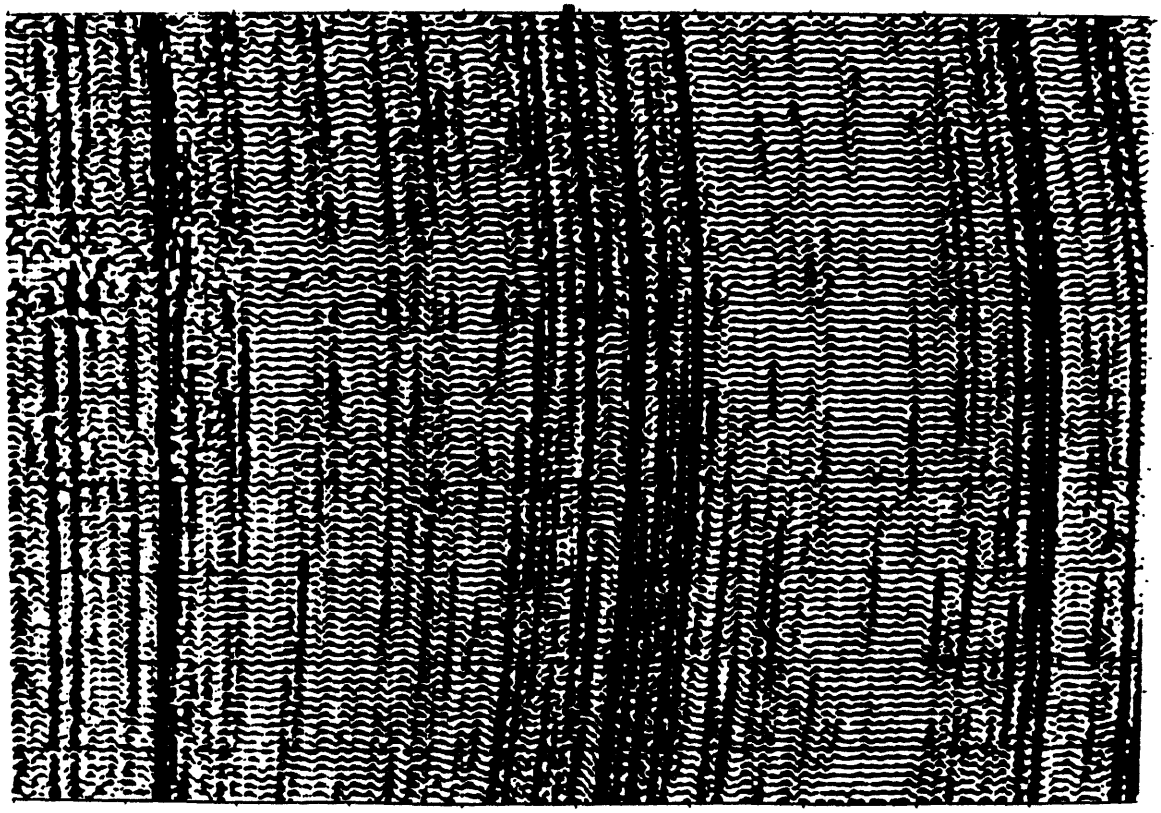

Figure 1(a)

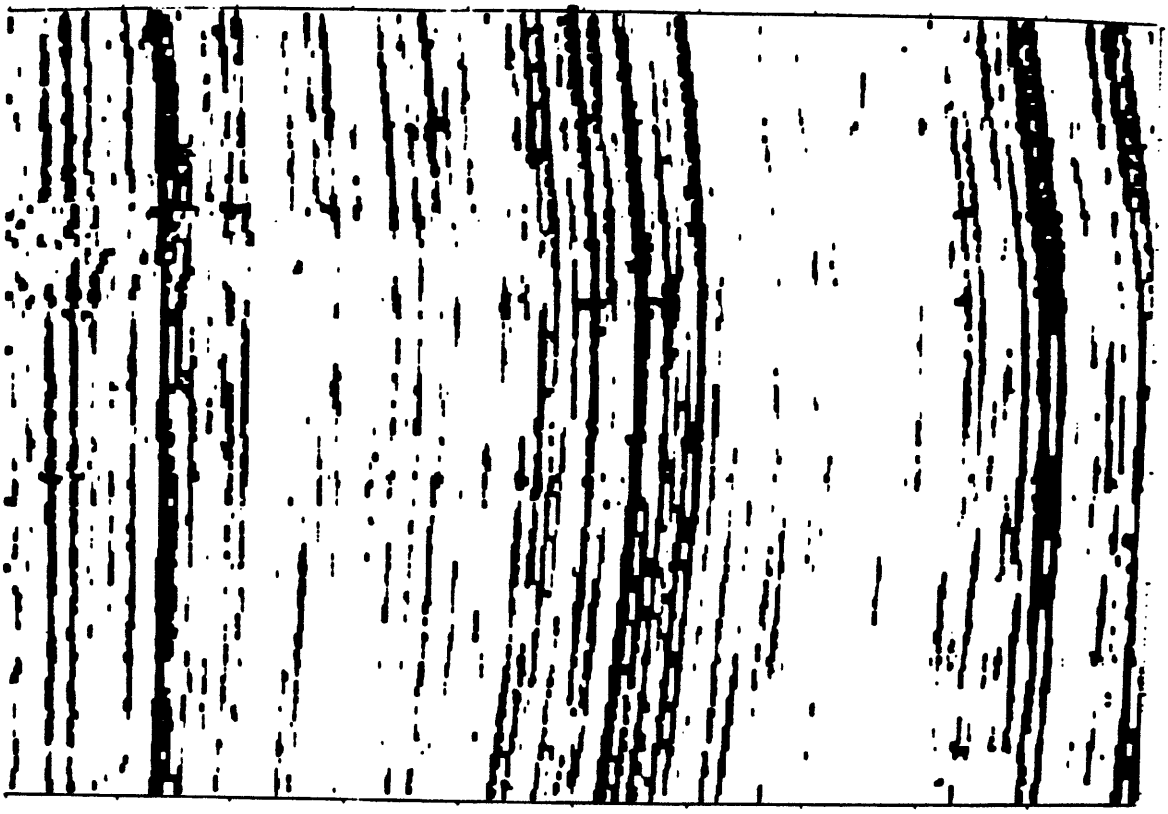

Figure 1(d)

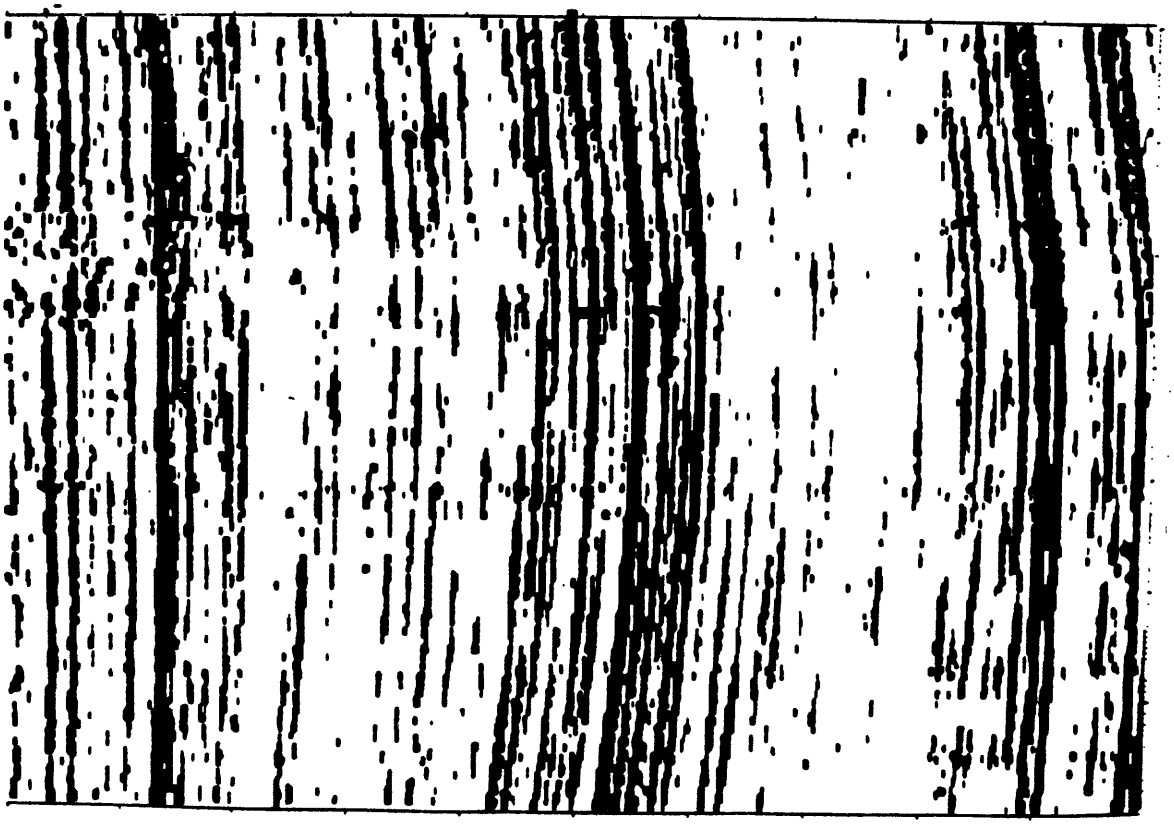

Figure 1(c)

Figure 1(f)

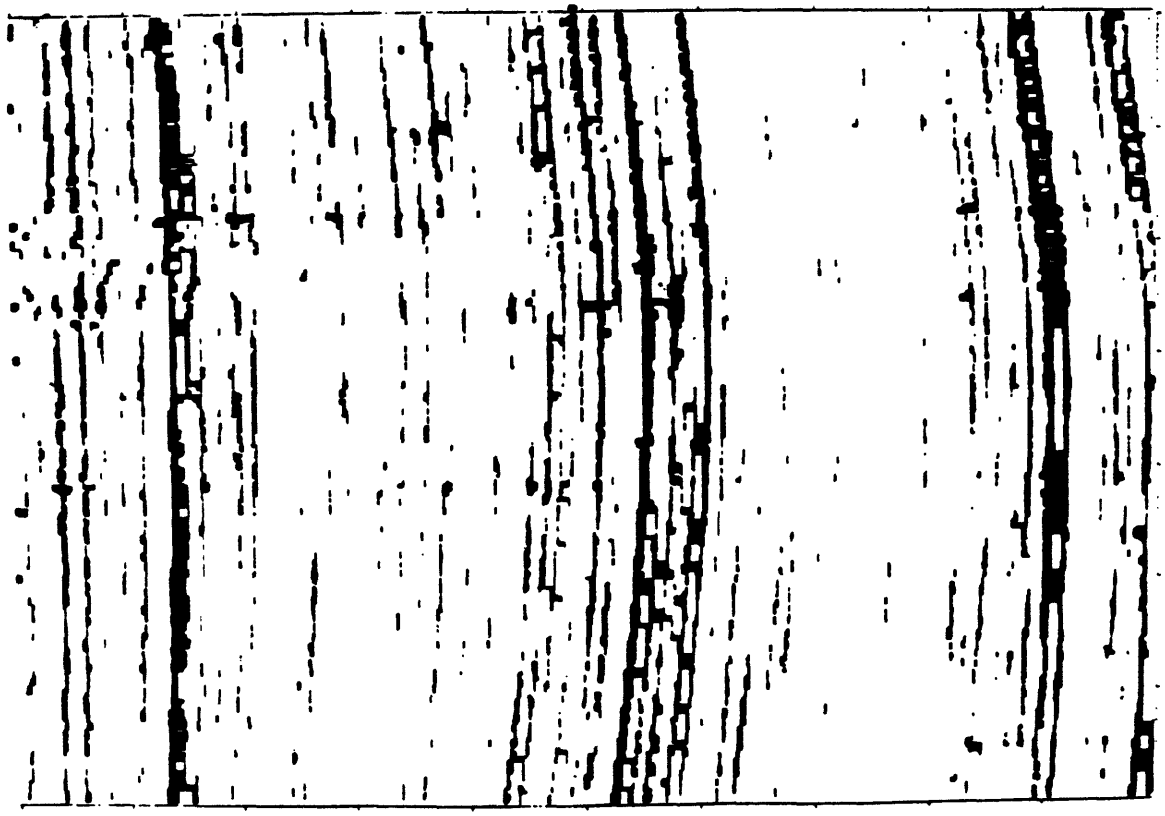

Figure 1(e)